UNIVERSITA' DEGLI STUDI DI BARI ALDO MORO

Dipartimento di Scienze del Suolo, della Pianta e degli Alimenti

DOTTORATO DI RICERCA IN SCIENZE DEL SUOLO E DEGLI ALIMENTI

CICLO XXXVIII

Settore Scientifico Disciplinare CHEM-01/A

CHARACTERIZATON OF NUTRACEUTICALS IN INNOVATIVE VEGETABLES (BRASSICA SP.) BY ADVANCED MASS SPECTROMETRY-BASED METABOLOMICS

Dottoranda: Dott.ssa Valeria Cinquepalmi

VALERIA CINQUEPALMI 20.04.2026 10:53:59 GMT+02:00

Supervisore: Ch.mo Prof. Ilario Losito

ILARIO LOSITO 20.04.2026 13:46:14 GMT+02:00

Coordinatore: Ch.ma Prof.ssa Erica Pontonio

ERICA PONTONIO 20.04.2026 13:08:13 GMT+01:00

ESAME FINALE 2026

Finanziato dall'Unione Europea - Next Generation EU, Missione 4 Componente 2, CUP H93C22000440007 Investimento 3.3 D.M. n. 352 del 9 Aprile 2022 – Piano Nazionale di Ripresa e Resilienza. Progetto:"Centro Nazionale per lo sviluppo delle Nuove Tecnologie in Agricoltura (AGRITECH)"

Index

Foreword……..…1

References…….....9

Chapter 1……...12

Investigation on characteristic fragmentation routes of cholesterol and phytosterols based on liquid chromatography-APCI-multistage mass spectrometry of selected 4-desmethyl-sterols and their deuterium-labelled analogues

1.1 Introduction……..13
1.2 Materials and Methods……16
1.2.1. Chemicals……...…16
1.2.2. Standard solutions preparation……...…17
1.2.3. RPLC-APCI-MS instrumentation and operating conditions……..17
1.3 Results and discussion……..18
1.3.1. RPLC-APCI(+)-FTMS analysis of standard sterols……...18
1.3.2. Fragmentation of Δ^5-sterols with saturated and unbranched side chain: cholesterol and hexa-deuterated cholesterol……..……...21
1.3.3. Fragmentation of Δ^5-sterols with a methyl or ethyl group at C24: campesterol and β-sitosterol……..…….....32
1.3.4. Fragmentation of Δ^5-sterols with a double bond at C22-C23: stigmasterol/ penta-deuterated stigmasterol and brassicasterol……...….36
1.3.5. Fragmentation of Δ^5-sterols and Δ^7-sterols with a double bond at C24-24': isofucosterol (Δ^5-avenasterol) and Δ^7-avenasterol……..…….....42
1.3.6. Correlation between specific product ions and structural features of 4-desmethyl sterols……..……....45
1.4 Conclusions……...…….....48
References……...50

Appendix 1……..56

Chapter 2……90

Study of diagnostic fragmentations of animal and fungal sterols/stanols obtained by APCI-tandem mass spectrometry to infer general rules for unknown free sterols identification

2.1 Introduction……..91
2.2 Materials and Methods……94
2.2.1. Chemicals……...94
2.2.2. Standard solutions preparation……95
2.2.3. Extraction of free sterols from baker's yeast……95
2.2.4. RPLC-APCI-MS^n instrumentation and operating conditions……95
2.3 Results and discussion……..97
2.3.1. RPLC-APCI(+)-FTMS analysis of standard sterols/stanols: chromatographic considerations……97

2.3.2. Fragmentation of Δ^7-sterols with Saturated and Unbranched Side Chain: Lathosterol……..……...101
2.3.3. Fragmentation of stanols with saturated and unbranched side chains: coprostanol and cholestanol……..106
2.3.4. Fragmentation of Δ^5- and Δ^8-sterols with a double bond at C24-C25: desmosterol, zymosterol and lanosterol……109
2.3.5. Fragmentation of $\Delta^{5,7}$-sterols with a double bond at C22-C23: ergosterol……..….116
2.3.6. Fragmentation of Δ^5-sterols with a double bond at C24–C24′ (methylene group at C24): chalinasterol……118
2.3.7. Identification of sterols in baker's yeast based on chromatographic and tandem MS data……120
2.3.8. Correlation Between Specific Product Ions and Structural Features of Major Animal, Fungal and Vegetal Sterols……123
2.4 Conclusions……..…132

References……..133

Appendix 2……....139

Chapter 3……..154

Comparative quantitative study of free sterols in kale and broccoli raab across growth stages and processing conditions using RPLC-APCI-FTMS

3.1 Introduction……155
3.2 Materials and Methods……..158
3.2.1. Chemicals……158
3.2.2. Plant samples production……..……158
3.2.3. Sample preparation……...…159
3.2.4. Sample extraction……159
3.2.5. Standard solutions for calibrations……160
3.2.6. LC-MS instrumentation and operating conditions……....160
3.3 Results and discussion……....161
3.3.1. Identification of sterols by RPLC-APCI(+)-FTMS and FTMS/MS analysis……161
3.3.2. Quantification of sterols: method development and validation……168
3.3.3. RPLC-APCI-FTMS-based quantification of free sterols in microgreens, micro leaves, baby leaves and adult plants of kale and broccoli raab cultivated in the winter growing cycle……...171
3.3.4. Effect of cultivation season on the FS content in microgreens and micro leaves…176
3.3.5. Quantification of FSs in adult plants of kale and broccoli raab subjected to steaming or boiling in water……177
3.4 Conclusions……....179

References……..182

Appendix 3……....192

Chapter 4……..…199

Quantification of carotenoids and α-tocopherol in innovative and conventional Brassica vegetables by RPLC-APCI-FTMS

4.1 Introduction……...200
4.2 Materials and Methods…….....205
4.2.1. Chemicals……..205
4.2.2. Plants cultivation……...206
4.2.3. Sample preparation……..…….206
4.2.4. Sample extraction……..207
4.2.5. Standard solutions…….....207
4.2.6. RPLC-DAD-APCI-FTMS instrumentation and operating conditions……..…208
4.2.7. RPLC-ESI-TWIMS-MS and MS/MS instrumentation and operating conditions…209
4.2.8. Collision cross section calibration curve……..210
4.3 Results and discussion……...210
4.3.1. Identification of carotenoids and α-tocopherol by RPLC-DAD-APCI(+)-FTMS analysis…….....210
4.3.2. RPLC-ESI-TWIMS-MS and IMS-MS/MS analysis of carotenoid isomers…….223
4.3.3. Development and validation of a quantitative method for carotenoids……230
4.3.4. RPLC-APCI(+)-FTMS quantification of carotenoids and α-tocopherol in microgreens, micro leaves, baby leaves and adult plants of broccoli raab and kale……..……...236
4.3.5. Quantification of carotenoids and α-tocopherol in steamed and boiled broccoli raab and kale adult plants……...242
4.4 Conclusions……..245

References……...…...247

Appendix 4……....254

Concluding remarks…….……260

Foreword

In recent decades, in a social context increasingly influenced by health-conscious consumers, the concept of functional foods has gained significant importance. Functional foods are defined as foods containing bioactive ingredients that can support specific physiological functions beyond basic nutrition[1]. Their relevance arises as a response to certain lifestyles, including sedentary behaviours and the widespread consumption of highly processed foods, stimulating a growing interest in dietary strategies aimed at maintaining health and reducing chronic diseases. As a result, consumer demand has progressively shifted towards food products that are designed not only to provide nutrition, but also to actively contribute to long-term well-being. In this evolving nutritional landscape, functional foods have become a new paradigm, strengthening the link between diet and health through the targeted intake of bioactive compounds.

In this context, microgreens have emerged as a particularly promising category of functional foods. First introduced in California in the 1980s, they initially attracted attention for their intense flavours, vivid colours, and culinary versatility[2,3]. Their relevance soon extended beyond gastronomy, however, as scientific evidence demonstrated that microgreens often contain markedly higher concentrations of bioactive compounds than their mature counterparts, leading to their recognition as *superfoods*[2,4–6]. Microgreens are defined as tender seedlings harvested between 7 and 21 days after germination, depending on the species, when the cotyledonary leaves are fully expanded and the first true leaves have emerged[2,7,8]. Their short production cycle is a key advantage, allowing rapid production and continuous availability for an increasing number of persons. From an agronomic point of view, the cultivation of microgreens takes place in soilless systems, such as hydroponics, and requires low water consumption and zero agrochemicals, in line with eco-sustainable agricultural practices[2,9,10]. In hydroponic growing systems, precise regulation of growing conditions is allowed, modulating the phytochemical composition of microgreens through targeted biofortification strategies[11–13] or the use

of additional LED lights[14–17]. This flexibility allows the development of products with tailored nutraceutical profiles, potentially suitable for specific dietary needs. Additional benefits are related to post-harvest quality, as microgreens are typically marketed together with their growing medium and harvested immediately before consumption, minimizing degradation processes. In addition, their common consumption in raw form helps to preserve the thermolabile bioactive compounds, thus increasing their nutritional value[6,18,19].

Along with microgreens, other innovative plant products, corresponding to slightly more advanced growth stages, but still not comparable to that of adult plants, like micro leaves and baby leaves, have been considered for their nutraceutical potential. Among them, micro leaves represent a completely new category of vegetables, that are harvested in an intermediate phenological phase between microgreens and baby leaves, in particular between the formation of the first and fifth true leaves, and which are grown following the same eco-friendly practices as microgreens. To date, micro leaves have not yet been characterized, and their phytochemical profile remains largely unknown. This lack of scientific evidence makes them particularly attractive for investigation, with the aim of evaluating their nutraceutical potential and therefore cataloguing them as functional foods. In contrast, baby leaves represent a more established category of fresh vegetables and are clearly defined by European Regulation No. 752/2014 as "young leaves and petioles of any product, harvested up to the stage of the eighth true leaf". Baby leaves are generally cultivated in both soil-based and soilless systems under controlled environmental conditions; however, unlike microgreens and micro leaves, their production typically requires the use of agrochemicals to ensure yield stability and product quality[2]. Despite these differences in cultivation practices, baby leaves have been widely studied and are recognized as valuable alternatives to mature vegetables, often exhibiting comparable or even enhanced nutraceutical profiles, depending on the plant species and compound class considered[20,21].

In this context, the present PhD thesis aims to characterize nutraceutical compounds in innovative plant products, including microgreens, micro leaves and baby leaves, all grown using hydroponics, with the purpose of enhancing their health-promoting properties and supporting their role in modern

and sustainable diets. Particular attention is paid to vegetables belonging to *Brassicaceae*, a botanical family widely recognized for its remarkable richness in bioactive compounds[22–24]. *Brassica* vegetables are well known to accumulate high levels of polyphenols and glucosinolates, secondary metabolites widely associated with antioxidant, anti-inflammatory and anticancer activities. These compounds play a key role in the health benefits traditionally attributed to cruciferous vegetables and make this family an ideal model for nutraceutical investigations[12,25,26]. In this PhD project, kale (*Brassica oleracea* L. var. *acephala*) and broccoli raab (*Brassica rapa* L. subsp. *sylvestris* L. Janch. var. *esculenta Hort*.) were selected as representative species of the *Brassicaceae*. These vegetables are deeply rooted in the agri-food tradition of the Apulia region in Southern Italy, where this project was developed, and represent an important component of the local diet. In addition to their nutritional relevance, they represent valuable genetic resources, whose characterization contributes to the conservation and enhancement of local agrobiodiversity. By focusing on these native varieties, this PhD project not only aims to clarify the nutraceutical potential of innovative plant products at different stages of development, but also to support the sustainable exploitation and protection of regional plant biodiversity, strengthening the link between food quality, human health and territorial identity.

To address the complexity associated with the characterization of nutraceuticals in complex matrices, including vegetal ones, omics sciences represent an effective and comprehensive analytical framework. Omics technologies encompass a set of complementary approaches, such as genomics, transcriptomics, proteomics, metabolomics and its related branches (lipidomics, glycomics and peptidomics), that allow an integrated characterization of food matrices from a biological and chemical point of view[27]. Among them, metabolomics plays a fundamental role also in food and plant research, giving the opportunity to obtain a profile of the small molecules potentially responsible for the nutritional, functional and bioactive properties of foods. Indeed, metabolomics is defined as the discipline dedicated to the qualitative and quantitative analysis of low molecular weight compounds (generally <1-2 kDa), including endogenous metabolites and exogenous compounds resulting from

environmental or technological factors[28–30]. Metabolomic studies can be performed using either targeted or untargeted strategies, each offering distinct yet complementary information. Targeted metabolomics focuses on the analysis of defined classes of metabolites and relies on selective extraction procedures and well-established analytical protocols, ensuring high confidence in compound identification and accurate quantification. In contrast, untargeted metabolomics aims to reveal the broadest possible spectrum of metabolites, including unknown compounds, thereby enabling a comprehensive exploration of the plant metabolome[29]. The combination of targeted and untargeted approaches is particularly valuable in vegetable characterization, as it allows both qualitative and quantitative evaluation of metabolites, with special emphasis on endogenous bioactive compounds. This strategy not only contributes to the valorisation of the nutraceutical profile of vegetables but also facilitates the identification of discriminant metabolic biomarkers associated with specific phenological stages, supporting a deeper understanding of plant development and quality traits.

The present PhD project was designed to develop a targeted metabolomics approach, exploiting the strong synergy between metabolomics and advanced analytical techniques, such as liquid chromatography combined with high-resolution mass spectrometry (LC-HRMS), in order to identify and quantify bioactive metabolites in innovative plant products and their corresponding mature forms. In particular, two main classes of nutraceutical compounds were investigated, namely phytosterols and carotenoids, along with tocopherols, all of which are widely recognized for their beneficial effects on human health. Phytosterols are known for their ability to modulate cholesterol metabolism and for their anti-inflammatory and antioxidant properties, while carotenoids and tocopherols play a central role in the regulation of oxidative stress, visual function and the prevention of chronic degenerative diseases. In this context, the present PhD thesis was concerned with the development of targeted metabolic approaches aimed at characterizing phytosterols and carotenoids from both a qualitative and quantitative point of view, with the dual purpose of demonstrating their overall nutraceutical potential and discriminating the plant products collected in different phenological phases. On this

basis, the work is organized into four interconnected chapters, each addressing a distinct but complementary analytical objective within a unified research framework.

Chapter 1 is dedicated to the development of a reversed-phase liquid chromatography (RPLC) method for the separation of phytosterols, in particular free 4-desmethyl-sterols, followed by an in-depth investigation on their fragmentation achieved using high/low resolution instrumentation with tandem (MS/MS) and/or sequential (MS^n, with $n \geq 3$) mass spectrometry capabilities and equipped with an atmospheric pressure chemical ionization (APCI) source for analyte ionization. From a chromatographic perspective, RPLC analyses demonstrated that phytosterol separation is predominantly governed by hydrophobic interactions between the sterol side chain and the adopted octadecyl stationary phase. Subtle differences in side chain length, degree of unsaturation and branching lead to distinct retention behaviors, allowing the resolution of closely related structural sterols and isomers under optimized conditions. Although tandem mass spectrometry (MS/MS) has long been recognized as a powerful analytical tool for sterol analysis, the interpretation of phytosterol MS/MS spectra has remained incomplete due to their inherent structural complexity. For this reason, a systematic clarification of phytosterol fragmentation pathways was achieved by a synergistic combination of low- and high-resolution multistage mass spectrometry (MS^2–MS^4), following the APCI process. The use of standard isotopically labeled sterols allowed the identification of low-level diagnostic ions produced from the side chain and revealed unexpected charge localization sites beyond the classical C3 position (to which the sterol OH group is linked), including the side chain itself and the C17 atom (according to the conventional atom numbering recommended by IUPAC). Overall, this chapter will provide a detailed and comprehensive framework for the interpretation of the MS/MS spectra of phytosterols, laying the groundwork for the subsequent reliable identification of minor and isomeric sterols in complex plant matrices.

The research described in **Chapter 2** stemmed from the results of the study discussed in **Chapter 1**, aiming at the extension of the RPLC method and the Higher Collisional Energy Dissociation-High-resolution tandem mass spectrometry (HCD-HRMS/MS) approach to animal and fungal sterols and

stanols. These compounds were intentionally selected because they have structures complementary to those of phytosterols. Their characteristics (*e.g.,* the location of the unsaturation(s) on the steroid core and the nature of the side chain) expanded the explored scenario and provided further insights into the mechanisms of sterol fragmentation that cannot be fully captured by plant sterols alone. By systematically examining the HCD-MS/MS spectra of sterols and stanols, this chapter will describe additional diagnostic pathways of fragmentation that arise from both the steroid backbone and the side chain. The correlation between product-specific ions and well-defined structural motifs allowed the recognition of recurrent "cholesterol-like" and "stigmasterol-like" fragmentation behaviors. This resulted in a consistent and expandable database of product diagnostic ions and fragmentation rules, specifically designed to support the identification of sterols in complex matrices. Overall, the chapter will demonstrate how the combined analysis of phytosterols, animal and fungal sterols can contribute to the construction of a robust MS/MS database, aimed at the characterization of known and unknown sterols in complex matrices, even in the absence of analytical standards.

In **Chapter 3** the concepts and methods developed in **Chapters 1** and **2** will be applied to the acquisition of structural knowledge on free sterols detected in plant matrices and not corresponding to major species, easily recognizable through a comparison with standards. Afterwards, the identification and quantification of sterols in kale and broccoli raab harvested at different phenological stages, *i.e.,* microgreens, micro leaves, baby leaves and adult vegetables will be described, following a discussion about the validation of the RPLC-APCI-MS method in real matrices. The outcome of multivariate statistical analysis of quantitative data, conducted by principal component analysis (PCA) and leading to a clear distinction of the different phenological stages based on their sterol profiles will be also discussed, as well as the impact of culinary processing on sterol composition, assessed by extending the quantitative analysis to mature vegetables subjected to two common cooking methods, namely boiling and steaming.

In **Chapter 4** the focus of the targeted metabolomics investigation will be shifted to carotenoids and α-tocopherol, further bioactive compounds central to both plant physiology and human nutrition. The

chapter will be devoted to the identification and quantification of these two metabolites in kale and broccoli raab collected at different phenological stages and will thus describe, in its first part, the development and validation of an RPLC-APCI-FTMS method for the complete quantification of α-tocopherol and of a large panel of carotenoids, including several minor xanthophyll isomers. Particular emphasis was placed during this work on these minor isomers, which are often overlooked in routine analyses despite their contribution to the total carotenoid content and their potential relevance to the overall bioactivity of vegetables. The effect of cooking was also evaluated, revealing that heat treatments mainly target oxygenated carotenoids, with xanthophylls being more susceptible to degradation than carotenes. In parallel with the quantification, an in-depth qualitative investigation was conducted to improve the structural characterization of minor carotenoid isomers and will thus be the object of one of the chapter sections. In particular, chromatographic behavior and patterns related to in-source fragmentation were combined with UV-Vis spectroscopy, which provides information-rich fingerprints due to the inherent absorption properties of carotenoids. To overcome the inherent limitations of MS/MS in discriminating isomeric species, traveling-wave ion mobility spectrometry (TWIMS) and ion mobility spectrometry-tandem mass spectrometry (IMS–MS/MS) were also integrated into the analytical workflow. By introducing an additional separation dimension based on ion shape and collision cross section, ion mobility enabled the resolution of mobility-resolved species. As discussed in the chapter, this approach highlighted the presence of distinct protomers and produced different MS/MS spectra for individual mobility peaks, greatly increasing structural confidence in carotenoid isomers assignment. Finally, multivariate statistical analyses, including PCA and hierarchical clustering, evidenced a clear distinction of phenological stages and plant species based on their carotenoids profile, underlining the importance of comprehensive metabolomic approaches for the evaluation of plant-derived nutraceuticals.

It is finally worth noting that most results described in **Chapter 1**, **2**, **3** and **4** were produced in the laboratories of the SMART inter-department research center, located in the Chemistry Department of the University of Bari “Aldo Moro”, under the supervision of Prof. Ilario Losito. The ion mobility

experiments described in **Chapter 4** were conducted in the laboratories of the Department of Plant and Environmental Science of the University of Copenhagen, under the supervision of Prof. Jan Christensen and Prof. Nikoline Nielsen, during a 3-months research stay.
Microgreens, micro leaves, baby leaves and adult plants of kale and broccoli raab were provided by the research team coordinated by Prof. Pietro Santamaria of the Department of Soil, Plant and Food Science of the University of Bari "Aldo Moro".

A heartfelt recognition is addressed to all the people who have been part of this path and who, in different ways, have contributed to the realization of this doctoral thesis. Their support and collaboration have been invaluable over the years, allowing scientific and personal growth. Thank you.

References

(1) Kaur, S.; Das, M. Functional Foods : An Overview. *Food Sci. Biotechnol.* **2011**, *20* (4), 861–875. https://doi.org/10.1007/s10068-011-0121-7.

(2) Di Gioia, F.; Renna, M.; Santamaria, P. Sprouts, Microgreens and "Baby Leaf" Vegetables. *Minim. Process. Refrig. Fruits Veg.* **2017**, No. 11, 403–432. https://doi.org/DOI 10.1007/978-1-4939-7018-6_11.

(3) Choe, U.; Yu, L. L.; Wang, T. T. Y. The Science behind Microgreens as an Exciting New Food for the 21st Century. *J. Agric. Food Chem.* **2018**, *66* (44), 1–39. https://doi.org/10.1021/acs.jafc.8b03096.

(4) Ebert, A. W. Sprouts and Microgreens—Novel Food Sources for Healthy Diets. *Plants* **2022**, *11* (4), 1–35. https://doi.org/10.3390/plants11040571.

(5) Kyriacou, M. C.; Rouphael, Y.; Di Gioia, F.; Kyratzis, A.; Serio, F.; Renna, M.; De Pascale, S.; Santamaria, P. Micro-Scale Vegetable Production and the Rise of Microgreens. *Trends Food Sci. Technol.* **2016**, *57*, 103–115. https://doi.org/10.1016/j.tifs.2016.09.005.

(6) Teng, J.; Liao, P.; Wang, M. The Role of Emerging Micro-Scale Vegetables in Human Diet and Health Benefits - An Updated Review Based on Microgreens. *Food Funct.* **2021**, *12* (5), 1914–1932. https://doi.org/10.1039/d0fo03299a.

(7) Xiao, Z.; Lester, G. E.; Luo, Y.; Wang, Q. Assessment of Vitamin and Carotenoid Concentrations of Emerging Food Products: Edible Microgreens. *J. Agric. Food Chem.* **2012**, *60* (31), 7644–7651. https://doi.org/https://doi.org/10.1021/jf300459b.

(8) Treadwell, D. D.; Hochmuth, R.; Landrum, L.; Laughlin, W. Microgreens: A New Specialty Crop: HS1164, Rev. 9/2020. *Edis 2020* **2020**, No. 5, 1–3. https://doi.org/https://doi.org/10.32473/edis-hs1164-2020.

(9) Weber, C. F. Broccoli Microgreens: A Mineral-Rich Crop That Can Diversify Food Systems. *Front. Nutr.* **2017**, *4* (March), 1–9. https://doi.org/10.3389/fnut.2017.00007.

(10) Sharma, S.; Shree, B.; Sharma, D.; Kumar, S.; Kumar, V.; Sharma, R.; Saini, R. Vegetable Microgreens: The Gleam of next Generation Super Foods, Their Genetic Enhancement, Health Benefits and Processing Approaches. *Food Res. Int.* **2022**, *155* (111038), 1–18. https://doi.org/10.1016/j.foodres.2022.111038.

(11) Pannico, A.; El-Nakhel, C.; Graziani, G.; Kyriacou, M. C.; Giordano, M.; Soteriou, G. A.; Zarrelli, A.; Ritieni, A.; De Pascale, S.; Rouphael, Y. Selenium Biofortification Impacts the Nutritive Value, Polyphenolic Content, and Bioactive Constitution of Variable Microgreens Genotypes. *Antioxidants* **2020**, *9* (4). https://doi.org/10.3390/antiox9040272.

(12) Rouphael, Y.; Colla, G.; De Pascale, S. Sprouts, Microgreens and Edible Flowers as Novel Functional Foods. *Agronomy* **2021**, *11* (12), 2–5. https://doi.org/10.3390/agronomy11122568.

(13) Renna, M.; Castellino, M.; Leoni, B.; Paradiso, V. M.; Santamaria, P. Microgreens Production with Low Potassium Content for Patients with Impaired Kidney Function. *Nutrients* **2018**, *10* (6). https://doi.org/10.3390/nu10060675.

(14) Samuoliene, G.; Brazaityte, A.; Jankauskiene, J.; Viršile, A.; Sirtautas, R.; Novičkovas, A.; Sakalauskiene, S.; Sakalauskaite, J.; Duchovskis, P. LED Irradiance Level Affects Growth and Nutritional Quality of Brassica Microgreens. *Cent. Eur. J. Biol.* **2013**, *8* (12), 1241–1249. https://doi.org/10.2478/s11535-013-0246-1.

(15) Zhang, X.; Bian, Z.; Yuan, X.; Chen, X.; Lu, C. A Review on the Effects of Light-Emitting Diode (LED) Light on the Nutrients of Sprouts and Microgreens. *Trends Food Sci. Technol.* **2020**, *99* (February), 203–216. https://doi.org/10.1016/j.tifs.2020.02.031.

(16) Brazaityte, A.; Sakalauskiene, S.; Samuoliene, G.; Jankauskiene, J.; Viršile, A.; Novičkovas, A.; Sirtautas, R.; Miliauskiene, J.; Vaštakaite, V.; Dabašinskas, L.; Duchovskis, P. The Effects of LED Illumination Spectra and Intensity on Carotenoid Content in Brassicaceae Microgreens. *Food Chem.* **2015**, *173*, 600–606. https://doi.org/10.1016/j.foodchem.2014.10.077.

(17) Samuolienė, G.; Viršilė, A.; Brazaitytė, A.; Jankauskienė, J.; Sakalauskienė, S.; Vaštakaitė, V.; Novičkovas, A.; Viškelienė, A.; Sasnauskas, A.; Duchovskis, P. Blue Light Dosage Affects Carotenoids and Tocopherols in Microgreens. *Food Chem.* **2017**, *228*, 50–56. https://doi.org/10.1016/j.foodchem.2017.01.144.

(18) Paradiso, V. M.; Castellino, M.; Renna, M.; Gattullo, C. E.; Calasso, M.; Terzano, R.; Allegretta, I.; Leoni, B.; Caponio, F.; Santamaria, P. Nutritional Characterization and Shelf-Life of Packaged Microgreens. *Food Funct.* **2018**, *9* (11), 5629–5640. https://doi.org/10.1039/c8fo01182f.

(19) Renna, M.; Paradiso, V. M. Ongoing Research on Microgreens: Nutritional Properties, Shelf-Life, Sustainable Production, Innovative Growing and Processing Approaches. *Foods* **2020**, *9* (6), 1–5. https://doi.org/10.3390/foods9060826.

(20) Martínez-Sánchez, A.; Gil-Izquierdo, A.; Gil, M. I.; Ferreres, F. A Comparative Study of Flavonoid Compounds, Vitamin C, and Antioxidant Properties of Baby Leaf Brassicaceae Species. *J. Agric. Food Chem.* **2008**, *56* (7), 2330–2340. https://doi.org/10.1021/jf072975+.

(21) Aires, A.; Carvalho, R.; Rosa, E. A. S.; Saavedra, M. J. Phytochemical Characterization and Antioxidant Properties of Baby-Leaf Watercress Produced under Organic Production System. *CYTA - J. Food* **2013**, *11* (4), 343–351. https://doi.org/10.1080/19476337.2013.769025.

(22) Saban, G. M.; Sanlier, N. The Benefits of Brassica Vegetables on Human Health. *J Hum. Heal. Res* **2018**, *1* (1), 104.

(23) Jahangir, M.; Kim, H. K.; Choi, Y. H.; Verpoorte, R. Health-Affecting Compounds in Brassicaceae. *Compr. Rev. Food Sci. Food Saf.* **2009**, *8* (Ferguson 1999), 31–43. https://doi.org/https://doi.org/10.1111/j.1541-4337.2008.00065.xDigital Object Identifier (DOI).

(24) Ramirez, D.; Abellán-Victorio, A.; Beretta, V.; Camargo, A.; Moreno, D. A. Functional Ingredients from Brassicaceae Species: Overview and Perspectives. *Int. J. Mol. Sci.* **2020**, *21* (6), 1–21. https://doi.org/10.3390/ijms21061998.

(25) Turner, E. R.; Luo, Y.; Buchanan, R. L. Microgreen Nutrition, Food Safety, and Shelf Life: A Review. *J. Food Sci.* **2020**, *85* (4), 870–882. https://doi.org/10.1111/1750-3841.15049.

(26) Galieni, A.; Falcinelli, B.; Stagnari, F.; Datti, A.; Benincasa, P. Sprouts and Microgreens: Trends, Opportunities, and Horizons for Novel Research. *Agronomy* **2020**, *10* (9), 1–45. https://doi.org/10.3390/agronomy10091424.

(27) Creydt, M.; Fischer, M. Omics Approaches for Food Authentication. *Electrophoresis* **2018**, *39* (13), 1569–1581. https://doi.org/10.1002/elps.201800004.

(28) Wishart, D. S. Metabolomics: Applications to Food Science and Nutrition Research. *Trends Food Sci. Technol.* **2008**, *19* (9), 482–493. https://doi.org/10.1016/j.tifs.2008.03.003.

(29) Hu, S.; Liu, C.; Liu, X. Innovative Application of Metabolomics on Bioactive Ingredients of Foods. *Foods* **2022**, *11* (19). https://doi.org/10.3390/foods11192974.

(30) Bok, K.; Ye, L.; Kim, J.; Jin, H.; Choi, J.; Kwang, J. Phytochemical Profiles of Brassicaceae Vegetables and Their Multivariate Characterization Using Chemometrics. *Appl. Biol. Chem.* **2018**, *61* (2), 131–144. https://doi.org/10.1007/s13765-017-0340-6.

Chapter 1

Investigation on characteristic fragmentation routes of cholesterol and phytosterols based on liquid chromatography-APCI-multistage mass spectrometry of selected 4-desmethyl-sterols and their deuterium-labelled analogues

The following journal article was based on results illustrated in the present chapter:

V. Cinquepalmi, I. Losito, A. Castellaneta, C. D. Calvano, T.R.I. Cataldi, "APCI-multistage mass spectrometry following liquid chromatography for selected 4-desmethyl-sterols and their deuterium-labelled analogues unveils characteristic fragmentation routes for cholesterol and phytosterols identification", *Rapid Communications in Mass Spectrometry*, *39*(13), e10039, doi: https://doi.org/10.1002/rcm.10039.

1.1 Introduction

Phytosterols (PSs) are sterols occurring in plant cell membranes, particularly in raft domains[1]. These ordered and nanoscale regions, where PSs exhibit association with sphingolipids and proteins, play a role in key cellular processes such as plant growth and development, signal transduction in response to environmental stresses and cell-to-cell communication through plasmodesmata[2,3]. As shown in **Figure 1**, PSs share the tetracyclic structure of cyclopenta[α]phenanthrene, in which *trans* junctures connect the four rings (A, B, C and D), two methyl groups are located at C18 and C19 and a side chain (SC) is linked to C17, according to the atom numbering recommended by the International Union of Pure and Applied Chemistry (IUPAC)[3-5]. Among PSs, free sterols (FSs) are characterized by a hydroxyl group at C3 having β stereochemistry[6], that can be either esterified by a free fatty acid, giving a steryl ester, or form a 1-*O*-β-glycosidic bond with a hexose, generating a steryl glycoside. If an acyl chain is bound to the C6' of the sugar, acylated steryl glycosides are obtained[7,8]. FSs can be generally subdivided in 4-desmethyl, 4α-methyl and 4,4-dimethyl sterols, depending on the number of substituents at C4[9], although the latter two species, acting as precursors of 4-desmethyl sterols, are scarcely present in plant tissues[10]. Among 4-desmethyl-sterols, Δ^5-, Δ^7-, $\Delta^{5,7}$- and Δ^8-sterols include one or two C=C bonds on the B ring (see **Figure 1**), distinguishing them from stanols, their saturated counterparts[8]. However, most of the over 250 PSs identified in nature so far[11] are Δ^5-4-desmethyl-sterols, which differ from each other for their side chain (SC), as shown in **Figure 1** for some of the most important FSs.

Cholesterol, the simplest species among Δ^5-sterols, characterized by an unsaturated and unbranched SC and representing the most abundant sterol in animal tissues, is also present, in low amounts, in plant cells[1,12]. As evidenced in **Figure 1**, the presence of a methyl or an ethyl group linked to C24 of cholesterol leads to the structures of campesterol and β-sitosterol, which are among the most abundant PSs[11]. The methylation reaction at C24 may generate both α and β epimers, while the introduction of an ethyl substituent preferentially produces α epimers[4]. Other relevant PSs are brassicasterol and

stigmasterol, corresponding to the unsaturated analogues of campesterol and β-sitosterol, respectively, both having a double bond on C22-C23[5,6] (see **Figure 1**). Modification of C24 may also introduce an ethylidene group, leading to isofucosterol, also known as Δ^5-avenasterol, representing another non negligible PS, often accompanied by its positional isomer Δ^7-avenasterol, having a C=C bond between C7 and C8 on ring B (see **Figure 1**).

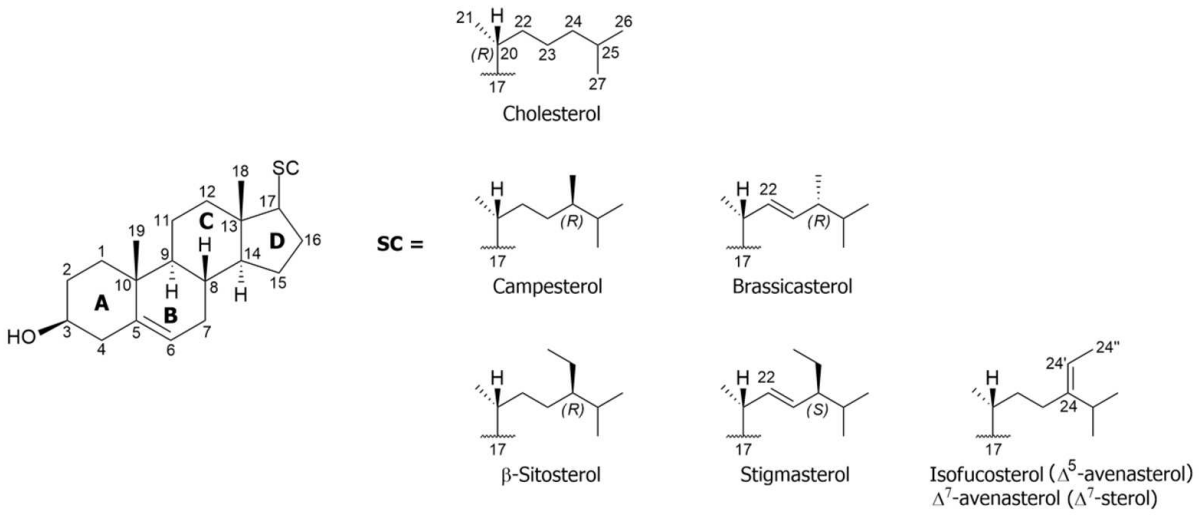


Figure 1. Left side) General chemical structure of Δ^5-desmethyl-sterols. Carbon atoms are numbered according to the rules established by IUPAC in 1989. Right side) side chain (SC) structures and common names for sterols considered in the present chapter. Δ^7-avenasterol shares the side chain with isofucosterol but has the C=C double bond on a different position of ring B (between C7 and C8). The numbering of all atoms on the side chain is shown in the case of cholesterol. The C24 configuration is highlighted in the case of campesterol, brassicasterol, β-sitosterol and stigmasterol.

The structural variability of PSs poses a challenge for their qualitative/quantitative analysis in plant extracts, aiming at the assessment of their nutraceutical potential, since PSs have been reported to lower cholesterol levels and exert anti-obesity, anti-inflammatory and anti-cancer activities[13–15].

Gas chromatography coupled with electron ionization mass spectrometry (GC-EI-MS) has long been the conventional method for sterol analysis, including PSs. In fact, major sterols can be separated effectively using low-medium polarity GC columns[11,16–20], provided they are preliminarily derivatized to trimethylsilyl (TMS) ethers or steryl acetates to enhance volatility and ionization efficiency[21,22]. With the advent of soft Atmospheric Pressure Ionization (API) sources, suitable for

the coupling between liquid chromatography and mass spectrometry, reverse phase liquid chromatography (RPLC) based on C8 or C18 stationary phases has emerged as a powerful alternative[1,23]. This approach eliminates the risks of incomplete derivatization and thermal degradation related to GC conditions. Among API processes, Electrospray Ionization (ESI) is usually performed on sterols after chemical derivatizations, such as the generation of picolinic esters, aimed at boosting the ionization efficiency[24–26]. Proton and sodium adducts are usually produced by sterols under positive ESI conditions[27,28]. Atmospheric pressure chemical ionization (APCI) in positive mode has significantly increased sensitivity (up to two orders of magnitude), leading only to the protonation of the sterols OH group, followed by in- source loss of water to form $[M+H-H_2O]^+$ ions[9,29,30]. As a result, RPLC-APCI-MS has become a popular method for identifying FSs in food products, including plant-based ones, although their quantification is limited to species for which standards are available[27,31–38].

Actually, the occurrence of several FS isomers, some of which not corresponding to available standards, is common in complex matrices like plant extracts. Tandem mass spectrometry (MS/MS), successfully adopted so far for the analysis of other lipid compounds, like glycerophospholipids, glycerolipids and sulfolipids[39–47], represents a promising approach to recognize structural features of sterols, even for species not matching available standards. However, to the best of our knowledge, only two studies have delved so far into a detailed characterization of MS/MS spectra obtained for FSs, which can be complex, due to the progressive fragmentation of their structures. Jiang *et al.*[30] used high resolution APCI-MS/MS relying on the so-called higher collisional energy dissociation (HCD) mode enabled by the Thermo Scientific Q-Exactive quadrupole-Orbitrap mass spectrometer (which actually corresponds to a typical collisionally-induced dissociation (CID) in terms of the ion energies involved) and APCI-MS^n (with n = 2, 3) based on a quadrupole-linear ion trap mass spectrometer to reconstruct the fragmentation patterns of stigmasterol, brassicasterol, β-sitosterol and campesterol. Munger *et al.*[48] compared CID-MS/MS spectra obtained for ESI-generated positive precursor ions of the aglycones of dietary steryl glycosides with those related to protonated and

dehydrated FS ions, which are isomeric with the aglycone ions. These studies highlighted product ions providing insights into the number and position of double bonds on the B ring of the sterol structure. Product ions related to neutral losses occurring from the side chain structure of sterols were also evidenced[48], suggesting that a careful interpretation of the sterol complex fragmentation patterns might yield valuable structural information.

Starting from this background, a systematic evaluation of fragmentation patterns of specific phytosterol standards has been undertaken during this thesis work using APCI-tandem/sequential mass spectrometry (APCI-MS^n, with n = 2-4). These experiments were performed under different mass resolution conditions. Cholesterol-d_6 and stigmasterol-d_5, isotopically labelled on the respective side chains, were also included among the analyzed species to clarify some of the fragmentation pathways. A detailed interpretation of the fragmentation patterns observed for FSs will be discussed in the present chapter, with a focus on the unexpected product ions arising from the sterol side chain. The latter suggested different possible locations of the positive charge of $[M+H-H_2O]^+$ ions of FSs. The differences observed for major Δ^5-sterols, as well as between them and Δ^7-avenasterol, will also be discussed, to provide general guidelines that might assist in identifying structural features of uncommon sterols, particularly when standards are unavailable.

1.2 Materials and methods

1.2.1 Chemicals. LC grade acetonitrile (ACN), water (H_2O) and formic acid (FA), used for RPLC separations, HPLC grade chloroform ($CHCl_3$) and ethanol (EtOH), employed as solvents for stock solutions were purchased from Merck (Milan, Italy). Standards of cholesterol-d_6 (cholest-5-en-26,26,26,27,27,27-d_6-3β-ol), cholesterol (cholest-5-en-3β-ol), campesterol (campest-5-en-3β-ol), brassicasterol (ergosta-5,22E-dien-3β-ol), β-sitosterol (stigmast-5-en-3β-ol), stigmasterol (stigmasta-5,22E-dien-3β-ol), isofucosterol (24Z-ethylidene-cholest-5-en-3β-ol) and Δ7-avenasterol (24Z-ethylidene-cholest-7-en-3β-ol) were acquired from Cayman Chemical (Ann Arbor, USA). Standard

stigmasterol-d_5 (stigmasta-5,22E-dien-24',24',24",24",24"-d_5-3β-ol) was purchased from Merck (Milan, Italy). The solutions required for the calibration of mass spectrometers under positive or negative polarity conditions were purchased from Thermo Scientific (Waltham, MA).

1.2.2 Standard solutions preparation. A stock solution of each standard (1 mg/mL) was prepared in an EtOH:$CHCl_3$ mixture (2:1 v/v) and a diluted solution (30 µg/mL) was subsequently obtained in 100% ACN. Moreover, through appropriate dilutions from stock solutions, a comprehensive mix of standards (10 µg/mL for each one) was prepared in 100% ACN.

1.2.3 RPLC-APCI-MS instrumentation and operating conditions. Mixtures of standard sterols were analysed using an Ultimate 3000 HPLC system coupled with a Q Exactive high-resolution quadrupole-Orbitrap Fourier-transform mass spectrometer through an APCI interface (Thermo Fisher, West Palm Beach, CA). A C18 Ascentis Express HPLC column (150 × 2.1mm i.d., 2.7µm particle size) (Supelco, Bellefonte, PA) and the following multistep binary elution gradient, based on H_2O as phase A and ACN as phase B, both containing 0.1% (v/v) FA, were adopted for the separation of FSs: 0-40 min, linear increase of B from 90% to 100%; 40-50 min, isocratic at 100% B; 50-52 min, linear decrease of B from 100% to 90%; 52−60 min, reconditioning at 90% B. Flow rate was set at 0.250 mL/min and column temperature was kept at 30°C; 5 µL sample volumes were injected. The parameters of the APCI interface and of the ion optics of the Q Exactive spectrometer were set as follows: sheath gas flow rate) 40 a.u.; auxiliary gas flow rate) 10 a.u.; capillary temperature) 300 °C; S-lens RF Level) 55 a.u.; vaporizer temperature) 250°C. Full scan MS acquisitions in positive ion mode were obtained in a 250-500 *m/z* interval, working with a 140000 resolving power at *m/z* 200; the Automatic Gain Control (AGC) level was set at 1×10^6 and the maximum injection time was 100 ms. HCD-FTMS/MS acquisitions were performed at a 35000 resolving power in a 50−500 *m/z* interval, selecting a 1.0 *m/z* isolation window for precursor ions and using normalized collisional energy (NCE) at a value of 30 units; the AGC level was set at 2×10^5 and maximum injection time

was 100 ms. The spectrometer was calibrated every two days by infusing, at a 30 μL/min flow rate, calibration solutions for positive or negative polarity acquisitions provided by the instrument manufacturer, thus obtaining a mass accuracy always better than 5 ppm.

APCI-direct infusion analyses (APCI-DIA) of individual standards solutions (30 μg/mL) were performed using both the Q-Exactive spectrometer, under the same conditions described before, and a Velos Pro mass spectrometer, equipped with a two-stage linear ion trap (Thermo Fisher, West Palm Beach, CA). Specifically, APCI-DIA-HCD-FTMS/MS spectra were collected for specific sterols (*vide infra*) in the former case, whereas APCI-DIA-CID-MS^n (n = 2,4) experiments were performed with the linear ion trap instrument, in order to elucidate major fragmentation patterns of all available FSs. The main operating parameters of the Velos Pro APCI interface and ion optics were set as follows: sheath gas flow rate) 40 a.u.; auxiliary gas flow rate) 10 a.u.; capillary temperature) 300 °C; S-lens RF Level) 60 a.u.; vaporizer temperature) 250°C. A 1.0 *m/z* isolation window for the precursor ion and a normalized collisional energy (NCE) of 40 units for MS/MS and 25 units for MS^3/MS^4 were adopted; the AGC level was set at 2×10^3 and the maximum injection time was 100 ms.

1.3 Results and discussion

1.3.1 RPLC-APCI(+)-FTMS analysis of standard sterols. As a first step of the present study RPLC-APCI(+)-FTMS was carried out on a mixture of standard sterols to explore the relationship between structure and retention time. Firstly, an isocratic separation based on 100% ACN containing 0.1% FA was attempted. However, a complete overlap was observed for peaks of positional isomers isofucosterol (Δ^5-avenasterol) and Δ^7-avenasterol, which share the same side chain (see **Figure 1**). After several tests based on gradient elution, with water added to mobile phase as the second solvent, suitable chromatographic conditions were identified, as detailed in the experimental section, allowing an effective separation of the two avenasterols. **Figure 2** shows multiple-Extracted Ion Current (EIC) chromatograms finally obtained for monoisotopic *m/z* ratios referred to the $[M+H-H_2O]^+$ ions

generated by APCI for standard sterols, grouped according to the characteristics of their side chain: A) not alkylated on C24; B) 24-methyl; C) 24-ethylidene and 24-ethyl.

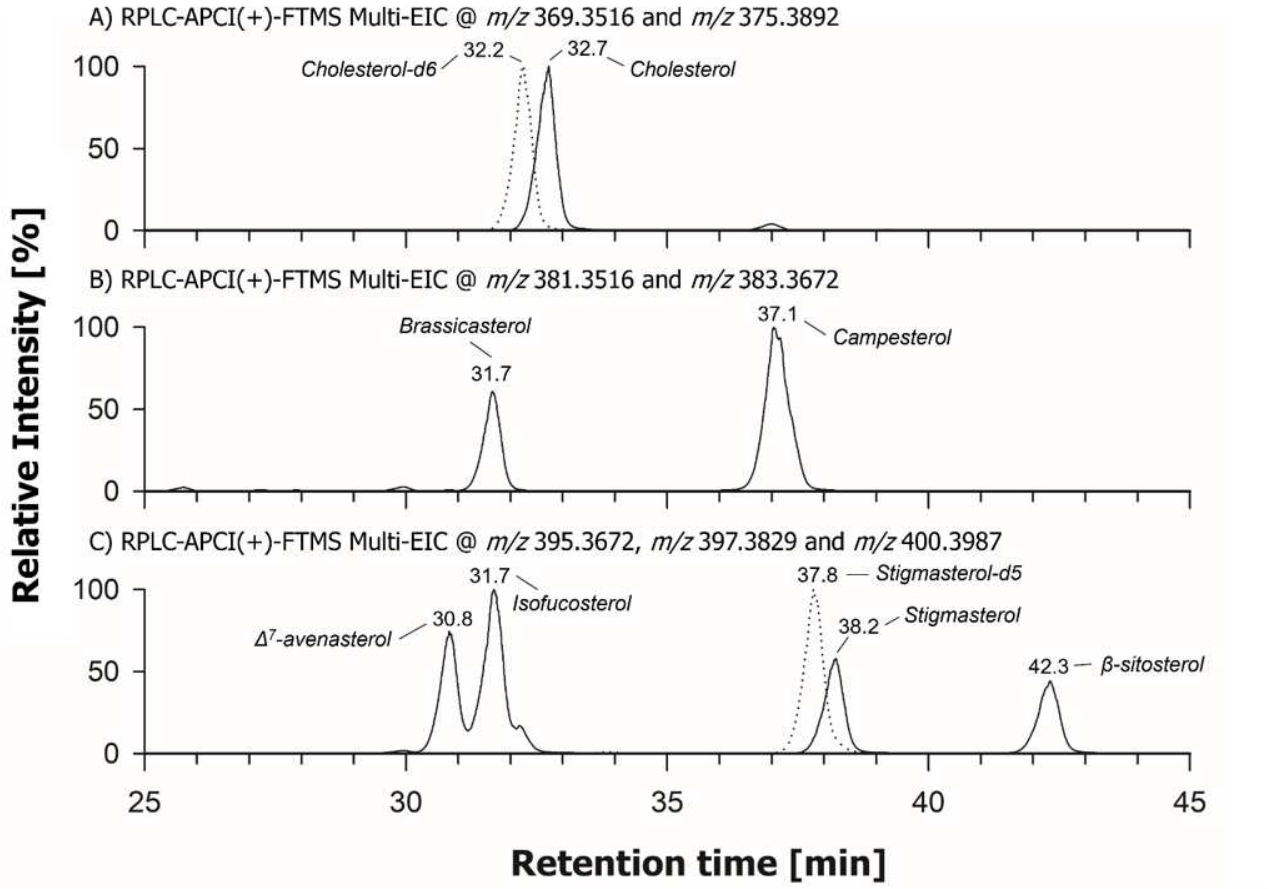


Figure 2. Detailed views of multiple-Extracted Ion Current (EIC) chromatograms referred to standard FSs considered in the present chapter, grouped according to their side chain (see **Figure 1**): A) cholesterol and its hexa-deuterated analogue, two FSs not alkylated on C24; B) 24-methyl-FSs; C) 24-ethyl- and 24-ethylidene-FSs. The following exact *m/z* values, referred to monoisotopic $[M+H-H_2O]^+$ ions, were selected for ion current extraction: cholesterol - 369.3516, cholesterol-d_6 - 375.3892, brassicasterol - 381.3516, campesterol - 383.3672, stigmasterol, Δ^7-avenasterol and isofucosterol (Δ^5-avenasterol) - 395.3672, β-sitosterol - 397.3829, and penta-deuterated stigmasterol - 400.3987.

The effect on the retention of deuteration of the two methyl groups linked to C25 in cholesterol-d_6 and of the ethyl group linked to C24 in stigmasterol-d_5 can be easily inferred from **Figure 2**, since a decrease (0.5/0.4 min) in retention time with respect to the corresponding non-deuterated analogues was observed (see **Figure 2**, panels A and C, respectively). On the other hand, **Figure 2** highlights the key role played by the sterol side chain in the interaction with the octadecylic stationary phase.

Sterols with the same number and position of double bonds on the B-ring but different side chains showed a clear pattern in retention. Based on their C24 substituent, those with a saturated side chain were retained in the order: H < methyl < ethyl, corresponding to cholesterol < campesterol < β-sitosterol (see **Figure 2**). A similar trend was observed for sterols including a double bond at C22-C23, with brassicasterol (methylated on C24) being less retained than stigmasterol (ethylated on C24). The occurrence of a C=C bond in the side chain reduced the retention time compared to species with a saturated SC, as clearly inferred from the comparison between retention times of stigmasterol and β-sitosterol in **Figure 2C**. This effect, consistent with that observed for fatty acids including one or more C=C bonds, when comparing their retention with the one of saturated fatty acids (see, for example, Ref. 49), varied depending on the C=C bond's location, being more relevant when it was closer to the end of the chain. Indeed, Δ^7-avenasterol and isofucosterol, having a C=C bond between C24 and C24', exhibited a more relevant reduction in retention time (over 10 min) with respect to β-sitosterol than stigmasterol (4 min), whose C=C bond is located between C22 and C23 (see **Figure 2**). The effect on retention exerted by the location of the C=C bond on ring B was more subtle. Indeed, Δ^7-avenasterol was less retained than its positional isomer isofucosterol (Δ^5-avenasterol), suggesting that the closer proximity to the side chain of the C=C bond between C7 and C8 reduced its interaction with the stationary phase. It is worth noting that an inversion in the respective retention times of the two isomeric avenasterols was observed by Jiang *et al.* using a C18 column and an isocratic elution based on ACN/methanol 99:1 (v/v), whereas the retention order of them, campesterol and β-sitosterol was in accordance with the one observed during the present study[30].

The chromatographic behaviour described so far suggests that relative retention might be one of the tools for the recognition of new isomeric sterols in complex matrices, especially to infer the characteristics of their side chain, by comparison with standards of known sterols. As shown in the following section, a careful interpretation of fragmentation pathways obtained by HCD-FTMS/MS and CID-MS^n for standard sterols, including those deuterated on appropriate positions of the

molecular structure, provided valuable additional information, potentially useful for the identification of new phytosterols.

1.3.2 Fragmentation of Δ^5-sterols with saturated and unbranched side chain: cholesterol and hexa-deuterated cholesterol. To understand the general fragmentation pattern of Δ^5-sterols with a fully saturated side chain, a comparison was made between cholesterol (CHO) and its analogue deuterated on the two methyl groups linked to C25 (abbreviated as CHO-d_6 in the following). The APCI (+)-HCD-FTMS/MS spectra acquired for the respective $[M+H-H_2O]^+$ ions (having exact *m/z* values: 369.3516 and 375.3892) are shown in **Figure 3**. For the sake of comparison, the APCI (+)-HCD-FTMS/MS spectra obtained for all the other sterols considered in the present study, excepting stigmasterol and its penta-deuterated counterpart (*vide infra*), are grouped in **Figure 4**. The complex fragmentation pattern typically observed in tandem MS spectra of free sterols reported in previous studies[30,48,50-52], leading to a characteristic distribution of product ion abundances, can be easily recognized in all spectra included in the two figures. Notably, a similar pattern has been systematically observed over more than four decades in sterol spectra obtained using electron ionization with high electron energy (70 eV)[53]. The comparison between spectra shown in **Figures 3** and **4** reveals that sterols fragmentation produces apparently similar clusters of peaks, yet subtle variations in their relative abundances can be recognized by a deeper evaluation. To explore the correlation between structural features and specific abundance profiles, a systematic interpretation of those patterns based also on CID-MS^n was undertaken in this thesis work, including MS^3 analyses (like in the study by Jiang *et al.* [30]) and, for the first time, also MS^4 acquisitions.

To facilitate the description of spectral features, peak signals related to product ions having the same number of carbon atoms but differing for the number of H or D atoms were grouped within a single cluster, identified by a capital letter. Moreover, *m/z* values referred to ions including D atoms were highlighted in red in **Figure 3B**. Experimental *m/z* values rounded off to the fourth decimal place,

molecular formulas inferred from them considering a maximum accuracy of 5 ppm, and relative intensities for peak signals detected in each cluster for CHO and CHO-d_6 are reported in **Table A1** of Appendix 1. Minor product ions, not labelled in **Figure 3**, for the sake of clarity, are also included in the table.

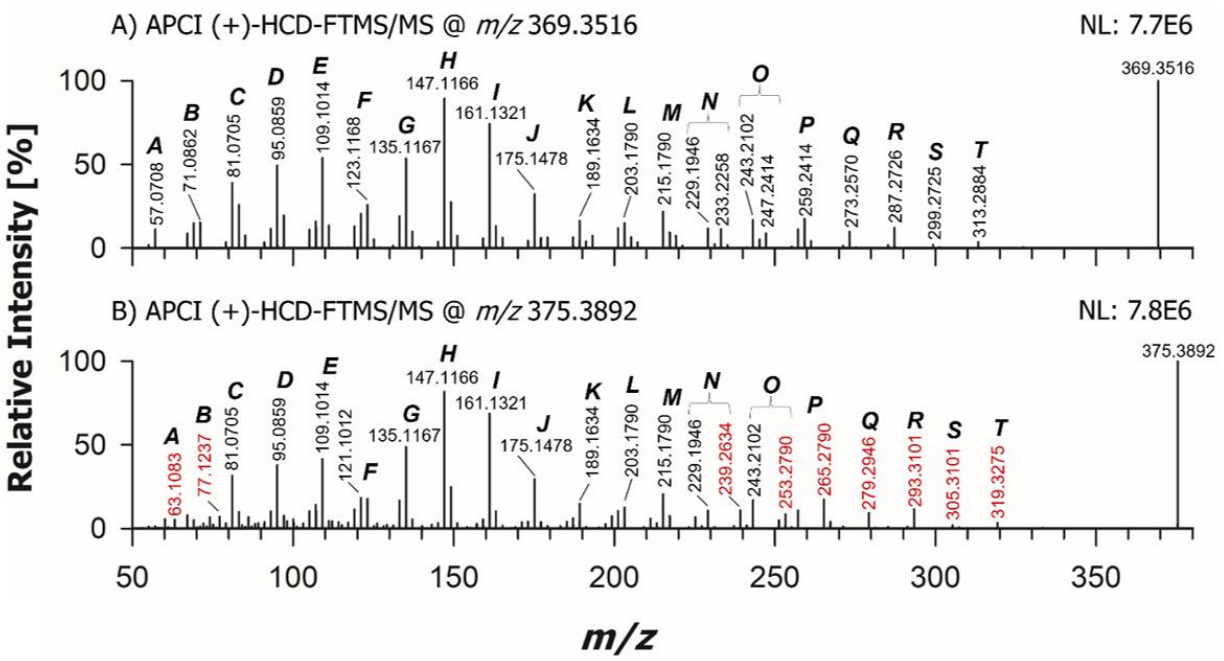


Figure 3. APCI(+)-HCD-FTMS/MS spectra referred to $[M+H-H_2O]^+$ ions of cholesterol (plot A) and cholesterol completely deuterated on methyl groups linked to C24 (cholesterol-d_6, plot B), having exact *m/z* 369.3516 and 375.3892, respectively. Ions sharing the same number of C atoms but differing for the number of H and/or D atoms were grouped within a single cluster, indicated by a capital letter. In the MS/MS spectrum of cholesterol-d_6 *m/z* values related to ions including six D atoms were reported in red. The NL numbers represent Normalization Levels (measured as counts/s) related to each spectrum. See text for details.

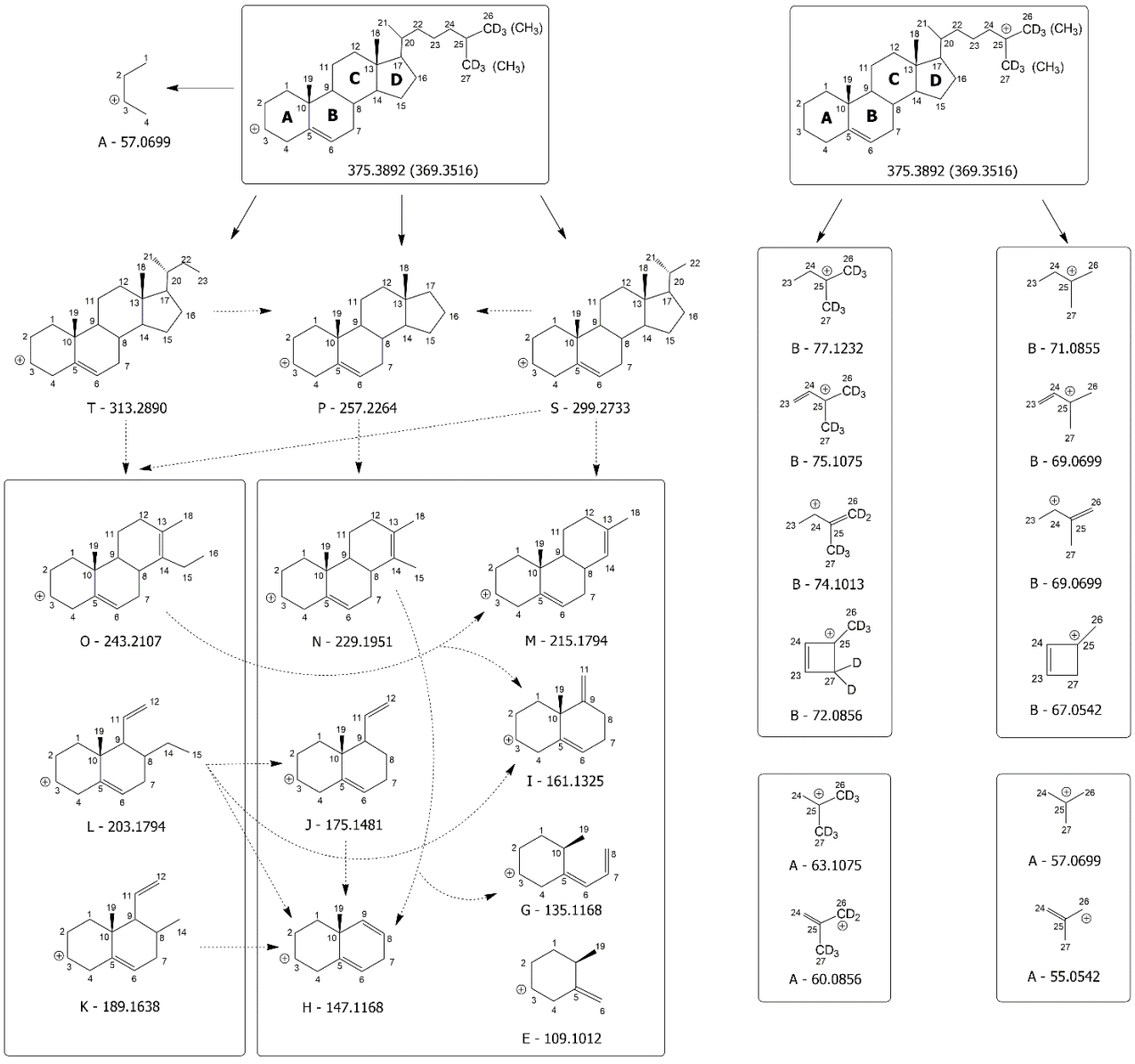
As emphasized by the red labels in **Figure 3B**, a 6-units shift in nominal *m/z* values was observed for several product ions when the precursor ion of CHO-d_6 was fragmented. This shift, found in clusters A, B, N, O, P, Q, R, S and T, indicates the presence of the deuterated part of the side chain in the corresponding structure. A systematic comparison across clusters provided further insights into this finding. Two extreme cases were identified: peak signals whose nominal *m/z* values were univocally displaced by 6 units (see bold *m/z* values in **Table A1**), and those which did not change at all their *m/z* values (apart from fluctuations on the fourth decimal digit, due to instrumental precision,

occurring in *m/z* values underlined in **Table A1**) when CHO-d_6 was fragmented. These results indicated which product ions included the side chain and which did not. For the remaining product ions, parallel mechanisms had to be considered. In these cases, both the *m/z* value already observed for not deuterated cholesterol and one or more new ones, suggesting the presence of 5 or 6 D atoms in the ion structure, were recognized in the FTMS/MS spectrum of CHO-d_6. For example, the product ion detected at *m/z* 57.0708 in the MS/MS spectrum of CHO (cluster A), consistent with a molecular formula $C_4H_9^+$ (exact *m/z* 57.0699), was observed as a very weak signal also in the MS/MS spectrum of CHO-d_6 (see **Table A1**) but it was accompanied by a relatively stronger signal at *m/z* 63.1083, compatible with the formula $C_4H_3D_6^+$ (exact *m/z* 63.1075). As shown on the right side of **Scheme 1**, this formula can be related to the structure of a hexa-deuterated *tert*-butyl carbocation, arising from a dissociation occurring on the side chain of CHO-d_6. The corresponding ion for CHO is a conventional *tert*-butyl carbocation, having an exact *m/z* 57.0699, whose structure is also reported in **Scheme 1**.

The generation of these product ions provided a very important and, to the best of our knowledge, unprecedented evidence of the presence of multiple possible locations of positive charge on the structure of the $[M+H-H_2O]^+$ precursor ions, alternative to C3, which is usually proposed as the unique location of positive charge for those ions (see, for example, Refs. 30 and 48). As illustrated in **Scheme 1**, the presence of positive charge on C25, leading to a tertiary carbocation, is required to explain the generation of the ion with exact *m/z* 63.1075 when CHO-d_6 is fragmented. By analogy, this feature also accounts for the generation of ions with exact *m/z* 71.0855 and 77.1232, when CHO and CHO-d_6 are fragmented, respectively. A detailed representation of the processes hypothesised to explain the generation of these ions and of all the other major product ions with *m/z* lower than 100 detected upon fragmentation of CHO and CHO-d_6 is provided in **Figure A1** of Appendix 1. In this case, as in most fragmentation process hypothesised to explain the generation of sterol product ions (*vide infra*), the proposed mechanism was a 1,3-H migration between two carbon atoms, with a bond breakage occurring between the second and the third atom involved in the migration and the

generation of a C=C bond between the first and the second atom, in accordance with a mechanism proposed in the literature for the charge remote fragmentation of long-chain functionalized alkanes and alkenes[54].

Interestingly, as indicated in the upper-left part of **Scheme 1**, a product ion with exact *m/z* 57.0699 might be generated also by CHO-d_6 if the positive charge was located on the typical C3 position,



Scheme 1. Fragmentation pathways hypothesised for cholesterol and cholesterol hexa-deuterated on methyl groups linked to C25 considering their $[M+H-H_2O]^+$ ions generated in the APCI source, with positive charge located: left side) on C3 (where the charge is originally located); right side) on one of the terminal carbon atoms of the side chain. Plain arrows indicate fragmentations observed in MS/MS spectra (under both HCD and CID conditions); dashed arrows indicate fragmentations observed in CID-MS^3/MS^4 spectra. Boxes include multiple product ions observed in a single MS^n (n = 2-4) spectrum. Exact *m/z* ratios (rounded off to the fourth decimal place) are reported for all product ions.

since it would result from the fragmentation of ring A. However, as shown in the fragmentation reaction reported at the top of **Figure A1**, this process would likely imply the release of a very strained neutral fragment. This might explain the appearance of a very weak peak signal at a *m/z* ratio 57.0708, consistent with the exact value 57.0699, in the MS/MS spectrum of CHO-d_6 (see **Table A1**).

Notably, other product ions detected in clusters A and B for CHO and CHO-d_6 could only be explained by considering additional possible locations of the positive charge near the end of the cholesterol side chain, specifically at C24 and C26 atoms (see the right side of **Scheme 1** and **Figure A1**), in addition to C25. The most plausible, though somewhat unusual, process leading to the displacement of the positive charge on positions like C24, C25 and C26 is a hydride transfer occurring from the carbon atom representing the new location of positive charge to C3, where the charge was initially located after the in-source loss of water from the protonated form of cholesterol. Notably, Bao *et al.*[55] previously proposed an intramolecular hydride transfer occurring upon collision-induced dissociation in the case of cyclopentenone oxylipins. On the other hand, hydride abstraction was reported to occur from hydrocarbon chains during positive ion APCI, leading to carbocations[56]. If occurring on sterols, this process would lead to $[M-H]^+$ ions or, in case of subsequent in-source water loss, to $[M-H-H_2O]^+$ ions, yet none of them showed a significant intensity in APCI(+)-FTMS spectra of sterols in the present case, thus strengthening the hypothesis that the protonation of the OH group, followed by water loss and generation of a carbocation on C3 was the prevailing ionization process occurring in the APCI(+) source.

A systematic interpretation of the spectral profiles displayed in **Figure 3** reveals that at least another possible location of positive charge on the structure of CHO and CHO-d_6 $[M+H-H_2O]^+$ ions needs to be hypothesised to explain major product ions detected in MS/MS spectra. A key approach during this step of the investigation, expanding the use of MS^3 already reported for some sterols by Jiang *et al.*[30], involved the acquisition of the MS^3 spectrum for each major product ion detected in HCD-FTMS/MS spectra shown in **Figure 3** and of MS^4 spectra for selected product ions detected in MS^3

spectra. These MS^3 and MS^4 spectra were obtained under low energy collisional-induced dissociation (CID) conditions using a linear ion trap mass spectrometer, after verifying that each product ion detected in HCD-MS/MS spectra was also present in low energy CID-MS/MS ones. A set of genealogical trees, describing schematically the information inferred from MS^3 and MS^4 acquisitions performed during the present study on sterols, is included in **Figure A2** of Appendix 1.

As a result, solid arrows in **Scheme 1** indicate transitions directly observed at the MS/MS stage, while dashed ones represent selected transitions observed at either the MS^3 or the MS^4 stage that led to product ions detected also in MS/MS spectra (the complete representation of all transitions experimentally observed is available in **Figure A2**). Additionally, boxes reported in the schemes include all major product ions detected directly in a MS/MS (if preceded by a solid arrow) or MS^3 (if preceded by a dashed arrow) spectrum, with the precursor being the ion preceding a specific box. For example, the product ions with exact *m/z* values 229.1951 and 215.1794 (belonging to clusters N and M, respectively) shown in a box on the left side of **Scheme 1** were detected in the 375 > 257 > MS^3 spectrum of CHO-d_6 and also in the 369 > 257 > MS^3 spectrum of CHO (see also the respective genealogical trees in **Figure A2**). In this case, the 375 > 313 > 243 > MS^4 spectrum clarified that the *m/z* 215.1794 ion could be generated from the 243 one (as indicated by the curved dashed arrow connecting the two ions in **Scheme 1**), whereas the *m/z* 229.1951 ion was directly generated from the precursor ion with exact *m/z* 257.2264 (see the genealogical trees for CHO-d_6 in **Figure A2**). The remarkable amount of spectral information obtained through the adopted multistage MS approach required a complex and careful interpretation, yet it provided an unprecedented level of detail for cholesterol fragmentation, representing a crucial foundation for explaining the spectral differences observed for other sterols under study, considering their structural differences.

As shown on the left side of **Scheme 1**, the typical location hypothesised for the positive charge in the cholesterol $[M+H-H_2O]^+$ ion, *i.e.*, C3 (where the original OH group is linked), was considered as a starting point for the interpretation of fragmentation pathways. This approach successfully

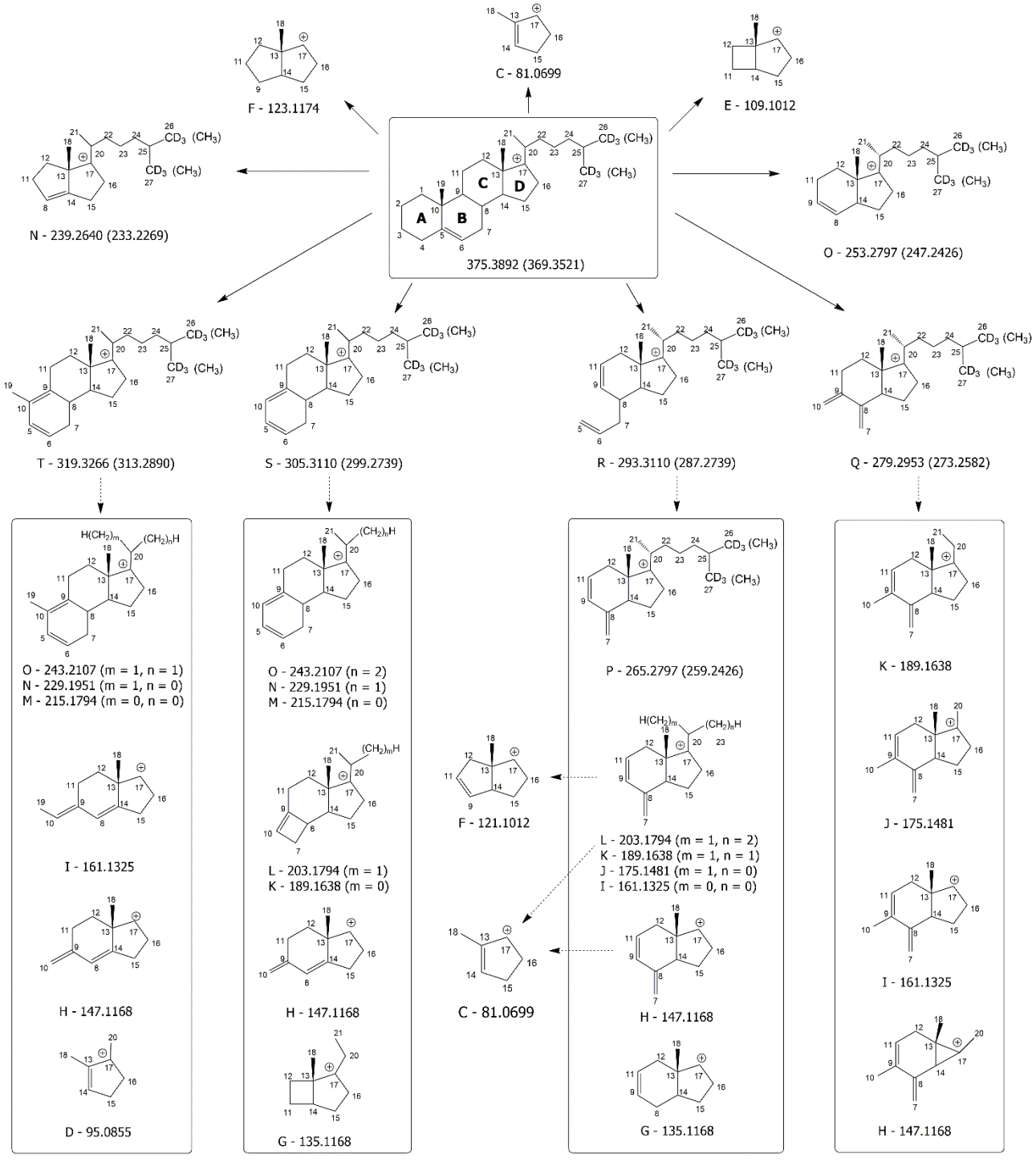
explained the formation of major product ions in clusters T (exact *m/z* 313.2890) and S (exact *m/z* 299.2739) and a minor ion in cluster P (exact *m/z* 257.2264) through dissociations involving the CHO side chain, with the complete detachment of the deuterated portion, if present. A description of the specific processes hypothesised to explain the generation of those ions is provided in **Figure A3** of Appendix 1. However, these mechanisms could not account for the generation of product ions with *m/z* values systematically shifted by 6 units in the case of CHO-d_6 (see **Figure 3B**), thus suggesting that further pathways had to be considered (*vide infra*). Notably, **Scheme 1** reports plausible product ions originating from product ions T, S and P, all with the positive charge located on C3 and detected in MS^3/MS^4 spectra. The corresponding fragmentation processes, described in detail in **Figure A3**, involve the sequential opening and fragmentation of rings D, C and B of CHO, without the displacement of the original C5-C6 double bond. As emphasised in **Figure A3**, the proposed processes often involve the already mentioned 1,3-H migration with a C-C bond breakage and a C=C bond formation. Moreover, the subsequent generation of different structures of the same ion has often to be invoked to finally account for the formation of a specific product ion. Notably, the structure proposed for the product ion consistent with an exact *m/z* 147.1168 (cluster H), which is the base peak in the HCD-FTMS/MS spectra of CHO (see **Figure 3**), matches exactly with the ones proposed by Jiang *et al.* in the fragmentation scheme for stigmasterol[30] and by Munger *et al.* [48], who identified that ion as a general diagnostic product ion for Δ^5 sterols. The structure shown for that ion in **Scheme 1** and **Figure A3** is also consistent with the detection of the most abundant product ion at nominal *m/z* 149 reported by Igarashi *et al.*[52] when fragmenting cholesterol including two ^{13}C atoms at C3 and C4. An excellent agreement was also found with the results reported by Trosken *et al.*[50] and Mo *et al.*[57] for the structure proposed in **Scheme 1** and **Figure A3** for another relevant product ion, the I one corresponding to an exact *m/z* 161.1325. Indeed, this structure corresponds to that of the product ion detected at nominal *m/z* 167 by those Authors when fragmenting cholesterol deuterated twice on C2 and C4 and once on C3 and C6 [50,57]. Notably, Trosken *et al.* detected further relevant product ions at

nominal *m/z* 81 and 95 for cholesterol deuterated on those carbon atoms[50]. However, no plausible mechanism could be found to produce ions with those *m/z* ratios assuming that the positive charge was on C3. This failure, along with the total lack of explanation for hexa-deuterated forms of ions T and S, and for major deuterated and non-deuterated ions belonging to clusters O, P, Q and R observed in the present study, strongly suggested that additional mechanisms, likely implying different charge locations with respect to those reported in **Scheme 1**, had to be hypothesised.

The key for the individuation of a new charge location was provided by the ion detected at *m/z* 81.0705 for both CHO and CHO-d_6 (see **Figure 3**), thus certainly not including the terminal part of the side chain. A plausible mechanism leading to a product ion with an exact *m/z* ratio (81.0699) consistent with that value (within a 5 ppm accuracy) involves the generation of an allylic carbocation with the pentacyclic structure shown at the top and the bottom of **Scheme 2**. This process might involve a retro-cycloaddition occurring at ring C, previously proposed in the literature[51], followed by the complete elimination of the side chain mediated by a 1,3-H transfer from C22 to C17 (see **Figure A4**). The mechanism suggests the location of positive charge on C17, a favourable position, since it corresponds to a tertiary carbocation, likely originated (like carbocations on the side chain commented before) through an intra-molecular hydride transfer, in this case occurring from C17 to the original location of positive charge, C3. As depicted in **Scheme 2**, the positive charge on C17 enables a complete interpretation of the CHO and CHO-d_6 fragmentation patterns, explaining the entire set of product ions labelled in the HCD-FTMS/MS spectra reported in **Figure 3**. A detailed representation of fragmentation steps leading to product ions reported in **Scheme 2** is provided in **Figures A5**, **A6** and **A7** of Appendix 1.

Structures for ions T, S, R, Q, P and O, compatible with the 6 units shift in nominal *m/z* ratio observed for them when CHO-d_6 was fragmented, could be found by considering the progressive fragmentation of rings A and B. As emphasized by one of the dashed arrows in **Scheme 2** and in **Figure A2**, the *m/z* 265.2797 ion, belonging to cluster P of deuterated cholesterol, was detected in the MS^3 spectrum of

the *m/z* 293.3110 ion of cluster R, thus facilitating its structural interpretation. Similarly, a complete set of product ions, enclosed in rectangular boxes in **Scheme 2**, was observed in the respective MS^3



Scheme 2. Fragmentation pathways hypothesised for cholesterol and cholesterol hexa-deuterated on methyl groups linked to C25 considering their $[M+H-H_2O]^+$ ions generated in the APCI source, with positive charge located on C17. Plain arrows indicate fragmentations observed in MS/MS spectra (under both HCD and CID conditions); dashed arrows indicate fragmentations observed in CID-MS^3/MS^4 spectra. Boxes include multiple product ions observed in a single MS^n (n = 3, 4) spectrum. Exact *m/z* ratios (rounded off to the fourth decimal place) are reported for all product ions.

spectra of ions T, S, R and Q reported in the scheme. The MS^4 spectra further highlighted the complex relationships existing between couples of product ions detected in those MS^3 spectra. For the sake of clarity, dashed arrows were not included inside those boxes in the case of **Scheme 2**, but the respective transitions were carefully analysed to validate each structure shown in the scheme and are evidenced in the genealogical trees in **Figure A2**. Notably, a 28 Da neutral loss corresponding to the detachment of an ethylene molecule, was very common, whereas a 14 Da neutral loss, putatively corresponding to a methylene loss, was rarely observed, although appearing consistent with the frequent detection of 14 *m/z* units-spaced ions in MS^3 spectra (see **Figure A2**). For instance, the *m/z* 215.1794 ion (cluster M) was never found in the fragmentation spectrum of the *m/z* 229.1951 one (cluster N) but exhibited a relevant signal in the spectrum of the precursor at *m/z* 243.2107 (cluster O). On the other hand, methylene losses were inevitably hypothesised to occur from ions with exact *m/z* 161.1325 and 135.1168 since they were inferred from the corresponding MS^3 spectra (see the second genealogical tree for the CHO-d_6 precursor ion in **Figure A2** and the fragmentation shown at the top-right side of **Figure A6**). The relationships found both upwards and downwards in the fragmentation cascades depicted in **Schemes 1** and **2** and in **Figure A2**, were very useful to formulate consistent structural hypothesis for each product ion, usually considering ring openings and H intramolecular transfers as the possible mechanisms.

As shown in **Scheme 2**, the progressive fragmentation of the side chain of ions T, S, R and Q, with the immediate loss of the deuterated portion in the case of CHO-d_6, was critical to explain the 6-unit shift in *m/z* ratios observed only for ions of clusters T to P in the MS/MS spectra reported in **Figure 3**. Notably, among product ions generated in the case of CHO-d_6, those with exact *m/z* 239.2640 and 253.2797, belonging to clusters N and O, respectively, were not detected in any of the MS^3 or MS^4 spectra discussed so far (see the genealogical trees for CHO-d_6 in **Figure A2**). This absence suggested that they were generated directly from the $[M+H-H_2O]^+$ precursor ion of CHO-d_6 and still included the six D atoms. Consequently, their formation likely implied the fragmentation or the complete loss

of rings A and B, and possibly part of ring C, but did not involve the side chain, as depicted in the upper part of **Scheme 2** and in the respective fragmentation processes in **Figure A5**. The corresponding non-deuterated ions, having exact *m/z* values 233.2269 and 247.2426, respectively, were formed and detected in the HCD-FTMS/MS spectrum when the $[M+H-H_2O]^+$ ion of CHO was fragmented. As highlighted in **Scheme 2**, all peak signals in the other clusters displayed identical *m/z* ratios for CHO and CHO-d_6, excepting those in clusters A and B, for the reasons previously explained (see **Scheme 1**).

The location of positive charge on C17 was also important to explain the generation of product ions with a relatively low *m/z* (< 150) among them. Indeed, the ion with exact *m/z* 123.1174 (corresponding to the major peak signal of cluster F, see **Figure 3**) was absent in all cholesterol-related MS^3 spectra concerning ions T, S, R and Q but it was detected in the MS^3 spectrum of the *m/z* 257.2264 ion (a minor ion of cluster P, not labelled in **Figure 3**). Therefore, it was assumed to be formed from the latter, as described in the top-right side of **Figure A5**. As shown in **Scheme 2** and in **Figure A5**, the corresponding structure was compatible with the retainment of ring D and part of ring C, and the positive charge on C17 was a determining feature for its generation. This was also the case for the structure shown in the upper part of **Scheme 2** for the *m/z* 109.1012 ion (cluster E), that can be considered complementary to the one proposed in **Scheme 1**. The positive charge on C17 was also important to provide an interpretation for product ions with *m/z* 121.1012 and 81.0699, detected in clusters F and C, respectively. As shown in **Scheme 2** and **Figure A2**, these ions were detected both in 375 > 203 > and in 375 > 147 > MS^3 spectra and in 375 > 293 > 203 and 375 > 293 > 147 MS^4 spectra, thus their direct precursors were ions with *m/z* ratios 203.1794 (cluster L) and 147.1168 (cluster H) and possible mechanisms for the respective generation from those precursors are reported in **Figures A6** and **A7**. This finding supported the hypothesized chemical structures for the two ions and confirmed the structure previously hypothesised for the *m/z* 81.0699 ion. It is worth noting that the mechanism previously hypothesised for the *m/z* 81.0699 ion, reported in **Figure A4**, remains

plausible, as the intermediate product ion of the process, that would have a *m/z* 199.2327 for CHO-d_6 and 193.1956 for CHO (see **Figure A1**), was detected in the respective HCD-FTMS/MS spectra, although with very low intensity (they were not labelled with *m/z* ratios in **Figure 3**). This consideration can be extended to other product ions as well. As exemplified in **Figure A8**, the *m/z* 215.1794 ion of cluster M might be explained also with a cycloelimination on ring D occurring directly on the $[M+H-H_2O]^+$ ions of both CHO and CHO-d_6, assuming the typical positive charge location on C3. Although the final structure would be the same reported in **Scheme 1**, this pathway would not explain the relationship with the *m/z* 243.2107 ion, inferred from MS^3 and MS^4 spectra (see **Figure A2**). The potential occurrence of multiple pathways leading to certain product ions can be thus considered a typical feature of the complex fragmentation processes involving cholesterol and other sterols.

As discussed in detail in the following sections, the careful interpretation of these complex fragmentation pathways allowed for the explanation of subtle differences in the fragmentation profiles observed for typical plant sterols with slightly different structures, paving the way for identifying general structure-fragmentation relationships.

1.3.3. Fragmentation of Δ^5-sterols with a methyl or ethyl group at C24: campesterol and β-sitosterol. As evidenced in **Figure 1**, campesterol and β-sitosterol, two of the most significant PSs, are closely related to CHO in terms of molecular structure, since they include the same steroidal backbone (with a C=C bond between C5 and C6) and a completely saturated side chain. The only structural difference lies in the presence of a methyl or ethyl group attached to C24, respectively. Therefore, the general similarity observed for APCI(+)-HCD-FTMS/MS spectra of CHO, campesterol and β-sitosterol (see **Figures 3** and **4**), is not surprising. Specifically, the profiles of ion clusters D through M were nearly identical for the three sterols, with the *m/z* 147.1166 ion (cluster H, exact *m/z* 147.1168) consistently appearing as the base peak in the MS/MS spectrum. This similarity

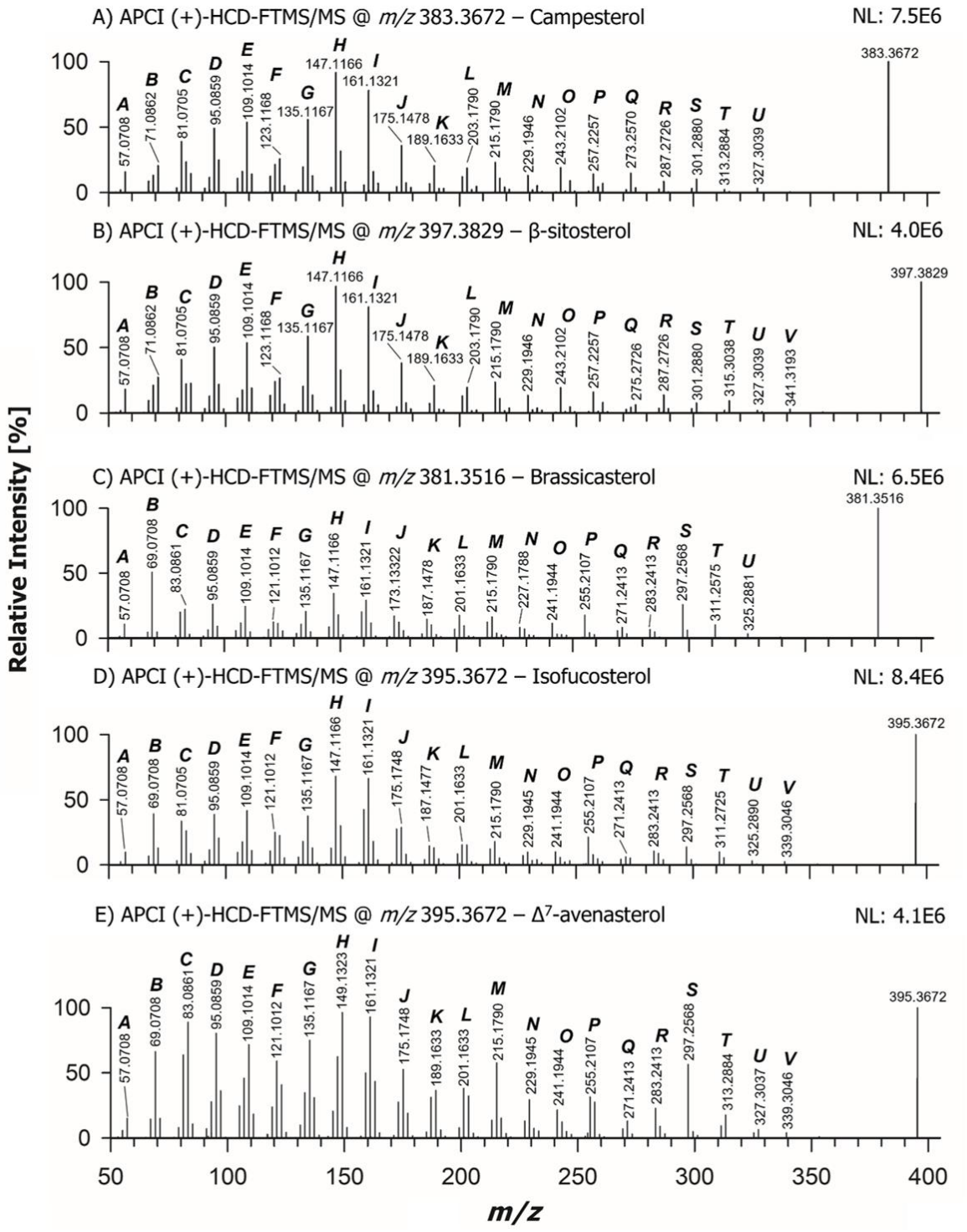
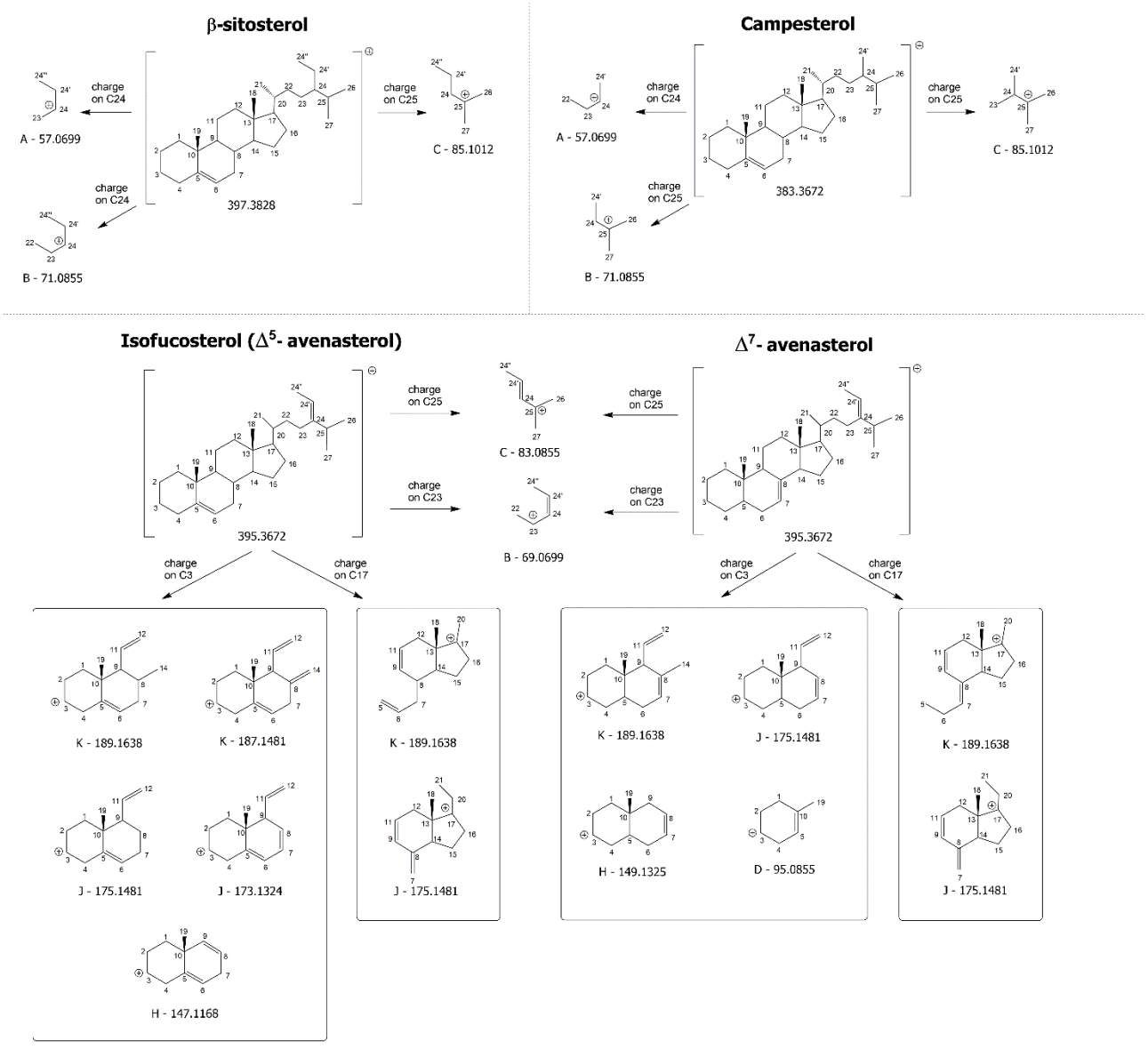


Figure 4. APCI(+)-HCD-FTMS/MS spectra acquired for the $[M+H-H_2O]^+$ ions of the standard sterols considered during the present study along with cholesterol and stigmasterol. Peak signals referred to product ions sharing the same number of carbon atoms and differing for the number of H atoms were grouped within a single cluster, identified by a capital letter. The experimental m/z ratio obtained for the most abundant signal in each cluster is reported. The NL numbers represent Normalization Levels (measured as counts/s) related *to* each spectrum.

is reasonable only if all product ions related to those clusters do not include the side chain, as proposed in **Schemes 1** and **2**. However, subtle but significant differences were recognized in other clusters. For instance, an increase was observed for the ion of cluster C with nominal *m/z* 85 in the case of β-sitosterol (it was not labelled in **Figure 4** for clarity). As depicted in **Scheme 3** and in **Figure A9**, this finding aligns with the generation of a tertiary carbocation, similar to the one at *m/z* 57.0699 depicted in the right side of **Scheme 1** but modified by the presence of the ethyl moiety linked to C24 (exact *m/z* 85.1012).

Scheme 3 further illustrates that when a methyl or ethyl group is attached to C24, the latter becomes another stable location for the positive charge on the side chain, like C25, as it corresponds to a tertiary carbocation. Accordingly, pathways leading to product ions with exact *m/z* 57.0699, 71.0855 and 85.1012 can be easily hypothesised both for campesterol and β-sitosterol by placing the positive charge on C24 or C25 (see **Figure A9**). As for product ions with a high *m/z* ratio, a significant difference in relative abundance was found for the ion of cluster N detected at *m/z* 233.2258 for CHO (see **Figure 3**), which was nearly undetectable for campesterol and β-sitosterol (see **Figure 4**). This finding further supports the structure hypothesised for that ion in **Scheme 2**. Indeed, the methylation/ethylation of C24 would lead to a 14/28-unit shift in the nominal *m/z* ratio of this product ion in the case of campesterol and β-sitosterol, explaining why signals at nominal *m/z* 247 (O) and 261 (P) were observed in the corresponding MS/MS spectra (see **Figures 4A** and **4B**). To maintain clarity, these two signals were not labelled with their *m/z* ratios in the figure. A similar reasoning applies to the *m/z* 247 ion (O) of CHO, which also includes the side chain (see **Scheme 2**) and was thus shifted to nominal *m/z* values of 261 for campesterol (cluster P, not labelled in **Figure 4A**) and 275 in the case of β-sitosterol (cluster Q, see **Figure 4B**). Despite exhibiting a low intensity, the latter signal can be considered a diagnostic product ion of β-sitosterol among Δ^5-sterols with a saturated side chain.

Another remarkable difference between the two sterols and CHO was found in cluster P, where the *m/z* 257 ion prevailed over the *m/z* 259 one, thus reversing the abundance ratio observed for CHO (see **Figures 3** and **4A** and **4B**). As described in **Scheme 1** and **Figure A3**, the *m/z* 257 ion (exact value 257.2264) might result from the complete elimination of the side chain from the CHO precursor ion having its charge on C3, through a 1,3 H migration already proposed by Munger *et al.*[48]. An alternative mechanism, illustrated in **Figure A10**, might explain why the resulting product ion was



Scheme 3. Structures hypothesised for product ions detected in the HCD-FTMS/MS spectra of the $[M+H-H_2O]^+$ ions of b-sitosterol, campesterol, isofucosterol (Δ^5-avenasterol) and Δ^7-avenasterol and recognized as relevant in the assessment of specific structural features of the four phytosterols. The location of positive charge required to explain the final structures is indicated for each (group of) product ion(s). See text for details.

more abundant in the case of campesterol and β-sitosterol. Specifically, a concerted process[51], involving a six-members transition state with a 1,5-H transfer from C24 to C17 could be hypothesised. As shown in **Figure A10**, this process would lead to the detachment of a propene molecule and of an alkene with double substitution (by an isopropyl group and by a methyl or ethyl group) on one of the carbon atoms involved in the C=C bond (C24), rather than the single substitution observed on that atom in the case of CHO.

As for other differences observed between cholesterol and campesterol/β-sitosterol, the counterparts of CHO product ions belonging to clusters P, Q, R, S and T shown in **Scheme 2** were detected in clusters Q/R, R/S, S/T, T/U and U/V, respectively, for campesterol/β-sitosterol (see **Figures 4A** and **4B**), in accordance with the 14/28 Da shift occurring on the side chain of these sterols. Notably, as shown by the genealogical trees reported for cholesterol, campesterol and β-sitosterol in **Figure A2**, the MS^3 spectra obtained for the corresponding ions detected in the respective MS/MS spectra displayed the same set of product ions, thus emphasizing the similarity between them, apart from the side chain. These findings indirectly supported the structural hypotheses made in **Scheme 2** for CHO product ions P, Q, R, S and T, which, as discussed before, are also consistent with the results obtained for CHO-d_6.

The comparison between MS/MS spectra of cholesterol, campesterol and β-sitosterol highlights the critical role played by the positive charge location on C17 in the fragmentation pathways of the respective $[M+H-H_2O]^+$ ions. It suggests that product ions including the entire side chain, having *m/z* ratio values close to that of the precursor ion, may enable the distinction between the three sterols. Additionally, an increase in product ions detected at nominal *m/z* 85 (cluster C) and 275 (cluster Q) was observed for β-sitosterol.

1.3.4. Fragmentation of Δ^5-sterols with a double bond at C22-C23: stigmasterol/penta-deuterated stigmasterol and brassicasterol. Both stigmasterol and brassicasterol, which are two

further significant plant sterols, possess a C=C bond between C22 and C23 along their side chain (see **Figure 1**). This feature is expected to influence their fragmentation patterns, thus potentially leading to differences with respect to sterols discussed so far in this study. By analogy with cholesterol, isotopically labelled stigmasterol including five D atoms on the ethyl group linked to C24 was analyzed during this study to recognize product ions including the terminal part of the side chain. The APCI(+)-FTMS/MS spectra of $[M+H-H_2O]^+$ ions for stigmasterol and stigmasterol-d_5 (having exact *m/z* values 395.3672 and 400.3986) are compared in **Figure 5**. Product ions clusters are labelled as in previous spectra, with *m/z* ratios referred to deuterated product ions reported in red. A detailed list of experimental *m/z* values, molecular formulas inferred from them, and relative abundances for all product ions detected in the two spectra is provided in **Table A2** of Appendix 1, using the same code adopted in the case of **Table A1** to mark *m/z* ratios.

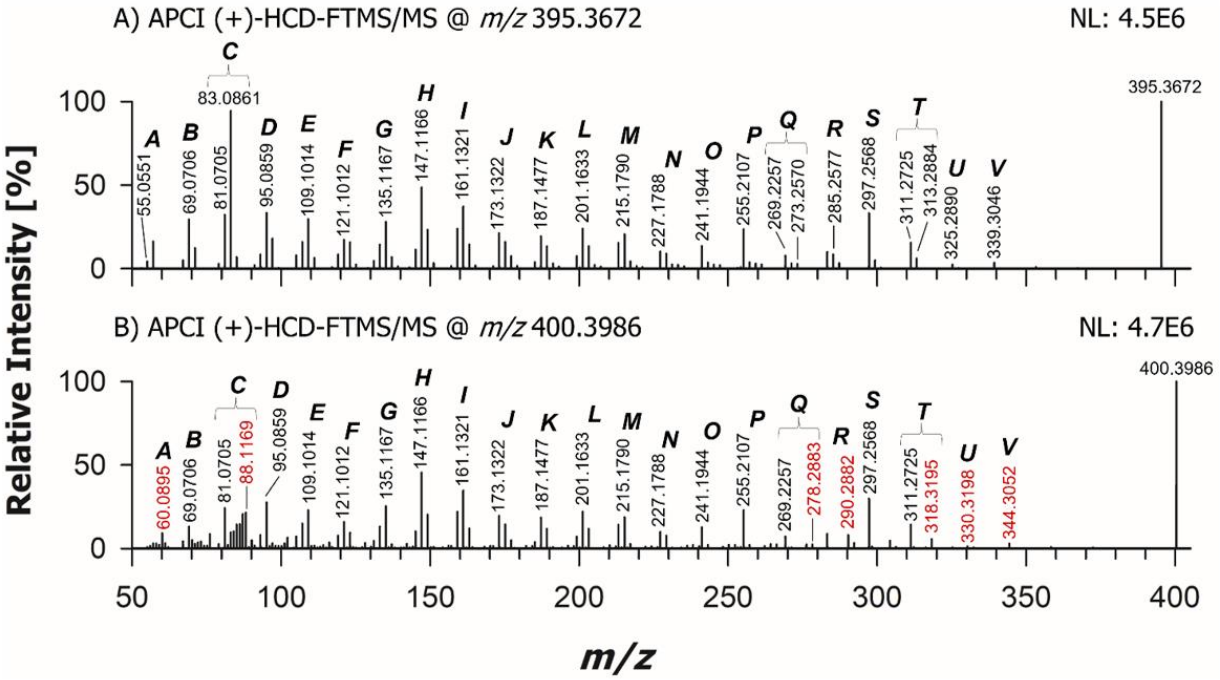


Figure 5. APCI(+)-HCD-FTMS/MS spectra referred to $[M+H-H_2O]^+$ ions of stigmasterol (plot A) and stigmasterol completely deuterated on the ethyl group linked to C24 (stigmasterol-d_5, plot B), having exact m/z values 395.3672 and 400.3986, respectively. Ions sharing the same number of C atoms but differing in the number of H and/or D atoms were grouped within a single cluster, indicated by a capital letter. In the MS/MS spectrum of stigmasterol-d_5 (plot B) m/z values related to ions including D atoms were reported in red. See text for details. The NL numbers represent Normalization Levels (measured as counts/s) related to each spectrum.

Comparing **Figures 3** and **5** clearly reveals that product ions in clusters from D to I had the same *m/z* ratios for both cholesterol and stigmasterol, as well as their deuterated derivatives. This finding supports the structures proposed in **Schemes 1** and/or **2** for those ions, as none of them involves the side chain, where CHO and stigmasterol differ between each other and each of them differs from its isotopically labelled counterpart. Conversely, differences between CHO and stigmasterol were observed for clusters A, B and C, thus confirming that they are directly related to the terminal part of the side chain (see **Scheme 1**). As illustrated in **Scheme A1**, which compares the structures proposed for relevant product ions of stigmasterol and stigmasterol-d_5, and in **Figure A11**, where pathways hypothesised for their formation are reported, most product ions in those clusters can be explained by considering the positive charge on C24. Indeed, this position corresponds to a carbocation which is both tertiary and allylic in the case of stigmasterol. Interestingly, the same structure could be hypothesised for the *m/z* 69.0699 ion in the case of CHO and stigmasterol (see **Schemes 1** and **A1**). In fact, this ion results from the loss of the ethyl chain linked to C24 (see **Figure A11**), where D atoms are located, and which is absent in the case of CHO. On the other hand, the *m/z* 83.0855 ion observed for stigmasterol can be explained by three possible structures, all corresponding to stable allylic (in one case also tertiary) carbocations. This interpretation may account for its role as the base peak in the HCD-FTMS/MS spectrum of stigmasterol (see **Figure 5A**) and highlights this ion as a distinctive marker for the presence of a C=C bond between C22 and C23 and of the ethyl moiety linked to C24. As evidenced in **Scheme A1** and **Figure A11**, one of the structures proposed for the *m/z* 83.0855 ion was confirmed by the detection of its penta-deuterated counterpart at *m/z* 88.1169, while the other two were supported by the detection of a tetra-deuterated product ion at *m/z* 87.1106 and a tris-deuterated product ion at *m/z* 86.1044, in the MS/MS spectrum of stigmasterol-d_5 (see **Figure 5B**, where the peak signals of these ions, in cluster C, were not labelled with their *m/z* ratios for the sake of clarity).

It is worth noting that two previous studies reported the detection of a *m/z* 83 ion in EI-MS[58] or MS/MS spectra[59] of stigmasterol, both suggesting structures lacking the ethyl moiety linked to C24. However, the analysis of stigmasterol deuterated on that group suggests that a different pathway likely generates the ion, at least under conditions related to the so-called HCD mode. Moreover, as inferred from **Figure 5B** and **Table A2**, a non negligible peak signal was detected for stigmasterol-d_5 at a *m/z* ratio consistent with the exact value 85.0950 (see **Table A2**), indicating the generation of a further product ion including four D atoms. As illustrated at the bottom of **Figure A11**, the structure proposed for this ion would imply the original transfer of a deuteride (instead of a hydride) from C24' to the original location of positive charge (C3), resulting in a positive charge on C24'. In principle, a further structure for the *m/z* 83.0855 ion (not reported in **Scheme A1**) would be possible for non-deuterated stigmasterol, according to the same pathway.

As mentioned before, comparing CHO and stigmasterol MS/MS spectra (see **Figures 3** and **5**) revealed significant differences in detected *m/z* ratios beginning from cluster J and extending to those with higher *m/z* ratios. These differences can mostly be explained considering product ions previously described for CHO in **Scheme 2**. Indeed, T, S, R, P ions and the *m/z* 247 ion of cluster O described in **Scheme 2**, all including the entire side chain, correspond, respectively, to the single ions detected in clusters V and U and to the minor ions in clusters T, R and Q (those having nominal *m/z* values 313, 285 and 273) in the case of stigmasterol. The shifts of +26 units in nominal *m/z* ratios are due to the presence of the ethyl group on C24 and the C=C bond between C22 and C23 (see **Scheme A1**). As expected, the penta-deuterated counterparts of those five ions were detected in the MS/MS spectrum of stigmasterol-d_5 (see red labelled *m/z* ratios in **Figure 4B** and the related structures in **Scheme A1**). As emphasized in **Scheme A1**, the positive charge of these ions is likely located on C24, as this is both a tertiary and an allylic carbon in the case of stigmasterol. However, charge remote fragmentations proposed to explain all the five product ions in the case of CHO (with the positive charge located on C17), involving rings A and/or B of the steroidal backbone, were confirmed (see

Schemes 2 and **A1**). A detailed representation of fragmentation processes hypothesised to explain the structures of stigmasterol and stigmasterol-d_5 product ions reported in **Scheme A1** and having *m/z* > 100 and the positive charge on C24 or C17 is provided, respectively, in **Figures A12** and **A13** of Appendix 1.

Remarkably, none of the other relevant peak signals detected in clusters from J to T in the case of stigmasterol showed the 5-unit shift related to the deuteration of the ethyl group in the case of stigmasterol-d_5, indicating the absence of that moiety in their structure. Among them, the *m/z* 311 ion of cluster T and the *m/z* 241 ion of cluster O represented the stigmasterol counterparts of the *m/z* 313 and 243 ions proposed for CHO in **Schemes 1** and **2**, respectively, considering the presence of a C=C bond between C22 and C23 (see **Scheme A1**). Conversely, structures identical to those proposed for ions with nominal *m/z* 95, 109, 135, 147, 161 and 215 in the case of CHO could be hypothesised for stigmasterol (see **Schemes 1**, **2** and **A1**), as the portion of side chain differing between the two molecules was absent in their structure.

A more complex evaluation was needed for the remaining product ions detected in the stigmasterol MS/MS spectrum and not showing the expected +5-unit shift when stigmasterol-d_5 was fragmented. Firstly, 395 > 297 > and 400 > 297 > CID-MS^3 spectra were acquired by fragmenting the *m/z* 297 ion (cluster S) originated by both stigmasterol and stigmasterol-d_5 $[M+H-H_2O]^+$ ions. As evidenced in the genealogical trees reported for the *m/z* 400.4 ion and for the *m/z* 395.4 ion of stigmasterol in **Figure A2**, both spectra revealed the same features, *i.e.*, a series of signals with 14-units spaced nominal *m/z* values from 269 to 135. As proposed in **Figure A14**, the *m/z* 297 ion (exact value 297.2577) might be generated through a two-step gas phase process. The first step would involve a cycloelimination, enabled by the C=C bond between C22 and C23 in the stigmasterol side chain, with loss of propene; this would be followed by the loss of but-1-ene, eventually penta-deuterated. Additionally, if the positive charge was initially located on C17, as shown in **Figure A14**, a very stable tertiary/allylic carbocation would be finally formed, thus explaining the significant abundance

of the *m/z* 297 ion in the MS/MS spectrum of stigmasterol and of its stigmasterol counterpart (see **Figure 5**). Nonetheless, the same mechanism might occur considering the positive charge on C3, as shown in **Figure A15**, and the resulting ion, indicated as 297.2577 A in **Scheme A1**, would coincide with the *m/z* 297 ion proposed by Munger *et al.*[48] as a typical feature of fragmentation for sterols with a C=C bond between C22-C23, although a different mechanism was hypothesised by those Authors. In the present study the 395 > 297 > and 400 > 297 > CID-MS^3 spectra clarified that the entire set of stigmasterol product ions mentioned earlier was preferentially generated by the *m/z* 297 ion, as emphasized in the right side of **Scheme A1**. The detailed fragmentation processes hypothesised for those ions, showed in **Figure A15**, suggested that even a further structure (297.2577 B in **Scheme A1)** had to be considered for the *m/z* 297 ion with the positive charge on C3 to enable an easier interpretation of all the detected product ions. Notably, the *m/z* 255 ion (cluster P), indicated by Munger *et al.*[48] as a characteristic product ion arising directly from the $[M+H-H_2O]^+$ ions of sterols having a C=C bond between C22-C23 and another one on the steroidal backbone, was included among them.

In the case of stigmasterol, a general agreement between structures hypothesised for product ions could be made, at least for the non-deuterated sterol, between the present study and the one by Jiang *et al.* [30], in which the quadrupole-Orbitrap mass spectrometer was also used. One of the relevant differences was the absence, in the fragmentation scheme proposed by those Authors, of product ions still keeping the side chain (*i.e.*, ion of clusters from Q to V reported on the right side of **Scheme A1**), although peak signals potentially corresponding to some of them seemed to be present in the FTMS/MS spectrum reported in Ref. 30. On the other hand, product ions with *m/z* < 100 were not considered by the Authors, since 100 was the lowest *m/z* value explored in their spectrum. As discussed so far in this chapter, those low *m/z* product ions can be very important to clarify the structural characteristics of the side chain of sterols, thus they should be included in the acquired MS/MS spectra of sterols, if possible.

Following stigmasterol, brassicasterol, that is another Δ^5-sterol including a C=C bond between C22 and C23 and differing from stigmasterol only for the presence of a methyl group, instead of an ethyl one, linked to C24, was examined. This structural similarity is evident in the APCI(+)-HCD-FTMS/MS spectra of the respective $[M+H-H_2O]^+$ ions, reported in **Figures 5A** and **4C**, at least for product ions that did not include the side chain portion where the structural difference occurs, namely all those corresponding to clusters from D to P and the *m/z* 297 one (cluster S, see **Scheme A1**). Among product ions with higher *m/z* ratios, brassicasterol ions with nominal *m/z* values 325 (U), 311 (T) and 271 (Q) correspond, respectively, to ions V, U and R detected for stigmasterol (see **Scheme A1**).

The most notable differences between brassicasterol and stigmasterol spectra were observed for lower *m/z* product ions, particularly those of clusters B and C. Indeed, the prevailing product ion observed at nominal *m/z* 83 for stigmasterol (see **Scheme A1**) became the *m/z* 69 ion in the case of brassicasterol, due to the replacement of the ethyl group with methyl at C24. Accordingly, the *m/z* 69 ion was the most abundant product ion detected for brassicasterol, making it a diagnostic feature to recognize the presence of a methyl group linked to C24 in conjunction with a double bond between C22 and C23.

1.3.5. Fragmentation of Δ^5-sterols and Δ^7-sterols with a double bond at C24-24': isofucosterol (Δ^5-avenasterol) and Δ^7-avenasterol. As illustrated in **Figure 1**, isofucosterol (Δ^5-avenasterol) and Δ^7-avenasterol are isomeric sterols sharing an ethylidene group linked to C24 and differing only for the position of the double bond on ring B. These compounds were thus studied to evaluate if the different position of that C=C bond might influence sterol fragmentation pathways. The APCI(+)-HCD-FTMS/MS spectra for the respective $[M+H-H_2O]^+$ ions (exact *m/z* 395.3672) are reported in Figure 4D and 4E. It is important to note that the presence of a C=C bond between carbon atoms C24 and C24' may favour the localization of positive charge on C25, C23 and C24'', as these would all

be allylic carbocations. As shown in **Scheme 3** and **Figures A16** and **A17**, the positive charge on C23 (corresponding to an allylic/secondary carbocation) and on C25 (an allylic/tertiary carbocation) enables an easy interpretation of product ions detected, respectively, at *m/z* 69.0708 and 83.0861 (consistent with exact values 69.0699 and 83.0855) for the two sterols (see Figures 4D and 4E), when considering side chain dissociations. However, due to the significantly higher abundance of the *m/z* 83.0861 ion in the case of Δ^7-avenasterol, an alternative interpretation was searched for. As a result, the process shown in **Figure A18** was proposed. Specifically, it involves the preliminary breakage of the C10-C9 bond, mediated by a 1,3 H transfer from C11 to C10 (and the formation of a C=C bond between C9 and C11), followed by the detachment from ring A of a pentacyclic secondary carbocation with an exact *m/z* 83.0855 and the release of a neutral molecule with an extended C=C bond conjugation. As inferred from **Figure A18**, this process requires the absence of a C=C bond between C5 and C6, thus explaining why it would be favoured in the case of Δ^7-avenasterol. For the same reason, the process is expected to be hindered also in the case of stigmasterol, thus explaining why the *m/z* 83 peak signal was very low in the case of stigmasterol-d_5 (see **Figure AB**). In this case, the specific structure of the *m/z* 83 ion proposed for stigmasterol was formed but including the deuterated portion of the molecule, thus leading to a set of product ions with nominal *m/z* values ranging from 85 to 88 (see the upper-right side of **Scheme A1**).

Excepting a higher abundance of the *m/z* 95 ion in cluster D for Δ^7-avenasterol, due to the possibility of direct generation from ring A (see the structure shown in **Scheme 3** and the fragmentation reported in **Figure A17**), a similar internal abundance distribution was observed for product ions of clusters from D to G and cluster I in the case of isofucosterol and Δ^7-avenasterol, with a good accordance also with the corresponding clusters observed for stigmasterol (see **Figures 4** and **5A**). This result is reasonable, as the three sterols share the same molecular formula ($C_{29}H_{48}O$), and aligns with the structures proposed for ions of those clusters in **Schemes 1** and **2**, referred to CHO but also valid for stigmasterol. The shift of the C=C bond from C5-C6 to C7-C8 would still make those structures

consistent with the experimental *m/z* ratios. However, this is not the case of the structure proposed for the important product ion with exact *m/z* 147.1168 (cluster H) discussed before. As evidenced in **Scheme 3** and **Figure A17**, the presence of a C=C bond between C7 and C8 would favour the generation of a product ion with exact *m/z* 149.1325 in the case of Δ^7-avenasterol, through a different mechanism involving a bond breakage between rings A/B and ring C. This hypothesis was experimentally confirmed, as the prevailing peak signal for cluster H was detected at *m/z* 149.1323 in the case of Δ^7-avenasterol (see **Figure 4**), making it a diagnostic product ion for the C=C bond location between C7 and C8.

Characteristic differences in relative abundances were observed for further signal clusters when comparing isofucosterol, Δ^7-avenasterol and stigmasterol, starting from cluster J. In the case of isofucosterol and Δ^7-avenasterol a signal with a *m/z* ratio compatible with the exact value 175.1481 was predominant, whereas a signal compatible with the exact *m/z* value 173.1324 showed the highest abundance for stigmasterol. As shown in **Scheme 3**, the structure proposed in **Scheme 1** for the *m/z* 175 ion, with the positive charge located on C3, would be valid for both isofucosterol and Δ^7-avenasterol. In contrast, the structure having an exact *m/z* ratio 173.1324 proposed for stigmasterol in **Scheme A1** would necessarily require the presence of a C=C bond between C5 and C6. A higher abundance can thus be predicted for this product ion also in the case of isofucosterol, compared to Δ^7-avenasterol, although it does not become more abundant than the *m/z* 175.1481 ion. This hypothesis was confirmed by the MS/MS spectra of the two compounds (see **Figure 4**). It is worth noting that an alternative structure was proposed for the *m/z* 175 ion in the case of CHO, with the positive charge located on C17 and involving the breakage of the C20-C22 bond (see **Scheme 2**). This structure is essential to explain the characteristic abundance of this product ion observed for sterols lacking a C=C bond between C22 and C23, namely CHO, campesterol, β-sitosterol, isofucosterol and Δ^7-avenasterol (see **Figures 3** and **4**), and its low abundance for sterols including that C=C bond, namely stigmasterol and brassicasterol (see **Figures 4C** and **5**). The breakage of the

C20-C22 bond leading to the *m/z* 175 ion with positive charge on C17 requires a 1,3 H transfer from C23 to C20. This process is significantly more difficult if C23 is involved in a C=C bond, as in stigmasterol and brassicasterol.

While comparing further product ions obtained for isofucosterol and Δ^7-avenasterol, an interesting inversion in abundance was observed for ions with nominal *m/z* values 187 and 189 in cluster K. As illustrated in **Scheme 3**, this finding can be explained by the easier generation of the *m/z* 187 ion in the case of isofucosterol since the C5-C6 double bond is already present and an additional C=C bond is formed between C8 and C14 during fragmentation (see **Figure A16**). Similar internal patterns were generally observed for clusters from L to V for the two species (see **Figure 4**), the only differences being an increased abundance of the *m/z* 215, 257 and 297 ions in the case of Δ^7-avenasterol. This finding aligns with the structures reported for ions in those clusters in **Schemes 1**, **2** and **A1**, as the position of the C=C bond on ring B is not expected to affect their validity. On the other hand, the increased abundance of the three specific ions cited before suggests that the C=C bond between C7 and C8 can positively influence their generation, due to the different molecular conformation induced by that position. More generally, this conformational effect might also explain the higher relative abundance of product ions with respect to the residual precursor ion observed for Δ^7-avenasterol compared to isofucosterol (see **Figure 4**).

1.3.6. Correlation between specific product ions and structural features of 4-desmethyl sterols.

The interpretation of fragmentation spectra for 4-desmethyl sterols discussed in the previous sections revealed subtle differences despite their general similarity. These differences might help in identifying the occurrence of specific structural features. This idea is highlighted by the comparison of relative intensities typically observed for all product ions related to the sterols considered during the present study, reported in **Table A3** of Appendix 1.

Table 1 summarizes the most informative product ions, linking specific structural features to intensities relationships based on the fragmentation spectra. This table might be employed to assess structural features like the position of the double bond on ring B, the presence of a double bond on the side chain (either between C22 and C23 or on the branch linked to C24), and the occurrence of an alkyl group linked to C24, by carefully considering the intensity ratios existing between peak signals in specific clusters or, in some cases, the relative intensity in the entire spectrum.

Table 1. Summary of correlations between specific structural features and intensity relationships for the most structurally informative product ions of 4-desmethyl-sterols, grouped according to clusters shown in **Figures 3**, **4** and **5**. The correlations are based on HCD-FTMS/MS and CID-MS^n (n = 2-4) analyses of selected standards. Exact *m/z* values rounded to four decimal places are reported. Starred percentages correspond to relative intensities observed in the MS/MS spectrum.

Cluster	Exact *m/z* value(s)	Intensity relationships	Structural features
B	69.0699	69.0699 >> 71.0855	$\Delta^{22(23)}$, $\Delta^{24(24')}$ and Δ^7-sterols
	71.0855	71.0855 > 69.0699	Δ^5-sterols with saturated SC, eventually alkylated at C24
C	81.0699	81.0699 > 83.0855	Δ^5-sterols with saturated SC, eventually alkylated at C24, and $\Delta^{5,24(24')}$
	83.0855	> 80% *	$\Delta^{5,22(23)}$ with ethyl group at C24 and Δ^7-sterols
	85.1012	~ 15%	Δ^5-sterols with saturated SC, alkylated at C24
D	95.0855	> 80%	Δ^7-sterols
F	121.1012	121.1012 > 123.1168	$\Delta^{22(23)}$ or $\Delta^{24(24')}$
	123.1168	123.1168 > 121.1012	saturated SC, eventually alkylated at C24
H	147.1168	147.1168 >> 149.1325	Δ^5-sterols
	149.1325	149.1325 > 147.1168	Δ^7-sterols
I	161.1325	161.1325 >> 163.1481	Δ^5-sterols and Δ^7-sterols
	163.1481	~ 40%	Δ^7-sterols
J	173.1324	173.1324 > 175.1481	$\Delta^{22(23)}$
	175.1481	175.1481 ~ 173.1324	$\Delta^{5,24(24')}$
		175.1481 >> 173.1324	Δ^5-sterols with saturated SC, eventually alkylated at C24, and $\Delta^{7,24(24')}$

K	187.1481	187.1481 > 189.1638	$\Delta^{22(23)}$
	189.1638	189.1638 ≥ 187.1481	$\Delta^{24(24')}$
		189.1638 >> 187.1481	sterols with saturated SC, eventually alkylated at C24
L	201.1638	201.1638 ~ 203.1794	$\Delta^{5,24(24')}$
		201.1638 > 203.1794	$\Delta^{22(23)}$ and $\Delta^{7,24(24')}$
	203.1794	203.1794 > 201.1638	sterols with saturated SC, eventually alkylated at C24
M	215.1794	> 60%	Δ^{7}-sterols
N	227.1794	227.1794 > 229.1946	$\Delta^{22(23)}$
	229.1946	229.1946 > 227.1794	sterols with saturated SC, eventually alkylated at C24, and $\Delta^{24(24')}$
O	241.1951	241.1951 >> 243.2107	$\Delta^{22(23)}$ and $\Delta^{24(24')}$
	243.2107	243.2107 >> 241.1951	sterols with saturated SC, eventually alkylated at C24
P	255.2103	255.2103 > 257.2269	$\Delta^{22(23)}$ or $\Delta^{24(24')}$ [48]
	257.2269	~ 30%	Δ^{7}-sterols
		257.2269 > 259.2426	Δ^{5}-sterols with saturated SC and alkylated at C24 [48]
	259.2426	259.2426 > 257.2269	Δ^{5}-sterols with saturated and unbranched SC
R	283.2420	283.2420 > 287.2733	$\Delta^{22(23)}$ and $\Delta^{24(24')}$
	287.2733	287.2733 > 283.2420	sterols with saturated SC, eventually alkylated at C24
S	297.2577	297.2577 >> 299.2739	$\Delta^{22(23)}$ and $\Delta^{24(24')}$ [48]
T	311.2733	311.2733 > 313.2890	$\Delta^{5,22(23)}$ and $\Delta^{5,24(24')}$
	313.2890	313.2890 > 311.2733	Δ^{5}-sterols with saturated SC, unbranched or with methyl group at C24 and Δ^{7}-sterols
	315.3046	315.3046 > 313.2890	Δ^{5}-sterols with saturated SC and ethyl group at C24

Combining this information with the precursor ion *m/z* ratio and the differences in *m/z* ratios observed between its peak signal and nearby signals in the MS/MS spectrum, reflecting neutral losses occurring on the side chain, might aid in identifying unknown plant sterols in vegetal samples.

1.4 Conclusions

The complex fragmentation patterns obtained for 4-desmethyl-sterols when subjected to positive ion tandem mass spectrometry were thoroughly analyzed using natural and isotopically labelled standard compounds. The study employed a complementary approach using accurate *m/z* values of MS/MS peak signals provided by a high-resolution mass spectrometer, insights gained from multistage mass spectrometry (MS^3-MS^4) using a linear ion trap, and comparisons of product ion *m/z* ratios between natural and isotopically labelled standards. The intricate nature of 4-desmethyl-sterols MS/MS spectra was found to arise from a combination of factors, the most relevant being the existence of multiple potential locations for the positive charge, which, to the best of our knowledge, was evidenced for the first time for sterols. This feature was likely caused by the occurrence of unique intramolecular hydride transfers, that displaced the positive charge of the original carbocation formed during the APCI process upon protonation of the OH group and subsequent loss of a water molecule, thus located on the carbon atom conventionally numbered as C3. In particular, indirect evidence was obtained for an alternative location of positive charge on carbons atoms conventionally labelled as C17, on the steroidal backbone, and C24/C25, on the side chain, due to their stabilization as tertiary carbocations. As a result, multiple fragmentation pathways were proposed to account for all detected product ions, with some ions possibly having several structures consistent with their *m/z* ratios. The investigation highlighted the important role played by low (< 100) *m/z* product ions, mainly arising from the side chain, and by product ions generated from the sterol $[M+H-H_2O]^+$ precursor ions through small neutral losses occurring from that chain, related to C-C bond breakages. Despite they had not received a specific attention in previous studies, those ions proved very useful to infer the

structural characteristics of the side chain (location of the C=C bond, nature of the substitution at C24). Indeed, significant correlations were found between the intensity ratios of selected product ions among them and the characteristics of the side chain. Other diagnostic correlations between intensity ratios and structural features were found for product ions whose generation was influenced by the position of C=C bond on ring B. These insights provided a starting basis for identifying unknown sterols in complex samples such as plant extracts. As described in the next chapter, the fragmentation of selected animal and fungal sterols was subsequently investigated to find diagnostic fragmentations related to further additional structural features potentially found also in phytosterols.

References

(1) Moreau, R. A., Nystrom, L., Whitaker, B.D., Winkler-Moser, J.K., Baer, D.J., Gebauer S.K., Hicks, K.B. Phytosterols and their derivatives: Structural diversity, distribution, metabolism, analysis, and health-promoting uses. *Prog. Lipid Res.* **70**, 35–61 (2018). DOI: 10.1016/j.plipres.2018.04.001

(2) Mongrand, S., Stanislas, T., Bayer, E. M. F., Lherminier, J., Simon-Plas, F. Membrane rafts in plant cells. *Trends Plant Sci.* **15**, 656–663 (2010). DOI: 10.1016/j.tplants.2010.09.003

(3) Valitova, J. N., Sulkarnayeva, A. G., Minibayeva, F. V. Plant sterols: Diversity, biosynthesis, and physiological functions. *Biochem.* **81**, 819–834 (2016). DOI: 10.1134/ S0006297916080046.

(4) Nes, W.D. Biosynthesis of cholesterol and other sterols. *Chem. Rev.* **111**, 6423–6451 (2011). DOI: 10.1021/cr200021m.

(5) IUPAC-IUB Joint Commission on Biochemical Nomenclature (JCBN). The nomenclature of steroids. Recommendations 1989. *Eur. J. Biochem.* **186**, 429–458 (1989). DOI: 10.1111/j.1432-1033.1989.tb15228.x.

(6) Piironen, V., Lindsay, D. G., Miettinen, T. A., Toivo, J., Lampi, A. M. Plant sterols: Biosynthesis, biological function and their importance to human nutrition. *J. Sci. Food Agric.* **80**, 939–966 (2000). DOI: 10.1002/(SICI)1097-0010(20000515)80:7<939::AID-JSFA644>3.0.CO;2-C.

(7) Ferrer, A., Altabella, T., Arró, M., Boronat, A. Emerging roles for conjugated sterols in plants. *Prog. Lipid Res.* **67**, 27–37 (2017). DOI: 10.1016/j.plipres.2017.06.002.

(8) Moreau, R.A., Whitaker, B. D., Hicks, K. B. Phytosterols, phytostanols, and their conjugates in foods: Structural diversity, quantitative analysis, and health-promoting uses. *Prog. Lipid Res.* **41**, 457–500 (2002). DOI: 10.1016/s0163-7827(02)00006-1

(9) Evtyugin, D. D., Evtuguin, D. V., Casal, S., Domingues, M. R. Advances and Challenges in Plant Sterol Research: Fundamentals, Analysis, Applications and Production. *Molecules* **28**, 1–45 (2023). DOI: 10.3390/molecules28186526.

(10) Hartmann, M. A., Benveniste, P. Plant Membrane Sterols: Isolation, Identification, and Biosynthesis. *Methods Enzymol.* **148**, 632–650 (1987). DOI: 10.1016/0076-6879(87)48060-9.

(11) Schlag, S., Vetter, W. Quantitative data of up to thirty sterols in vegetable oils and fats. *Eur. Food Res. Technol.* **250**, 469–482 (2024). DOI: 10.1007/s00217-023-04397-5.

(12) Sonawane, P.D., Pollier, J., Panda S., *et al.* Plant cholesterol biosynthetic pathway overlaps

with phytosterol metabolism. *Nat. Plants* **3**, 1–13 (2016). DOI: 10.1038/nplants.2016.205.

(13) Trautwein, E.A., Duchateau, G.S.M.J.E., Lin, Y., *et al.* Proposed mechanisms of cholesterol-lowering action of plant sterols. *Eur. J. Lipid Sci. Technol.* **105**, 171–185 (2003). DOI: 10.1002/ejlt.200390033.

(14) Poudel, P., Petropoulos, S. A., Di Gioia, F. *Plant Tocopherols and Phytosterols and Their Bioactive Properties*. *Natural Secondary Metabolites* (2023). DOI: 10.1007/978-3-031-18587-8_8.

(15) Woyengo, T. A., Ramprasath, V. R., Jones, P. J. H. Anticancer effects of phytosterols. *Eur. J. Clin. Nutr.* **63**, 813–820 (2009). DOI: 10.1038/ejcn.2009.29.

(16) Schlag, S., Huang, Y., Vetter, W. GC/EI-MS method for the determination of phytosterols in vegetable oils. *Anal. Bioanal. Chem.* **414**, 1061–1071 (2022). DOI: 10.1007/s00216-021-03730-9.

(17) Xu, B., Zhang, L., Wang, H., Luo, D., Li, P. Characterization and authentication of four important edible oils using free phytosterol profiles established by GC-GC-TOF/MS. *Anal. Methods* **6**, 6860–6870 (2014). DOI: 10.1039/C4AY01194E.

(18) Cunha, S. S., Fernandes, J. O., Oliveira, M. B. P. P. Quantification of free and esterified sterols in Portuguese olive oils by solid-phase extraction and gas chromatography-mass spectrometry. *J. Chromatogr. A* **1128**, 220–227 (2006). 10.1016/j.chroma.2006.06.039.

(19) Feng, S., Wang, L., Shao, P., Lu, B., Chen, Y., Sun, P. Simultaneous analysis of free phytosterols and phytosterol glycosides in rice bran by SPE/GC–MS. *Food Chem.* **387**, 132742 (2022). DOI: 10.1016/j.foodchem.2022.132742.

(20) Zhang, J., Zhang, T., Tao, G., *et al.* Characterization and determination of free phytosterols and phytosterol conjugates: The potential phytochemicals to classify different rice bran oil and rice bran. *Food Chem.* **344**, 128624 (2021). DOI: 10.1016/j.foodchem.2020.128624.

(21) Gachumi, G., El-Aneed, A. Mass Spectrometric Approaches for the Analysis of Phytosterols in Biological Samples. *J. Agric. Food Chem.* **65**, 10141–10156 (2017). DOI: 10.1021/acs.jafc.7b03785.

(22) Mäeorg, E., Lääniste, P., Jõudu, J., Mäeorg, U. Some important aspects of sterol analysis of vegetable oils. *Proc. Est. Acad. Sci. Chem.* **56**, 59–66 (2007). DOI: 10.3176/chem.2007.2.01.

(23) Uddin, M. S., Sahena, F., Jahurul H.A., Kashif, G., Rukshana, A.H., Eaqub, A. Techniques for the extraction of phytosterols and their benefits in human health: a review. *Sep. Sci. Technol.* **53**, 2206–2223 (2018). DOI: 10.1080/01496395.2018.1454472.

(24) Honda, A., Miyazaki, T., Ikegami, T., *et al.* Highly sensitive and specific analysis of sterol profiles in biological samples by HPLC-ESI-MS/MS. *J. Steroid Biochem. Mol. Biol.* **121**, 556–

564 (2010). 10.1016/j.jsbmb.2010.03.030.

(25) Griffiths, W. J., Abdel-Khalik, J., Crick, P. J., Yutuc, E., Wang, Y. New methods for analysis of oxysterols and related compounds by LC–MS. *J. Steroid Biochem. Mol. Biol.* **162**, 4–26 (2016). DOI: 10.1016/j.jsbmb.2015.11.017.

(26) Quirke, J. M. E., Hsu, Y. L., Van Berkel, G.J. Ferrocene-based electroactive derivatizing reagents for the rapid selective screening of alcohols and phenols in natural product mixtures using electrospray-tandem mass spectrometry. *J. Nat. Prod.* **63**, 230–237 (2000). DOI: 10.1021/np990407l.

(27) Cañabate-Díaz, B., Segura-Carretero, A., Fernandez-Gutierrez, A. *et al.* Separation and determination of sterols in olive oil by HPLC-MS. *Food Chem.* **102**, 593–598 (2007). DOI: 10.1016/j.foodchem.2006.05.038

(28) Baila-Rueda, L., Cenarro, A., Cofan, M., *et al.* Simultaneous determination of oxysterols, phytosterols and cholesterol precursors by high performance liquid chromatography tandem mass spectrometry in human serum. *Anal. Methods* **5**, 2249–2257 (2013). DOI: 10.1039/C3AY26395A.

(29) Li, W., Xu, X., Tang, Z., Guo, Y., Fei, D., Yan, N., Hu, F. Analysis of 14 terpenoids and sterols and variety discrimination of Codonopsis Radix using ultra-high-performance liquid chromatography-quadrupole-time-of-flight mass spectrometry. *J. Sep. Sci.* **46**, (2023). 10.1002/jssc.202200835.

(30) Jiang, K., Gachumi, G., Poudel, A., Shurmer, B., Bashi, Z., El-Aneed, A.. The Establishment of Tandem Mass Spectrometric Fingerprints of Phytosterols and Tocopherols and the Development of Targeted Profiling Strategies in Vegetable Oils. *J. Am. Soc. Mass Spectrom.* **30**, 1700–1712 (2019). DOI: 10.1007/s13361-019-02242-2.

(31) Millán, L., Sampedro, M.C., Sanchez, A., *et al.* Liquid chromatography–quadrupole time of flight tandem mass spectrometry–based targeted metabolomic study for varietal discrimination of grapes according to plant sterols content. *J. Chromatogr. A* **1454**, 67–77 (2016). DOi: 10.1016/j.chroma.2016.05.081.

(32) Lu, B., Zhang, Y., Wu, X., Shi, J. Separation and determination of diversiform phytosterols in food materials using supercritical carbon dioxide extraction and ultraperformance liquid chromatography-atmospheric pressure chemical ionization-mass spectrometry. *Anal. Chim. Acta* **588**, 50–63 (2007). DOI: 10.1016/j.aca.2007.01.067.

(33) Gu, Q., Yi, X, Zhang, Z., *et al.* A facile method for simultaneous analysis of phytosterols, erythrodiol, uvaol, tocopherols and lutein in olive oils by LC-MS. *Anal. Methods* **8**, 1373–1380 (2016). 10.1039/C5AY02193F.

(34) Bedner, M., Schantz, M.M., Sander, L.C., Sharpless, K.E. Development of liquid chromatographic methods for the determination of phytosterols in Standard Reference Materials containing saw palmetto. *J. Chromatogr. A* **1192**, 74–80 (2008). DOI:

10.1016/j.chroma.2008.03.020.

(35) Careri, M., Elviri, L., Mangia, A. Liquid chromatography-UV determination and liquid chromatography-atmospheric pressure chemical ionization mass spectrometric characterization of sitosterol and stigmasterol in soybean oil. *J. Chromatogr. A* **935**, 249–257 (2001). DOI: 10.1016/s0021-9673(01)01079-2.

(36) Segura-Carretero, A., Carrasco-Pancorbo, A., Cortacero, S., Gori, A., Cerretani, L. Fernandez-Gutierrez, A. A simplified method for HPLC-MS analysis of sterols in vegetable oil. *Eur. J. Lipid Sci. Technol.* **110**, 1142–1149 (2008). DOI: 10.1002/ejlt.200700237.

(37) Rozenberg, R., Ruibal.Mendieta, N., Petitjean, G., *et al.* Phytosterol analysis and characterization in spelt (Triticum aestivum ssp. spelta L.) and wheat (T. aestivum L.) lipids by LC/APCI-MS. *J. Cereal Sci.* **38**, 189–197 (2003). DOI: 10.1016/S0733-5210(03)00022-5.

(38) Ruibal-Mendieta, N.L., Rozenberg, R., Delacroix, D.L. *et al.* Spelt (Triticum spelta L.) and winter wheat (Triticum aestivum L.) wholemeals have similar sterol profiles, as determined by quantitative liquid chromatography and mass spectrometry analysis. *J. Agric. Food Chem.* **52**, 4802–4807 (2004). DOI: 10.1021/jf049772v.

(39) Hsu, F.F., Turk, J. Charge-Driven Fragmentation Process in Diacyl Glycerophosphatidic Acids upon Low-Energy Collisional Activation: A Mechanistic Proposal. *J. Am. Soc. Mass Spectrom.* **11**, 892–899 (2000). DOI: 10.1016/S1044-0305(00)00151-3.

(40) Hsu, F.F., Turk, J. Studies on glycerophospholipids with triple quadrupole tandem mass spectrometry with electrospray ionization: Structural characterization and fragmentation processes. *Proc. 50th ASMS Conf. Mass Spectrom. Allied Top.* **0305**, 79–80 (2002). DOI: 10.1002/cfg.207.

(41) Hsu, F.F., Turk, J. Charge-Remote and Charge-Driven Fragmentation Process in Diacyl Glycerophosphoethanolamine upon Low-Energy Collisional Activation: A Mechanistic Proposal. *J. Am. Soc. Mass Spectrom.* **11**, 892–899 (2000). DOI: 10.1016/S1044-0305(00)00159-8.

(42) Hsu, F.F., Turk, J. Electrospray ionization with low-energy collisionally activated dissociation tandem mass spectrometry of glycerophospholipids: Mechanisms of fragmentation and structural characterization. *J. Chromatogr. B Anal. Technol. Biomed. Life Sci.* **877**, 2673–2695 (2009). DOI: 10.1016/j.jchromb.2009.02.033

(43) Hsu, F.F., Turk, J. Studies on phosphatidylserine by tandem quadrupole and multiple stage quadrupole ion-trap mass spectrometry with electrospray ionization: Structural characterization and the fragmentation processes. *J. Am. Soc. Mass Spectrom.* **16**, 1510–1522 (2005). DOI: 10.1016/j.jasms.2005.04.018.

(44) Hsu, F.F., Turk, J. Electrospray ionization/tandem quadrupole mass spectrometric studies on phosphatidylcholines: The fragmentation processes. *J. Am. Soc. Mass Spectrom.* **14**, 352–363 (2003). 10.1016/S1044-0305(03)00064-3.

(45) Hsu, F.F., Turk, J. Structural Characterization of Unsaturated Glycerophospholipids by Multiple-Stage Linear Ion-Trap Mass Spectrometry with Electrospray Ionization. *J. Am. Soc. Mass Spectrom.* **19**, 1681–1691 (2008). DOI: 10.1016/j.jasms.2008.07.023.

(46) Zianni, R.; Bianco, G.; Lelario, F.; Losito, I.; Palmisano, F.; Cataldi, T.R.I. Fatty acid neutral losses observed in tandem mass spectrometry with collision-induced dissociation allows regiochemical assignment of sulfoquinovosyl-diacylglycerols. *J. Mass Spectrom.* **2013**, *48*, 205–215. DOI: 10.1002/jms.3149.

(47) Ventura, G., Calvano, C. D., Cinquepalmi, V., Losito, I., Cataldi, T. R. I. Characterization of Glucuronosyl-diacyl/monoacylglycerols and Discovery of Their Acylated Derivatives in Tomato Lipid Extracts by Reversed-Phase Liquid Chromatography with Electrospray Ionization and Tandem Mass Spectrometry. *J. Am. Soc. Mass Spectrom.* **32**, 2227–2240 (2021). DOI: 10.1021/jasms.1c00162.

(48) Münger, L. H., Boulos, S., Nyström, L. UPLC-MS/MS based identification of dietary steryl glucosides by investigation of corresponding free sterols. *Front. Chem.* **6**, (2018). DOI: 10.3389/fchem.2018.00342.

(49) Schlotterbeck, J.; Kolb, A.; Lämmerhofer, M. Free fatty acid profiling in marine algae extract by LC-MS/MS and isolation as well as quantification of the ω-3 fatty acid hexadeca-4,7,10,13-tetraenoic acid. *J. Sep. Sci.* **2018**, 41, 4286–4295. DOI: 10.1002/jssc.201800780.

(50) Trösken, E.R.; Straube, E.; Lutz, W.K.; Völkel, W.; Patten, C. Quantitation of lanosterol and its major metabolite FF-MAS in an inhibition assay of CYP51 by azoles with atmospheric pressure photoionization based LC-MS/MS. *J. Am. Soc. Mass Spectrom.* **2004**, *15*, 1216–1221. DOI: 10.1016/j.jasms.2004.04.036.

(51) Griffiths, W.J. Tandem mass spectrometry in the study of fatty acids, bile acids, and steroids. *Mass Spectrom. Rev.* **2003**, *22*. DOI:10.1002/mas.10046.

(52) Igarashi, F.; Hikiba, J.; Ogihara, M.H.; Nakaoka, T.; Suzuki, M.; Kataoka, H. A highly specific and sensitive quantification analysis of the sterols in silkworm larvae by high performance liquid chromatography-atmospheric pressure chemical ionization-tandem mass spectrometry. *Anal. Biochem.* **2011**, *419*, 123–132. DOI: 10.1016/j.ab.2011.08.046.

(53) Amos, B.A.; Tokes, L. Electron impact induced fragmentation of cholesterol and related C-5 unsaturated steroids. *J. Org. Chem.* **1977**, *42*, 725-732. DOI: 10.1021/jo00424a033.

(54) Wysocki, V.H.; Ross, M.M. Charge-remote fragmentation of gas-phase ions: mechanistic and energetic considerations in the dissociation of long-chain functionalized alkanes and alkenes. Int. J. Mass Spectrom. Ion Proc. 1991, 104, 179-211. DOI: 10.1016/0168-1176(91)80009-C.

(55) Bao, J.; Gao, X.; Jones, A.D. Unusual negative charge-directed fragmentation: collision-induced dissociation of cyclopentenone oxylipins in negative ion mode. *Rapid Commun. Mass Spectrom.*, **2014**, *28*, 457-464. DOI: 10.1002/rcm.6803.

(56) Kolakowski, B.M.; Grossert, J.S.; Ramaley, L. Studies on the positive-ion mass spectra from atmospheric pressure chemical ionization of gases and solvents used in liquid chromatography and direct liquid injection. *J. Am. Soc. Mass Spectrom.* **2004**, *15*, 311-324. DOI: 10.1016/j.jasms.2003.10.019.

(57) Mo, S.; Dong, L.; Hurst, W.J.; Van Breemen, R.B. Quantitative analysis of phytosterols in edible oils using APCI liquid chromatography-tandem mass spectrometry. *Lipids* **2013**, *48*, 949–956. DOI:10.1007/s11745-013-3813-3.

(58) Laine, R.A.; Elbein, A.D. Steryl Glucosides in Phaseolus aureus. Use of Gas-Liquid Chromatography and Mass Spectrometry for Structural Identification. *Biochemistry* **1971**, *10*, 2547–2553. DOI: 10.1021/bi00789a020.

(59) Neto, R.R.; Thompson, A.; Wolff, G.A. Determination of steryl sulphates in invertebrate tissue by liquid chromatography-tandem mass spectrometry. *Anal. Bioanal. Chem.* **2005**, *383*, 938–946. DOI:10.1007/s00216-005-0122-6.

Appendix 1

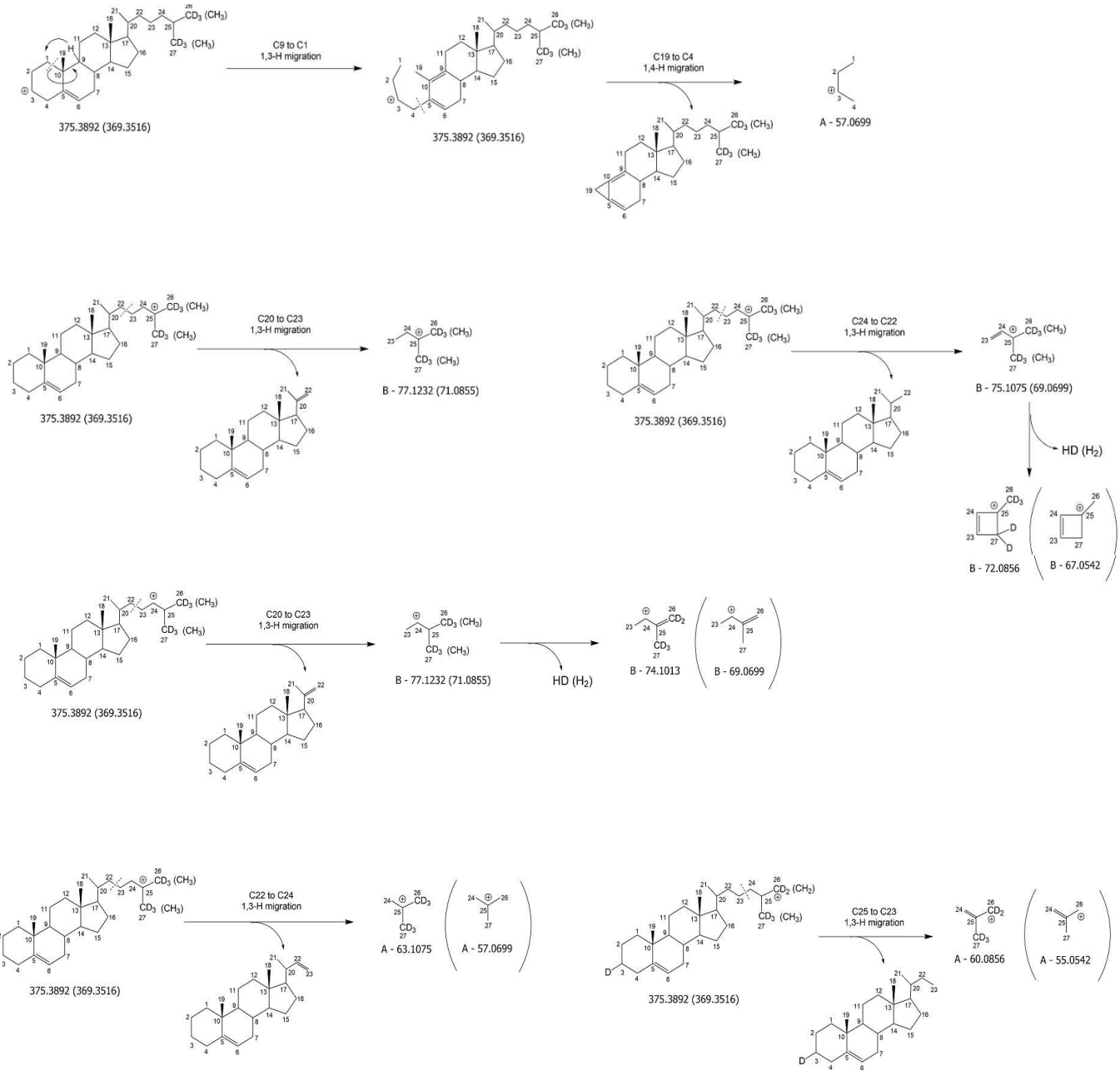
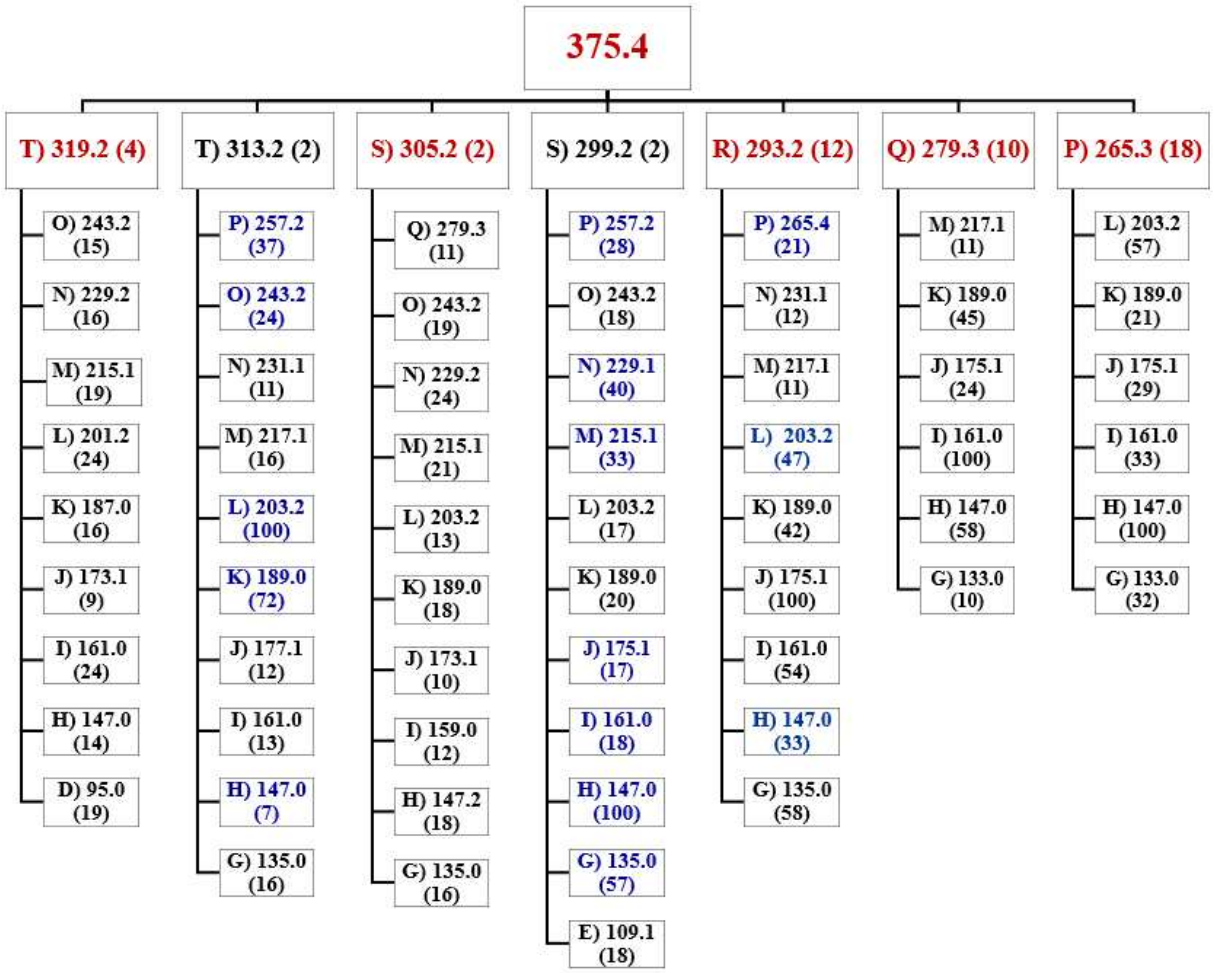


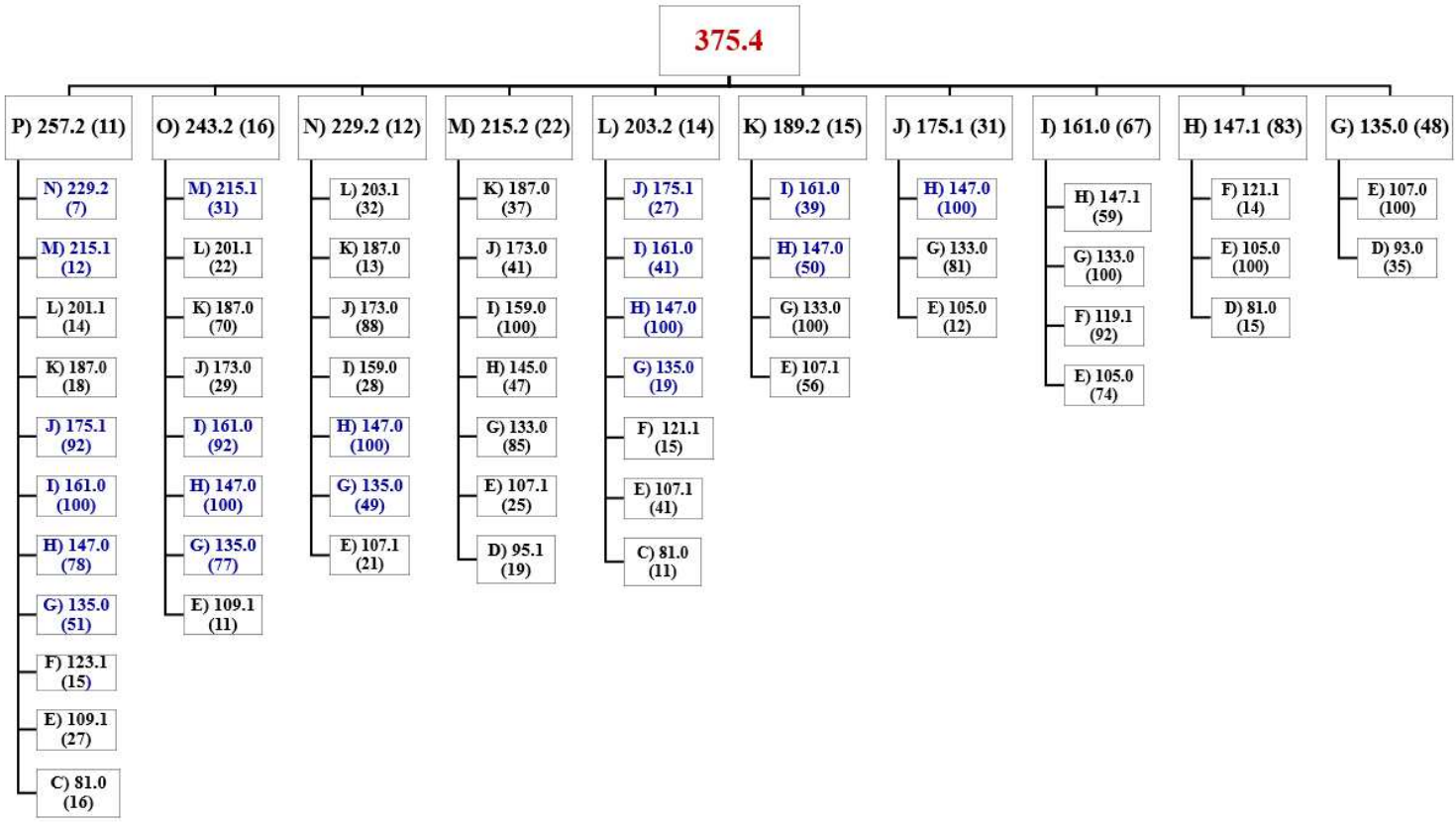
Figure A1. Mechanisms hypothesised to explain the generation of low *m/z* (< 100) product ions shown in **Scheme 1** from the $[M+H-H_2O]^+$ ions of cholesterol (CHO) and of cholesterol (CHO-d_6) completely deuterated on the methyl groups linked to C25. For the sake of clarity, the transfer of H, with concurrent breakage of a C-C bond and the formation of a new C=C bond is depicted explicitly only in the first process drawn in the scheme. Nonetheless, the C-C bond broken as a consequence of this process is highlighted in all fragmentation reactions using a transversal dashed line. Exact *m/z* ratios, rounded off to the fourth decimal place, are reported.

Figure A2. Genealogical trees constructed for sterol $[M+H-H_2O]^+$ ions to describe the information inferred from HCD-FTMS/MS and CID-MS^3/MS^4 acquisitions performed, respectively, using a quadrupole-Orbitrap and a linear ion trap mass spectrometer. The *m/z* ratio of the precursor ion involved in the HCD-FTMS/MS acquisition is reported on top of each tree and is then connected to boxes representing the *m/z* ratios and percentual relative intensities observed, in the HCD-FTMS/MS spectrum, for the resulting product ions that were subsequently subjected to CID-MS^3 acquisitions (note that the same set of product ions was observed in HCD-FTMS/MS and in CID-MS/MS spectra of sterol $[M+H-H_2O]^+$ ions). Each of those boxes is then connected to a series of boxes describing *m/z* ratios and relative intensities observed for ions detected in CID-MS^3 spectra. Among the latter, boxes with *m/z* ratios and relative intensities written in blue colour represent precursor ions selected for subsequent CID-MS^4 acquisitions. In this case, the set of *m/z* ratios of major peak signals detected in the MS^4 spectrum was not explicitly indicated since it corresponded to the set inferred from the MS^3 spectrum acquired on the same precursor ion and reported in one of the genealogical trees for the same sterol. Notes: 1) the *m/z* ratios of ions including D atoms in their structures are written in red character; 2) the letter adopted to mark each product ion cluster in FTMS/MS spectra has been reported also for all ions inside the trees; 3) for the sake of consistency, all *m/z* ratios have been rounded to the first decimal place, in accordance with the precision level available with the linear ion trap mass spectrometer. The figure follows in the next seven pages.

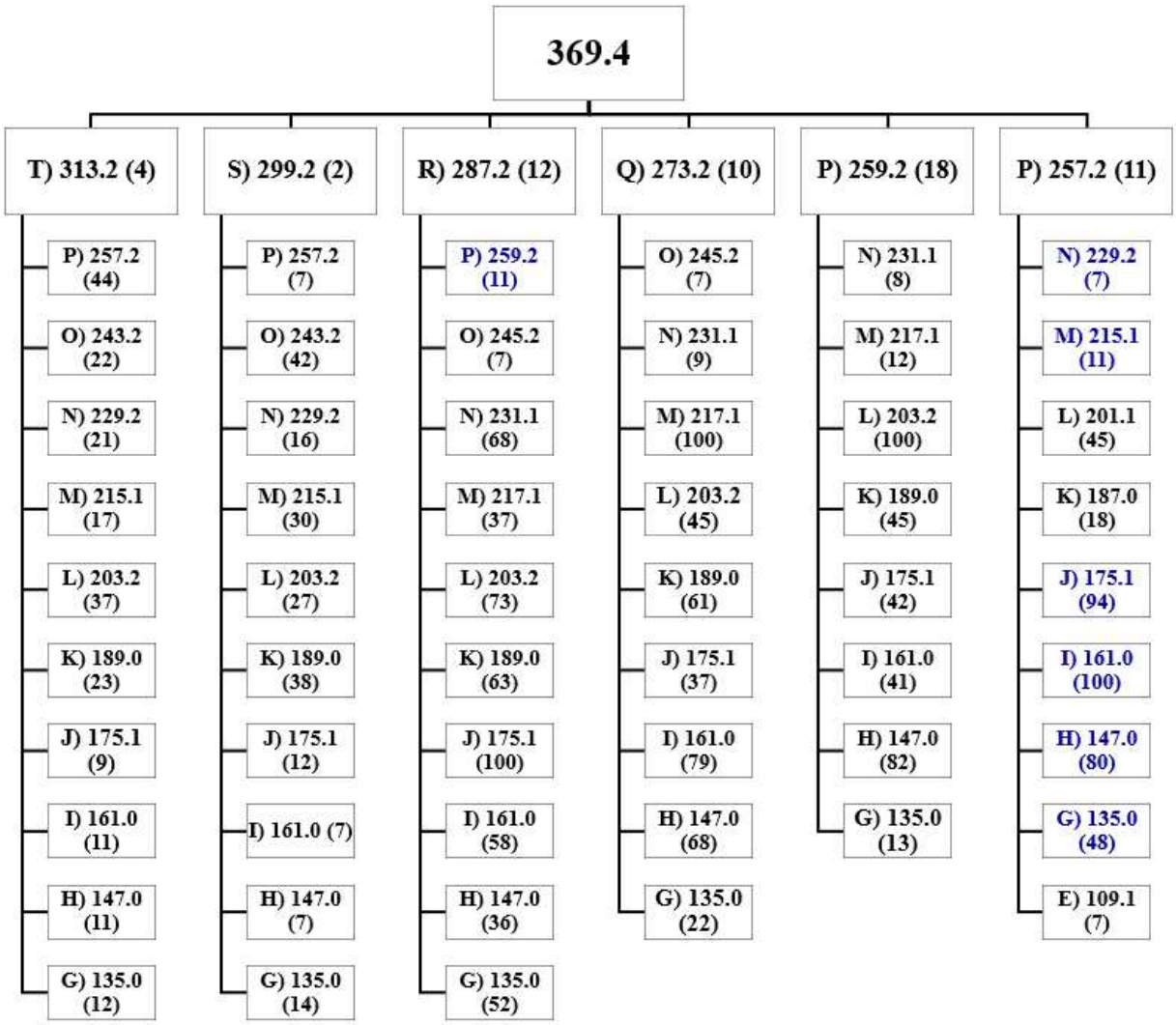
Cholesterol-d_6 (first part)



Cholesterol-d_6 (second part)

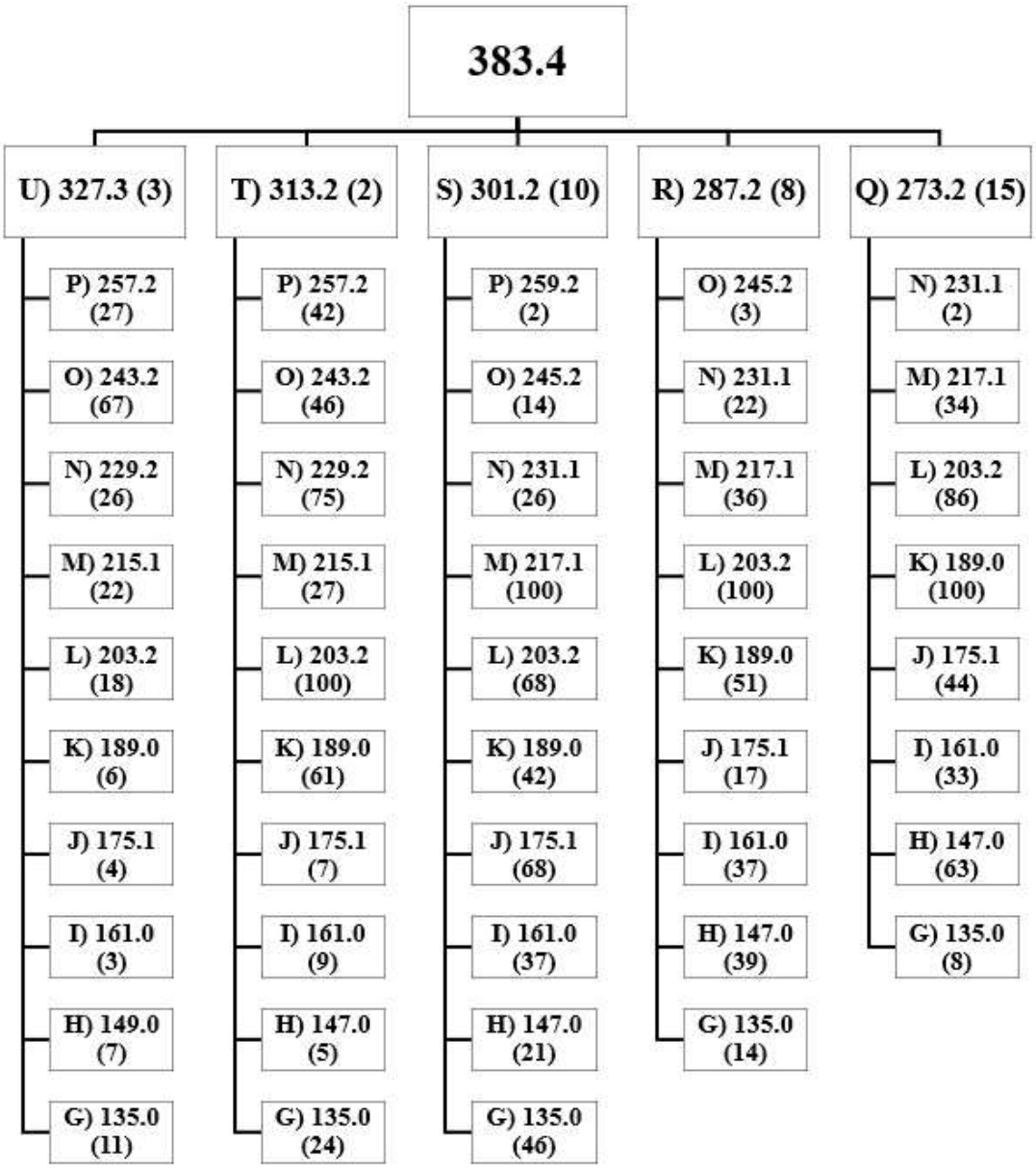


Cholesterol

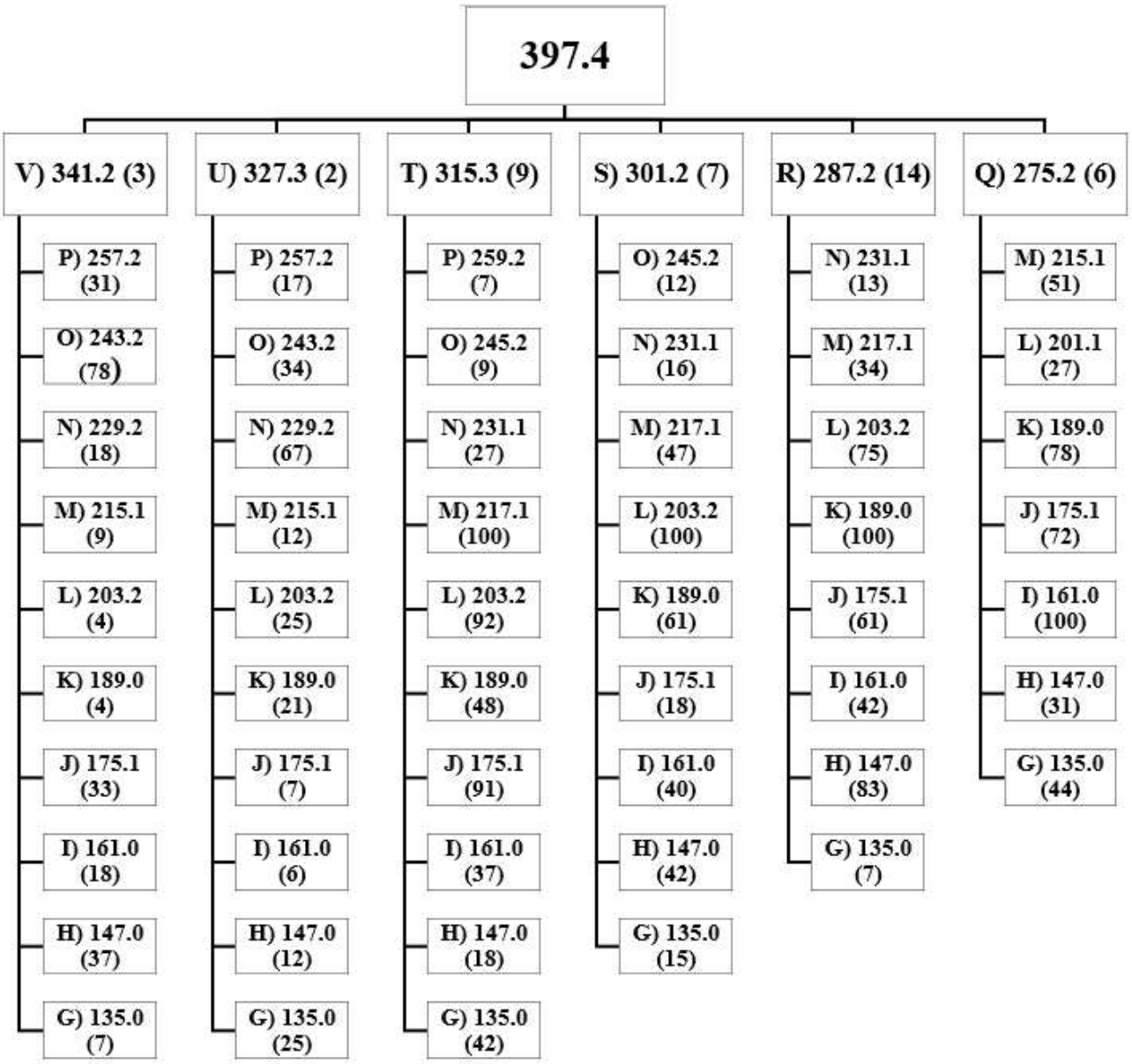


Note: in order to avoid redundancy, only MS^3 and MS^4 transitions characteristic of cholesterol $[M+H-H_2O]^+$ ions are represented in this scheme. Indeed, MS^3 spectra obtained for ions of clusters O to G shown in the second genealogical tree of cholesterol-d_6 $[M+H-H_2O]^+$ ions (see page 4) were practically identical to those obtained for the corresponding precursor ions generated from the cholesterol $[M+H-H_2O]^+$ ions, since the precursor ions had the same structure in both cases.

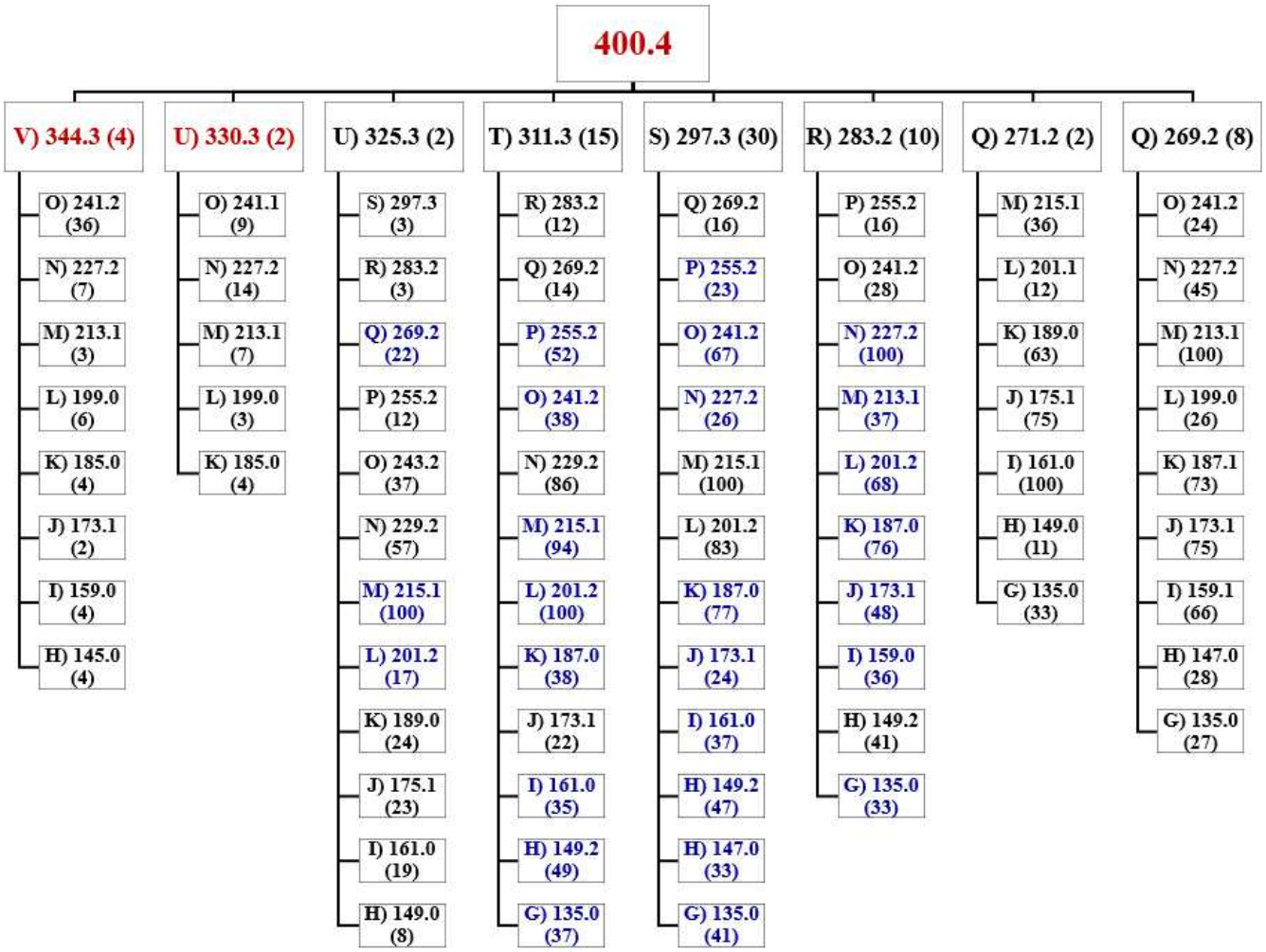
Campesterol



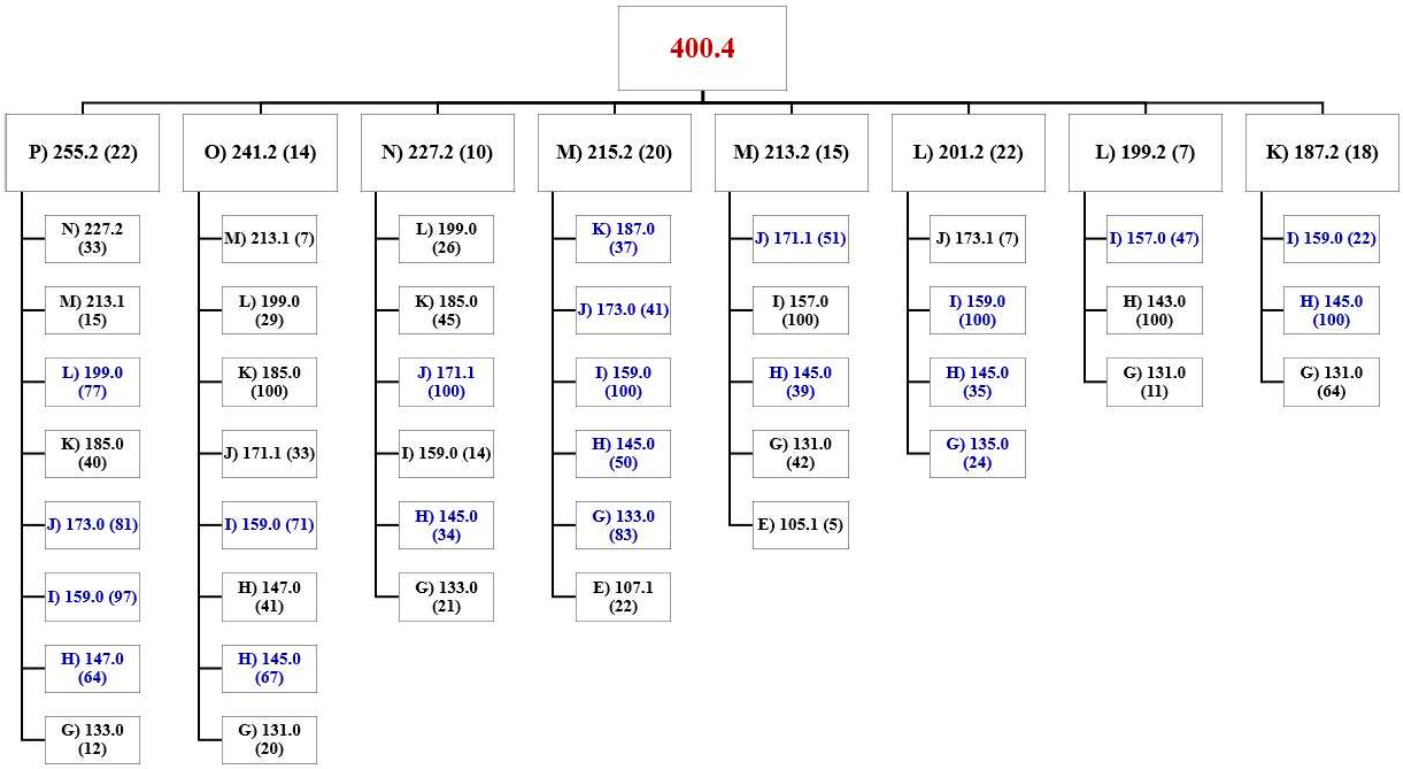
β-sitosterol

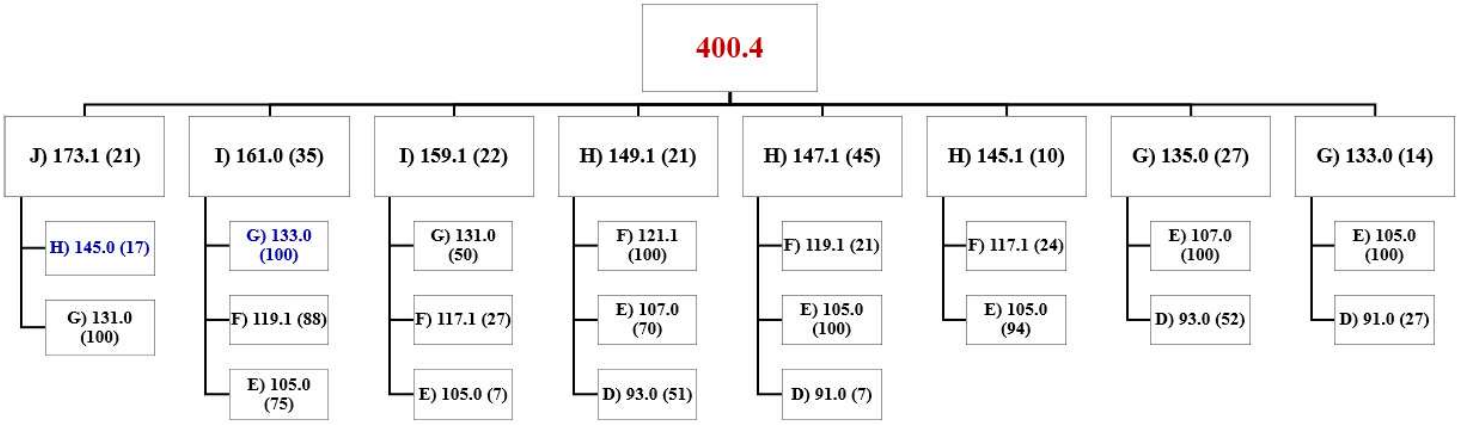


Stigmasterol-d_5 (first part)

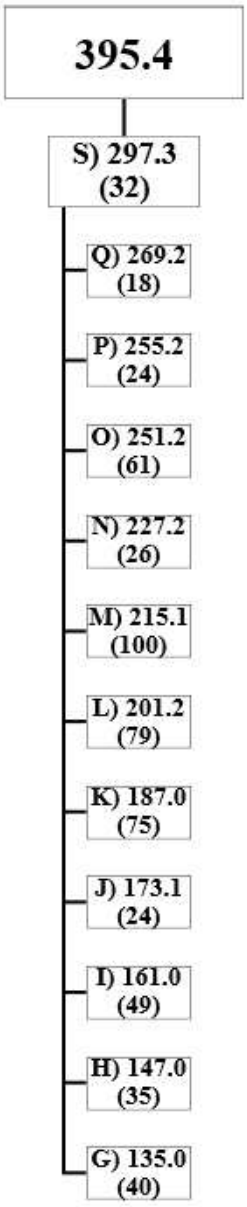


Stigmasterol-d_5 (second and third part)





Stigmasterol



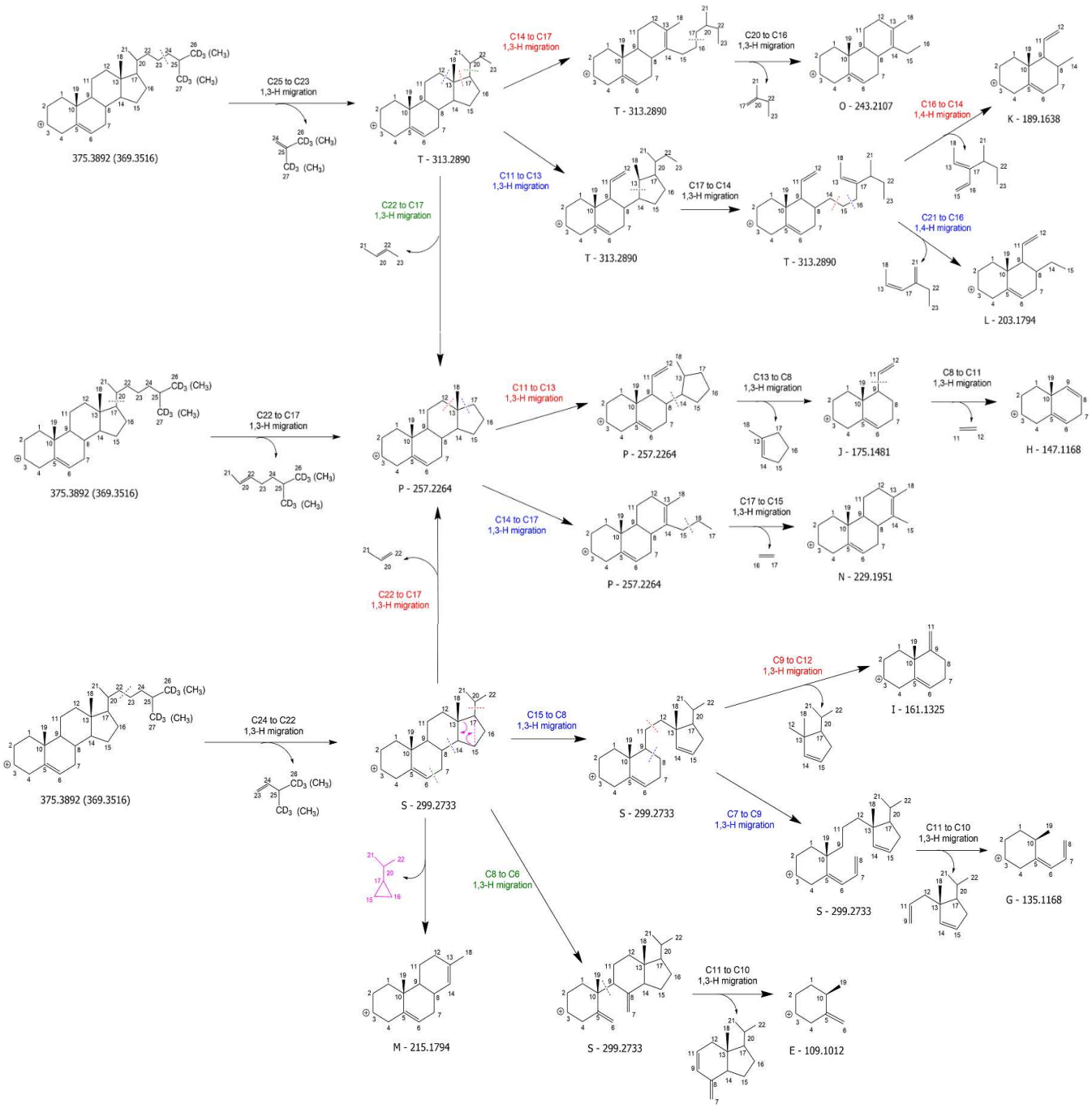


Figure A3. Mechanisms hypothesised to explain the generation of product ions with *m/z* > 100 shown in **Scheme 1** from the $[M+H-H_2O]^+$ precursors ions of cholesterol (CHO) and of cholesterol-d_6 (CHO-d_6). The C-C bonds broken during fragmentation steps are highlighted using a transversal dashed line, eventually coloured to relate the bond breakage to a specific process. Exact *m/z* ratios, rounded off to the fourth decimal place, are reported.

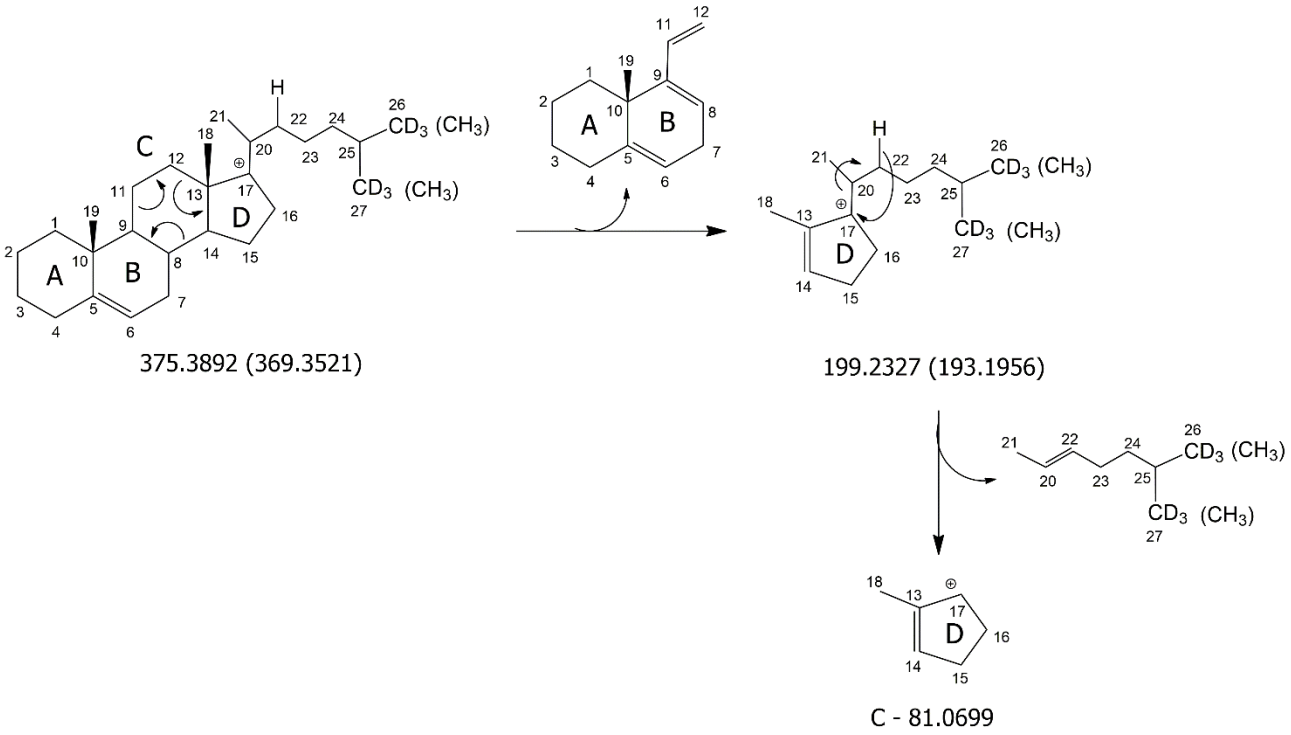


Figure A4. Mechanism potentially responsible for the formation of the product ion detected at *m/z* 81.0705 directly from the $[M+H-H_2O]^+$ ion of cholesterol and cholesterol-d6. It involves a retro-cycloaddition at the C-ring and the removal of the side chain through a 1,3-H transfer from C22 to C17, with breakage of the C17-C20 bond and formation of a C=C bond between C20 and C22. Exact *m/z* ratios, rounded off to the fourth decimal place, are reported.

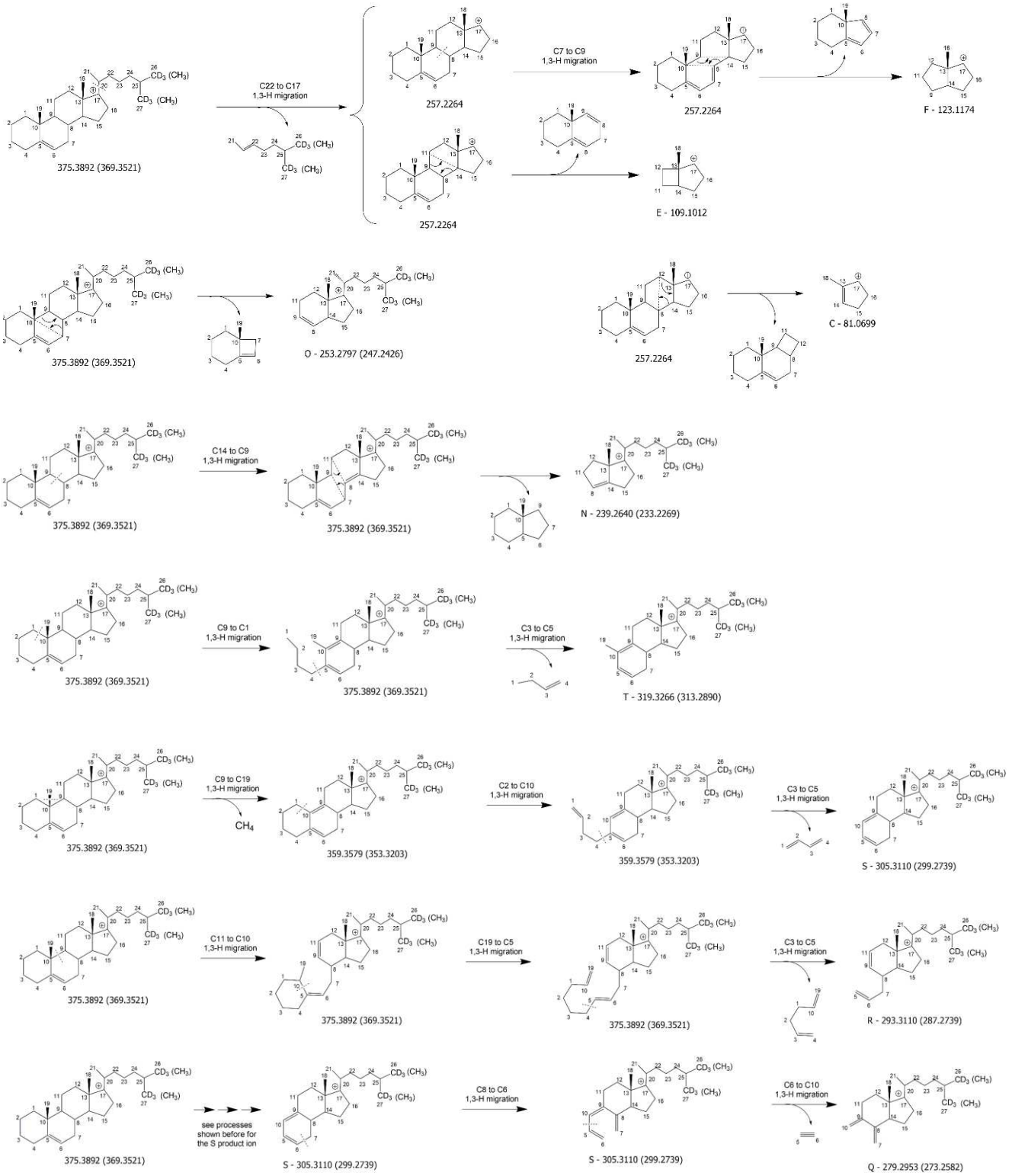


Figure A5. Mechanisms hypothesised to explain the generation of product ions shown in the upper half of **Scheme 2** from the $[M+H-H_2O]^+$ precursors ions of cholesterol (CHO) and of cholesterol-d_6 (CHO-d_6). The C-C bonds broken during fragmentation steps are highlighted using a transversal dashed line. Exact *m/z* ratios, rounded off to the fourth decimal place, are reported.

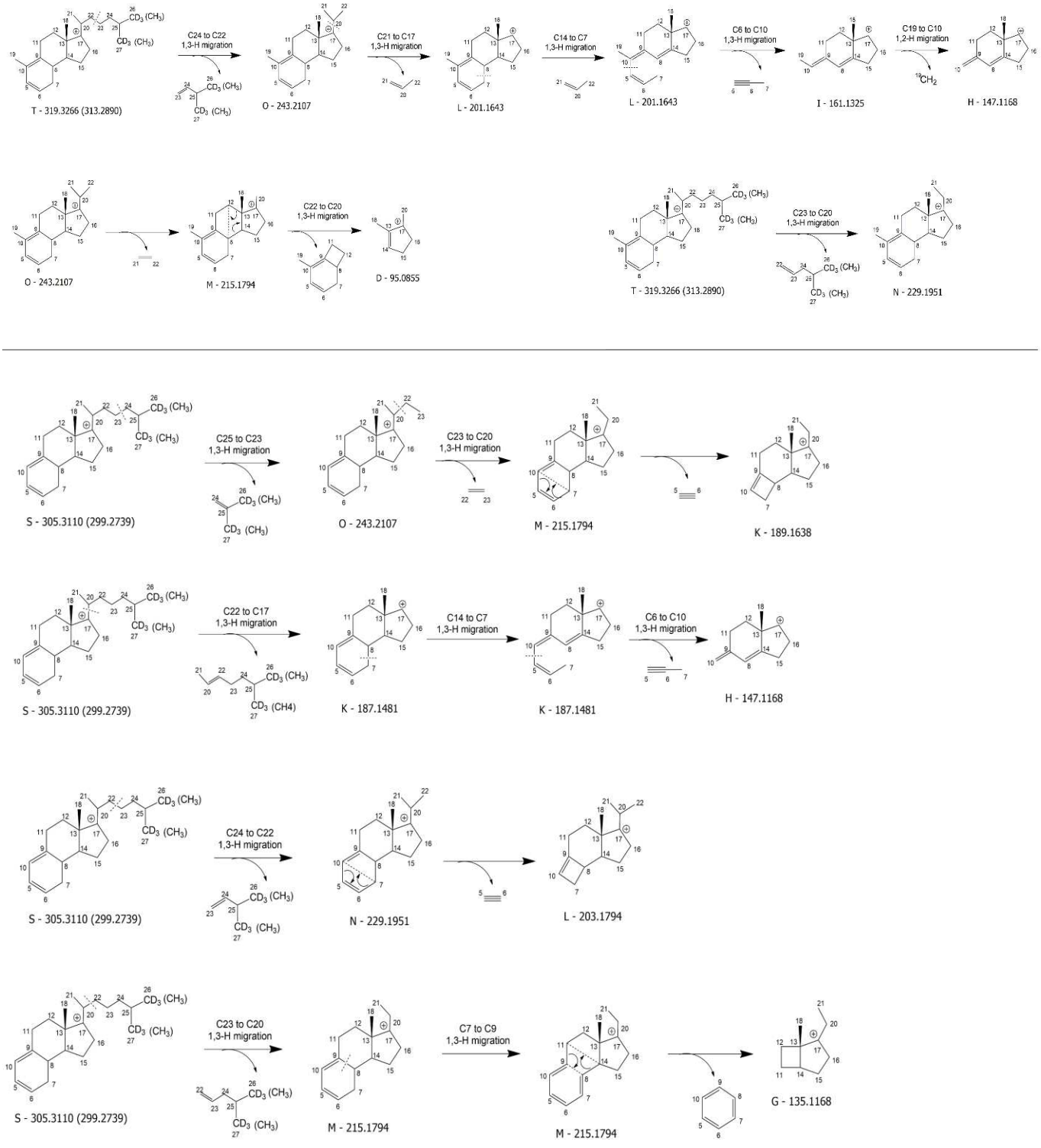


Figure A6. Mechanisms hypothesised to explain the generation of product ions related to ions with *m/z* 319.3266/313.2890 (upper part) and 305.3110/299.2739 (lower part) shown in **Scheme 2**, representing product ions of the $[M+H-H_2O]^+$ ions of cholesterol (CHO) and of cholesterol-d_6 (CHO-d_6). The C-C bonds broken during fragmentation steps are highlighted using a transversal dashed line. Exact *m/z* ratios, rounded off to the fourth decimal place, are reported.

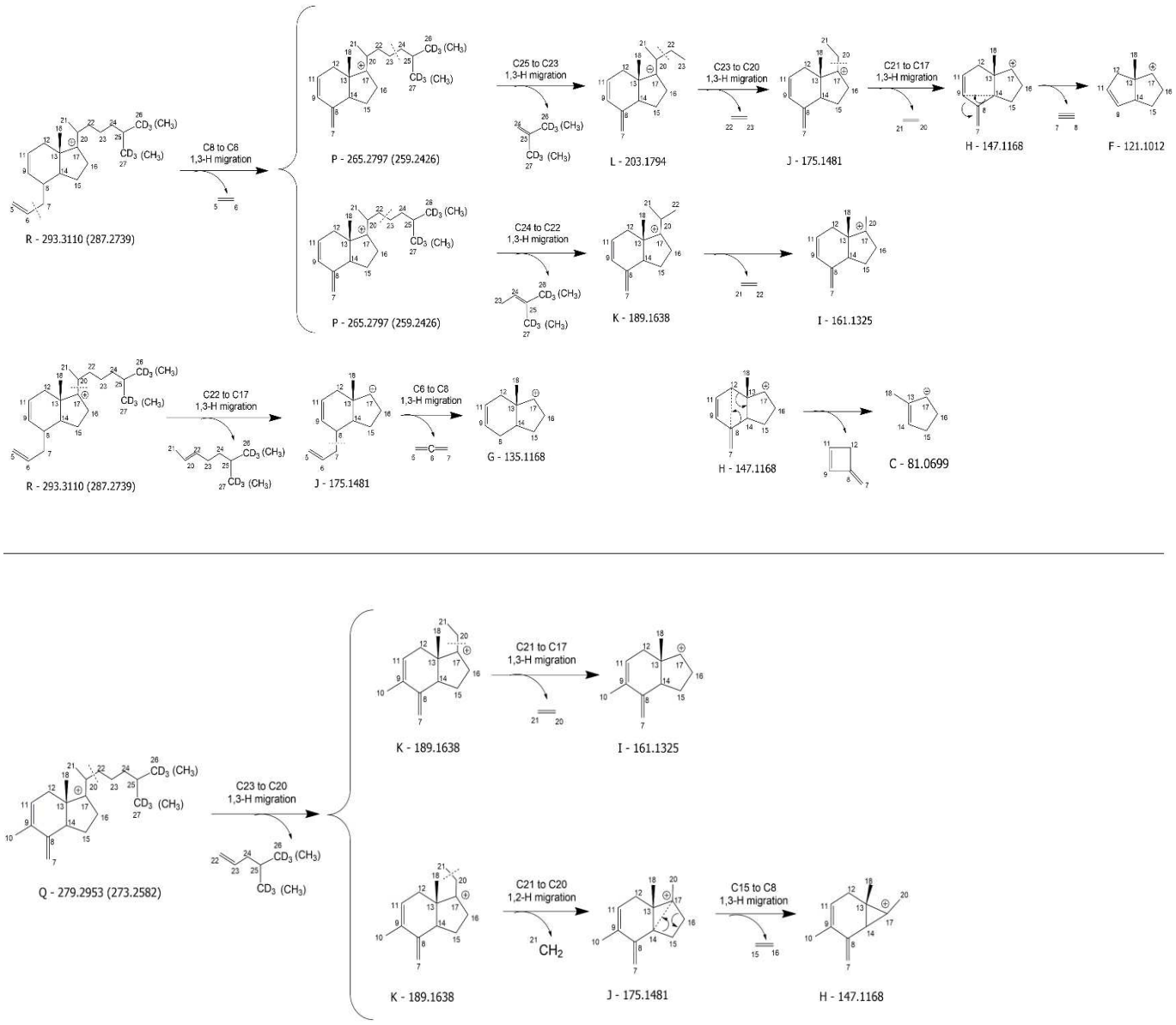


Figure A7. Mechanisms hypothesised to explain the generation of product ions related to ions with *m/z* 293.3110/287.2739 (upper part) and 279.2953/273.2582 (lower part) shown in **Scheme 2**, representing product ions of the $[M+H-H_2O]^+$ ions of cholesterol (CHO) and of cholesterol-d_6 (CHO-d_6). The C-C bonds broken during fragmentation steps are highlighted using a transversal dashed line. Exact *m/z* ratios, rounded off to the fourth decimal place, are reported.

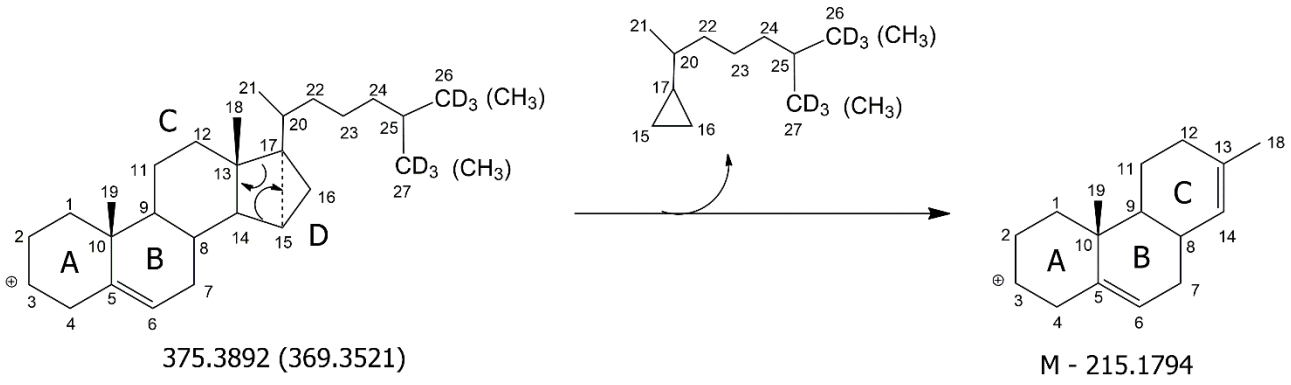


Figure A8. Mechanism hypothesised for the generation of the product ion at *m/z* 215.1790 directly from the $[M+H-H_2O]^+$ ion of cholesterol or cholesterol-d6. The displayed process is a cycloelimination on ring D, leading also to the complete detachment of the side chain. Exact *m/z* ratios, rounded off to the fourth decimal place, are reported.

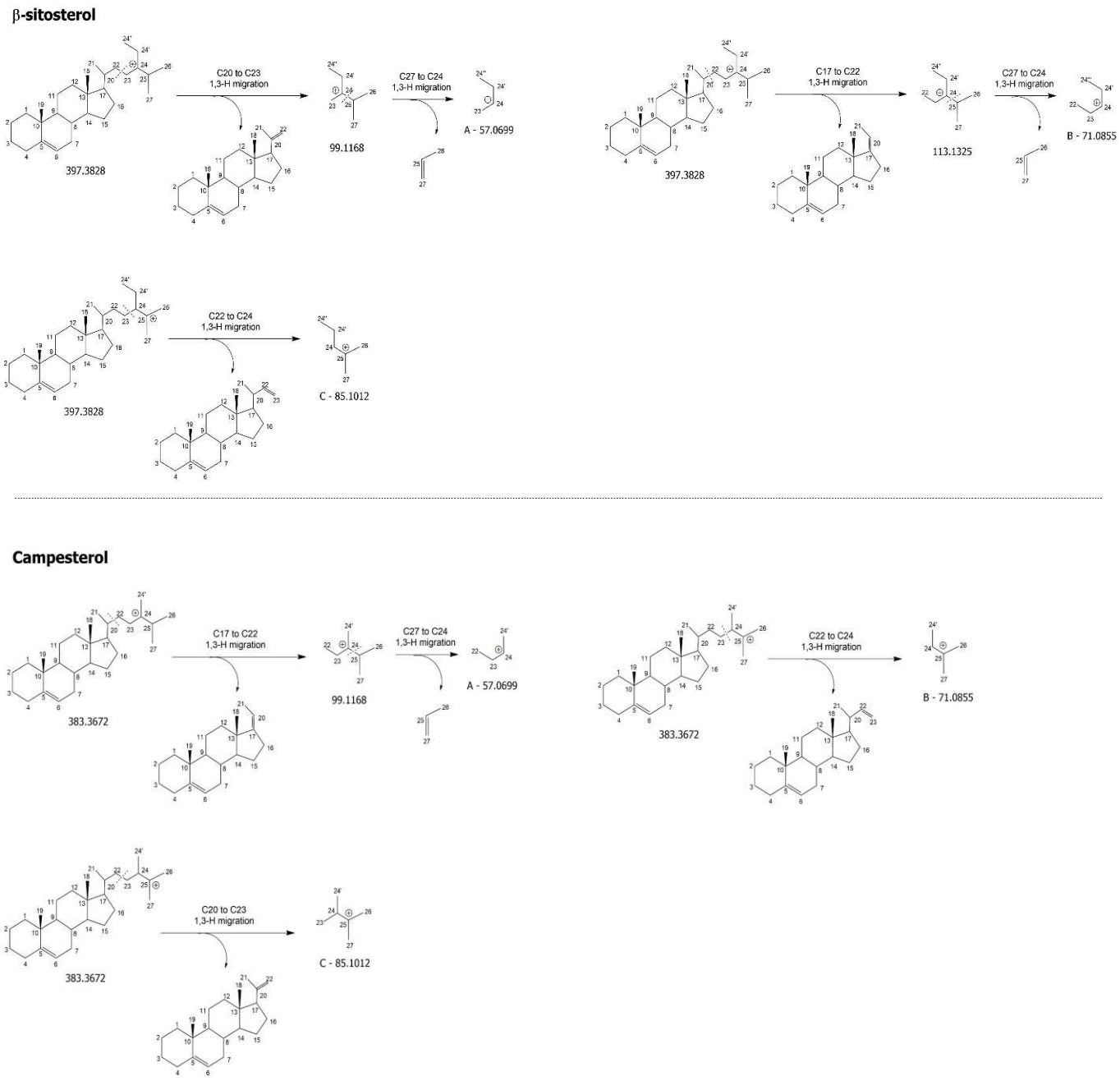


Figure A9. Mechanisms hypothesised to explain the generation of product ions with $m/z < 100$ from $[M+H-H_2O]^+$ ions of b-sitosterol and campesterol. The C-C bonds broken during fragmentation steps are highlighted using a transversal dashed line. Exact *m/z* ratios, rounded off to the fourth decimal place, are reported.

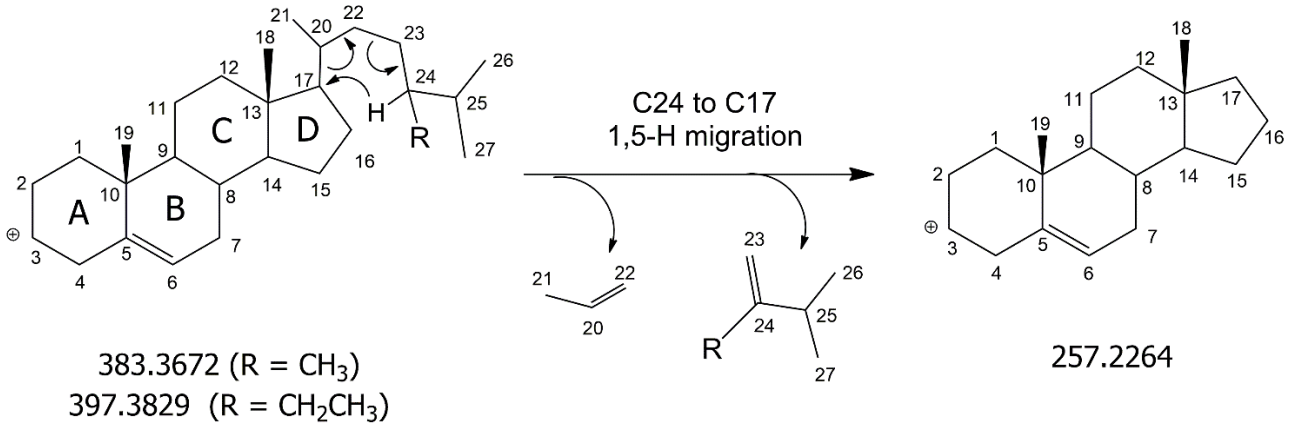


Figure A10. Alternative mechanism proposed for the generation of the product ion detected at *m/z* 257.2257 in the APCI(+)-HCD-FTMS/MS spectra of the $[M+H^+-H_2O]^+$ ions of campesterol (R = CH_3) and b-sitosterol (R = CH_2CH_3). Exact *m/z* ratios, rounded off to the fourth decimal place, are reported.

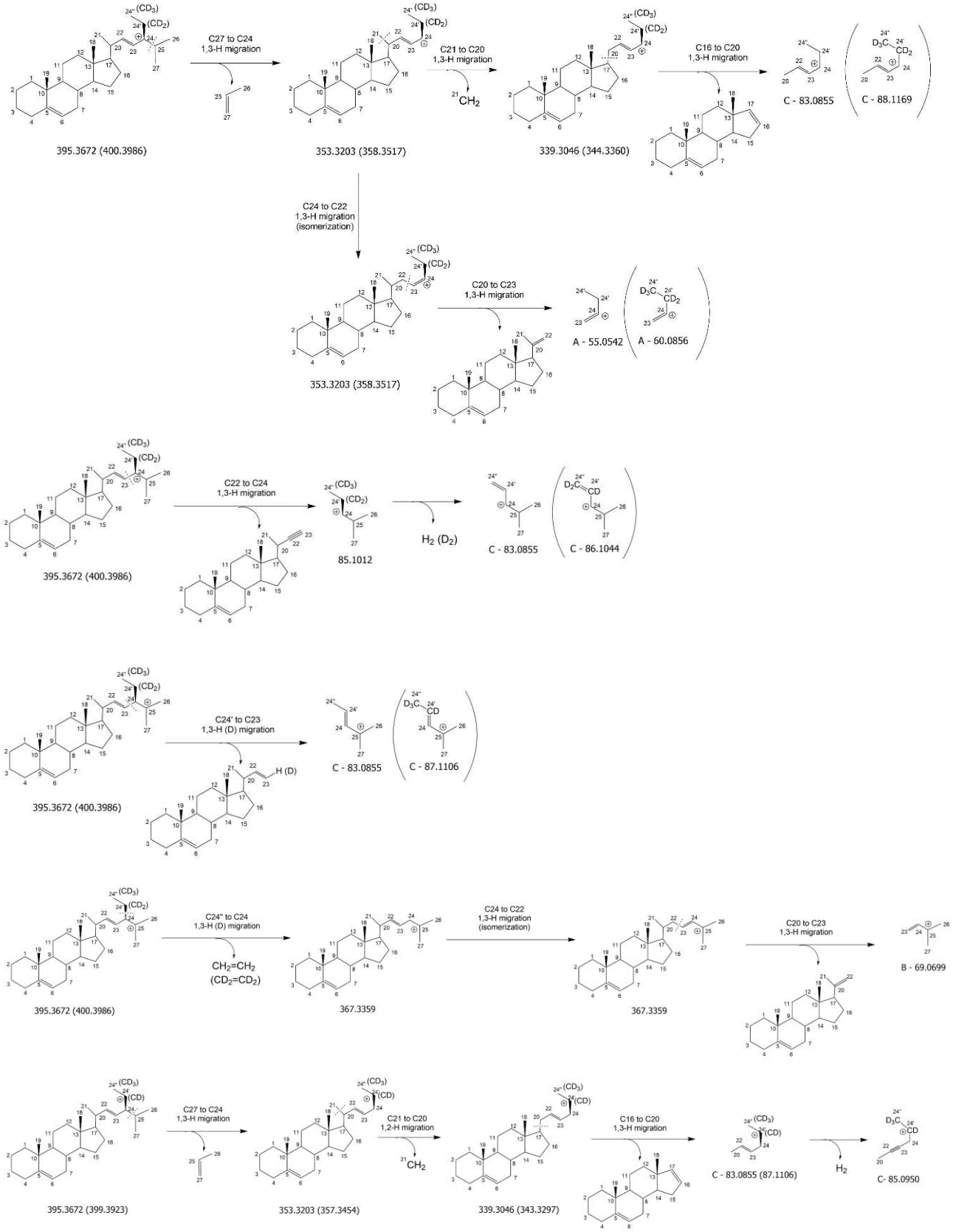


Figure A11. Mechanisms hypothesised to explain the generation of low *m/z* (< 100) product ions shown in **Scheme A1** from the $[M+H-H_2O]^+$ precursor ions of stigmasterol and of stigmasterol completely deuterated on the ethyl group linked to C24. The C-C bonds broken during fragmentation steps are highlighted using a transversal dashed line. Exact *m/z* ratios, rounded off to the fourth decimal place, are reported.

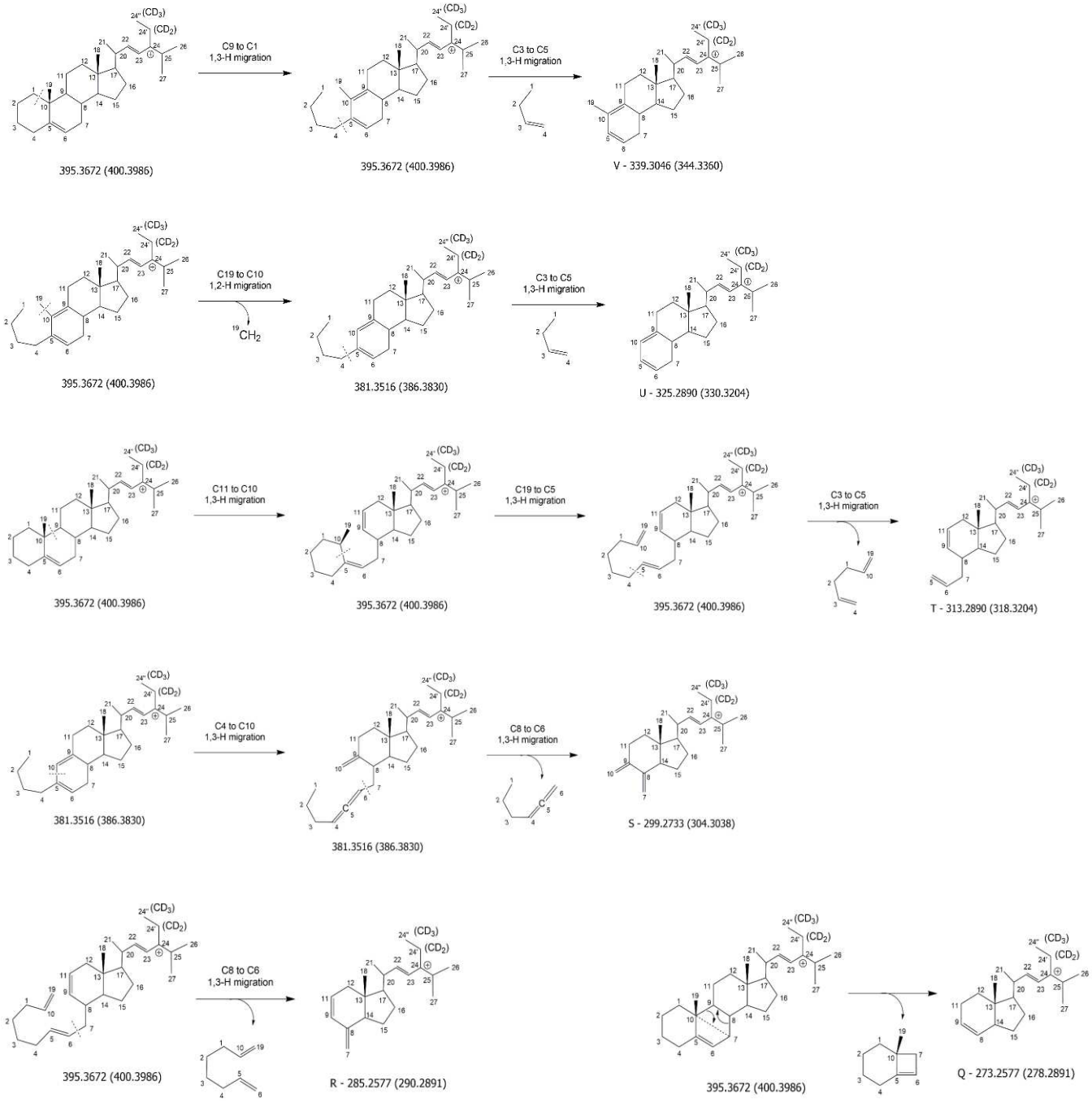


Figure A12. Mechanisms hypothesised to explain the generation from the $[M+H-H_2O]^+$ precursor ions of stigmasterol and stigmasterol-d_5 of product ions with positive charge on C24 shown in **Scheme A1** for clusters Q to V. The C-C bonds broken during fragmentation steps are highlighted using a transversal dashed line. Exact *m/z* ratios, rounded off to the fourth decimal place, are reported.

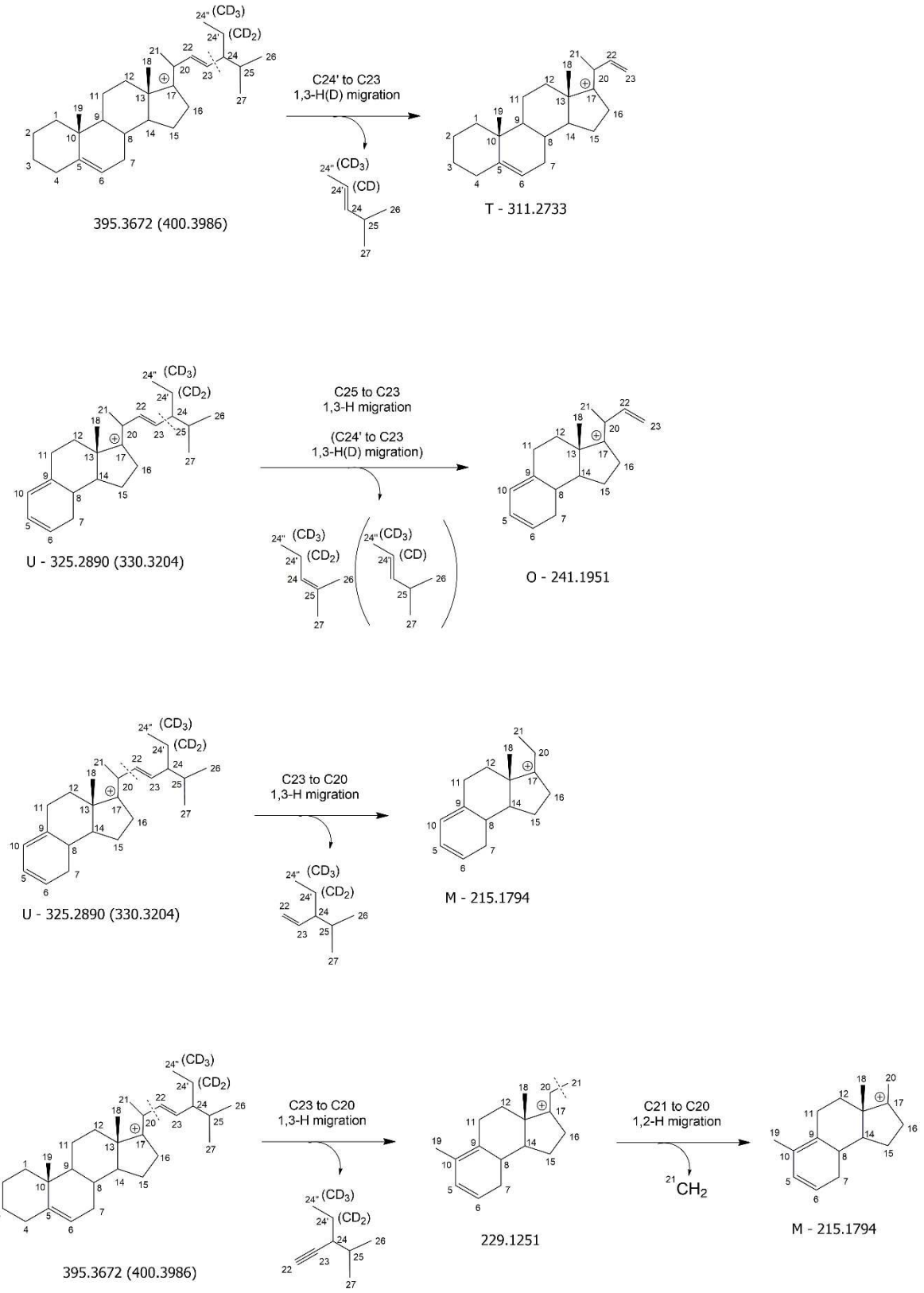


Figure A13. Mechanisms hypothesised to explain the generation from the $[M+H-H_2O]^+$ precursor ions of stigmasterol and stigmasterol-d_5 of product ions with positive charge on C17 shown in **Scheme A1**. The C-C bonds broken during fragmentation steps are highlighted using a transversal dashed line. Exact *m/z* ratios, rounded off to the fourth decimal place, are reported.

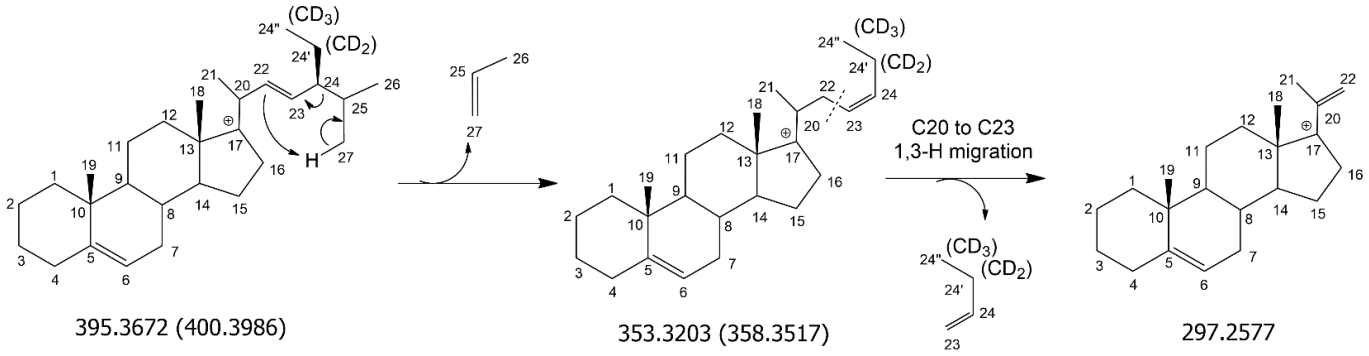


Figure A14. Fragmentation pathway proposed to explain the generation of a product ion with a *m/z* ratio consistent with the exact value 297.2577 upon fragmentation of the $[M+H^+-H_2O]^+$ ions of stigmasterol/stigmasterol-d_5. Note that the same pathway might be considered if the positive charge was located on C3 (see **Figure A15**). Exact *m/z* ratios, rounded off to the fourth decimal place, are reported.

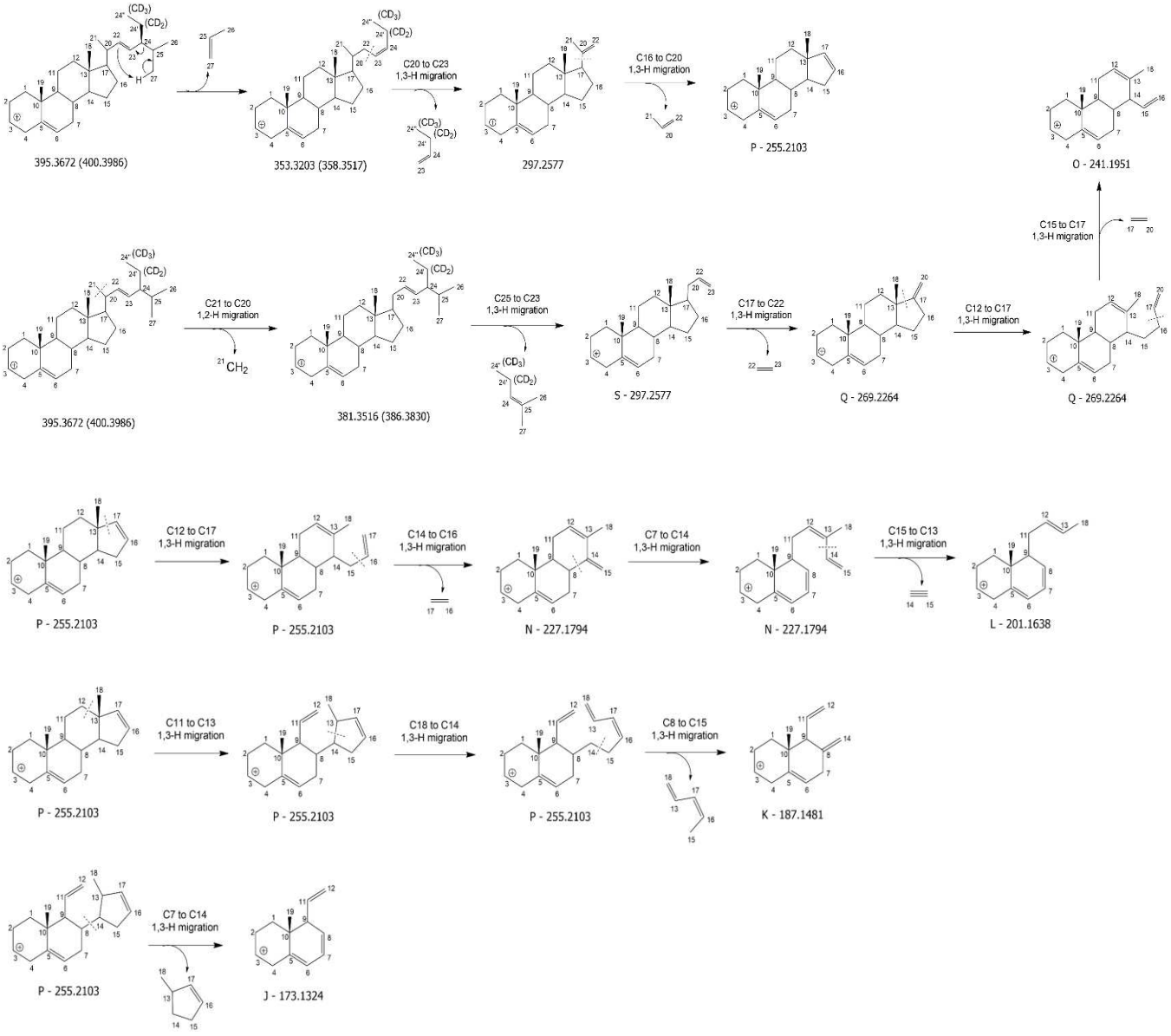


Figure A15. Mechanisms hypothesised to explain the generation from the $[M+H-H_2O]^+$ precursor ions of stigmasterol and stigmasterol-d_5 of product ions with positive charge on C3 shown on the right side of **Scheme A1**. The C-C bonds broken during fragmentation steps are highlighted using a transversal dashed line. Exact *m/z* ratios, rounded off to the fourth decimal place, are reported.

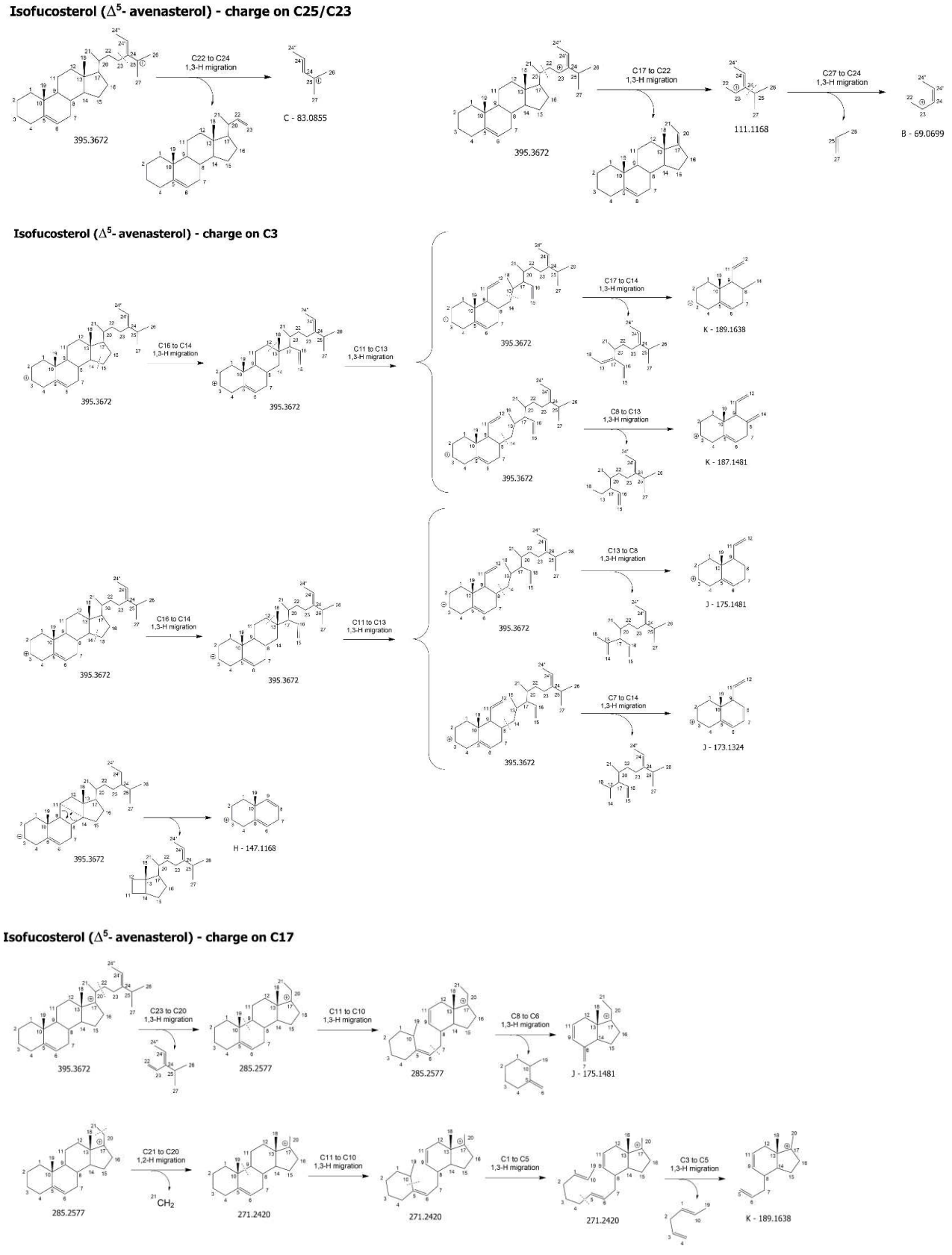


Figure A16. Mechanisms hypothesised to explain the generation of specific product ions arising from the $[M+H-H_2O]^+$ precursor ions of isofucosterol and reported in **Scheme 3**. The C-C bonds broken during fragmentation steps are highlighted using a transversal dashed line. Exact *m/z* ratios, rounded off to the fourth decimal place, are reported.

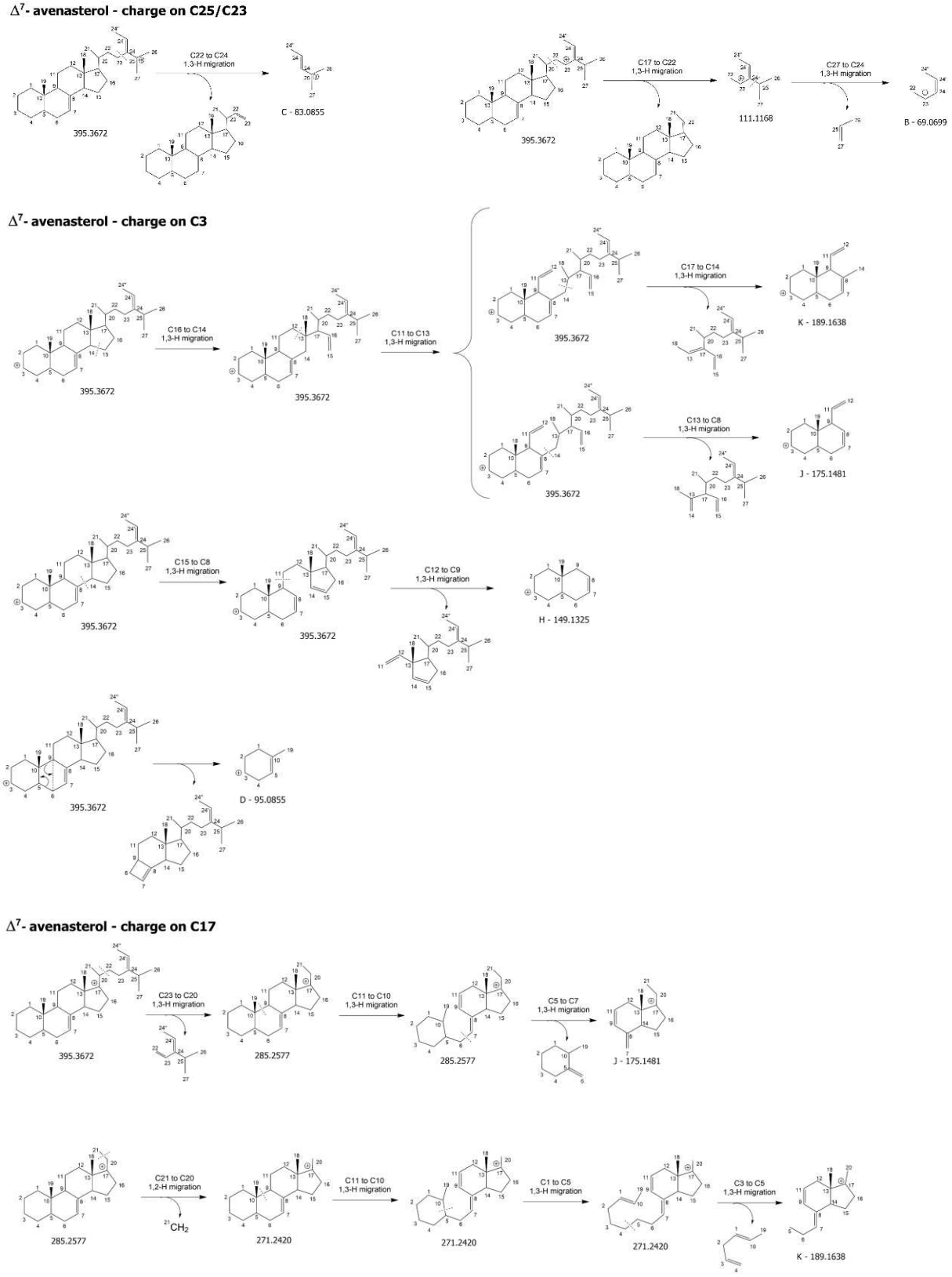


Figure A17. Mechanisms hypothesised to explain the generation of specific product ions arising from the $[M+H-H_2O]^+$ precursor ions of Δ^7-avenasterol and reported in **Scheme 3**. The C-C bonds broken during fragmentation steps are highlighted using a transversal dashed line. Exact *m/z* ratios, rounded off to the fourth decimal place, are reported.

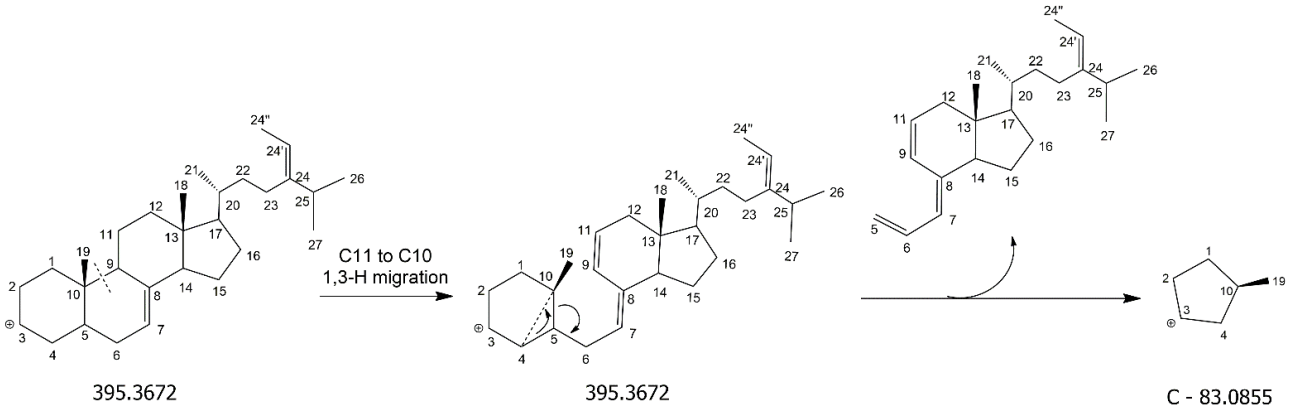
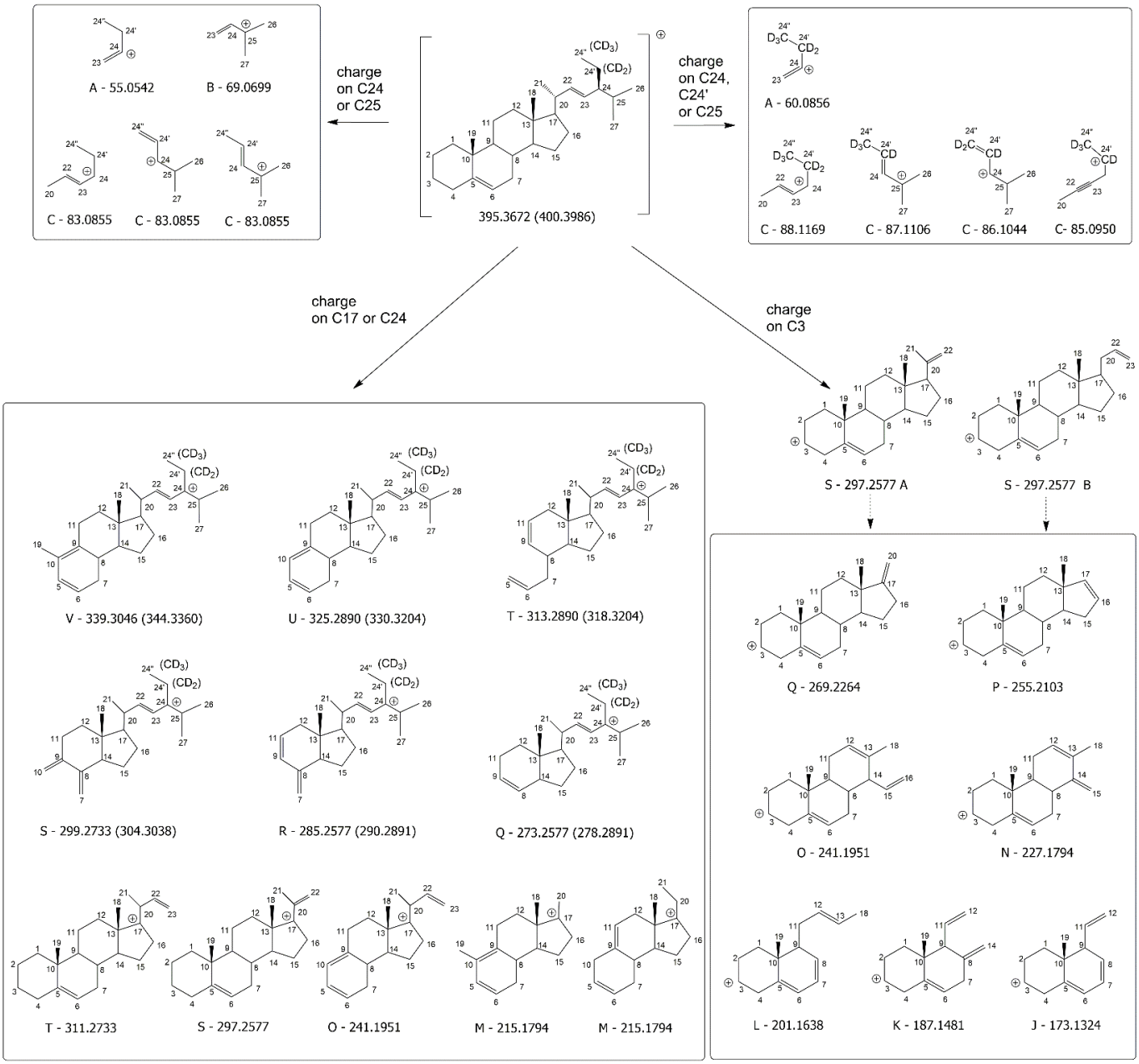


Figure A18. Alterative fragmentation pathway proposed to explain the enhanced generation of a product ion with a *m/z* ratio consistent with the exact value 83.0855 upon fragmentation of the $[M+H^+-H_2O]^+$ ion of Δ^7-avenasterol. Exact *m/z* ratios, rounded off to the fourth decimal place, are reported.



Scheme A1 Fragmentation pathways hypothesised for stigmasterol and stigmasterol penta-deuterated on the ethyl group linked to C24 considering their $[M+H-H_2O]^+$ ions generated in the APCI source as precursor ions, with the positive charge located on different possible sites. Plain arrows indicate fragmentations observed in MS/MS spectra (under both HCD and CID conditions); the dashed arrow indicate fragmentations observed in the 395 > 297 > CID-MS^3 spectrum. Boxes include multiple product ions observed in a single MS^n (n = 2-3) spectrum. Exact *m/z* ratios (rounded off to the fourth decimal place) are reported for all product ions. Values between parentheses are referred to deuterated stigmasterol. Note that structures hypothesized for product ions belonging to clusters from D to I were not reported since they are identical to those proposed in **Schemes 1** and **2** for cholesterol. See text for details.

Table A1. Experimental *m/z* values and relative intensities referred to peak signals detected in the HCD-FTMS/MS spectra of cholesterol and its analogue deuterated on methyl groups linked to C25 (cholesterol-d_6). Molecular formulas consistent with *m/z* values (accuracy < 5 ppm) are also reported. Product ions sharing the same number of C atoms are grouped within a single cluster identified by a capital letter, as in **Figure 3**. *m/z* values of cholesterol product ions for which deuterated counterpart(s) were not detected at all in the cholesterol-d_6 spectrum are underlined; those referred to product ions for which only hexa-deuterated analogues were detected in the cholesterol-d_6 spectrum are reported with bold character.

	Cholesterol			**Cholesterol-d6**				
Ion cluster label	**Molecular Formula**	**Experim. *m/z***	**Rel.Int. (%)**	**Experim. *m/z***	**Rel.Int. (%)**	**Molecular Formula**	**Experim. *m/z***	**Rel.Int. (%)**
A	C_4H_7	55.0551	<2	55.0550	<2	$C_4H_2D_5$	60.0865	6
	C_4H_9	57.0708	11	57.0708	<2	$C_4H_3D_6$	63.1083	6
B	C_5H_7	67.0549	9	67.0550	8	$C_5H_2D_5$	72.0856	<2
	C_5H_9	69.0706	15	69.0706	6	$C_5H_4D_5$ $C_5H_3D_6$	74.1013 75.1082	7 3
	C_5H_{11}	71.0862	15	71.0862	<2	$C_5H_5D_6$	77.1238	10
C	C_6H_7	79.0548	4	79.0548	4			
	C_6H_9	81.0705	39	81.0705	32			
	C_6H_{11}	83.0861	26	83.0861	10	$C_6H_8D_3$ $C_6H_5D_6$	86.1014 89.1237	6 4
	C_6H_{13}	85.1017	8	85.1017	<2	$C_6H_7D_6$	91.1388	5
D	C_7H_7	91.0546	4	91.0546	4			
	C_7H_9	93.0703	11	93.0703	10			
	C_7H_{11}	95.0859	49	95.0859	38	$C_7H_5D_6$	101.1235	<2
	C_7H_{13}	97.1015	19	97.1015	7	$C_7H_7D_6$	103.1392	4
E	C_8H_9	105.0701	11	105.0701	10			
	C_8H_{11}	107.0858	16	107.0857	14			
	C_8H_{13}	109.1014	53	109.1014	42	$C_8H_7D_6$	115.1388	<2
	C_8H_{15}	111.1170	14	111.1170	5	$C_8H_9D_6$	117.1546	4
F	C_9H_{11}	119.0856	13	119.0856	12			
	C_9H_{13}	121.1012	21	121.1012	19			
	C_9H_{15}	123.1168	26	123.1168	18	$C_9H_9D_6$	129.1545	2
	C_9H_{17}	125.1324	5	125.1324	<2	$C_9H_{11}D_6$	131.1701	3
G	$C_{10}H_{11}$	131.0854	2	131.0854	2			
	$C_{10}H_{13}$	133.1010	19	133.1010	18			
	$C_{10}H_{15}$	135.1167	53	135.1167	48			
	$C_{10}H_{17}$	137.1323	10	137.1323	6	$C_{10}H_{11}D_6$	143.1699	3
H	$C_{11}H_{13}$	145.1009	4	145.1010	4			
	$C_{11}H_{15}$	147.1166	91	147.1166	83			
	$C_{11}H_{17}$	149.1323	28	149.1323	24			
	$C_{11}H_{19}$	151.1479	7	151.1479	3	$C_{11}H_{13}D_6$	157.1856	2
I	$C_{12}H_{15}$	159.1166	6	159.1166	5			
	$C_{12}H_{17}$	161.1321	76	161.1322	67			
	$C_{12}H_{19}$	163.1475	14	163.1475	11	$C_{12}H_{13}D_6$	169.1856	<2
	$C_{12}H_{21}$	165.1636	7	165.1636	<2	$C_{12}H_{15}D_6$	171.2014	4
J	$C_{13}H_{17}$	173.1323	4	173.1323	4			

	$C_{13}H_{19}$	175.1478	33	175.1478	31			
	$C_{13}H_{21}$	177.1635	6	177.1635	4	$C_{13}H_{15}D_6$	183.2014	<2
	$C_{13}H_{23}$	179.1790	7	179.1790	<2	$C_{13}H_{17}D_6$	185.2169	5
K	$C_{14}H_{19}$	187.1477	6	187.1478	6			
	$C_{14}H_{21}$	189.1634	17	189.1634	15			
	$C_{14}H_{23}$	191.1790	4	191.1790	<2	$C_{14}H_{17}D_6$	197.2168	3
	$C_{14}H_{25}$	**193.1947**	7			$C_{14}H_{19}D_6$	199.2324	8
L	$C_{15}H_{21}$	201.1633	12	201.1635	12			
	$C_{15}H_{23}$	203.1790	16	203.1790	14			
	$C_{15}H_{25}$	205.1947	7	205.1947	<2	$C_{15}H_{19}D_6$	211.2324	6
	$C_{15}H_{27}$	**207.2103**	4			$C_{15}H_{21}D_6$	213.2480	4
M	$C_{16}H_{23}$	215.1790	22	215.1790	22			
	$C_{16}H_{25}$	217.1946	10	217.1946	8			
	$C_{16}H_{27}$	**219.2103**	7			$C_{16}H_{21}D_6$	225.2478	7
	$C_{16}H_{29}$	**221.2257**	7			$C_{16}H_{23}D_6$	227.2634	<2
N	$C_{17}H_{25}$	229.1946	12	229.1945	12			
	$C_{17}H_{27}$	231.2102	2	231.2103	<2	$C_{17}H_{21}D_6$	237.2478	2
	$C_{17}H_{29}$	**233.2258**	11			$C_{17}H_{23}D_6$	239.2634	11
	$C_{17}H_{31}$	**235.2418**	2			$C_{17}H_{25}D_6$	241.2791	2
O	$C_{18}H_{27}$	243.2102	16	243.2102	16			
	$C_{18}H_{29}$	**245.2258**	5			$C_{18}H_{23}D_6$	251.2634	5
	$C_{18}H_{31}$	**247.2414**	9			$C_{18}H_{25}D_6$	253.2790	8
P	$C_{19}H_{29}$	257.2257	11	257.2257	11			
	$C_{19}H_{31}$	**259.2414**	18			$C_{19}H_{25}D_6$	265.2790	18
	$C_{19}H_{33}$	**261.2577**	4			$C_{19}H_{27}D_6$	267.2946	4
Q	$C_{20}H_{33}$	**273.2570**	10			$C_{20}H_{27}D_6$	279.2946	10
R	$C_{21}H_{33}$	**285.2564**	2			$C_{21}H_{27}D_6$	291.2946	2
	$C_{21}H_{35}$	**287.2726**	12			$C_{21}H_{29}D_6$	293.3101	12
S	$C_{22}H_{35}$	299.2725	2	299.2731	<2	$C_{22}H_{29}D_6$	305.3101	2
T	$C_{23}H_{37}$	313.2884	4	313.2884	<2	$C_{23}H_{31}D_6$	319.3275	4
Precursor ion	$C_{27}H_{45}$	369.3516	100			$C_{27}H_{39}D_6$	375.3892	100

Table A2. Experimental *m/z* values and relative intensities referred to peak signals detected in the HCD-FTMS/MS spectra of stigmasterol and its analogue penta-deuterated on the ethyl group linked to C24 (stigmasterol-d_5). Molecular formulas consistent with *m/z* values (accuracy < 5 ppm) are also reported. Product ions sharing the same number of C atoms are grouped within a single cluster, identified by a capital letter, as in **Figure 5**. *m/z* values of stigmasterol product ions for which deuterated counterpart(s) were not detected at all in the stigmasterol-d_5 spectrum are underlined; those referred to product ions for which only penta-deuterated analogues were detected in the cholesterol-d6 spectrum are reported with bold character.

	Stigmasterol			**Stigmasterol-d_5**				
Ion cluster label	**Molecular Formula**	**Experim. *m/z***	**Rel.Int. (%)**	**Experim. *m/z***	**Rel.Int. (%)**	**Molecular Formula**	**Experim. *m/z***	**Rel.Int. (%)**
A	C_4H_7	55.0551	4	55.0551	<2	$C_4H_4D_3$	58.0739	3
						$C_4H_2D_5$	60.0895	4
	C_4H_9	57.0708	16	57.0707	3	$C_4H_4D_5$	62.1013	<2
B	C_5H_7	67.0549	5	67.0549	3	$C_5H_4D_3$	70.0731	4
	C_5H_9	69.0706	29	69.0706	14	$C_5H_6D_3$	72.0877	4
						$C_5H_4D_5$	74.1013	<2
	C_5H_{11}	71.0862	12	71.0862	<2	$C_5H_6D_5$	76.1175	8
C	C_6H_7	<u>79.0548</u>	3	79.0548	3			
	C_6H_9	81.0705	32	81.0704	25	$C_6H_5D_4$	85.0950	12
	C_6H_{11}	83.0861	94	83.0861	9	$C_6H_8D_3$	86.1044	14
						$C_6H_7D_4$	87.1111	21
						$C_6H_6D_5$	88.1174	22
	C_6H_{13}	85.1017	7			$C_6H_8D_5$	90.1313	4
D	C_7H_7	<u>91.0546</u>	2	91.0546	<2			
	C_7H_9	<u>93.0703</u>	9	93.0703	7			
	C_7H_{11}	<u>95.0859</u>	33	95.0859	28			
	C_7H_{13}	97.1015	18	97.1014	<2	$C_7H_{10}D_3$	100.1200	<2
						$C_7H_9D_4$	101.1263	<2
						$C_7H_8D_5$	102.1326	4
E	C_8H_9	<u>105.0701</u>	8	105.0701	6			
	C_8H_{11}	<u>107.0857</u>	15	107.0857	16			
	C_8H_{13}	109.1014	29	109.1014	22	$C_8H_8D_5$	114.1326	<2
	C_8H_{15}	111.1170	6	111.1170	<2	$C_8H_{10}D_5$	116.1482	3
F	C_9H_{11}	<u>119.0856</u>	8	119.0855	7			
	C_9H_{13}	<u>121.1012</u>	17	121.1012	16			
	C_9H_{15}	123.1168	16	123.1168	12	$C_9H_{10}D_5$	128.1482	4
	C_9H_{17}	125.1324	2	125.1324	<2	$C_9H_{12}D_5$	130.1639	2
G	$C_{10}H_{11}$	<u>131.0854</u>	5	131.0855	4			
	$C_{10}H_{13}$	<u>133.1010</u>	14	133.1010	14			
	$C_{10}H_{15}$	135.1167	27	135.1166	27	$C_{10}H_{12}D_3$	140.1478	<2
	$C_{10}H_{17}$	137.1323	7	137.1322	<2	$C_{10}H_{12}D_5$	142.1639	3
H	$C_{11}H_{13}$	<u>145.1010</u>	11	145.1009	10			
	$C_{11}H_{15}$	<u>147.1166</u>	48	147.1165	45			
	$C_{11}H_{17}$	149.1323	22	149.1322	21	$C_{11}H_{14}D_3$	154.1639	<2
	$C_{11}H_{19}$	151.1479	3	151.148	<2	$C_{11}H_{14}D_5$	156.1795	2
I	$C_{12}H_{15}$	<u>159.1166</u>	23	159.1165	22			
	$C_{12}H_{17}$	161.1321	37	161.1321	35			

	$C_{12}H_{19}$	163.1475	14	163.1475	12	$C_{12}H_{14}D_5$	168.1790	<2
	$C_{12}H_{21}$	165.1636	2	165.1636	<2	$C_{12}H_{16}D_5$	170.1952	2
J	$C_{13}H_{17}$	173.1323	21	173.1322	21			
	$C_{13}H_{19}$	175.1478	16	175.1478	16			
	$C_{13}H_{21}$	177.1635	8	177.1634	5	$C_{13}H_{16}D_5$	182.1952	<2
	$C_{13}H_{23}$	**179.1790**	2			$C_{13}H_{18}D_5$	184.2105	2
K	$C_{14}H_{17}$	185.1321	4	185.1321	4			
	$C_{14}H_{19}$	187.1478	19	187.1477	18			
	$C_{14}H_{21}$	189.1634	13	189.1633	11	$C_{14}H_{18}D_3$	194.1946	<2
	$C_{14}H_{23}$	191.1790	3	191.1790	<2	$C_{14}H_{18}D_5$	196.2104	2
L	$C_{15}H_{19}$	199.1478	7	199.1478	7			
	$C_{15}H_{21}$	201.1633	23	201.1633	22			
	$C_{15}H_{23}$	203.1790	13	203.1790	12	$C_{15}H_{20}D_3$	208.2103	<2
	$C_{15}H_{25}$	**205.1947**	2			$C_{15}H_{20}D_5$	210.2259	<2
M	$C_{16}H_{21}$	213.1632	15	213.1632	15			
	$C_{16}H_{23}$	215.1790	21	215.1789	20			
	$C_{16}H_{25}$	217.1946	4	217.1945	3	$C_{16}H_{20}D_5$	222.2260	<2
N	$C_{17}H_{23}$	227.1788	10	227.1788	10			
	$C_{17}H_{25}$	229.1946	9	229.1945	8			
	$C_{17}H_{27}$	231.2102	2	231.2102	<2	$C_{17}H_{22}D_5$	236.2414	2
	$C_{17}H_{29}$	**233.2258**	2			$C_{17}H_{24}D_5$	238.2570	<2
O	$C_{18}H_{25}$	241.1944	14	241.1944	14			
	$C_{18}H_{27}$	243.2102	4	243.2101	2			
	$C_{18}H_{29}$	**245.2258**	2			$C_{18}H_{24}D_5$	250.2570	2
	$C_{18}H_{31}$	**247.2414**	2			$C_{18}H_{26}D_5$	252.2728	2
P	$C_{19}H_{27}$	255.2107	23	255.2107	22			
	$C_{19}H_{29}$	257.2257	4	257.2257	2			
	$C_{19}H_{31}$	**259.2414**	3			$C_{19}H_{26}D_5$	264.2726	<2
	$C_{19}H_{33}$	**261.2570**	2			$C_{19}H_{28}D_5$	266.2883	<2
Q	$C_{20}H_{29}$	269.2257	8	269.2257	8			
	$C_{20}H_{31}$	271.2413	3	271.2413	<2	$C_{20}H_{28}D_3$	276.2725	2
	$C_{20}H_{33}$	**273.2570**	3			$C_{20}H_{28}D_5$	278.2883	2
R	$C_{21}H_{31}$	283.2412	10	283.2412	10			
	$C_{21}H_{33}$	**285.2564**	8			$C_{21}H_{28}D_5$	290.2882	7
	$C_{21}H_{35}$	**287.2726**	3			$C_{21}H_{30}D_5$	292.3039	3
S	$C_{22}H_{33}$	297.2568	32	297.2568	30			
	$C_{22}H_{35}$	**299.2725**	5			$C_{22}H_{30}D_5$	304.3038	5
T	$C_{23}H_{35}$	311.2575	15	311.2725	15			
	$C_{23}H_{37}$	**313.2884**	6			$C_{23}H_{32}D_5$	318.3195	6
U	$C_{24}H_{37}$	325.2883	2	325.2883	<2	$C_{24}H_{32}D_5$	330.3198	2
V	$C_{25}H_{39}$	**339.3046**	4			$C_{23}H_{34}D_5$	344.3352	4
Precursor ion	$C_{29}H_{47}$	395.3672	100			$C_{27}H_{40}D_5$	400.3987	100

Table A3. Summary of typical relative intensities obtained for specific ions detected in APCI(+)-HCD-FTMS/MS spectra acquired for the $[M+H-H_2O]^+$ ions of sterols investigated in the present study. Experimental *m/z* values and molecular formulas inferred from them considering an accuracy not higher than 5 ppm are also reported. Ions are grouped according to the number of C atoms in their structures, in clusters labelled as in **Figures 3**, **4** and **5**, according to the case. The prevailing relative intensity in each cluster is reported in bold character.

			Cholesterol	**Campesterol**	**β-sitosterol**	**Stigmasterol**	**Brassicasterol**	**Isofucosterol**	**Δ^7-avenasterol**
Ion cluster	**Molecular formula**	**Experim. *m/z***	**Relative Intensity [%]**						
A	C_4H_7	55.0551	<2	2	<2	4	<2	2	6
	C_4H_9	57.0708	**11**	**16**	**18**	**16**	**11**	**10**	**15**
B	C_5H_7	67.0549	9	9	9	5	4	7	14
	C_5H_9	69.0708	15	13	21	**29**	**51**	**39**	**66**
	C_5H_{11}	71.0862	**15**	**21**	**27**	12	5	13	15
C	C_6H_7	79.0548	4	3	4	3	2	3	8
	C_6H_9	81.0705	**39**	**39**	**40**	32	20	**32**	64
	C_6H_{11}	83.0861	26	23	22	**94**	**22**	25	**89**
	C_6H_{13}	85.1017	8	15	22	7	3	9	11
D	C_7H_7	91.0546	4	3	3	2	/	3	7
	C_7H_9	93.0703	11	12	13	9	6	11	28
	C_7H_{11}	95.0859	**49**	**49**	**50**	**33**	**26**	**39**	**80**
	C_7H_{13}	97.1015	19	24	21	18	9	20	35
E	C_8H_9	105.0701	11	11	11	8	/	10	25
	C_8H_{11}	107.0858	16	15	17	15	11	17	45
	C_8H_{13}	109.1014	**53**	**52**	**52**	**29**	**24**	**40**	**70**
	C_8H_{15}	111.1170	14	14	19	6	5	11	18
F	C_9H_{11}	119.0856	13	12	13	8	7	10	23
	C_9H_{13}	121.1012	21	21	24	**17**	**13**	**24**	**59**
	C_9H_{15}	123.1168	**26**	**26**	**27**	16	12	22	41
	C_9H_{17}	125.1324	5	5	6	2	5	5	4

G	$C_{10}H_{11}$	131.0854	2	/	/	5	4	6	10
	$C_{10}H_{13}$	133.1010	19	19	20	14	11	18	35
	$C_{10}H_{15}$	135.1167	**53**	**54**	**56**	**27**	**20**	**35**	**73**
	$C_{10}H_{17}$	137.1323	10	13	13	7	5	13	31
H	$C_{11}H_{13}$	145.1009	4	4	4	11	9	13	21
	$C_{11}H_{15}$	147.1166	**91**	**91**	**95**	**48**	**34**	**66**	62
	$C_{11}H_{17}$	149.1323	28	30	31	22	17	28	**93**
	$C_{11}H_{19}$	151.1479	7	8	9	3	2	6	8
I	$C_{12}H_{13}$	157.1012	/	/	/	/	/	2	2
	$C_{12}H_{15}$	159.1166	6	6	6	23	20	41	49
	$C_{12}H_{17}$	161.1321	**76**	**77**	**80**	**37**	**29**	**65**	**92**
	$C_{12}H_{19}$	163.1475	14	16	17	14	12	18	43
	$C_{12}H_{21}$	165.1636	7	7	6	2	2	4	4
J	$C_{13}H_{15}$	171.1168	/	/	/	/	/	2	2
	$C_{13}H_{17}$	173.1323	4	4	4	**21**	**17**	26	27
	$C_{13}H_{19}$	175.1478	**33**	**36**	**38**	16	13	**28**	**53**
	$C_{13}H_{21}$	177.1635	6	7	7	8	6	8	19
	$C_{13}H_{23}$	179.1790	7	4	3	2	/	/	/
K	$C_{14}H_{17}$	185.1321	/	/	/	4	3	4	5
	$C_{14}H_{19}$	187.1477	6	7	7	**19**	**14**	**14**	31
	$C_{14}H_{21}$	189.1633	**17**	**20**	**21**	13	10	13	**36**
	$C_{14}H_{23}$	191.179	4	3	3	3	3	5	6
	$C_{14}H_{25}$	193.1947	7	3	2	/	/	/	/
L	$C_{15}H_{19}$	199.1477	/	/	/	7	7	8	8
	$C_{15}H_{21}$	201.1633	12	12	12	**23**	**17**	**15**	**37**
	$C_{15}H_{23}$	203.1790	**16**	**19**	**19**	13	10	**15**	32
	$C_{15}H_{25}$	205.1947	7	/	/	2	2	3	4
	$C_{15}H_{27}$	207.2103	4	5	2	/	/	/	/
M	$C_{16}H_{21}$	213.1633	/	/	/	15	13	12	14

	$C_{16}H_{23}$	215.1790	**22**	**23**	**23**	**21**	**16**	**18**	**58**
	$C_{16}H_{25}$	217.1946	10	11	11	4	4	5	15
	$C_{16}H_{27}$	219.2103	7	4	/	/	3	2	4
	$C_{16}H_{29}$	221.2257	7	2	4	/	/	/	/
N	$C_{17}H_{23}$	227.1789	/	/	/	**10**	**8**	7	13
	$C_{17}H_{25}$	229.1946	**12**	**13**	**13**	9	7	**10**	**29**
	$C_{17}H_{27}$	231.2102	2	/	/	2	3	4	7
	$C_{17}H_{29}$	233.2258	11	5	4	2	2	2	5
	$C_{17}H_{31}$	235.2418	2	/	/	/	/	/	/
O	$C_{18}H_{25}$	241.1944	/	/	/	**14**	**12**	**10**	**22**
	$C_{18}H_{27}$	243.2102	**16**	**19**	**19**	4	3	5	12
	$C_{18}H_{29}$	245.2258	5	/	/	2	3	2	5
	$C_{18}H_{31}$	247.2414	9	9	5	2	2	3	/
P	$C_{19}H_{27}$	255.2107	/	/	/	**23**	**17**	**20**	**31**
	$C_{19}H_{29}$	257.2257	11	**14**	**16**	4	4	8	28
	$C_{19}H_{31}$	259.2414	**18**	10	/	3	3	5	3
	$C_{19}H_{33}$	261.2577	4	7	8	2	/	/	/
Q	$C_{20}H_{29}$	269.2257	/	/	/	**8**	6	4	7
	$C_{20}H_{31}$	271.2413	/	2	3	3	**8**	**6**	**13**
	$C_{20}H_{33}$	273.2570	**10**	**15**	4	3	4	5	/
	$C_{20}H_{35}$	275.2726	/	4	**6**	/	/	/	/
R	$C_{21}H_{31}$	283.2412	/	/	/	**10**	**6**	**10**	**22**
	$C_{21}H_{33}$	285.2564	2	3	3	8	5	8	9
	$C_{21}H_{35}$	287.2726	**12**	**8**	**14**	3	/	/	/
	$C_{21}H_{37}$	289.2890	/	/	3	/	/	/	/
S	$C_{22}H_{33}$	297.2568	/	/	/	**32**	**25**	**13**	**55**
	$C_{22}H_{35}$	299.2725	**2**	3	3	5	6	4	5
	$C_{22}H_{37}$	301.2880	/	**10**	**7**	/	/	/	/
T	$C_{23}H_{35}$	311.2725	/	/	/	**15**	**10**	**10**	9

	$C_{23}H_{37}$	313.2884	**4**	**2**	2	6	/	5	**18**
	$C_{23}H_{39}$	315.3041	/	/	**9**	/	/	/	/
U	$C_{24}H_{37}$	325.2881	/	/	/	**2**	**3**	**3**	4
	$C_{24}H_{39}$	327.3039	/	**3**	**2**	/	/	/	**7**
V	$C_{25}H_{39}$	339.3046	/	/	/	**4**	/	**3**	**4**
	$C_{25}H_{41}$	341.3203	/	/	**3**	/	/	/	/
Precursor ion	$C_{27}H_{45}$	369.3516	**100**	/	/	/	/	/	/
	$C_{28}H_{45}$	381.3516	/	/	/	/	**100**	/	/
	$C_{28}H_{47}$	383.3672	/	**100**	/	/	/	/	/
	$C_{29}H_{47}$	395.3672	/	/	/	**100**	/	**100**	**100**
	$C_{29}H_{49}$	397.3829	/	/	**100**	/	/	/	/

Chapter 2

Study of diagnostic fragmentations of animal and fungal sterols/stanols obtained by APCI-tandem mass spectrometry to infer general rules for unknown free sterols identification

The following journal article was based on results illustrated in the present chapter:

V. Cinquepalmi, I. Losito, A. Castellaneta, C. D. Calvano, T.R.I. Cataldi, "Diagnostic Fragmentations of Animal and Fungal Sterols/Stanols Obtained by APCI–Tandem Mass Spectrometry: A Route Towards Unknown Free Sterol Identification", *Metabolites*, 15(10), 674, doi: https://doi.org/10.3390/metabo15100674.

2.1 Introduction

As discussed before for phytosterols, sterols play a crucial role in maintaining the structural integrity and regulating the fluidity and permeability of the lipid bilayer in eukaryotic plasma membranes[1–4]. From a general biosynthetic perspective, sterols originate from the isoprene pathway and are derived through the oxygenation and cyclisation of squalene[1,5,6]. These transformations yield the characteristic tetracyclic structure already discussed before for phytosterols, which imparts all sterols their amphipathic nature[5,7,8]. Also in non-vegetal sterols the four rings of the steroidal backbone, labelled A, B, C, and D (**Figure 1**), adopt an all-*trans*-*anti* configuration, resulting in a nearly planar molecular conformation[3,8]. The same atom numbering described before for phytosterols, based on IUPAC recommendations issued in 1989[9], is generally applied also to non-vegetal sterols, which, like vegetal ones, may possess none (4-desmethyl-sterols), one (4-methyl-sterols), or two (4,4-dimethyl-sterols) methyl groups at C4. Additionally, a methyl group may be present at C14, as observed in lanosterol (**Figure 1**). Sterols are further classified based on the number and position of double bonds on the B ring, giving rise to Δ^5-, Δ^7-, $\Delta^{5,7}$-, and Δ^8-sterols. Stanols, in contrast, are their fully saturated counterparts[3,8].

As discussed before, the specific sterol and stanol profiles are strongly organism-dependent, as their biosynthesis follows phylum-specific pathways[5]. Consequently, if in plants *sterol methyltransferases* (SMTs) introduce characteristic alkyl branches at C24, producing major plant sterols, such as β-sitosterol and campesterol[10,11], both animal and fungal sterols are biosynthesized from a common precursor, lanosterol, which features a C=C double bond between C24 and C25 (**Figure 1**). From lanosterol, two parallel pathways diverge: the Bloch pathway, which leads to sterols such as desmosterol and zymosterol, that retain lanosterol's side chain but differ in B-ring unsaturation[5,7] and the Kandutsch-Russell pathway, which gives rise to sterols with saturated, unbranched side chains, such as lathosterol, a Δ^7 positional isomer of cholesterol[5,6,12,13]. Notably, both lathosterol and desmosterol serve as biosynthetic precursors to cholesterol, the most abundant sterol in animal cells[2].

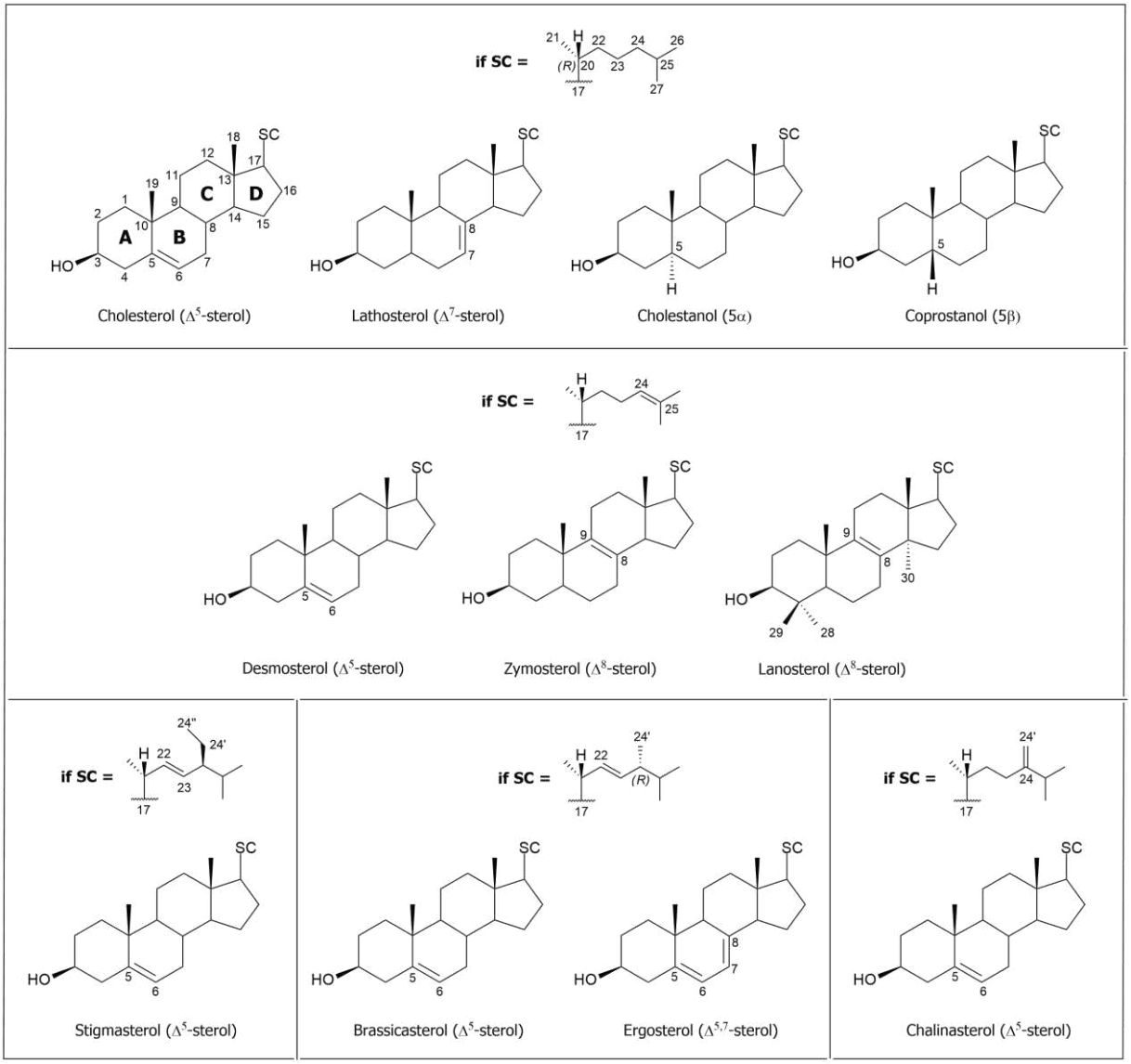


Figure 1. Molecular structures of the animal and fungal sterols whose analysis is described in this chapter, alongside cholesterol and the phytosterols stigmasterol and brassicasterol, which are included for comparative purposes (see text for additional details). Compounds are grouped based on the side chain (SC) structures. Atom numbering follows the IUPAC guidelines established in 1989. The stereochemical configurations at C20 and C24 are indicated where relevant: R configuration at C20 for cholesterol and related sterols, and R configuration at C24 for brassicasterol and ergosterol.

Sterols discussed so far are critical to human health, and imbalances in their levels have been linked to disorders of the nervous and skeletal systems[12]. Among cholesterol metabolites, cholestanol and coprostanol are epimers with saturated B rings and differ only in the stereochemistry of the hydrogen at C5 (α or β, respectively; **Figure 1**), yielding either a planar or a bent A ring conformation. Both metabolites are produced from cholesterol in the digestive tract[14–17], although cholestanol has also

been reported in higher plants[18]. Fungal sterols also originate from lanosterol. In fungi, zymosterol proceeds along a modified Bloch pathway involving several enzymatic transformations, ultimately producing ergosterol, a $\Delta^{5,7}$-sterol with a double bond between C22 and C23 and a methyl group at C24 in the R configuration (**Figure 1**)[4,13]. Ergosterol is the dominant sterol in fungal cells, including yeasts and molds, where it plays a role analogous to cholesterol in animal membranes, supporting membrane integrity and cell proliferation[2,4,19]. Among the sterols illustrated in **Figure 1**, chalinasterol is a Δ^5-sterol containing a methylene group at C24. It is a positional isomer of brassicasterol and a biosynthetic precursor of campesterol, both of which are important plant sterols[20]. Also known as 24-methylene-cholesterol or ostreasterol, chalinasterol is considered a "marine sterol" due to its initial identification in molluscs[21] and subsequent detection in algae[22–24], though it is also present in various vegetable oils[25].

Like phytosterols, non-vegetal sterols pose a significant challenge in terms of analytical characterization, due to their structural diversity. Gas chromatography–mass spectrometry with electron ionization (GC- EI-MS) remains a standard technique also for non-vegetal sterol analysis[26–31]. As an alternative, reversed-phase liquid chromatography coupled with soft ionization mass spectrometry techniques such as electrospray ionization (ESI) or atmospheric pressure chemical ionization (APCI) has become increasingly popular[32,33]. APCI, especially in positive ion mode, has shown superior sensitivity for sterol analysis due to the predominant formation of $[M+H–H_2O]^+$ ions[8,32,34,35] and avoids the risk of thermal degradation associated with GC.

Animal sterols and stanols are typically studied in biological matrices like plasma, serum, and feces[31–34,36–39], whereas ergosterol serves as a marker of fungal and mold contamination in samples such as soil and yeast[40–42]. Nevertheless, these sterols can also be found in plant-derived matrices and algae[24,25,43–45]. During chromatographic separation, complex traces with multiple peaks are frequently observed, suggesting the presence of isomeric sterols not corresponding to available standards. In such cases, even high-resolution mass spectrometry (HRMS) fails in providing useful information, and the use of tandem or multistage mass spectrometry (MS/MS or MS^n) is required to achieve a

deeper structural insight. In recent years, novel approaches for sterol/stanol analysis based on MS/MS have been proposed in the literature, focusing on the all-ion fragmentation technique[46], on fast chromatography[47], or, very recently, on prior derivatization with 3-(chlorosulfonyl)benzoic acid, aiming at detecting sterols as negatively charged ions[48].

As demonstrated in the previous chapter and in Ref 49 for phytosterols, the combination of high-resolution tandem MS with low-resolution MS^n (n = 2–4) on $[M+H-H_2O]^+$ ions generated by APCI can reveal diagnostic product ions, which in turn may enable the identification of key structural features, such as side chain unsaturation/branching and variations in the C=C bond location on the steroidal core. The study described in this chapter applies the same analytical strategy to a broader selection of animal and fungal sterols, exhibiting structural diversity beyond that of cholesterol and plant sterols. The resulting identification of new diagnostic fragment ions, linked to the presence or absence of C=C bonds on ring B and on the side chain and to specific methylation patterns in the steroidal backbone will be discussed in detail, culminating in a comprehensive summary of fragmentation behaviours that may facilitate the structural elucidation of novel sterols from animal, fungal, and plant sources.

2.2 Materials and Methods

2.2.1 Chemicals. LC-MS grade acetonitrile (ACN), water (H_2O) and formic acid (FA), adopted for RPLC separations, and HPLC grade chloroform ($CHCl_3$), ethanol (EtOH), methanol (MeOH) and hexane, employed as solvents for the preparation of sterol stock solutions and for the extraction of free sterols from commercial baker's yeast were purchased from Merck (Milan, Italy). Standards of cholesterol (cholest-5-en-3β-ol, ≥ 95% purity), lathosterol (cholest-7-en-3β-ol, ≥ 95% purity), cholestanol (5α-cholestan-3β-ol, ≥ 95% purity), coprostanol (5β-cholestan-3β-ol, ≥ 95% purity), desmosterol (cholest-5,24-dien-3β-ol, ≥ 98% purity), lanosterol (lanosta-8,24-dien-3β-ol, ≥ 95% purity) and ergosterol (ergosta-5,7,22E-trien-3β-ol, ≥ 95% purity) were procured from Cayman

Chemical (Ann Arbor, MI, USA). Standards of zymosterol (5α-cholesta-8,24-dien-3β-ol, ≥ 99% purity) and chalinasterol (24-methylene-cholest-5-en-3β-ol, ≥ 99% purity) were purchased from Merck (Milan, Italy). Solutions for mass spectrometers calibration under positive or negative polarity conditions were acquired from Thermo Scientific (Waltham, MA, USA).

2.2.2. Standard solutions preparation. A stock solution of each standard sterol (1 mg/mL) was prepared in an ethanol/chloroform mixture (2:1 v/v) and a diluted solution (30 μg/mL) was subsequently obtained in 100% acetonitrile. A comprehensive mix of standards (10 μg/mL for each one) was obtained in 100% acetonitrile through appropriate mixing and dilution of the respective stock solutions.

2.2.3. Extraction of free sterols from baker's yeast. Baker's yeast, purchased in a local store, was selected as an example of sterol-containing complex matrix and was subjected to extraction of free sterols following the protocol reported in the study by Castellaneta *et al.*[44], with appropriate modifications. In detail, 50 mg of baker's yeast were weighed, 1 mL of MeOH was added and the obtained suspension was sonicated in a water bath for 15 min at 30 °C. Then, 3.5 mL of H_2O and 3.75 mL of hexane were added to extract free sterols. The mixture was vortexed for 2 min and centrifuged at 5000 rpm for 10 min. Following complete phase separation, the supernatant was collected, and the extraction was repeated to increase the recovery of free sterols. The two supernatants were then joined and dried under a gentle flow of nitrogen. The dry residue was then dissolved in 500 μL of a MeOH/$CHCl_3$ solution (2:1 v/v) and diluted by a factor of 1:1 (v/v) with ACN before RPLC-APCI(+)-FTMS analysis.

2.2.4. RPLC-APCI-MS^n instrumentation and operating conditions. APCI-MS^n (n = 1-3) analyses of sterols/stanols were performed, according to the case, with one of two platforms including an

Ultimate 3000 HPLC system coupled either with a Q Exactive high-resolution quadrupole-Orbitrap Fourier-transform mass spectrometer or with a Velos Pro linear ion trap mass spectrometer (ThermoFisher, West Palm Beach, CA, USA) through an APCI source. A C18 Ascentis Express HPLC column (150 × 2.1 mm i.d., particle size 2.7 μm) (Supelco, Bellefonte, PA, USA) was used for preliminary chromatographic tests aimed at assessing the possibility of separating isomeric sterols under either isocratic or binary elution gradient conditions similar to those adopted for cholesterol and phytosterols in the previous chapter and in Ref. 49. In the first case, 100% ACN with 0.1% (v/v) FA was used as a mobile phase, working at a flow rate of 0.200 mL/min for 40 minutes. In the second case, the following elution gradient based on H_2O as phase A and ACN as phase B, both containing 0.1% (v/v) of FA, was adopted for sterol separation: 0-40 min, linear increase of B from 90% to 100%; 40-50 min, isocratic at 100% B; 50-52 min, linear decrease of B from 100% to 90%; 52−60 min, isocratic at 90% B (column reconditioning). In both cases, the column temperature was maintained at 30°C and 5 μL sample volumes were injected. The parameters of the APCI interface and of the ion optics of the Q Exactive spectrometer were set as follows: sheath gas flow rate) 40 a.u.; auxiliary gas flow rate) 10 a.u.; capillary temperature) 300 °C; S-lens RF Level) 55 a.u.; vaporizer temperature) 250°C. Full scan FTMS acquisitions in positive ion mode were obtained in a 250-500 *m/z* interval, working with a 140000 resolving power at *m/z* 200; the Automatic Gain Control (AGC) level was set at 1×10^6 and maximum injection time was 100 ms. HCD-FTMS/MS acquisitions were performed by the Q-Exactive spectrometer at a 35000 resolving power, selecting precursor ions in a 1.0 m/z units-wide isolation window, using a normalized collisional energy (NCE) of 30 units and acquiring the tandem mass spectrum in a 50−500 *m/z* interval; the AGC level was set at 2×10^5 and maximum injection time was 100 ms. The spectrometer was calibrated every two days by infusing, at a 30 μL/min flow rate, calibration solutions for positive or negative polarity acquisitions provided by the instrument manufacturer. As a result, a mass accuracy better than 5 ppm was achieved, with the exception of product ions obtained by HCD-FTMS/MS with *m/z* values lower than 100, for which an accuracy better than 16 ppm was, in any case, achieved (*vide infra*).

APCI-direct infusion analyses (APCI-DIA) of individual standards solutions (30 μg/mL) were performed using the Q Exactive spectrometer, under the same conditions described before, and, in specific cases, the Velos Pro mass spectrometer. Specifically, APCI-DIA-HCD-FTMS/MS spectra were acquired for each sterol (*vide infra*) using the Q Exactive spectrometer, whereas APCI-DIA-collisionally induced dissociation (CID)-MS^3 experiments were performed with the Velos Pro spectrometer on specific precursor ions previously detected in CID-MS/MS spectra obtained with the same spectrometer, in order to elucidate some fragmentation patterns observed under HCD-FTMS/MS conditions. The main operating parameters of the Velos Pro APCI interface and ion optics were set as follows: sheath gas flow rate) 40 a.u.; auxiliary gas flow rate) 10 a.u.; capillary temperature) 300 °C; S-lens RF Level) 60 a.u.; vaporizer temperature) 250°C. A 1.0 *m/z* units-wide isolation window was adopted for the isolation of the precursor ion and a normalized collisional energy (NCE) of 25 units was selected for fragmentation in the case of CID-MS/MS and CID-MS^3 acquisitions performed using the linear ion trap spectrometer; the AGC level was set at 2×10^3 and the maximum injection time was 100 ms.

2.3 Results and Discussion

2.3.1. RPLC-APCI(+)-FTMS analysis of standard sterols/stanols: chromatographic considerations. Preliminary RPLC separations were conducted on the mixture of animal and fungal sterols and stanols of interest, with the addition of cholesterol, to assess their chromatographic behavior, particularly the resolution of isomeric species, and to gain a deeper insight into how sterol molecular structure influences retention. The findings complement results described for cholesterol and phytosterols in the previous chapter and in Ref. 49, based on the same chromatographic conditions. In that case, a binary gradient elution program using water and acetonitrile containing 0.1% formic acid was developed to separate Δ^7-avenasterol from its Δ^5 counterpart, isofucosterol. Applying the same gradient program, along with an isocratic elution using 100% acetonitrile, to the

current sterol/stanol mixture produced the multiple-extracted ion current (EIC) chromatograms shown in **Figure 2**. These chromatograms were targeted at the exact monoisotopic *m/z* values of the sterol/stanol respective $[M+H-H_2O]^+$ ions. As expected, isocratic elution yielded a faster separation, due to the higher elution strength of the mobile phase. The elution order observed under isocratic conditions generally mirrored that of the gradient method, with a few notable exceptions.

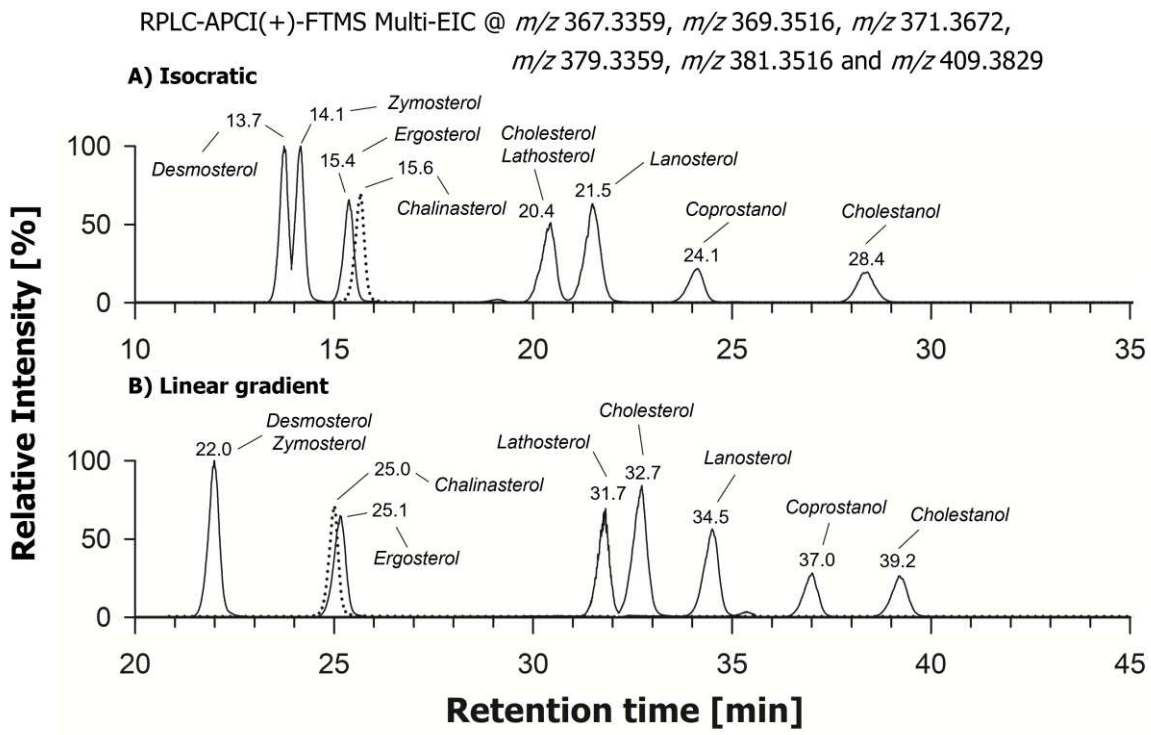


Figure 2. Multiple-extracted ion current (EIC) chromatograms obtained from the RPLC-APCI(+)-FTMS analysis, performed using the Q Exactive mass spectrometer, of the standard sterols and stanols discussed in this chapter, along with cholesterol, based on: A) isocratic elution and B) linear gradient elution. Ion currents were extracted using the exact monoisotopic *m/z* values of the $[M+H-H_2O]^+$ ions of the compounds: *m/z* 367.3359 for desmosterol and zymosterol; *m/z* 379.3359 for ergosterol; m/z 381.3516 for chalinasterol (dashed line); *m/z* 369.3516 for cholesterol and lathosterol; *m/z* 409.3829 for lanosterol; and *m/z* 371.3672 for coprostanol and cholestanol. The chromatograms illustrate the retention profiles and resolution achieved for structurally related sterols and stanols under both elution conditions.

Stanols, which lack unsaturations, were consistently eluted as last and were well resolved under both conditions, highlighting the significant impact of the steroidal backbone stereochemistry on the retention behavior on C18 stationary phases. In particular, coprostanol, in which the β-configuration at C5 imposes a cis junction between the A and B rings, eluted earlier than cholestanol, for which the

canonical trans-planar structure is preserved[17]. This behavior is reminiscent of that observed, under RPLC conditions, with unsaturated fatty acids, where a *cis* C=C bond introduces a kink that weakens the interactions with the C18 chains of the stationary phase, resulting in earlier elution than the trans counterpart[50]. Lanosterol's retention behavior further illustrates the complex role played by the backbone structure. Despite the polarity induced by the occurrence of a C=C bond between C24 and C25 (see **Figure 1**), a feature previously found to significantly impact retention[49], lanosterol was consistently eluted after cholesterol, which has a saturated side chain. This result might be tentatively explained by the presence of two methyl groups at C4 in lanosterol, which form a localized hydrophobic domain near the hydroxyl group. This domain likely reduces the effect of OH polarity, enhancing the sterol affinity for the C18 phase.

The first critical resolution challenge, moving from longer to shorter retention times, was the separation of cholesterol from its isomer lathosterol. These sterols differ only in the position of a single double bond on the B ring (**Figure 1**). Like Δ^5/Δ^7-avenasterols[49], these isomers could not be separated under isocratic conditions. However, gradient elution (see **Figure 2B**) allowed lathosterol (a Δ^7 sterol, thus having its C=C bond closer to the side chain) to elute earlier than cholesterol (a Δ^5 sterol). This trend agrees with previous findings by McDonald *et al.*[37] and Honda *et al.*[33,34], suggesting that a slow, gradient-based increase in acetonitrile content is more effective in separating sterols based on double bond position within the steroidal backbone. Unexpectedly, however, isocratic elution outperformed gradient elution in resolving the remaining four sterols under study. As shown in **Figure 2A**, ergosterol and chalinasterol were consistently eluted before the cholesterol/lathosterol pair, as expected due to the presence of a side chain double bond. On the other hand, the complex interplay between the different position of this C=C bond and the different level of unsaturation on ring B, being ergosterol a $\Delta^{5,7}$ sterol and chalinasterol a Δ^5 one (see **Figure 1**), resulted in a very similar retention for the two compounds. Surprisingly, isocratic elution slightly improved their resolution, due to the 0.1 min increase in the retention time difference, compared to gradient elution (**Figure 2A**). This outcome is emphasized by values of resolution and selectivity evaluated for all the species'

couples under both chromatographic setups, which have been summarized in **Table A1** of Appendix 2. In any case, the distinct *m/z* values, due to ergosterol's additional double bond compared to chalinasterol, allowed a clear identification of the two compounds via the respective EIC chromatograms. Further support for the influence of the side chain C=C bond position on retention was obtained when comparing chalinasterol with brassicasterol, which shares the same backbone and was analyzed during our previous investigation[49]. Chalinasterol, including a C=C bond between C24 and C24' (**Figure 1**), eluted far earlier than brassicasterol, whose double bond is closer to the backbone (between C22 and C23). Indeed, under the same gradient conditions, brassicasterol showed a retention time of 31.7 min[49], over 6.7 min longer than chalinasterol.

An advantage for isocratic elution was observed also with isomeric species desmosterol and zymosterol (**Figure 2**). Both sterols feature a C=C bond between C24 and C25, significantly reducing their retention compared to all others, including lanosterol, which shares their side chain but has additional methylations at C4 and C14. The two sterols could be slightly separated only under isocratic conditions, which would thus be crucial for identifying them in real samples, given the identical *m/z* value for the respective ions. Interestingly, desmosterol (the Δ^5 isomer) eluted before zymosterol (the Δ^8 isomer), in contrast to trends observed under gradient elution conditions for Δ^5/Δ^7 couples, like the two avenasterols[49] and cholesterol/lathosterol. One possible explanation for this finding likely lies in the accessibility of the C8–C9 double bond in zymosterol, which may be hindered by nearby axial methyl groups on C18 and C19. This steric hindrance could reduce the interaction with the C18 stationary phase, lessening the retention decrease typically associated with double bonds near the side chain. Notably, McDonald *et al.*[37] and Honda *et al.*[34] achieved desmosterol–zymosterol separation using RPLC with a water/methanol-based mobile phase but failed to separate cholesterol from lathosterol. In contrast, Skubic *et al.*[31] achieved excellent separation of animal sterols, including Δ^7 and Δ^8 isomers, using two pentafluorophenyl columns in series and a methanol–isopropanol mobile phase, observing shorter retention for Δ^7 and Δ^8 isomers relative to Δ^5 analogues.

Taken together with previous findings on cholesterol and major phytosterols obtained under the same chromatographic conditions[49], these results indicate that relationships between retention time and structural features exist for several sterols. The side chain composition seems to be the most influential structural feature in terms of retention, at least on a C18 stationary phase. However, even the number and position of C=C double bonds on the steroidal backbone and the methylation of specific positions on the latter appear to play a role. This explains why the chromatographic behavior of some critical couples of sterols appears to depend significantly on specific experimental conditions, including not just mobile phase composition or stationary phase type but, in some cases, even the column brand, maybe due to differences in the coverage of support packing particles by octadecyl moieties. A detailed modelling of the sterol/stanol chromatographic behavior might provide a deeper explanation for the findings reported in this section. Nonetheless, given a certain set of chromatographic conditions, retention time comparisons with known standards might support structural inferences for novel sterols detected in real matrices. Moreover, the combined use of isocratic and gradient elution can be considered particularly effective in distinguishing positional isomers, representing the initial step towards the identification of unknown sterols. As shown in the following sections, fragmentation patterns obtained by HCD-FTMS/MS analysis of standard sterols and stanols offered extensive structure-specific information. When combined with chromatographic data, this information might be very helpful for a comprehensive characterization of sterols in complex samples.

2.3.2. Fragmentation of Δ^7- Sterols with Saturated and Unbranched Side Chain: Lathosterol. In our study on cholesterol and major phytosterols, diagnostic product ions arising from their side chains were evidenced by comparison with the results of the RPLC-APCI(+)-FTMS/MS analysis of isotopically labelled cholesterol and stigmasterol standards (see the previous chapter and Ref. 49). These product ions were best explained by assuming alternative locations of the positive charge

initially formed at the C3 position, following water loss from protonated sterols during APCI. The positive charge migration was attributed to intramolecular hydride transfers towards C3 occurring in the gas phase, especially from carbons like C25, C17, or C24 (when alkyl-substituted), which better stabilize the positive charge[49]. Starting from this background, APCI(+)-HCD-FTMS/MS spectra were systematically acquired also for the animal/fungal sterols/stanols considered in this chapter, using the same NCE value adopted for cholesterol and phytosterols, *i.e.* 30. The spectra were first acquired under DIA conditions and their intensity profiles were subsequently confirmed by those resulting from spectral averaging under the sterol/stanol chromatographic peaks detected upon RPLC-APCI(+)-HCD-FTMS/MS analysis of standard mixtures, performed using linear gradient elution for all sterols/stanols but desmosterol and zymosterol, since the latter could be at least partially separated only under isocratic conditions (see **Figure 2A**). In this case the RPLC-APCI(+)-HCD-FTMS/MS spectra for the two sterols were obtained by careful spectral averaging in retention time intervals in which the chromatographic peaks overlap was minimal.

Notably, preliminary DIA-APCI(+)-HCD-FTMS/MS acquisitions were performed on all sterols/stanols considering also other NCE values, namely 10, 50 and 70. As evidenced in **Figures A1-A3** in the Appendix 2, at NCE = 10 the fragmentation yield was very low, as expected. Fragmentation was much more effective in generating low *m/z* product ions when 50 and 70 were adopted as NCE values, thus reducing important information related to higher *m/z* ions. Consequently, the NCE = 30 value, the same previously adopted on cholesterol and phytosterols, emerged as the one leading to the best distribution of spectral intensity among product ions clusters, including those at higher *m/z* values, thus potentially providing the maximum amount of structural information.

The fragmentation pattern of lathosterol, the Δ^7 analogue of cholesterol, was examined firstly among those of the animal and fungal sterols investigated. The APCI(+)-HCD-FTMS/MS spectrum at NCE = 30 of its $[M+H-H_2O]^+$ ion (exact *m/z* for M+0 isotopologue: 369.3516) is shown in **Figure 3A**. Product ions with the same carbon count but differing in hydrogen content were grouped into clusters (denoted by capital letters). **Table A1** in the Appendix 2 lists all product ions detected for lathosterol

(and for all the other analyzed sterols/stanols), including those corresponding to unlabelled peak signals in **Figure 3A**. For each ion the experimental *m/z* value (rounded to four decimal places), the corresponding molecular formula, inferred considering the best mass accuracy among those related to possible molecular formulas (usually not exceeding 5 ppm, with the exception of *m/z* values lower than 96, for which an accuracy up to 16 ppm was considered), and the relative intensity, for each sterol, expressed as mean ± standard deviation calculated from three independent replicates, are reported in the table.

While the HCD-MS/MS spectra of lathosterol and cholesterol (see **Figure 3A** in the previous chapter for the latter) were broadly similar, some notable differences emerged. A prominent peak at *m/z* 69.0708 (consistent with an exact *m/z* 69.0699), attributed to a side chain-derived fragment (Panel 1, **Scheme 1**), was observed for lathosterol. This feature matched that observed for cluster B in Δ^7-avenasterol (see **Figure 4E** in the previous chapter) and points to an alternative structure consistent with that *m/z* value, originating from ring A (Panel 2, **Scheme 1**), possible only if no C=C bond is located between C5 and C6. This makes the higher abundance of the *m/z* 69.0699 ion in cluster B a feature of Δ^7-sterols and, as discussed later in this chapter, also of sterols with no C=C bond on ring B. Actually, the presence of an unsaturation on the side chain, like in the case of desmosterol, can determine the formation of an alternative product ion with the same *m/z* ratio, thus increasing the corresponding peak signal (*vide infra*). Similarly to the *m/z* 69.0699 ion, the *m/z* 83.0861 one (exact *m/z* 83.0855),

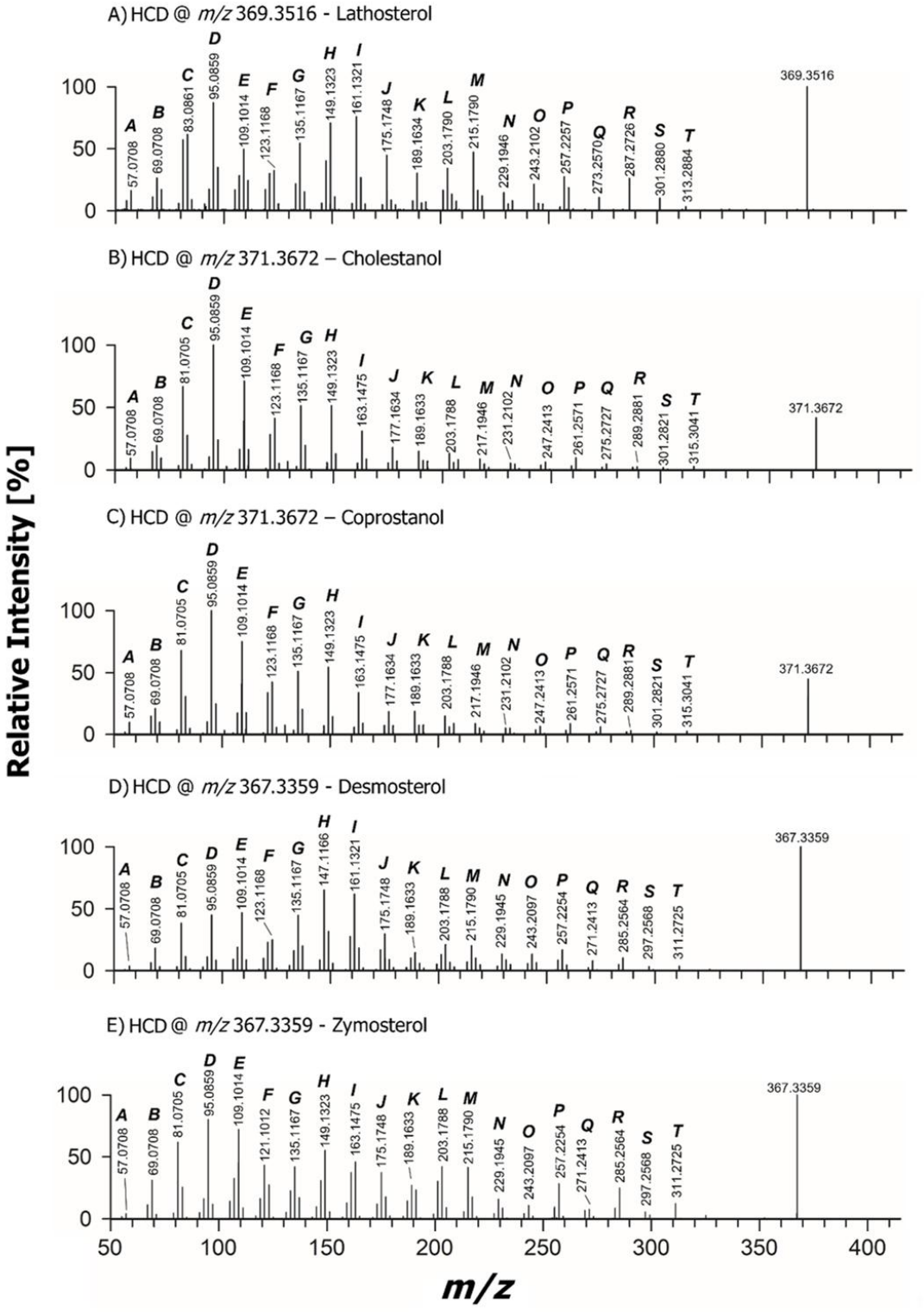
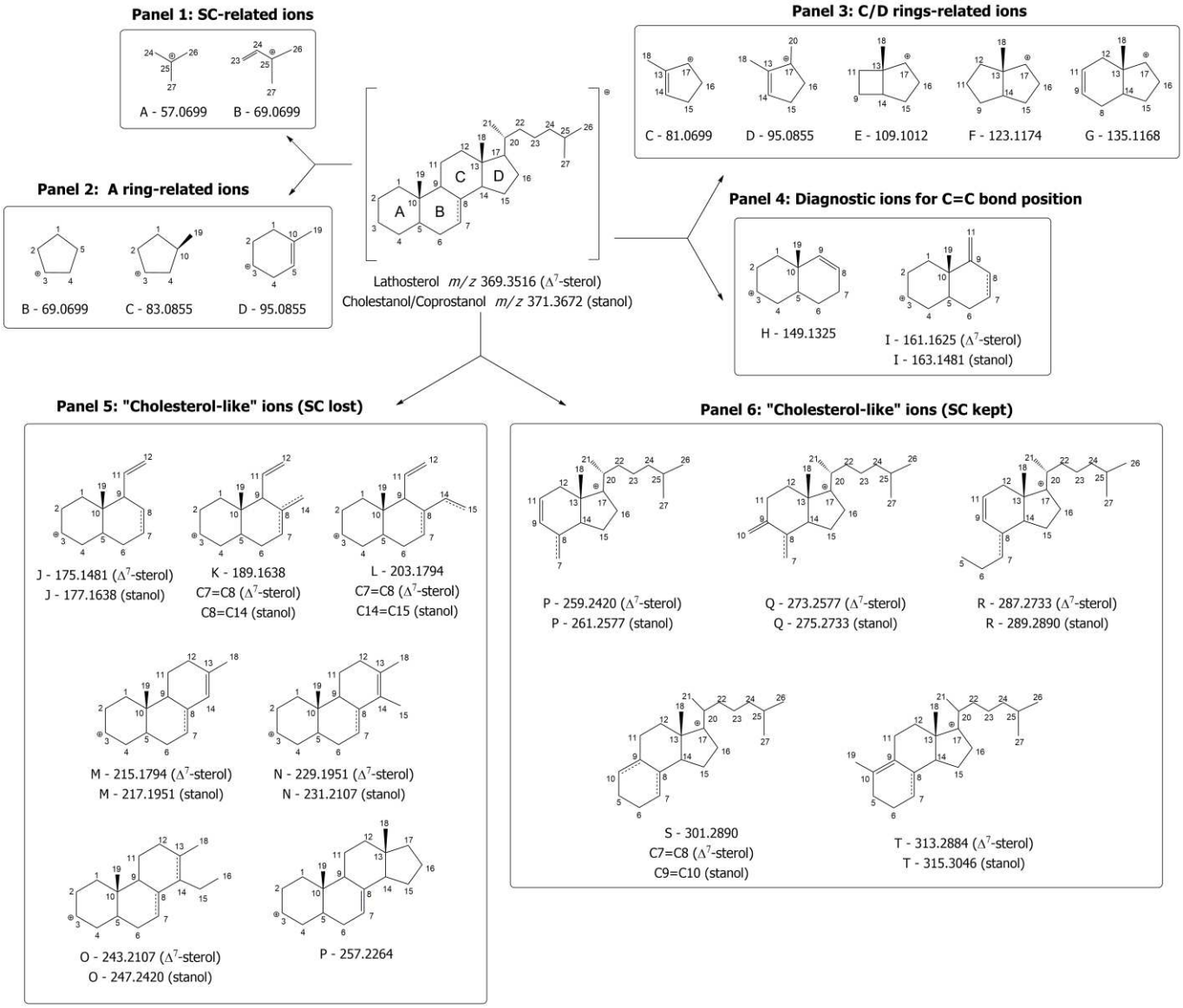


Figure 3. APCI(+)-HCD-FTMS/MS spectra obtained using the Q Exactive mass spectrometer for the $[M+H-H_2O]^+$ ions of selected sterols and stanols analyzed in this chapter. Peak signals referred to product ions sharing the same number of carbon atoms but differing for the number of H atoms are grouped into clusters, each labelled with a capital letter. For each cluster, the experimental *m/z* value of the most abundant ion is usually indicated. The reported spectra were obtained through direct infusion analysis and confirmed by those resulting from spectral averaging under the respective peaks detected in RPLC-APCI(+)-HCD-FTMS/MS chromatograms (see text for details). HCD-FTMS/MS spectra were obtained at NCE = 30, with the HCD cell filled with nitrogen.

slightly prevailing in cluster C for both lathosterol (**Figure 3A**) and Δ^7-avenasterol (see **Figure 4E** in the previous chapter), can also arise from ring A via cleavage of the C5–C10 and C4–C5 bonds, again requiring the absence of a C=C bond between C5 and C6. Notably, alternative side-chain-derived structures were proposed for the two ions for Δ^7-avenasterol, yet their formation involved the presence of an ethylidene group at C24 (see **Scheme 3** in the previous chapter), a feature that is not present in lathosterol. Another shared feature between lathosterol and Δ^7-avenasterol is the prominent *m/z* 95.0859 ion (exact *m/z* 95.0855) in cluster D. As evidenced in Panel 3 of **Scheme 1**, one of its possible structures is related to ring D (with the positive charge on C17) and is expected to be common to different sterols. However, an alternative structure involving ring A (Panel 2, **Scheme 1**) may also be formed in the case of Δ^7-sterols via a retro-Diels–Alder reaction (see **Figure A4**), enabled by the presence of a C=C bond between C7 and C8. Clusters E–J displayed similar relative ion intensities for both cholesterol and lathosterol, with the exception of the *m/z* 149.1323 (exact *m/z* 149.1325) ion in cluster H, which was more abundant in Δ^7-sterols, as confirmed in the previous chaptter and in Ref. 49 and by Munger *et al.*[51]. Its most likely structure is reported in Panel 4 of **Scheme 1**. From clusters I to T, fragmentation profiles remained highly comparable between lathosterol and cholesterol, validating the previously proposed structures for the respective product ions[49]. The latter may arise either from neutral losses on the side chain, shared by both sterols, or from ring cleavages unaffected by the position of the double bond (see Panels 5 and 6, **Scheme 1**). The only significant exception in cluster similarity was the prevalence of the *m/z* 301.2880 ion (exact *m/z* 301.2890) in cluster S, in place of the *m/z* 299.2733 ion observed for cholesterol. As previously discussed[49], multiple structures can account for this ion. The one resulting from a breakage of the side chain, with the positive charge on C3 (see **Scheme 1** in the previous chapter) seems to be less relevant in the case of lathosterol. On the other hand, the alternative structure, having the positive charge on C17 and keeping the entire side chain (see **Scheme 2** in Ref. 49), is able to explain the detection of the *m/z* 301.2890 in the case of lathosterol considering only a C=C bond between C7 and C8. This is clarified by the structure reported in Panel 6 of **Scheme 1** for this ion in the case of Δ^7 sterols.



Scheme 1. Proposed structures for product ions generated from the $[M+H–H_2O]^+$ ions of lathosterol, cholestanol, and coprostanol under HCD-MS/MS conditions. For the sake of simplicity, epimeric differences at C5 in stanols are not depicted. Exact *m/z* values are indicated for each ion. Unless otherwise noted, dashed-line double bonds are present only in lathosterol (Δ^7-sterol). See text for details.

2.3.3. Fragmentation of stanols with saturated and unbranched side chains: coprostanol and cholestanol. The APCI(+)-HCD-FTMS/MS spectra of the $[M+H-H_2O]^+$ ions of cholestanol and coprostanol (exact *m/z* 371.3672) are presented in **Figures 3B** and **3C**, respectively. As expected, the fragmentation profiles of these two epimeric sterols were virtually identical but the extent of fragmentation was more extensive than that of cholesterol, their mono-unsaturated analogue, under equivalent collisional energy conditions. Clusters A to G included product ions with *m/z* values

identical to those observed for cholesterol. This finding confirmed the structures previously proposed for them considering cholesterol[49], that are illustrated in Panels 1 and 3 of **Scheme 1**. Indeed, none of them include the C5=C6 double bond, which is the only structural difference between cholesterol and the two stanols. However, an important distinction was noted, since the ion at *m/z* 95.0859 (cluster D, exact *m/z* 95.0855) appeared with greater intensity in the case of stanols. As evidenced in **Figure A5**, the same structure reported for the *m/z* 95.0855 ion in the case of lathosterol (see Panel 2 in **Scheme 1** and **Figure A1**), with the positive charge on C3, can be formed in the case of stanols through a retro-cycloaddition on ring B. This route complements the one previously proposed to account for that product ion in the case of cholesterol[49], with the positive charge located at C17 (see the structure reported in Panel 3, **Scheme 1**). The combined contributions of both pathways likely explain the enhanced signal intensity for the *m/z* 95.0855 ion in stanols. Additionally, as seen for lathosterol, alternative structures for ions at *m/z* 69.0699 and 83.0855 shown in Panel 2 of **Scheme 1** are feasible in stanols, due to the absence of a C5=C6 double bond, which would otherwise hinder such fragmentation.

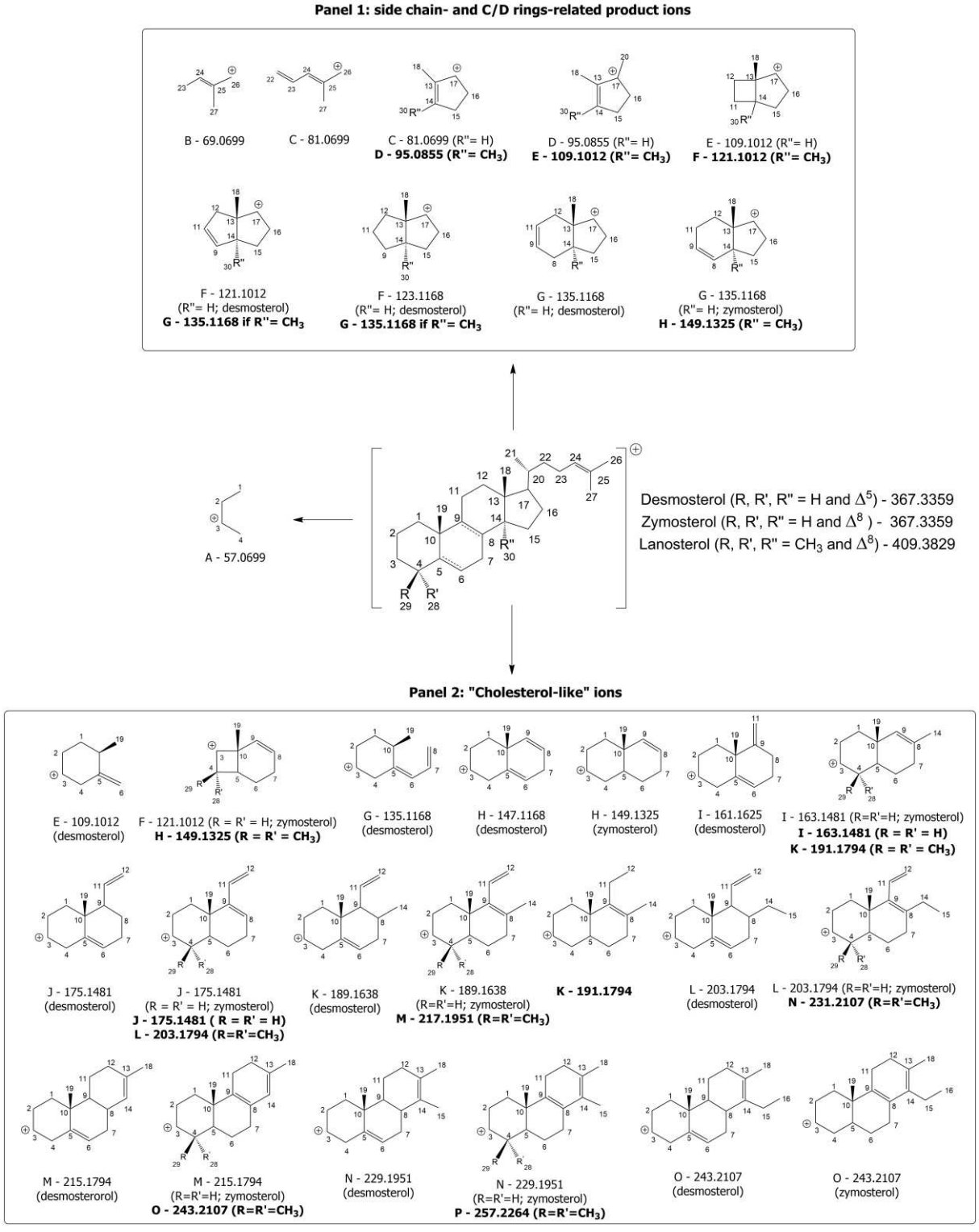
The saturated nature of ring B in cholestanol and coprostanol was reflected in the *m/z* ratios found for ions in clusters H and I, compatible with exact values 149.1325 and 163.1481, respectively. Indeed, as evidenced in Panel 4 of **Scheme 1**, the structures proposed for those ions (consistent also with those reported by Munger *et al.*[51]) only included one C=C bond between C8 and C9, arising from the fragmentation process, but lacked the additional C=C bond at C5-C6 of cholesterol or at C7-C8 of Δ^7-sterols. For clusters J to T, most stanol product ions demonstrated a consistent +2 shift in nominal *m/z* values compared to the corresponding cholesterol ions. The structures shown in Panels 5 and 6 of **Scheme 1**, which feature a positive charge at either C3 or C17, account for this shift as a result of saturation of the C5-C6 bond. This observation supports the structures previously proposed for cholesterol[49]. One notable exception to the +2 *m/z* shift was observed in cluster K, since the dominant product ion for stanols remained at a *m/z* value consistent with the exact value 189.1638, as for cholesterol. This indicates the formation of a second double bond along with the C11=C12 bond

generated by ring C fragmentation. In lathosterol, this double bond is initially placed between C7 and C8, whereas in stanols it is proposed to be formed between C8 and C14 via a 1,3-hydrogen shift (see the structure in Panel 5 of **Scheme 1**). This hypothesis was confirmed by the detection of a weak peak signal at nominal *m/z* 187 in cluster K for lathosterol (see **Figure 3A**) and for cholesterol and Δ^5/Δ^7 phytosterols[49], since it would be consistent with the generation of the C8-C14 double bond, along with the one between C11 and C12, during fragmentation, and with the presence of the original double bond between C5-C6 or C7-C8. As expected, no such ion was detected for stanols (**Figures 3B** and **3C**), which lack the necessary original C=C bond in ring B. A similar scenario was observed in cluster L, whose principal product ion was found at a *m/z* ratio consistent with the exact value 203.1794. As evidenced by the structure reported in Panel 5 of **Scheme 1**, this ion was likely generated through the formation of a C14=C15 double bond during fragmentation. This bond accounts for the -2 *m/z* units shift like the ring B double bonds characteristic of cholesterol and Δ^7-sterols. The same process was likely responsible for the detection of a further product ion at nominal *m/z* 201 in cluster L both for lathosterol (see **Figure 3A**) and for cholesterol and Δ^5/Δ^7 phytosterols[49]. A third exception to the +2 *m/z* shift expected between lathosterol/cholesterol and stanols product ions was observed in cluster O, where the dominant stanol product ion appeared at *m/z* 247.2413 (exact *m/z* 247.2420), representing a +4 shift with respect to the lathosterol/cholesterol counterparts. As illustrated in Panel 5 of **Scheme 1**, this shift correlates with the absence of a C=C bond in ring B and reflects a modified fragmentation mechanism, ultimately keeping a single bond between C13 and C14.

It is finally worth noting that the distribution of relative intensities observed within most peak clusters detected in the HCD-FTMS/MS spectra of cholestanol and coprostanol $[M+H-H_2O]^+$ ions is coherent with that found for the respective clusters in MS/MS spectra acquired by Munger *et al.*[51] for the same sterols using electrospray ionization and a quadrupole-time of flight mass spectrometer. This finding, which was confirmed also for other sterols common between the two studies, suggests that the structure-fragmentation correlations inferred during the present investigation might be extended also

to MS/MS spectra obtained under conditions different from those of HCD, provided they ensure an extensive fragmentation, including both the side chain and the steroidal core.

2.3.4. Fragmentation of Δ^5- and Δ^8-sterols with a double bond at C24-C25: desmosterol, zymosterol and lanosterol. Desmosterol, zymosterol, and lanosterol were considered in this chapter as representative sterols featuring a C=C bond between C24 and C25. The APCI(+)-HCD-FTMS/MS spectrum of desmosterol (**Figure 3D**) was compared with that of cholesterol[49] to elucidate spectral features specific to Δ^5-sterols carrying a C=C bond at C24–C25. Among low *m/z* product ions, only one was detected in cluster A, at *m/z* 57.0708 (exact value: 57.0699). Due to the occurrence of the C=C bond at C24–C25, this ion cannot correspond to the t-butyl carbocation with the charge on C25 inferred by fragmentation of hexa-deuterated cholesterol[49]. Rather, its occurrence in desmosterol supports the alternative structure previously proposed for deuterated cholesterol[49], corresponding to an n-butyl carbocation with the charge on C3, detached from ring A (see **Scheme 2**). In cluster B, the dominant ion at *m/z* 69.0708 (compatible with an exact value 69.0699) reflects the presence of the C24–C25 unsaturation. This facilitates its generation as an allylic carbocation via cleavage of the C22–C23 bond, mediated by a 1,3-H transfer from C20 to C23 (**Figure 6A**), with positive charge located on C26 or C27 (**Scheme 2**, Panel 1). Desmosterol product ions detected in clusters C to O align with structures previously assigned to cholesterol, as detailed in **Scheme 2** (Panels 1 and 2). For clusters P to T, product ions were interpreted either by considering cholesterol-related product ion with positive charge on C17 including the additional C=C bond at C24–C25 (**Scheme 3**, Panel 1) or by alternative structures, corresponding to those previously proposed for stigmasterol[49], featuring the positive charge on C3 and arising form partial side-chain loss (**Scheme 3**, Panel 2). Notably, like for cholestanol and coprostanol, the HCD-FTMS/MS spectrum of desmosterol was in excellent



Scheme 2. Proposed structures for major product ions detected in clusters A to O and A to P found in the APCI-HCD-MS/MS spectra of $[M+H–H_2O]^+$ ions of desmosterol/zymosterol and lanosterol, respectively. Exact *m/z* values are reported for all ions with four decimal places. The *m/z* values referring to common product ions for desmosterol and zymosterol are reported with plain character, without further specifications. The *m/z* values referring to product ions of lanosterol are reported with bold character, excepting those for product ions of clusters A, B and the non -cyclic product ion of cluster C, which are common to the three sterols. See text for details.

accordance, in terms of within-cluster intensity distribution, with the one obtained by Munger *et al.*[51] using a Q-ToF mass spectrometer[51].

The APCI(+)-HCD-FTMS/MS spectrum of zymosterol ($[M+H-H_2O]^+$ precursor with exact *m/z* 367.3359; **Figure 3E**) was generally similar to that of desmosterol in terms of internal abundance profiles of clusters, with exceptions in clusters F, H, and I. In cluster F, the main ion became the one at *m/z* 121.1012, instead of the desmosterol's prevalent ion at *m/z* 123.1168. Mechanisms of formation proposed for the two ions in the case of cholesterol and phytosterols[49] could be extended also to desmosterol, leading to structures including rings C and D and with positive charge on C17 shown in Panel 1 of **Scheme 2**. However, those processes were hindered by the presence of a C=C bond between C8 and C9 in the case of zymosterol, thus a specific mechanism had to be hypothesized (see **Figure A7**) to explain the generation of the *m/z* 121.1012 ion from this sterol, with the proposed structure shown in Panel 2 of **Scheme 2**. As evidenced in **Figure A7**, the process likely involved the generation, as intermediate, of an ion with exact *m/z* 149.1325, corresponding to the leading product ion detected at *m/z* 149.1323 in cluster H for zymosterol (see **Figure 3E**). A novel mechanism (see **Figure A8**) was also necessary to explain the generation of the ion detected at *m/z* 163.1479 (exact *m/z* 163.1481) in cluster I of zymosterol, leading to the structure reported in Panel 2 of **Scheme 2**. In fact, the mechanisms proposed in the previous chapter and in ours and Munger's papers[49,51] could not be applied to product ions prevailing in clusters H and I, since none of the sterols involved in the two studies was a Δ^8 sterol, like zymosterol, and the presence of a C=C bond between C8 and C9 would have made those processes impossible.

Notably, despite an *m/z* 135.1167 ion dominated in cluster G for both zymosterol and desmosterol, a different structural interpretation was required for the two sterols. Structures previously proposed considering cholesterol (with positive charge either on C3 or on C17)[49] were consistent with the structure of desmosterol (see Panels 1 and 2 in **Scheme 2**) but incompatible with that of zymosterol, due to the presence of the C8=C9 bond. Consequently, a new structure was proposed for the product ion in the case of zymosterol, including rings C and D and with the positive charge on C17 (see Panel

1 of **Scheme 2**). Prevailing ions in clusters J to O for both sterols could be interpreted considering structures already proposed in the case of cholesterol[49] but, obviously, including the C=C bond on ring B between C5 and C6 for desmosterol and between C8 and C9 for zymosterol (**Scheme 2**, Panel 2). Finally, prevailing ions in clusters P to T for zymosterol could not be explained considering cholesterol-like structures, like those proposed for desmosterol (**Scheme 3**, Panel 1), due to the presence of the C8=C9 bond. On the other hand, stigmasterol-like structures (**Scheme 3**, Panel 2), previously proposed as alternatives for desmosterol ions of clusters N to T, could be extended also to zymosterol, simply considering the different location of the C=C bond in ring B.

Among Δ^8-sterols considered in this study, lanosterol was chosen for its unique structural characteristics, related to the additional methylations on C4 (two methyl groups) and C14 (**Figure 1**). Not surprisingly, a distinct abundance profile was observed in its APCI(+)-HCD-MS/MS spectrum (**Figure 4A**). Despite this, lanosterol shared spectral features with zymosterol through cluster J, including identical *m/z* values for dominant ions. Prevailing ion in clusters A and B were assigned the same structures proposed for desmosterol and zymosterol (**Scheme 2**), as they arise from parts of molecular structure shared by the three sterols. Notably, the structure proposed for the *m/z* 69.0699 ion in **Scheme 2** was the same hypothesised by Feng *et al.*[42] when studying the fragmentation of lanosterol, even though the transfer of positive charge from C3 to C26 (or C27), that is fundamental to generate that product ion, was not discussed in their paper.

As for cluster C, the prevailing ion could not be assigned the pentacyclic structure proposed before in this chapter for desmosterol and zymosterol (**Scheme 2**, Panel 1, exact *m/z* 81.0699), due to the methylation at C14. Instead, the conjugated allylic carbocation with positive charge at C26 (**Scheme 2**, Panel 1), formed via a 1,3-H transfer from C23 to C20 and cleavage of the C20–C22 bond, could be easily assigned also to lanosterol. As apparent from Panel 1 of **Scheme 2**, prevailing product ions in clusters from D to H of lanosterol could be nicely explained considering structures proposed for ions in clusters from C to G for desmosterol/zymosterol (and, previously, for cholesterol and

phytosterols[49]), all with the positive charge located on C17, just by keeping into account the mass shift induced by the methylation of C14. This finding provides a strong further confirmation of the

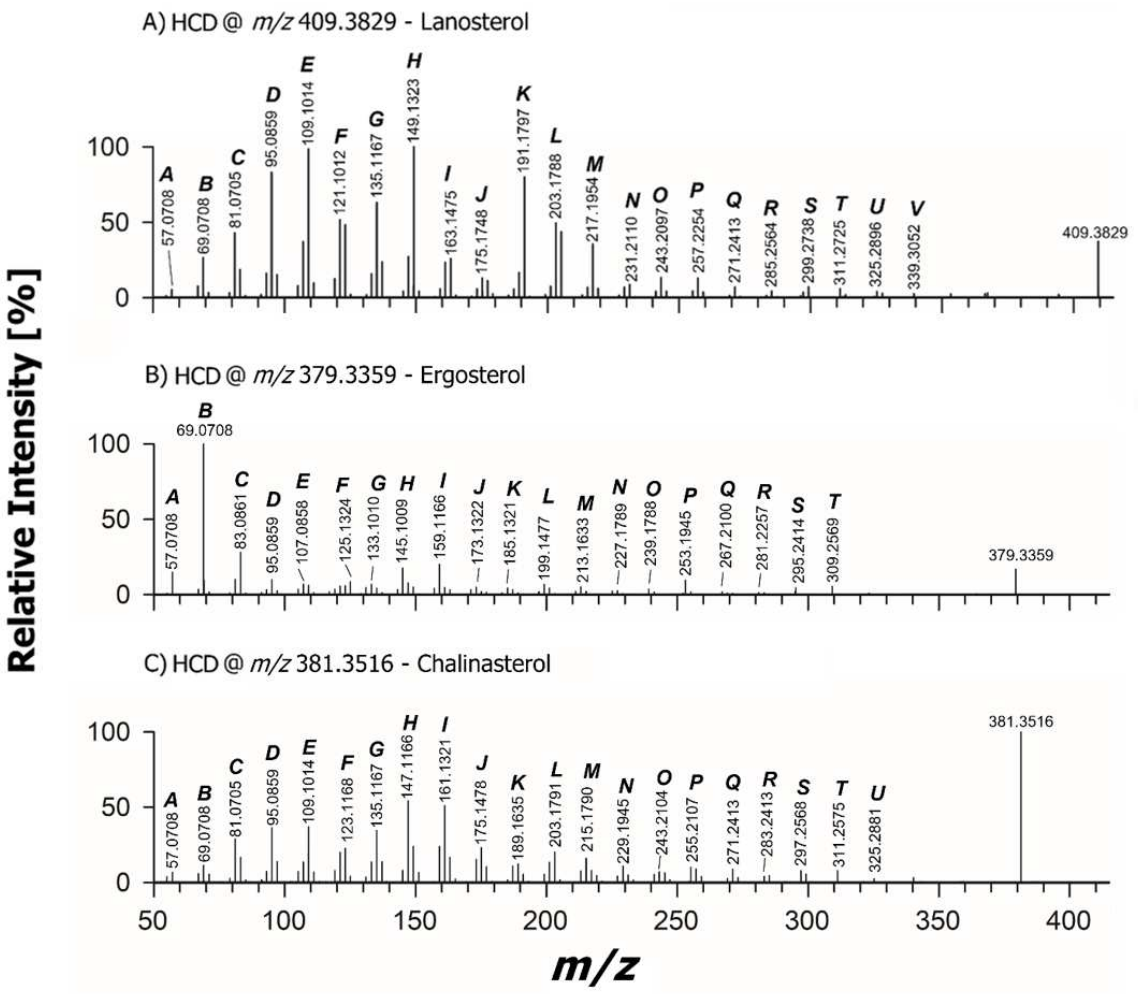
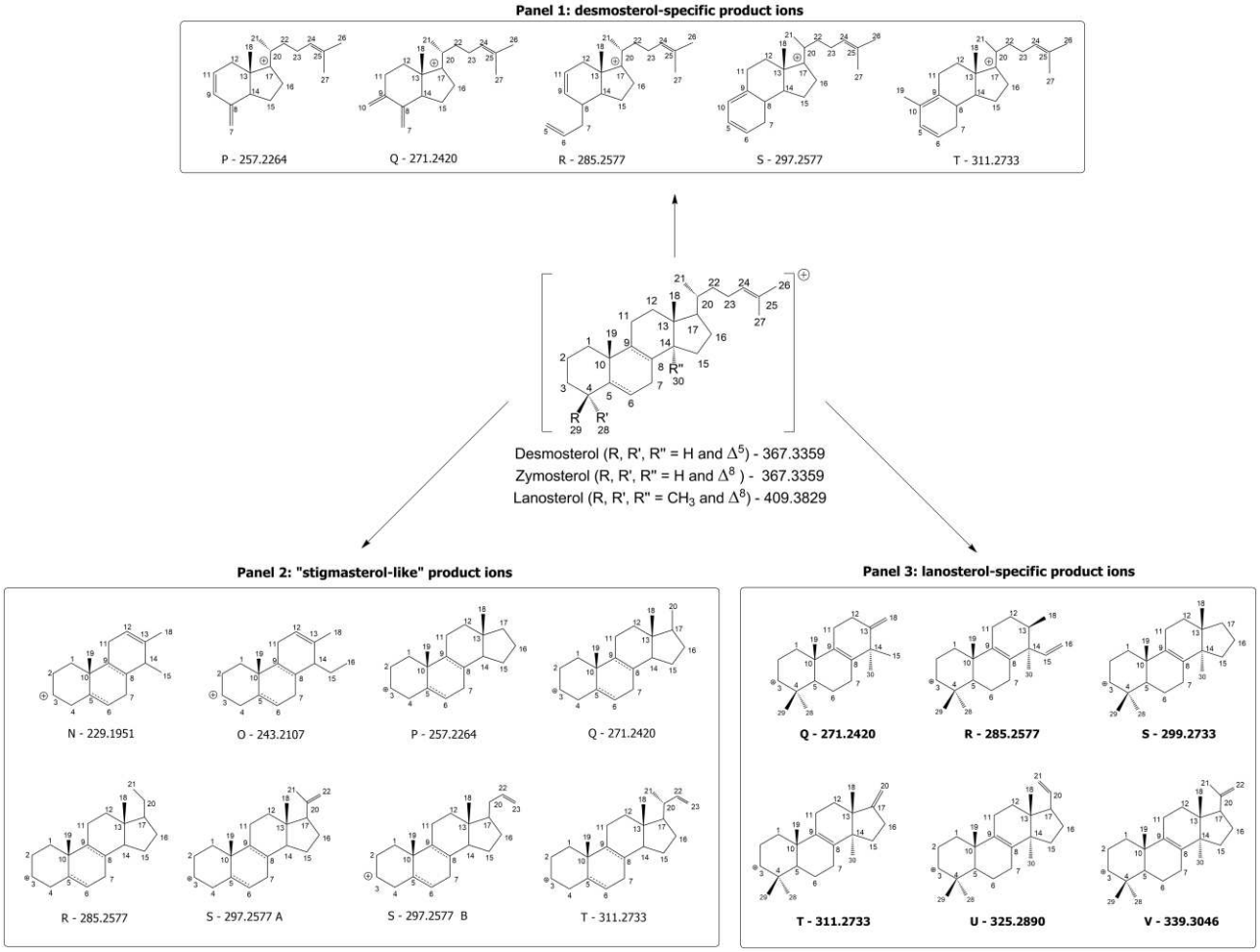


Figure 4. APCI(+)-HCD-FTMS/MS spectra obtained using the Q Exactive mass spectrometer for the $[M+H-H_2O]^+$ ions of selected sterols analyzed in this chapter: A) lanosterol; B) ergosterol; C) chalinasterol. Peak signals referred to product ions sharing the same number of carbon atoms but differing for the number of H atoms are grouped into clusters, each labelled with a capital letter. For each cluster, the experimental *m/z* value of the most abundant ion is usually indicated. The reported spectra were obtained through direct infusion analysis and confirmed by those resulting from spectral averaging under the respective peaks detected in RPLC-APCI(+)-HCD-FTMS/MS chromatograms (see text for details). HCD-FTMS/MS spectra were obtained at NCE = 30, with the HCD cell filled with nitrogen.

structures previously proposed for ions of clusters C to G in sterols non methylated on C14. However, a further interpretation of the prevailing ion in cluster H for lanosterol (exact *m/z* 149.1325) could be found by considering the structure previously discussed for the major ion in cluster F of zymosterol (exact *m/z* 121.1012) and the double methylation on C4 (see Panel 2 of **Scheme 2** and **Figure A7**). The potential existence of at least two routes for the generation of the *m/z* 149.1325 ion might be responsible for the remarkable intensity shown by its peak signal in the HCD-FTMS/MS spectrum of lanosterol (see **Figure 4A**), an almost unique feature in the MS/MS spectra of the sterols considered in this chapter.

A second striking feature of lanosterol's spectrum was the prominent *m/z* 191.1797 ion in cluster K. Interestingly, Mo *et al.*[52] observed the same ion in the APCI(+)-CID-MS/MS spectrum of cycloartenol, which is perfectly isobaric with lanosterol, featuring two methyl groups on C4, missing the C=C bond between C8 and C9 and having a methylene bridge between C10 and C19 (corresponding to the methyl group at C19 in lanosterol). Based on the structural hypothesis proposed by Mo *et al.*[52], the prevailing ion in cluster K for lanosterol would correspond to the *m/z* 163.1481 ion of zymosterol with two methyl groups linked to C4, resulting in an exact *m/z* value 191.1794 (**Scheme 2**, Panel 2). However, the CID-MS^3 analysis of this product ion of lanosterol, performed during this study using the Velos Pro linear ion trap mass spectrometer, revealed the generation of product ions identical to those found for the corresponding ion of cholesterol (nominal *m/z* 163, 149, 135, 121, 109, 95), thus suggesting a possible alternative origin. A further structure was thus proposed (**Scheme 2**, Panel 2), involving an initial ethylene loss from the C4 dimethyl groups mediated by hydrogen migrations (**Figure A9**). This process could be fundamental to explain the formation of ions prevailing in clusters I and J of lanosterol (respective exact *m/z* 163.1481 and 175.1481), which would correspond to those reported for zymosterol in Panel 2 of **Scheme 2**. In fact, no other plausible route could be hypothesized for the generation of those product ions, considering the double methylation at C4. However, as evidenced in **Scheme 2**, plausible structures for product ions prevailing in clusters from L to P in the case of lanosterol could be obtained considering those proposed for clusters from

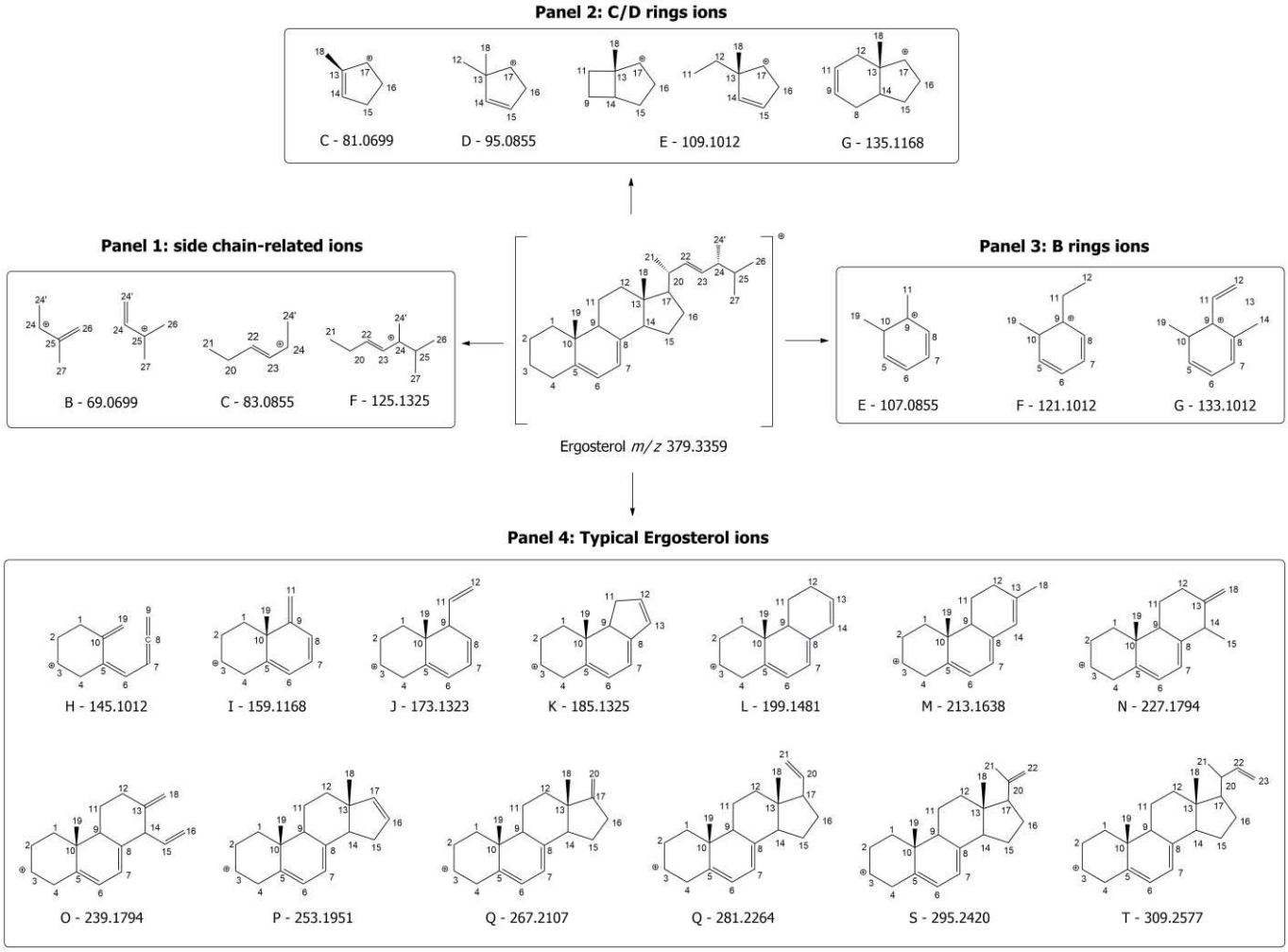
J to N of zymosterol, respectively, and taking into account the presence of two methyl groups on C4. This finding emphasizes that the eventual preliminary loss of those methyl groups cannot be generalized to the entire population of lanosterol precursor ions. Finally, as emphasized in Panel 3 of **Scheme 3**, specific structures had to be hypothesized for product ions belonging to clusters from Q to V detected in the HCD-FTMS/MS spectrum of lanosterol, all of which exhibiting weak peak signals (see **Figure 4A**). They arose from fragmentations involving the side chain and then ring D, resembling those observed for cholesterol[49].



Scheme 3. Proposed structures for major product ions detected in clusters N to T and Q to V found in the APCI-HCD-MS/MS spectra of $[M+H–H_2O]^+$ ions of desmosterol/zymosterol and lanosterol, respectively. Exact *m/z* values are reported for all ions with four decimal places. For structures reported in Panel 2, that are common to desmosterol and zymosterol, the double bond inside ring B is meant to be present only in the respective correct position (C5-C6 and C8-C9, respectively). See text for details.

2.3.5. Fragmentation of $\Delta^{5,7}$-sterols with a double bond at C22-C23: ergosterol. Ergosterol was selected in this study as a representative of $\Delta^{5,7}$-sterols. As shown in **Figure 1**, it features a double bond between C22 and C23 and a methyl group at C24, similarly to brassicasterol. The APCI(+)-HCD-FTMS/MS spectrum of the $[M+H-H_2O]^+$ ion of ergosterol (exact *m/z* 379.3359), reported in **Figure 4B**, was dominated by the peak of cluster B at *m/z* 69.0708. This value is consistent with the exact value 69.0699, corresponding to a recurring product ion observed for sterols under HCD conditions (see also Ref. 49), and thus discussed also in previous sections of this chapter. As demonstrated in the previous chpater, considering stigmasterol pentadeuterated on its side chain and brassicasterol, this ion originates from the sterol side chain and is particularly prominent when a methyl (or ethyl) group is present at C24. In such configurations, C24 is both tertiary and allylic, facilitating positive charge stabilization. A plausible mechanism for its formation in the case of ergosterol involves a 1,3-hydrogen shift from C26 (or C27) to C24, followed by cleavage of the C23–C24 bond. This generates a stable allylic carbocation, shown on the left in Panel 1 of **Scheme 4**. Alternatively, if positive charge is located on the tertiary carbon atom C25, a 1,3-H shift from C24' to C23 can yield another stable allylic/tertiary carbocation (**Scheme 4**, Panel 1). These processes can explain the high abundance of the *m/z* 69.0699 ion in ergosterol's MS/MS spectrum.

The second most abundant product ion of ergosterol was detected in cluster C and its *m/z* value was consistent with the exact value 83.0855. Several structures could be proposed for this ion in the case of stigmasterol[49]; however, none of them is suitable to explain the ergosterol product ion, since this sterol has a methyl group, not an ethyl one, linked to C24. After evaluating multiple hypotheses, the structure depicted in Panel 1 of **Scheme 4** emerged as the most likely. It assumes initial charge localization on C24 and involves two bond cleavages, between C24–C25 and C17–C20, facilitated by 1,3-H migrations (see **Figure A10**). This pathway results in a secondary/allylic carbocation. Furthermore, the dominant ion in cluster F (*m/z* 125.1325) likely serves as a precursor to the *m/z* 83.0855 ion, retaining the isopropyl moiety at the end of the side chain (**Figure A7**).



Scheme 4. Proposed structures for product ions generated from the $[M+H–H_2O]^+$ ion of ergosterol (exact *m/z* 379.3359) under HCD-MS/MS conditions. Exact *m/z* values rounded to four decimal places are indicated for each ion. See text for details.

As shown in **Figure 4B** and corroborated by the intensity values reported in **Table A1**, all other product ions detected in the HCD-MS/MS spectrum of ergosterol fall below the 10% relative intensity threshold. This result suggests that the presence of conjugated double bonds in the B-ring reduces fragmentation along the steroidal backbone in favor of side-chain fragmentations, at least when a relatively high collisional energy is available, like under HCD conditions. Nevertheless, structures similar to those previously proposed for cholesterol[49], all bearing the positive charge on C17, could be hypothesised for product ions including rings C and/or D that were detected in clusters C, D, E and G, either as leading or as secondary ions (Panel 2, **Scheme 3**). On the other hands, novel structural hypotheses were required for the dominant product ions detected in clusters E (*m/z* 107.0858) and G

(*m/z* 133.1010) for ergosterol. As illustrated in Panel 3 of **Scheme 4**, the presence of a double bond between C7 and C8 makes C9 an allylic and tertiary carbon atom, *i.e.,* a viable site for positive charge localization. A fragmentation involving partial cleavage of ring C and elimination of the left side of ring A as 1,3-butadiene may thus account for the formation of B-ring related ions with exact *m/z* values 107.0855 and 133.1012 (see panel 3 of **Scheme 4**), consistent with experimental ones. Additionally, a secondary ion in cluster F (exact *m/z* 121.1012) may also arise from this mechanism (**Scheme 4**, Panel 3). Product ions observed in clusters H, I, and P for ergosterol (consistent with exact *m/z* values 145.1012, 159.1168, and 253.1951, respectively) had been previously characterized by Munger *et al.*[51] as typical ergosterol product ions with positive charge retention at the original ionization site (C3). The same structures were thus depicted in Panel 4 of **Scheme 4**. Finally, it was possible to propose plausible structures for the dominant ions in all remaining clusters in ergosterol's MS/MS spectrum, also displayed in Panel 4 of **Scheme 3**. These ions appear to result from progressive side-chain detachment and subsequent fragmentation of ring D, with the charge consistently residing at C3.

2.3.6. Fragmentation of Δ^5-sterols with a double bond at C24–C24′ (methylene group at C24): chalinasterol. The final sterol examined in this study was chalinasterol, an isomer of brassicasterol. Chalinasterol is characterized by a methylene group at C24, *i.e.,* a C=C double bond between C24 and C24′, whose influence on the fragmentation pattern was specifically investigated. As shown in **Figure 4C**, the APCI(+)-HCD-MS/MS spectrum of the $[M+H–H_2O]^+$ ion of chalinasterol (exact *m/z* 381.3516) reveals a dominant peak in cluster B, consistent with the recurring exact *m/z* value 69.0699. **Figure A11** emphasizes that this ion can be readily formed if the positive charge is initially localized on C25, a carbon that is both tertiary and allylic in the case of chalinasterol. The formation process involves a typical 1,3-hydrogen migration, accompanied by cleavage of the C23–C24 bond.

For clusters C to F, the dominant ions correspond to structures proposed in the previous chapter and in Ref. 49 for cholesterol but also reported for stanols and lathosterol in this chapter (see Panel 3 of **Scheme 1**). These structures are appropriate here because they do not involve the side chain, where the unique structural feature of chalinasterol is located. Similarly, product ions dominating clusters G to O of chalinasterol can be explained using the same structures proposed for cholesterol and desmosterol (see Panel 2 of **Scheme 2**), since the side chain is not involved and the position of the C=C bond in ring B is identical.

A specific point of interest for chalinasterol is cluster P, where the ion at *m/z* 255.2107 slightly predominates. This represents a unique feature among the sterols analyzed in this study. In desmosterol, cluster P is dominated by an ion at *m/z* 257.2264, whose proposed structure is shown in Panel 3 of **Scheme 2**. However, due to differences in the side chain, this structure cannot explain the *m/z* 255.2107 ion observed for chalinasterol. One plausible structure for this ion could be obtained, in principle, considering the positive charge on C3 and a 1,3-hydrogen migration between C16 and C20, leading to cleavage of the C17–C20 bond and formation of a new C=C bond between C16 and C17. Mechanistically, this process should be feasible in all sterols considered so far. However, as evidenced in **Figures 3** and **4**, and also in the previous chapter and in Ref. 49, this ion was not detected in other sterols, suggesting that the pathway described above is not generally favored. An alternative, more efficient route to generate the *m/z* 255.2107 ion when a C=C bond is located inside the side chain of sterols was suggested by Munger *et al.*[51]. These Authors proposed that for sterols with a C=C bond at C24–C24′, such as chalinasterol (referred to in their work as 24-methylene-cholesterol), the *m/z* 255.2107 ion may arise from a retro-ene reaction. The presence of the C=C bond at C24–C24′ is essential for this reaction to proceed. Notably, this retro-ene process leads also to the formation of an intermediate product ion, which corresponds to the dominant peak observed in cluster S for chalinasterol (see **Figure 4C**). The structure of this ion is identical to that reported with the *m/z* label 297.2577 A in Panel 2 of **Scheme 3**, consistent with a stigmasterol-like product ion.

The structures proposed in the same panel for clusters Q to T, based on a B-ring double bond between C5 and C6, can be easily extended to chalinasterol. An additional noteworthy ion was detected for this sterol in cluster R, with a *m/z* value consistent with the exact one 283.2420. This product ion is expected to resemble the one assigned to cluster R in Panel 2 of **Scheme 3** (*m/z* 285.2577), with the addition of a C=C bond between C20 and C21.

2.3.7. Identification of sterols in baker's yeast based on chromatographic and tandem MS data.

To corroborate the robustness of HCD-MS/MS data obtained for standard sterol/stanols and thus verify the possibility of identifying these compounds in a real matrix through a combination of chromatographic and tandem mass spectrometric information, a sterol extract obtained from commercial baker's yeast was subjected to RPLC-APCI(+)-FTMS and FTMS/MS analysis under the same conditions adopted in this chapter for standards. In particular, gradient elution was employed in a first step. FTMS spectra averaged under all peaks detected in the resulting Total Ion Current chromatogram were considered to evaluate the eventual presence of sterols/stanols, based on the detection of the *m/z* values of their $[M+H-H_2O]^+$ ions. As a result, *m/z* ratios consistent with exact values 367.3359, 379.3359 and 409.3829 emerged and the corresponding multi-EIC trace was generated (see **Figure 5A**).

The comparison of retention times of peaks detected in the multi-EIC trace with those previously found, under linear gradient conditions, for animal/fungal standard sterols (see **Figure 2B**) indicated the occurrence of zymosterol (t_R = 21.9 min), ergosterol (t_R = 25.1 min) and lanosterol (t_R = 34.4 min). Actually, since standard zymosterol and desmosterol were found to be co-eluting under linear gradient conditions, an additional analysis of the baker's yeast extract was performed under isocratic conditions, like those related to **Figure 2A**, ensuring separation between the two sterols. As a result, the presence of desmosterol in the extract was excluded. This outcome was also confirmed by the

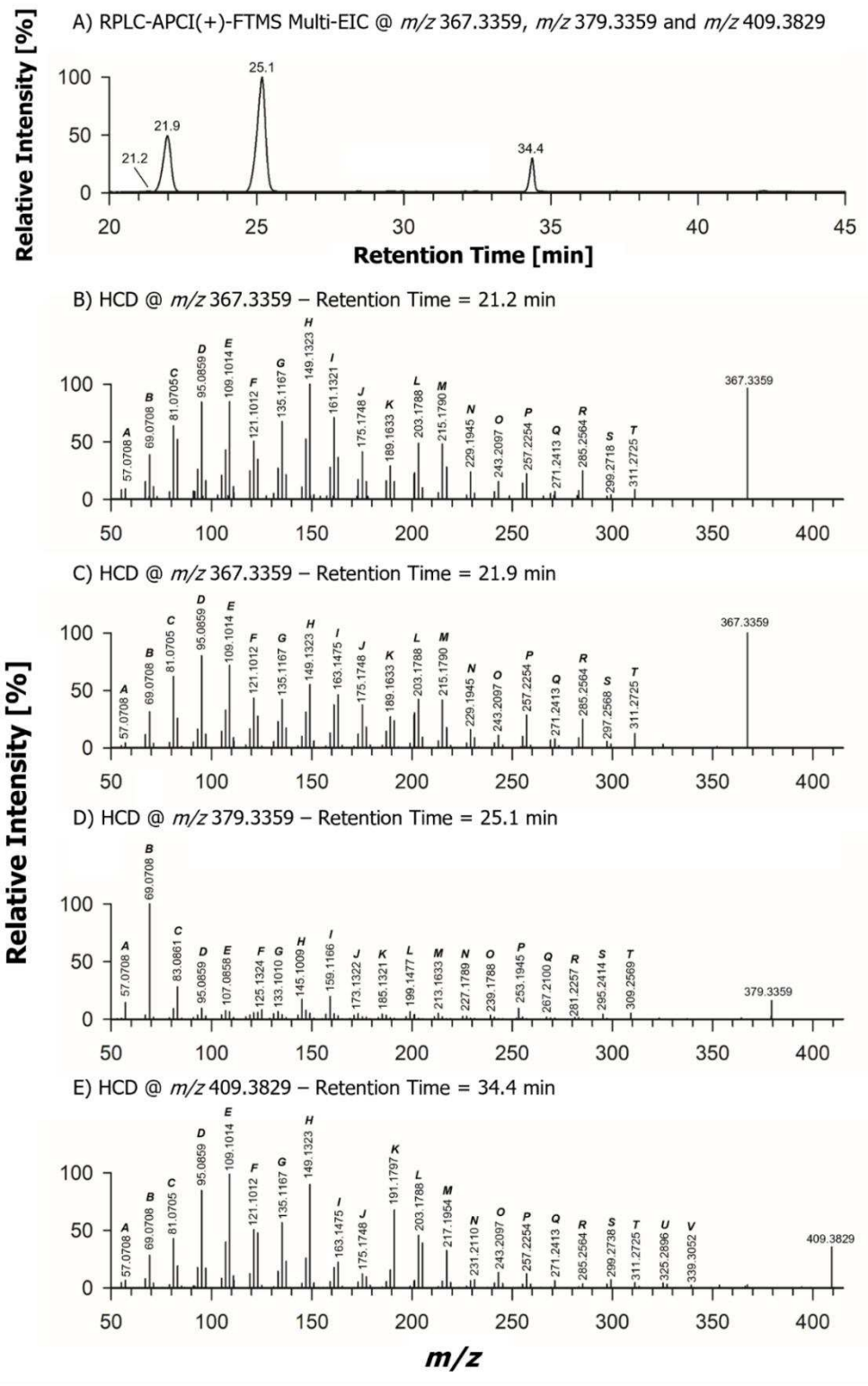


Figure 5. A) Multiple-extracted ion current (EIC) chromatogram obtained from the RPLC-APCI(+)-FTMS analysis, performed under linear gradient conditions and using the Q Exactive mass spectrometer, of the sterol extract of baker's yeast. C-E) HCD-FTMS/MS spectra averaged under peaks detected, respectively, at 21.2, 21.9, 25.1 and 34.4 min in the chromatographic trace shown in panel A. The peaks were assigned, respectively, to 5-a-cholesta-7,24-dien-3-b-ol (the D^7-analogue of zymosterol), zymosterol, ergosterol and lanosterol. See text for details.

comparison of the APCI-FTMS/MS spectrum averaged under the peak eluting at 21.9 min, shown in **Figure 5C**, with the one obtained for standard zymosterol (**Figure 3E**).

An excellent agreement was obtained, thus further excluding the occurrence of desmosterol, which, if present, would have led to an alteration of the spectral profile, due to the interference caused by its product ions. A very good agreement was also found between APCI-FTMS/MS spectra averaged under peaks eluting at 25.1 and 34.4 min (**Figures 5D** and **5E**, respectively) and those obtained for standard ergosterol and lanosterol (**Figures 4B** and **4A**), respectively, thus confirming the identification based on retention time alignment.

The results discussed so far in this section highlight that the chromatographic and MS/MS information related to standard sterols/stanols can represent a solid base for their identification even in real complex matrices. Indeed, the possibility that other compounds co-extracted with sterols/stanols and almost isobaric with them are also co-eluted with them, thus leading to co-isolation and fragmentation of the respective ions, with a potential interference on the typical sterol/stanol MS/MS spectral profiles, is unlikely. Moreover, even if these unlikely circumstances occur, the MS/MS spectral profile of sterols/stanols is so characteristic, provided enough collisional energy is available, that at least a part of it would reasonably be not affected by the interference due to a co-eluted, isobaric non sterolic/stanolic compound, thus still providing useful information.

Interestingly, the multi-EIC chromatogram obtained for the baker's yeast extract evidenced the presence of a weak peak eluting just before the one related to zymosterol (t_R = 21.2 min) and not corresponding to any of the standards considered in this chapter and in the previous one. The evaluation of the corresponding FTMS spectrum clearly showed that it was related to a sterol $[M+H-H_2O]^+$ ion with the same *m/z* value as zymosterol. The corresponding APCI-HCD-FTMS/MS spectrum, reported in **Figure 5B**, was then considered to infer information on its structural features. First, a good agreement with the intra-cluster profiles of zymosterol MS/MS spectrum was obtained for clusters J through T, those related to the characteristics of the side chain, thus suggesting that the unknown compound included a side chain with a C=C bond between C24 and C25. As for the

steroidal backbone, key information was inferred from clusters C, D and H. in which product ions consistent with exact *m/z* 83.0855, 95.0855 and 149.1325 exhibited relevant intensities. As discussed before, and as further evidenced in the next section of this chapter and in **Table 1**, these spectral features are all coherent with the occurrence of a C=C bond between C7 and C8. Based on these considerations, the unknown sterol was tentatively assigned as the Δ^7 analogue of zymosterol, nominally 5-alpha-cholesta-7,24-dien-3-b-ol, which is known to be a biosynthetic precursor of ergosterol[53]. As discussed before, the latter was clearly detected in the baker's yeast extract, being a typical fungal sterol. Notably, chromatographic information was consistent with the tentative identification of the unknown sterol as the Δ^7 analogue of zymosterol. Indeed, it was eluted slightly before zymosterol under linear gradient conditions, which also means that it would have been eluted slightly before desmosterol, its Δ^5 analogue, if this sterol had been present, being zymosterol and desmosterol co-eluting under those conditions. In other words, the presumed Δ^7 analogue of zymosterol/desmosterol exhibited a slightly lower retention time compared to its Δ^5 counterpart. This finding is in accordance with the relative retention under linear gradient conditions of lathosterol and cholesterol (Δ^7 vs Δ^5), evidenced in this chapter, and the one of Δ^7 and Δ^5 avenasterols, discusses in the previous chapter. The procedure described for the identification of the ergosterol precursor in the baker's yeast extract emphasizes how important the evaluation of MS/MS data on sterols/stanols can be, especially if integrated with chromatographic information, when compounds not corresponding to major sterols/stanols, whose standards might be unavailable, emerge from the analysis of real complex matrices.

2.3.8. Correlation Between Specific Product Ions and Structural Features of Major Animal, Fungal and Vegetal Sterols. As highlighted in **Figure 1**, the principal animal and fungal sterols differ structurally in several respects. These include variations in the composition and branching of the side chain, the number and positional isomerism of C=C double bonds along the steroidal backbone, and

the presence of additional methyl groups, such as those at C4 and C14 in the case of lanosterol. The systematic evaluation of their MS/MS spectral profiles, as presented in the preceding sections, revealed clear correlations between these molecular features and the fragmentation pathways. These correlations are consistent with patterns previously identified for cholesterol and the major plant sterols[49], where relative intensities of diagnostic product ions were shown to reflect specific structural characteristics.

To consolidate these findings, a summary of the structure-product ion correlations inferred after carefully evaluating the HCD-MS/MS spectra obtained both for animal/fungal sterol considered in the present study and for cholesterol and phytosterols considered in the previous chapter and in Ref. 49 is reported in **Table 1**. The correlations are evidenced following the increasing order of product ions *m/z* values, thus spanning clusters B through T; cluster A is not included, as its ions are not structurally informative. It is worth noting that the indications reported in **Table 1** are those that were found to be consistent between animal, fungal and plant sterols/stanols when considering compounds with the c23ructural characteristics. In the last four columns the table also reports an indication of the most likely origin of a specific product ion, *i.e.*, if it is expected to be formed at the level of the side chain or the steroidal backbone (in the case of lighter ions) and, from cluster H on, if its structure can be assimilated to the one of a product ion with the same *m/z* generated from cholesterol or stigmasterol. **Table 1** might be employed as a practical tool for interpreting the MS/MS spectra of unknown sterols that do not match with available standards but may be present in various animal, fungal or vegetal matrices. In particular, the relative intensities of ions within each cluster can offer valuable information about the number and position of unsaturations, the structure of the side chain, and the occurrence of specific methylations or branching patterns.

Table 1. Summary of the possible correlations between structural features of sterols and stanols, namely C=C bond(s) position(s) and side chain type, and intensity relationships between product ions belonging to specific signal clusters detected in the HCD-FTMS/MS spectra (acquired at NCE = 30) of $[M+H-H_2O]^+$ ions of standard animal/vegetal/fungal sterols and stanols discussed in the present chapter and in Ref. 49. The tentative assignment of a product ion to a specific portion of the sterol/stanol molecule or the similarity with the corresponding product ion previously detected in the case of cholesterol or stigmasterol[49] are evidenced in the last four columns. Exact *m/z* values, rounded to four decimal places, are reported for each ion. The name "stanol" in the table is referred to stanols with the same side chain as cholesterol.

Cluster	Exact *m/z* values	Intensity relationships	Type of product ion and related structural features			
			Side chain-related ion	A/B or C/D rings ion	Cholesterol-like ion	Stigmasterol-like ion
B	69.0699	69.0699 >> 71.0855	$\Delta^{24(24')}$, $\Delta^{24(25)}$ $\Delta^{22(23)}$, $\Delta^{5,22(23)}$	Δ^7 and stanols		
	71.0855	71.0855 > 69.0699	Δ^5 with saturated SC			
C	81.0699	81.0699 > 83.0855		Δ^5 with saturated SC $\Delta^{24(24')}$, $\Delta^{24(25)}$, and stanols		
	83.0855	83.0855 > 81.0699	$\Delta^{22(23)}$ alkylated at C24			
		83.0855 > 50%		Δ^7		
D	95.0855	95.0855 > 80%		Δ^7 and stanols		
F	121.1012	121.1012 > 123.1168		$\Delta^{5,22(23)}$, Δ^5 and Δ^7 with ethylene group at C24, and $\Delta^{8,24(25)}$		
	123.1168	123.1168 > 121.1012		Δ^5 and Δ^7 with saturated SC, stanols, $\Delta^{5,24(25)}$, Δ^5 with methylene group at C24		
	125.1325	125.1325 > 123.1168	$\Delta^{5,7,22(23)}$ methylated at C24			

G	133.1012	133.1012 > 135.1168	$\Delta^{5,7}$	
H	145.1012	145.1012 > 147.1168	$\Delta^{5,7}$	
	147.1168	147.1168 >> 149.1325	Δ^{5}	
	149.1325	149.1325 >> 147.1168	Δ^{7}, Δ^{8} and stanols	
I	159.1168	159.1168 > 161.1325	$\Delta^{5,7}$	
	161.1325	161.1325 >> 163.1481	Δ^{5} and Δ^{7}	
	163.1481	163.1481 > 161.1325	Δ^{8} and stanols	
J	173.1324	173.1324 > 175.1481		$\Delta^{,22(23)}$
	175.1481	175.1481 >> 173.1324	$\Delta^{24(24')}$, $\Delta^{24(25)}$ and sterols with saturated SC	
	177.1638	177.1638 > 175.1481	stanols	
K	185.1325	185.1325 > 187.1481		$\Delta^{5,7,,22(23)}$
	187.1481	187.1481 > 189.1638		$\Delta^{,22(23)}$
	189.1638	189.1638 > 187.1481	$\Delta^{24(25)}$, sterols with saturated SC and stanols	
	191.1794	191.1794 >> 189.1638	4,4-dimethyl-$\Delta^{8,24(25)}$	
L	199.1481	199.1481 > 201.1638		$\Delta^{5,7,,22(23)}$
	201.1638	201.1638 > 203.1794		$\Delta^{22(23)}$
	203.1794	203.1794 ≥ 205.1951	4,4-dimethyl-$\Delta^{8,24(25)}$	
M	213.1638	213.1638 > 215.1790	$\Delta^{5,7}$	

	217.1951	217.1951 > 215.1790	4,4-dimethyl-Δ^8 and stanols	
N	227.1794	227.1794 > 229.1946		$\Delta^{22(23)}$
	229.1946	229.1946 > 227.1794	Δ^5 and Δ^7 with saturated SC, $\Delta^{24(24')}$ and $\Delta^{24(25)}$	
	231.2107	231.2107 > 229.1946	4,4-dimethyl-$\Delta^{8,24(25)}$ and stanols	
O	239.1794	239.1794 > 241.1951		$\Delta^{5,7,22(23)}$
	241.1951	241.1951 > 243.2107		$\Delta^{22(23)}$ and $\Delta^{24(24')}$ with ethylene group at C24
	243.2107	243.2107 > 241.1951	sterols with saturated SC, stanols, $\Delta^{24(24')}$ with methylene group at C24 and $\Delta^{24(25)}$	
	247.2420	247.2420 > 243.2107	stanols	
P	253.1951	253.1951 > 255.2103		$\Delta^{5,7,22(23)}$
	255.2103	255.2103 ≥ 257.2269		$\Delta^{22(23)}$ and $\Delta^{24(24')}$ with ethylene group at C24
	257.2269	257.2269 > 259.2426	sterols with saturated SC alkylated at C24, Δ^7 with saturated unbranched SC	$\Delta^{24(25)}$
	259.2426	259.2426 > 257.2269	Δ^5 with saturated unbranched SC	
	261.2577	261.2577 > 259.2426	stanols	

R	281.2264	281.2264 > 283.2420		$\Delta^{5,7,22(23)}$
	283.2420	283.2420 > 285.2577		$\Delta^{22(23)}$ and $\Delta^{24(24')}$
	285.2577	285.2577 > 283.2420		$\Delta^{24(25)}$
	287.2733	287.2733 > 283.2420	sterols with saturated SC	
	289.2890	289.2890 > 287.2733	stanols	
S	295.2420	295.2420 > 297.2577		$\Delta^{5,7,22(23)}$
	297.2577	297.2577 > 299.2739		$\Delta^{24(24')}$ and $\Delta^{24(25)}$
	299.2733	299.2739 > 297.2577	Δ^{5}-with saturated and unbranched SC. 4,4-dimethyl-$\Delta^{8,24(25)}$	
	301.2890	301.2890 > 299.2733	Δ^{7}-and stanols	
T	309.2577	309.2577 > 311.2733		$\Delta^{5,7,22(23)}$
	311.2733	311.2733 > 313.2890		$\Delta^{5,22(23)}$, $\Delta^{5,24(24')}$ and $\Delta^{24(25)}$
	315.3046	315.3046 > 313.2890	Δ^{5} with ethyl group at C24, stanols	

As an additional step to emphasize the consistency of structure-fragmentation correlations reported in **Table 1** for sterols/stanols of different origin, MS/MS data obtained for compounds considered in this and in the previous chapter and in Ref. 49 were subjected to a processing based on well-known chemometrical unsupervised approaches, namely Hierarchical Cluster Analysis (HCA) and Principal Components Analysis (PCA). At this aim, besides sterols/stanols considered in this study, standard cholesterol and phytosterols considered in Ref. 49 were subjected to DIA-APCI(+)-HCD-FTMS/MS

analysis in triplicate, under the same experimental conditions. The relative intensities of product ions inferred from each spectrum were then stored in a dataset and HCA and PCA were performed considering each compound as a statistical object and each product ion as a variable, labelled with the corresponding nominal *m/z* ratio. The relative intensity obtained for each product ion in each spectrum was considered as its value as an input variable for HCA and PCA. The values were preliminarily autoscaled, then HCA and PCA were performed using the Metaboanalyst 6.0 software, freely accessible on the Internet (https://www.metaboanalyst.ca/). In the case of HCA, Euclidean distances and the Ward agglomeration algorithm were employed for clustering. The outcome of HCA, consisting of a double dendrogram (horizontal for objects, vertical for variables) and the corresponding heatmap, is reported in **Figure 6**. The outcome of PCA, represented by the scores and loadings plots, is reported in **Figure A12** of the Appendix 2.

First, the already discussed reproducibility of MS/MS spectral relative intensities can be inferred by the proximity of symbols corresponding to the three replicates for each compound in the PCA scores plot and by the generally excellent clustering of replicates for a specific sterol/stanol observed in the HCA dendrogram, the only exception occurring for the two stanols, due to the remarkable similarity of their MS/MS spectra. Moreover, as emphasized by labels added to the horizontal dendrogram in **Figure 6**, HCA on MS/MS relative intensities data was able to create clusters and sub-clusters clearly related to structural features. Indeed, sterols/stanols were clearly separated in the two major clusters, based on the nature of the side chain, *i.e.,* saturated vs unsaturated. The cluster of compounds with a saturated side chain was then sub-clustered according to the saturation (stanols) or unsaturation (Δ^5 and Δ^7 sterols) of the steroidal backbone. On the other hand, the major cluster of sterols with an unsaturated side chain was nicely sub-clustered according to the position and the number of C=C bonds on the steroidal backbone. Indeed, ergosterol represented a single sub-cluster, due to its unique double unsaturation on the backbone among the studied compounds, determining a peculiar profile of product ions, clearly visible in the HCA heatmap. Δ^7-avenasterol was also separated as a single cluster, whereas the two Δ^8 sterols (zymosterol and lanosterol) were surprisingly grouped together

despite the additional triple methylation characterizing lanosterol. This outcome suggests that the identical position of the C=C bond on the steroidal backbone and the identity of the side chains was more important in determining the fragmentation pathways of the two sterols than those methylations. Finally, all Δ^5 sterols with unsaturated side chain were sub-clustered together in the dendrogram (see **Figure 6**), then their sub-cluster was further split in two groups, reflecting the position of the C=C bond on the side chain, namely, the proximity of that bond to the steroidal backbone, thus indicating how refined can be the influence of structural features on the profile of MS/MS spectra.

The interesting information arising from HCA was confirmed by PCA. Indeed, as emphasized in **Figure A12**, all compounds including a saturated side chain were grouped in the lower left quadrant of the scores plot, with scores referring to stanols being very close, as expected, although symbols corresponding to the respective replicated samples were not mixed like in the case of HCA. On the other hand, sterols with C=C bonds on the side chain were located at positive values of PC2 and then, once again, separated according to the position of the unsaturation on the steroidal backbone. Finally, as observed in the HCA dendrogram, ergosterol and D^7-avenasterol were located in characteristic positions of the plot, due to their very specific structural features.

The outcomes of HCA and PCA on HCD-MS/MS data strengthen the concept that an extensive fragmentation of sterol/stanol $[M+H-H_2O]^+$ ions, achievable by a careful tuning of the collisional energy, according to the available tandem MS instrumentation, can provide a remarkable amount of information and open interesting perspectives for the recognition of the structural features of novel or poorly characterized sterols in complex matrices, including vegetal ones.

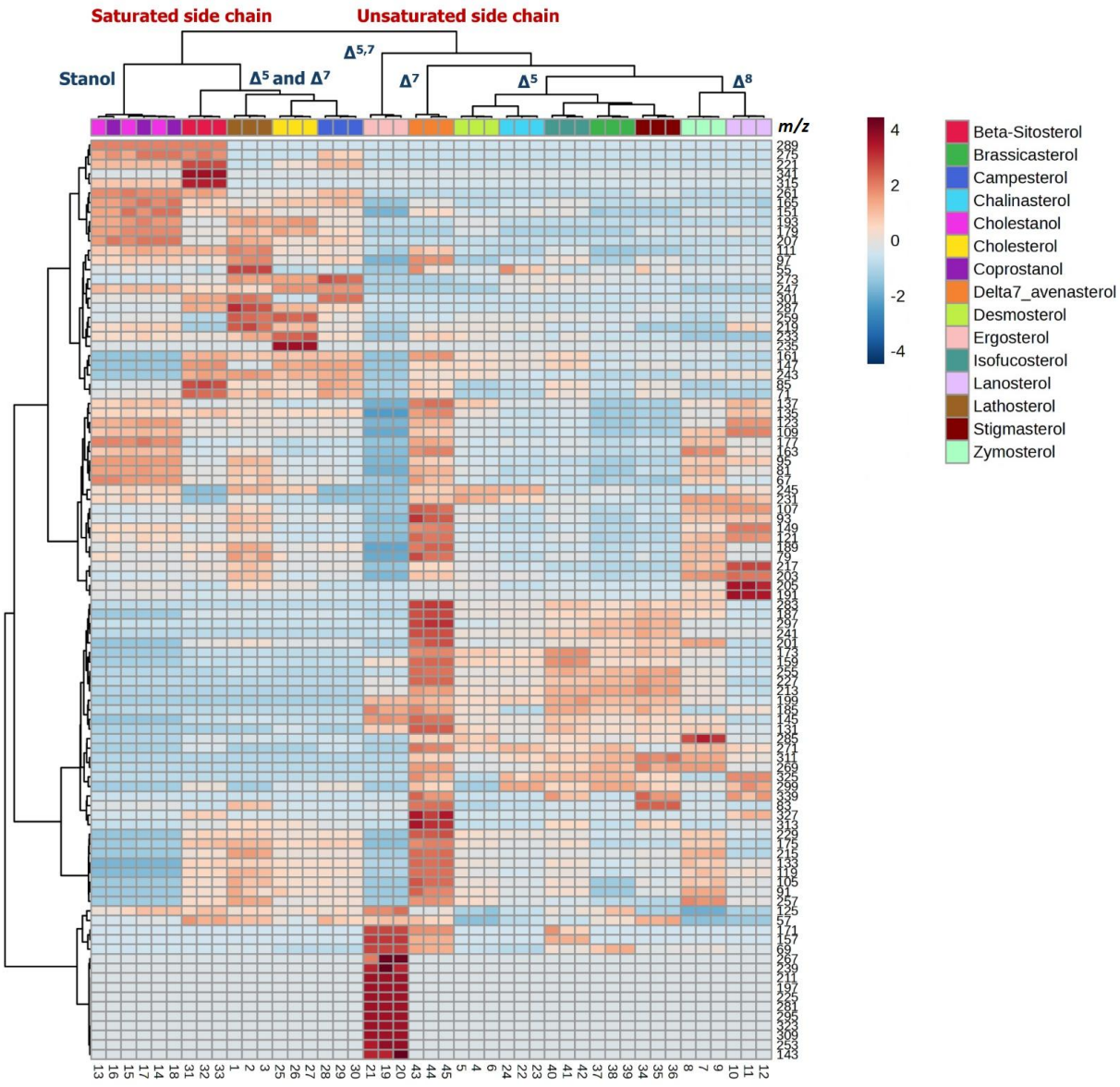


Figure 6. Double dendrogram (horizontal for objects, vertical for variables) with heatmap obtained from the Hierarchical Cluster Analysis of relative intensities data referred to product ions detected in APCI(+)-HCD-FTMS/MS spectra of animal/fungal sterols/stanol analyzed in the present study and cholesterol and phytosterols considered in Ref. 49. Each compound was analyzed in triplicate; thus, three small squares are referred to each compound at the base of the object dendrogram. Major structural characteristics related to groups or single compounds, namely the saturation or unsaturation of the side chain and the absence (stanols) or presence of C=C bonds (D) on the steroidal backbone and on the side chain are evidenced in the object dendrogram. Numbers reported at the end of variables rows represent the nominal *m/z* ratios of the corresponding product ions, that were used as variables for HCA.

2.4 Conclusions

Tandem mass spectrometry under HCD conditions, applied to $[M+H–H_2O]^+$ ions generated via APCI, proved highly effective for characterizing representative animal and fungal sterols, as previously shown for cholesterol and major plant sterols. Despite the inherent spectral complexity, marked by the detection of recurring fragment clusters, a systematic interpretation was enabled by considering alternative locations of the positive charge with respect to the original position (C3), in particular allylic or tertiary carbocations. This allowed for the proposal of plausible structures for major product ions and revealed consistent correlations between their relative abundances and specific structural features, including the position of C=C bonds, side chain alkylation, and additional methylations (like those occurring in lanosterol). These fragmentation trends closely mirrored those previously observed for cholesterol and plant sterols. This consistency was confirmed by the chemometric processing, through HCA and PCA, of MS/MS spectral data obtained for the entire ensemble of compounds, including them and the animal/fungal sterol/stanols considered in this chapter. Indeed, chemometrics outcomes emphasized the similarity in fragmentation behaviour in the presence of common structural features, apart from the origin of the compounds under study. Finally, the application of RPLC-APCI(+)-HCD-FTMS/MS analysis to the sterol extract of baker's yeast, selected as an example of complex matrix, confirmed the power of MS/MS data, along with chromatographic outcomes, in terms of recognition of novel sterols isomeric with known ones, with a Δ^7 analogue of zymosterol being identified along with the latter and other well-known fungal sterols.

Overall, the study described in this chapter offers a comprehensive framework for interpreting MS/MS spectra of diverse free sterols/stanols, paving the way for the structural elucidation of novel compounds of those classes in complex matrices.

References

1) Hannich, J.T.; Umebayashi, K.; Riezman, H. Distribution and functions of sterols and sphingolipids. *Cold Spring Harb. Perspect. Biol.* 2011, *3*, 1-14. doi:10.1101/cshperspect.a004762.

2) Dufourc, E.J. Sterols and membrane dynamics. *J. Chem. Biol.* 2008, *1*, 63-77. doi:10.1007/s12154-008-0010-6.

3) Piironen, V.; Lindsay, D.G.; Miettinen, T.A.; Toivo, J.; Lampi, A.M. Plant sterols: Biosynthesis, biological function and their importance to human nutrition. *J. Sci. Food Agric.* 2000, *80*, 939-966. doi:10.1002/(SICI)1097-0010(20000515)80:7<939::AID-JSFA644>3.0.CO;2-C.

4) Jordá, T.; Puig S. Regulation of ergosterol biosynthesis in saccharomyces cerevisiae. *Genes (Basel)* 2020, *11*, 1-18. doi:10.3390/genes11070795.

5) Nes, W.D. Biosynthesis of cholesterol and other sterols. *Chem. Rev.* 2011, *111*, 6423-6451. doi:10.1021/cr200021m.

6) Ačimovič, J.; Rozman D. Steroidal triterpenes of cholesterol synthesis. *Molecules* 2013, *18*, 4002-4017. doi:10.3390/molecules18044002.

7) Cerqueira, N.M.F.S.A.; Oliveira, E.F.; Gesto, D.S., Santos-Martins, D.; Moreira, C.; Moorthy, H.N.; Ramos, M.J.; Fenrandes, P.A. Cholesterol Biosynthesis: A Mechanistic Overview. *Biochemistry* 2016, *55*, 5483-5506. doi:10.1021/acs.biochem.6b00342.

8) Evtyugin, D.D.; Evtuguin, D.V.; Casal, S.; Domingues, M.R. Advances and Challenges in Plant Sterol Research: Fundamentals, Analysis, Applications and Production. *Molecules* 2023, *28*, 1-45. doi:10.3390/molecules28186526.

9) IUPAC-IUB Joint Commission on Biochemical Nomenclature (JCBN). The nomenclature of steroids. Recommendations 1989. *Eur J Biochem.* 1989, *186*, 429-458. doi:10.1351/pac197645010011.

10) Valitova, J.N.; Sulkarnayeva, A.G.; Minibayeva, F.V. Plant sterols: Diversity, biosynthesis, and physiological functions. *Biochemistry* 2016, *81*, 819-834. doi:10.1134/S0006297916080046.

11) Moreau, R.A.; Nyström, L.; Whitaker, B.D.; Winkler-Maser, J.K.; Baer, D.J.; Gebauer, S.H.; Hicks, K.B. Phytosterols and their derivatives: Structural diversity, distribution, metabolism, analysis, and health-promoting uses. *Prog. Lipid Res.* 2018, *70*, 35-61. doi:10.1016/j.plipres.2018.04.001.

12) Skubic, C.; Rozman, D. Sterols from the Post-Lanosterol Part of Cholesterol Synthesis: Novel Signaling Players. In *Mammalian Sterols. Novel Biological Roles of Cholesterol Synthesis Intermediates, Oxysterols and Bile Acids*; Rozman, D., Gebhardt, R., Eds; Springer Nature Switzerland: Cham, Switzerland, 2020; pp. 1-22. doi:10.1007/978-3-030-39684-8.

13) Alcazar-Fuoli, L.; Mellado, E. Ergosterol biosynthesis in Aspergillus fumigatus: Its relevance as an antifungal target and role in antifungal drug resistance. *Front. Microbiol.* 2012, *3*, 1-6. doi:10.3389/fmicb.2012.00439.

14) Skrede, S.; Bjorkhem, I.; Buchmann, M.S.; Hopen, G; Fausa, O. A novel pathway for biosynthesis of cholestanol with 7α-hydroxylated C27-steroids as intermediates, and its importance for the accumulation of cholestanol in cerebrotendinous xanthomatosis. *J. Clin. Invest.* 1985, 75, 448-455. doi:10.1172/JCI111719.

15) Björkhem, I.; Karlmar, K.E. Biosynthesis of cholestanol: Conversion of cholesterol into 4-cholesten-3-one by rat liver microsomes. *Biochim. Biophys. Acta. Lipids Lipid Metab.* 1974, *337*, 129-131. doi:10.1016/0005-2760(74)90046-0.

16) Björkhem, I.; Gustafsson, J. Mechanism of Microbial Transformation of Cholesterol into Coprostanol. *Eur. J. Biochem.* 1971, *21*, 428-432. doi:10.1111/j.1432-1033.1971.tb01488.x.

17) Juste, C.; Gérard, P. Cholesterol-to-coprostanol conversion by the gut microbiota: What we know, suspect, and ignore. *Microorganisms* 2021, *9*, 1-18. doi:10.3390/microorganisms9091881.

18) Nakajima, N.; Fujioka, S.; Tanaka, T.; Takatsuto, S.; Yoshida S. Biosynthesis of cholestanol in higher plants. *Phytochemistry* 2002, *60*, 275-279. doi:10.1016/S0031-9422(02)00113-9.

19) Nes, W.R.; Sekula, B.C.; Nes, W.D.; Adler, J.H. The functional importance of structural features of ergosterol in yeast. *J. Biol. Chem.* 1978, *253*, 6218-6225. doi:10.1016/s0021-9258(17)34602-1.

20) Sonawane, P.D.; Pollier, J.; Panda, S., Szymanski, J.; Massalha, H.; Yona, M.; Unger, T.; Malitsky, S.; Arendt, P.; Pauwels, L.; Almekias-Siegl, E.; Rogachev, I., Meir, S.; Cardenas, P.D.; Masri, A.; Petrikov, M.; Schaller, H.; Schaffer, A.A.; Kamble, A.; Giri, A.P.; Goossens, A.; Aharoni, A. Plant cholesterol biosynthetic pathway overlaps with phytosterol metabolism. *Nat. Plants.* 2016, *3*, 1-13. doi:10.1038/nplants.2016.205.

21) Idler, D.R.; Fagerlund, U.H.M. Marine Sterols. I. Isolation of 24-Methylenecholesterol from Molluscs. *J. Am. Chem. Soc.* 1955, *77*, 4142-4144. doi:10.1021/ja01620a050.

22) Hakim, M.M.; Patel, I.C. A review on phytoconstituents of marine brown algae. *Futur. J. Pharm. Sci.* 2020, *6*, 1-11. doi:10.1186/s43094-020-00147-6.

23) Sohn, S.I.; Rathinapriya, P., Balaji, S.; Balan, D.J.; Swetha, T.K.; Durgadevi, R.; Alagulakshmi, S.; Singaraj, P.; Pandian, S. Phytosterols in seaweeds: An overview on biosynthesis to biomedical applications. *Int. J. Mol. Sci.* 2021, *22*, 1-26. doi:10.3390/ijms222312691.

24) Sánchez-Machado, D.I.; López-Hernández, J.; Paseiro-Losada, P.; López-Cervantes, J. An HPLC method for the quantification of sterols in edible seaweeds. *Biomed. Chromatogr.* 2004, *18*, 183-190. doi:10.1002/bmc.316.

25) Schlag, S.; Huang, Y.; Vetter, W. GC/EI-MS method for the determination of phytosterols in vegetable oils. *Anal. Bioanal. Chem.* 2022, *414*, 1061-1071. doi:10.1007/s00216-021-03730-9.

26) Parkinson, D.R.; Warren, J.M.; Pawliszyn, J. Analysis of ergosterol for the detection of mold in soils by automated on-fiber derivatization headspace extraction-SPME-GC/MS. *Anal. Chim. Acta* 2010, *661*, 181-187. doi:10.1016/j.aca.2009.12.027.

27) Saraiva, D.; Semedo, R.; Castilho, M da C.; Silva, J.M.; Ramos, F. Selection of the derivatization reagent-The case of human blood cholesterol, its precursors and phytosterols GC-MS analyses. *J. Chromatogr. B* 2011, *879*, 3806-3811. doi:10.1016/j.jchromb.2011.10.021.

28) Ahmida, H.S.M.; Bertucci, P.; Franzò, L.; Massoud, R.; Cortese, C.; Lala, A.; Federici, G. Simultaneous determination of plasmatic phytosterols and cholesterol precursors using gas chromatography-mass spectrometry (GC-MS) with selective ion monitoring (SIM). *J. Chromatogr. B* 2006, *842*, 43-47. doi:10.1016/j.jchromb.2006.05.024.

29) Ačimovič, J.; Lövgren-Sandblom, A.; Monostory, K.; Rozman, D.; Golicnik, M.; Lütjohann, D.; Björkhem, I. Combined gas chromatographic/mass spectrometric analysis of cholesterol precursors and plant sterols in cultured cells. *J. Chromatogr. B* 2009, *877*, 2081-2086. doi:10.1016/j.jchromb.2009.05.050.

30) Kunz. S; Matysik, S. A comprehensive method to determine sterol species in human faeces by GC-triple quadrupole MS. *J. Steroid Biochem. Mol. Biol.* 2019, *190*, 99-103. doi:10.1016/j.jsbmb.2019.03.014.

31) Skubic, C.; Vovk, I.; Rozman, D.; Križman, M. Simplified LC-MS method for analysis of sterols in biological samples. *Molecules* 2020, *25*, 1-10. doi:10.3390/molecules25184116.

32) Baila-Rueda, L.; Cenarro, A.; Cofán, M.; Orera, I.; Barcelo-Batllori, S.; Pocovì, M.; Ros, E.; Civeira, F.; Nerin, C.; Domeno, C. Simultaneous determination of oxysterols, phytosterols and cholesterol precursors by high performance liquid chromatography tandem mass spectrometry in human serum. *Anal Methods* 2013, *5*, 2249-2257. doi:10.1039/c3ay26395a.

33) Honda, A.; Yamashita, K.; Miyazaki, H., Shirai, M.; Ikegami, T.; Xu, G.; Numazawa, M.; Hara, T.; Matsuzaki, Y. Highly sensitive analysis of sterol profiles in human serum by LC-ESI-MS/MS. *J. Lipid Res.* 2008, *49*, 2063-2073. doi:10.1194/jlr.D800017-JLR200.

34) Honda, A.; Miyazaki, T.; Ikegami, T.; Iwamoto, J.; Yamashita, K.; Numazawa, M.; Matsuzaki, Y. Highly sensitive and specific analysis of sterol profiles in biological samples by HPLC-ESI-MS/MS. *J. Steroid Biochem. Mol. Biol.* 2010, *121*, 556-564. doi:10.1016/j.jsbmb.2010.03.030.

35) Li, W.; Xu, X.; Tang, Z.; Guo, Y., Fei, D.; Yan, N.; Hu, F. Analysis of 14 terpenoids and sterols and variety discrimination of Codonopsis Radix using ultra-high-performance liquid chromatography-quadrupole-time-of-flight mass spectrometry. *J. Sep. Sci.* 2023, *46*, 1-13. doi:10.1002/jssc.202200835.

36) Mendiara, I.; Domeño, C.; Nerín, C. Development of a fast sample treatment for the analysis of free and bonded sterols in human serum by LC-MS. *J. Sep. Sci.* 2012, *35*, 3308-3316. doi:10.1002/jssc.201200519.

37) McDonald, J.G.; Smith, D.D.; Stiles, A.R.; Russell, D.W. A comprehensive method for extraction and quantitative analysis of sterols and secosteroids from human plasma. *J. Lipid Res.* 2012, *53*, 1399-1409. doi:10.1194/jlr.D022285.

38) Schött, H.F.; Krautbauer, S.; Höring, M.; Liebisch, G.; Matysik, S. A Validated, Fast Method for Quantification of Sterols and Gut Microbiome Derived 5α/β-Stanols in Human Feces by Isotope Dilution LC-High-Resolution MS. *Anal. Chem.* 2018, *90*, 8487-8494. doi:10.1021/acs.analchem.8b01278.

39) van der Ham, M.; Gerrits, J.; Prinsen, B.; van Hasselt, P.; Fuchs, S.; Jans, J.; Willems, A.; de Sain-van der Velden, M.G.M. UPLC-Orbitrap-HRMS application for analysis of plasma sterols. *Anal. Chim. Acta* 2024, *1296*, 1-10. doi:10.1016/j.aca.2024.342347.

40) Toh, T.H.; Prior, B.A.; Van Der Merwe, M.J. Quantification of plasma membrane ergosterol of Saccharomyces cerevisiae by direct-injection atmospheric pressure chemical ionization/tandem mass spectrometry. *Anal. Biochem.* 2001, *288*, 44-51. doi:10.1006/abio.2000.4877.

41) Birk, J.J.; Dippold, M.; Wiesenberg, G.L.B.; Glaser, B. Combined quantification of faecal sterols, stanols, stanones and bile acids in soils and terrestrial sediments by gas chromatography-mass spectrometry. *J. Chromatogr A.* 2012, *1242*, 1-10. doi:10.1016/j.chroma.2012.04.027.

42) Feng, M.; Jin, Y.; Yang, S.; Joachim, A.M.; Ning, Y.; Mori-Quiroz, L.M.; Fromm, J.; Perera, C.; Zhang, K.; Werbovetz, K.A.; Wang, M.Z. Sterol profiling of Leishmania parasites using a new HPLC-tandem mass spectrometry-based method and antifungal azoles as chemical

probes reveals a key intermediate sterol that supports a branched ergosterol biosynthetic pathway. *Int. J. Parasitol. Drugs Drug Resist.* 2022, *20*, 27-42. doi:10.1016/j.ijpddr.2022.07.003.

43) Jäpelt, R.B.; Silvestro, D.; Smedsgaard, J.; Jensen, P.E.; Jakobsen, J. LC-MS/MS with atmospheric pressure chemical ionisation to study the effect of UV treatment on the formation of vitamin D3 and sterols in plants. *Food Chem.* 2011, *129*, 217-225. doi:10.1016/j.foodchem.2011.04.029.

44) Castellaneta, A.; Losito, I.; Leoni, B.; Renna, M.; Mininni, C.; Santamaria, P. Calvano, C.D.; Cataldi, T.R.I.; Liebisch, G.; Matysik, S. A targeted GC-MS/MS approach for the determination of eight sterols in microgreen and mature plant material. *J. Steroid Biochem. Mol. Biol.* 2023, *232*, 1-10. doi:10.1016/j.jsbmb.2023.106361.

45) Wewer, V.; Dombrink, I.; Vom Dorp, K.; Dörmann, P. Quantification of sterol lipids in plants by quadrupole time-of-flight mass spectrometry. *J. Lipid Res.* 2011, *52*, 1039-1054. doi:10.1194/jlr.D013987.

46) Qiu, J.; Li, T.; Zhu, Z.-J. Multi-dimensional characterization and identification of sterols in untargeted LC-MS analysis using all ion fragmentation technology. *Anal. Chim. Acta* 2021, *1142*, 108-117. doi: 10.1016/j.aca.2020.10.058.

47) Gachumi, G.; Demelenne, A.; Poudel, A.; Bashi, Z.D.; El-Aneed, A. Novel Fast Chromatography-Tandem Mass Spectrometric Quantitative Approach for the Determination of Plant-Extracted Phytosterols and Tocopherols. *Molecules* 2021, *26*, 1402. doi: 10.3390/molecules26051402.

48) Peterka, O.; Kadyrbekova, Y.; Jirásko, R.; Lásko, Z.; Melichar, B.; Holčapek, M. Novel Charge-Switch Derivatization Method Using 3-(Chlorosulfonyl)benzoic Acid for Sensitive RP-UHPLC/MS/MS Analysis of Acylglycerols, Sterols, and Prenols. *Anal. Chem.,* 2025, *97*, 7157–7164. doi: 10.1021/acs.analchem.4c06496.

49) Cinquepalmi, V.; Losito, I.; Castellaneta, A.; Calvano, C.D.; Cataldi, T.R.I. APCI-Multistage Mass Spectrometry Following Liquid Chromatography for Selected 4-Desmethyl-Sterols and Their Deuterium-Labelled Analogues Unveils Characteristic Fragmentation Routes for Cholesterol and Phytosterols Identification. *Rapid Commun. Mass Spectr.* 2025, 39, e10039. doi: 10.1002/rcm.10039.

50) Losito, I.; Facchini, L.; Valentini, A.; Cataldi, T.R.I.; Palmisano, F. Fatty acidomics: Evaluation of the effects of thermal treatments on commercial mussels through an extended characterization of their free fatty acids by liquid chromatography – Fourier transform mass spectrometry. *Food Chem.* 2018, *255*, 309-322. doi:10.1016/j.foodchem.2018.02.073.

51) Münger, L.H.; Boulos, S.; Nyström, L. UPLC-MS/MS based identification of dietary steryl glucosides by investigation of corresponding free sterols. *Front. Chem.* 2018, *6*, 1-19. doi:10.3389/fchem.2018.00342.

52) Mo, S.; Dong, L.; Hurst, W.J.; Van Breemen, R.B. Quantitative analysis of phytosterols in edible oils using APCI liquid chromatography-tandem mass spectrometry. *Lipids* 2013, *48*, 949-956. doi:10.1007/s11745-013-3813-3.

53) Souza, C.M.; Schwabe, T.M.E.; Pichler, H.; Ploier, B.; Leitner, E.; Guan, X.L.; Wenk, M.R.; Riezman, I.; Riezman, H. A Stable Yeast Strain Efficiently Producing Cholesterol Instead of Ergosterol Is Functional for Tryptophan Uptake, but Not Weak Organic Acid Resistance. *Metab. Eng.* 2011, *13*, 555–569. doi: 10.1016/j.ymben.2011.06.006.

Appendix 2

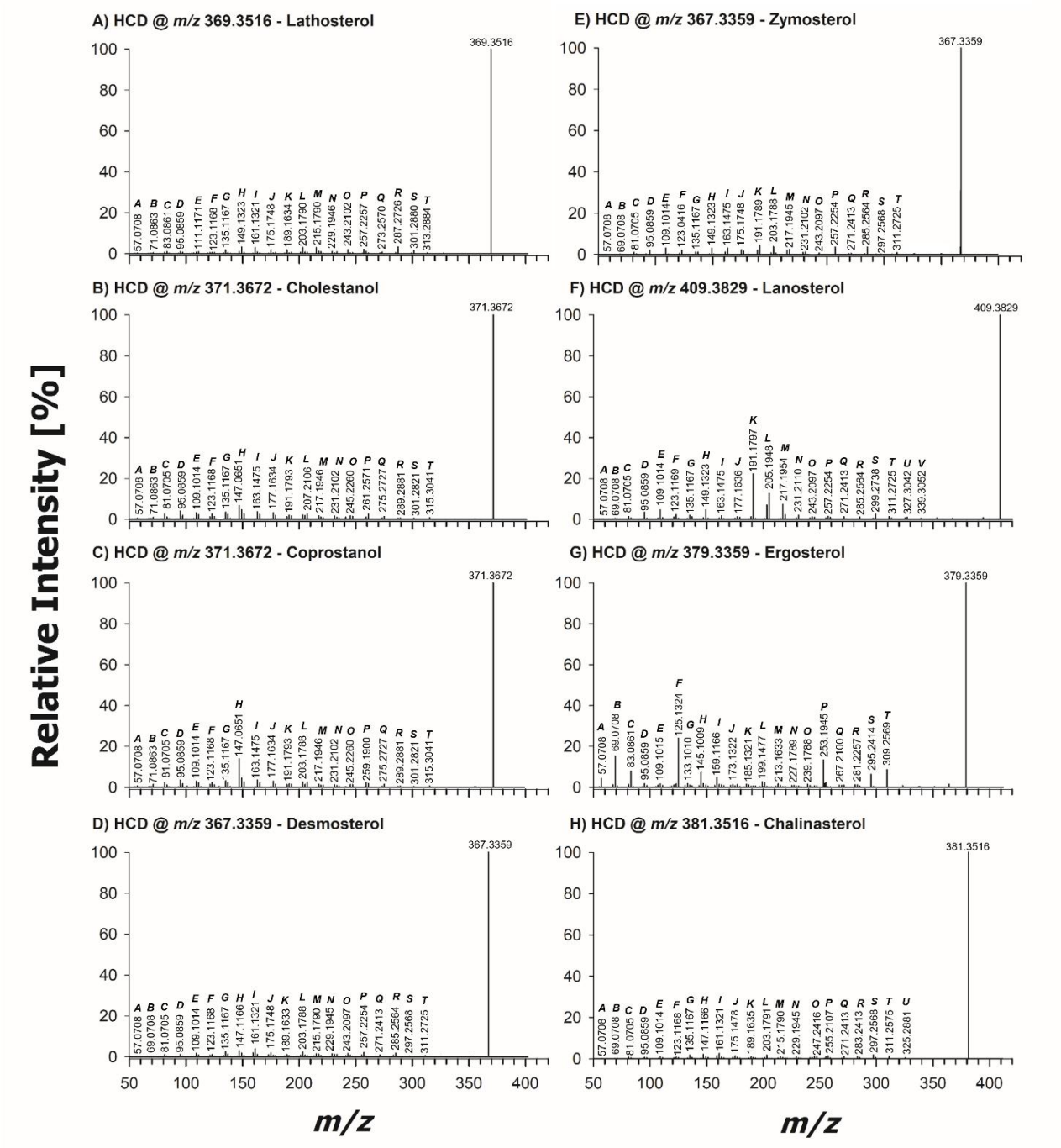


Figure A1. APCI(+)-HCD-FTMS/MS spectra obtained using the Q Exactive mass spectrometer for the $[M+H-H_2O]^+$ ions of sterols and stanols analyzed in this study considering a Normalized Collisional Energy (NCE) value equal to 10. Peak signals referred to product ions sharing the same number of carbon atoms but differing for the number of H atoms were grouped into clusters, each labelled with a capital letter. For the sake of clarity, the experimental *m/z* value of only one ion (usually the most abundant) is reported for each cluster.

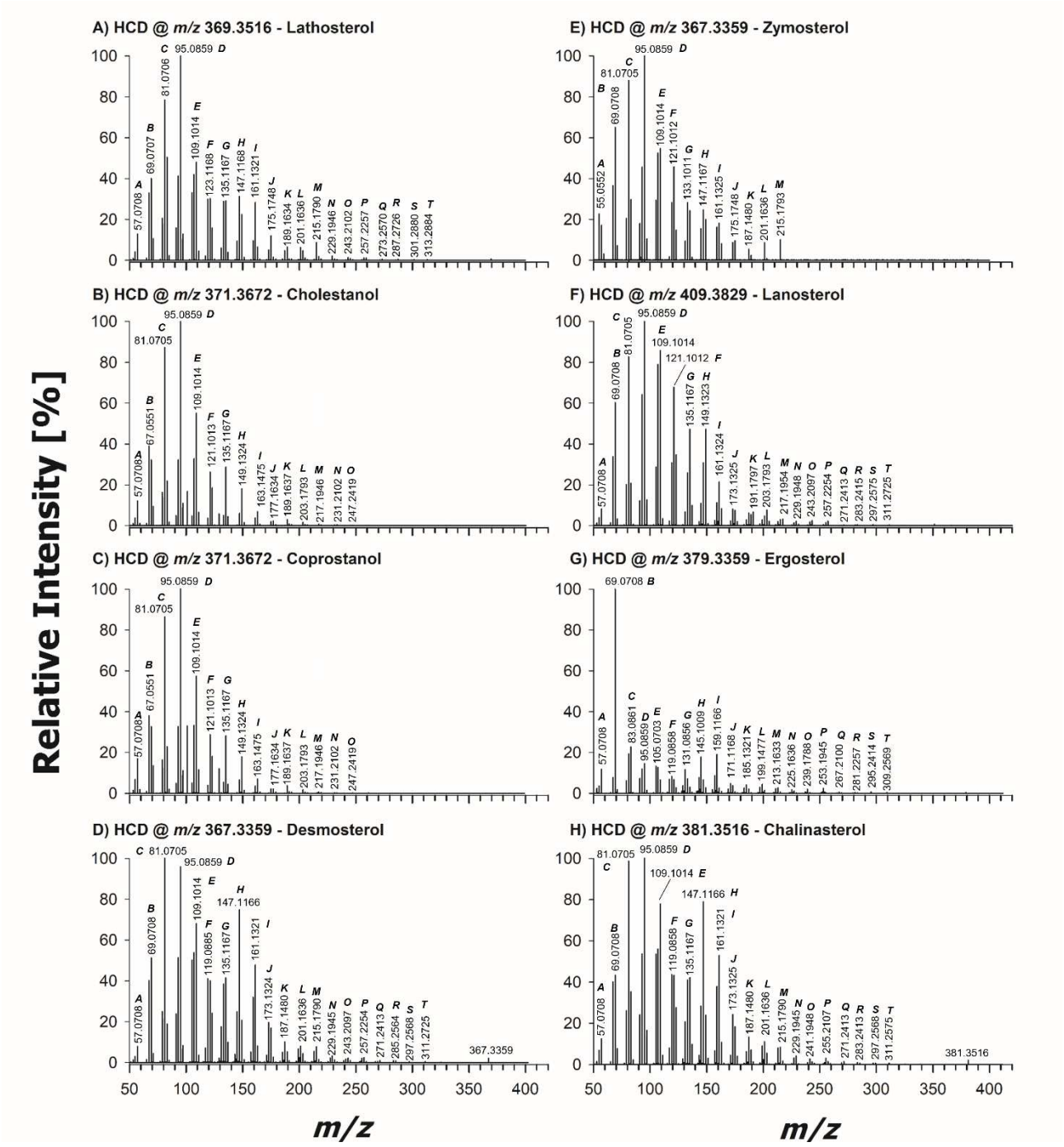


Figure A2. APCI(+)-HCD-FTMS/MS spectra obtained using the Q Exactive mass spectrometer for the $[M+H-H_2O]^+$ ions of sterols and stanols analyzed in this study considering a NCE value equal to 50. Peak signals referred to product ions sharing the same number of carbon atoms but differing for the number of H atoms were grouped into clusters, each labelled with a capital letter. For the sake of clarity, the experimental *m/z* value of only one ion (usually the most abundant) is reported for each cluster.

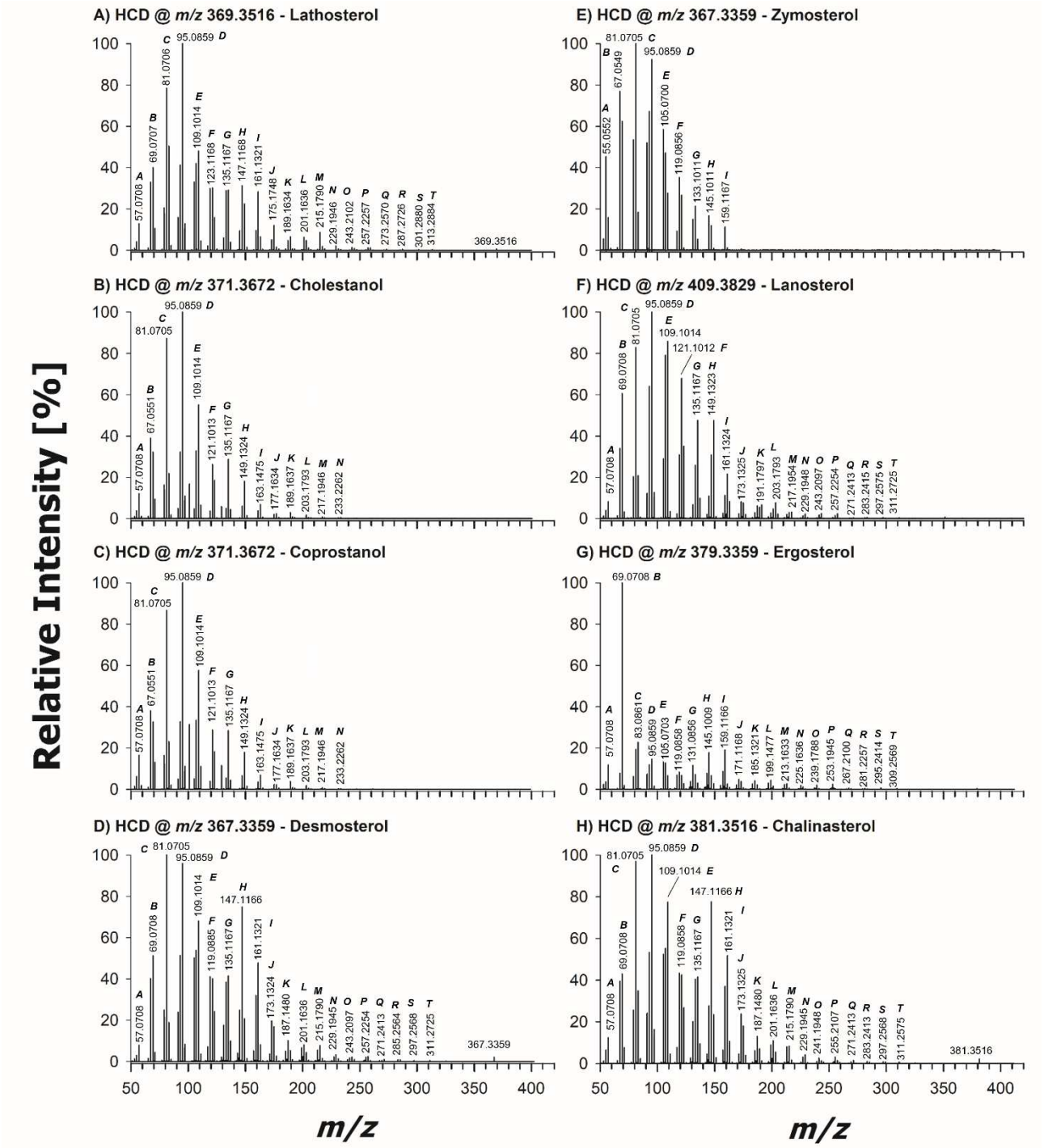


Figure A3. APCI(+)-HCD-FTMS/MS spectra obtained using the Q Exactive mass spectrometer for the $[M+H-H_2O]^+$ ions of sterols and stanols analyzed in this study considering a NCE value equal to 70. Peak signals referred to product ions sharing the same number of carbon atoms but differing for the number of H atoms were grouped into clusters, each labelled with a capital letter. For the sake of clarity, the experimental *m/z* value of only one ion (usually the most abundant) is reported for each cluster.

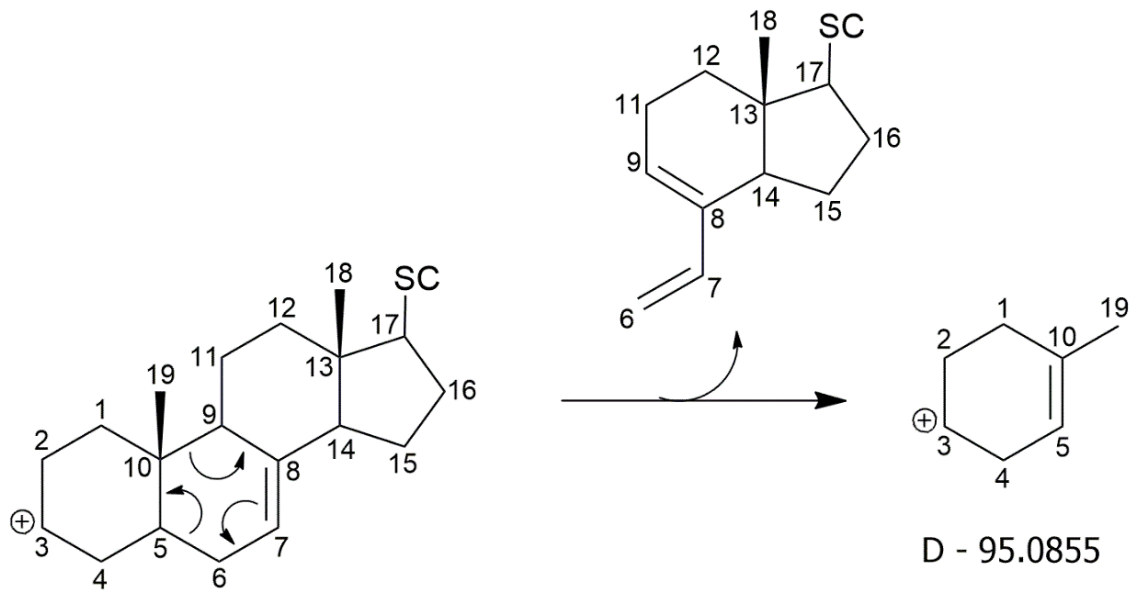


Figure A4. Proposed mechanism for the gas-phase formation of an A-ring-derived product ion, detected in cluster D, from the $[M+H-H_2O]^+$ ion of a generic Δ^7-sterol. The process involves a retro-Diels–Alder reaction initiated from a structure bearing the positive charge localised at C3. The exact *m/z* value, rounded to four decimal places, is reported for the product ion.

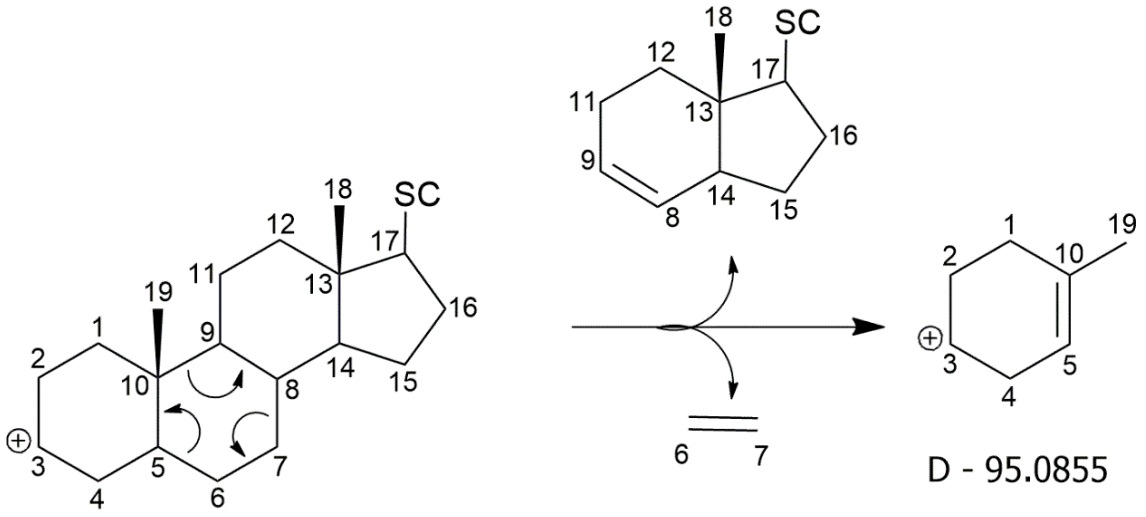


Figure A5. Proposed mechanism for the gas-phase formation of a product ion detected in cluster D and having an exact *m/z* 95.0855 from the $[M+H-H_2O]^+$ ion of a generic stanol. The process involves a retro-cycloaddition on ring B, initiated from a structure bearing the positive charge on C3. The exact *m/z* value, rounded to four decimal places, is reported for the product ion.

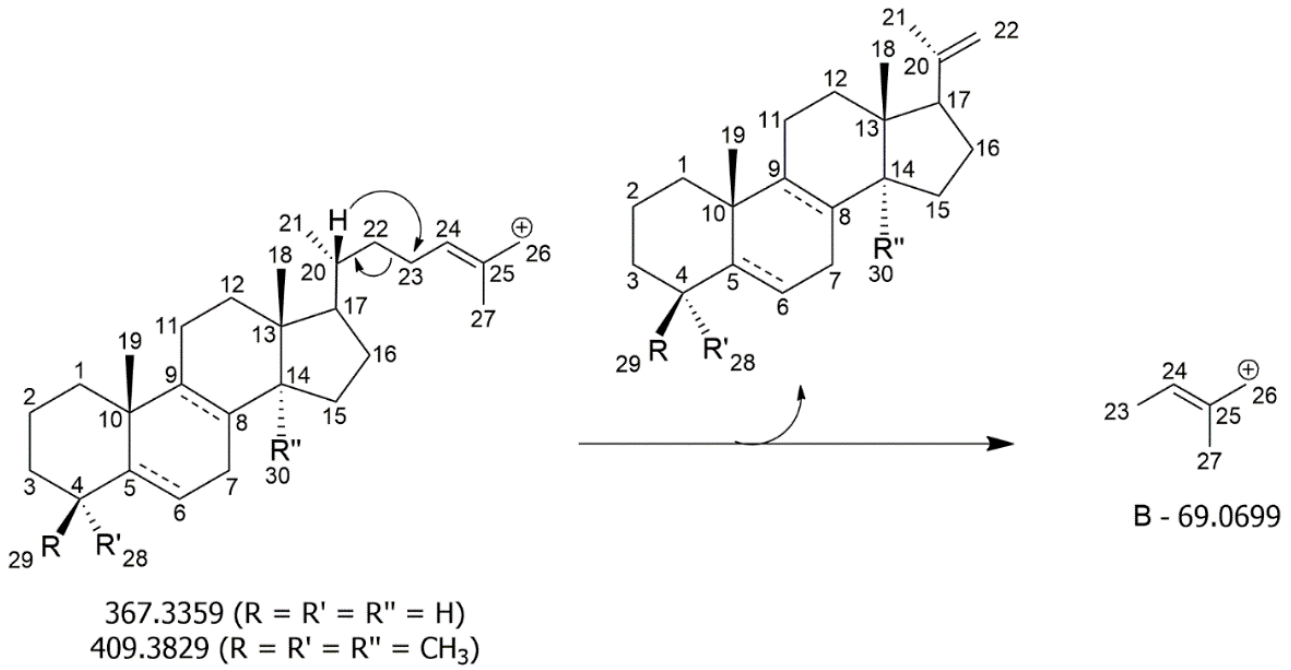


Figure A6. Proposed mechanism for the gas-phase formation of a product ion detected in cluster B in the APCI(+)-HCD-FTMS/MS spectra of the $[M+H-H_2O]^+$ ions of desmosterol and zymosterol (R = R′ = R″ = H; C=C bond at C5–C6 and C8–C9, respectively) and lanosterol (R = R′ = R″ = CH_3; C=C bond at C8–C9). Exact *m/z* ratios are reported to four decimal places.

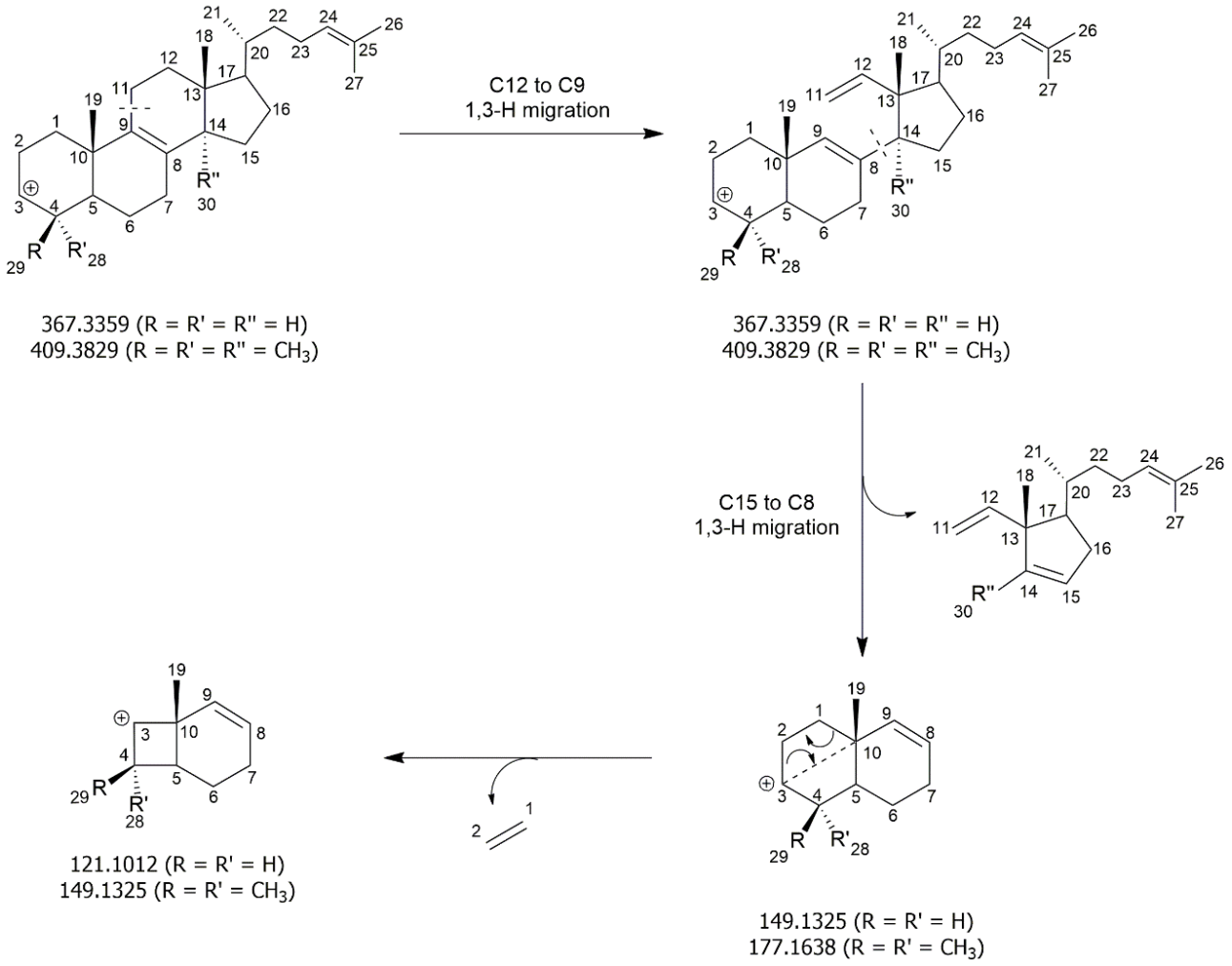


Figure A7. Proposed mechanism for the gas-phase formation of product ions with exact *m/z* values 149.1325/177.1638 and 121.1012/149.1325, corresponding to those observed in the APCI(+)-HCD-FTMS/MS spectra of the $[M+H-H_2O]^+$ ions of zymosterol/lanosterol. Exact *m/z* ratios are reported with four decimal places.

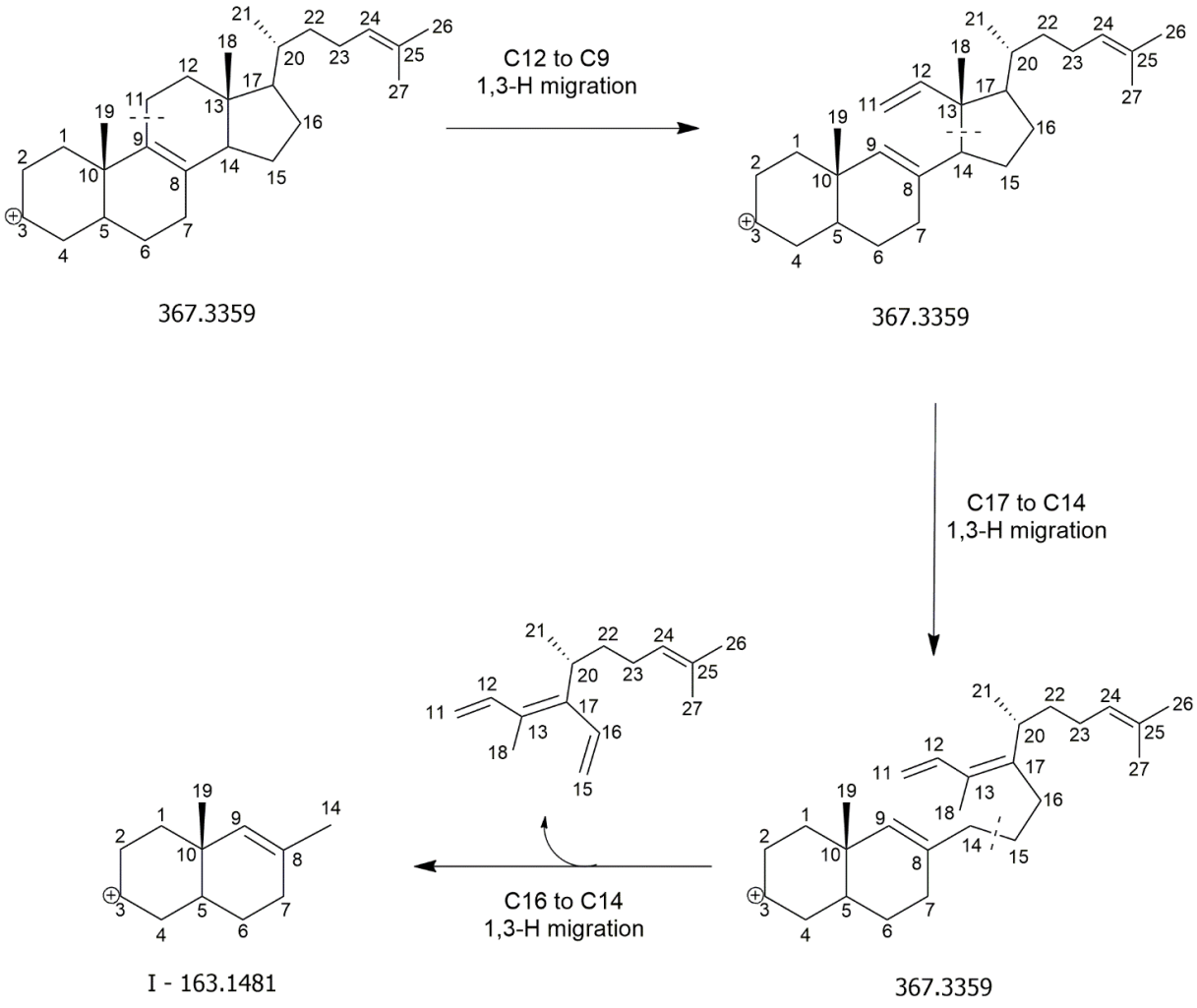


Figure A8. Proposed mechanism for the gas-phase formation of a product ion detected in cluster I in the APCI(+)-HCD-FTMS/MS spectrum of the $[M+H-H_2O]^+$ ion of zymosterol. Exact *m/z* ratios are reported to four decimal places.

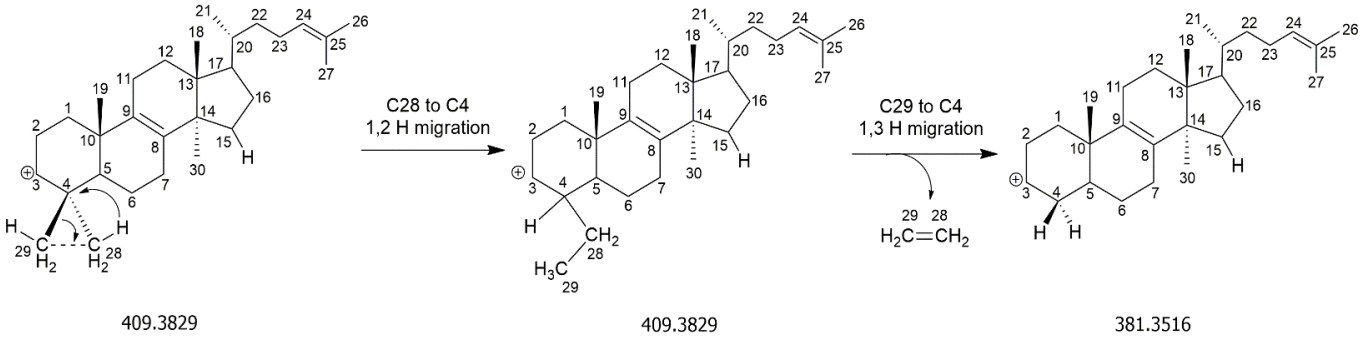


Figure A9. Mechanism tentatively proposed to explain the gas-phase neutral loss of ethylene from the $[M+H-H_2O]^+$ ion of lanosterol, resulting in the replacement of the methyl groups at C4 with hydrogen atoms. Exact *m/z* ratios are reported to four decimal places.

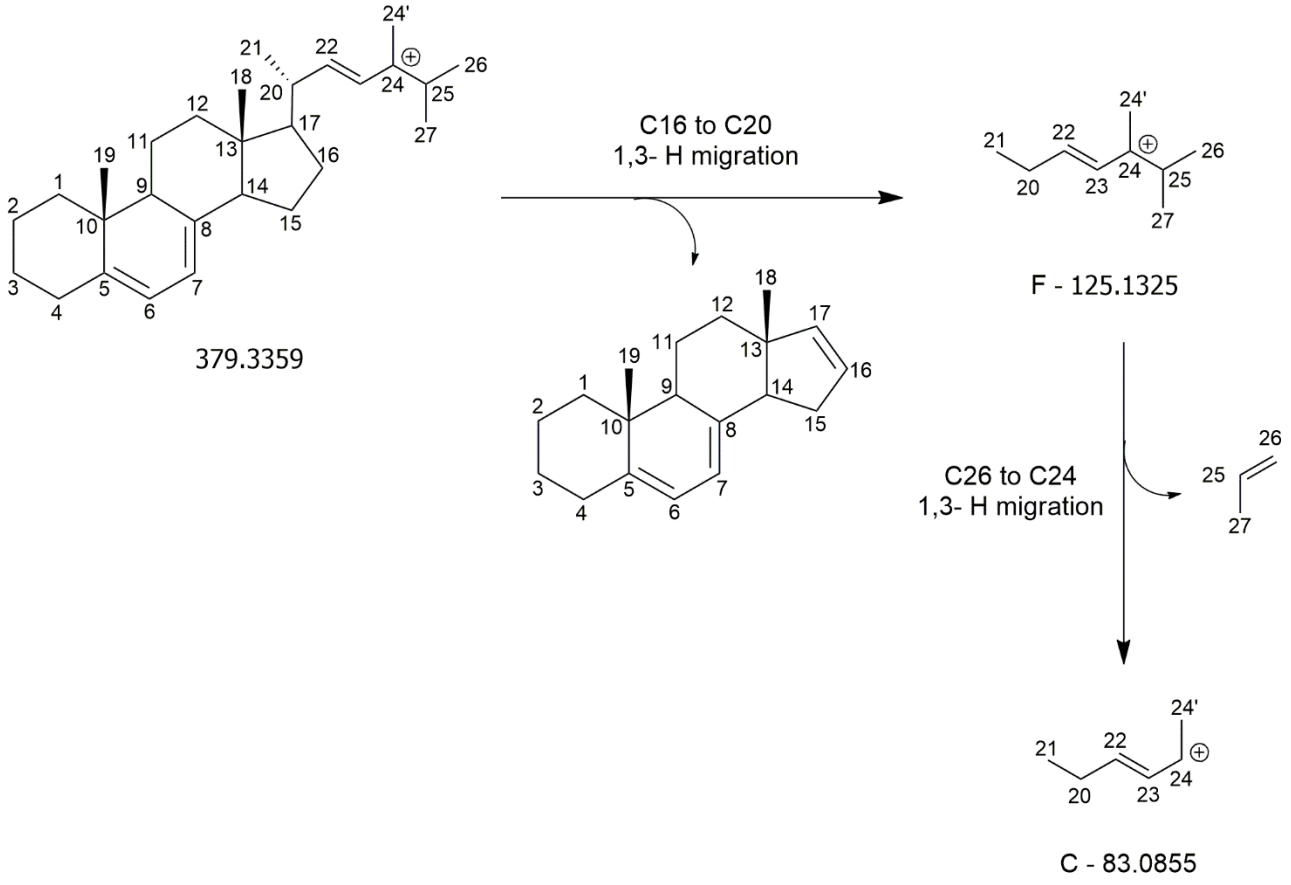


Figure A10. Proposed mechanism for the gas-phase formation of product ions detected in clusters C and F in the APCI-HCD-MS/MS spectrum of the $[M+H-H_2O]^+$ ion of ergosterol. Exact *m/z* ratios are reported to four decimal places.

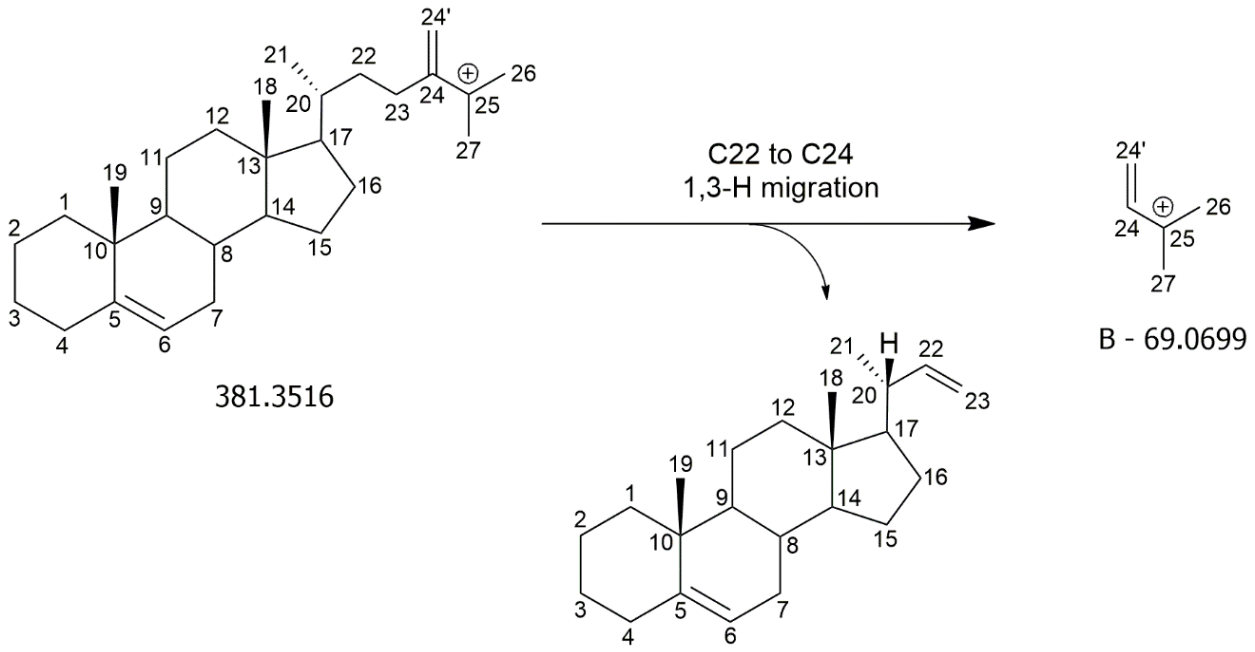


Figure A11. Proposed mechanism for the gas-phase formation of the product ion detected in cluster B in the APCI-HCD-MS/MS spectrum of the $[M+H-H_2O]^+$ ion of chalinasterol. The process involves a 1,3-H transfer from C22 to C24. Exact *m/z* ratios, rounded off to the fourth decimal place, are reported.

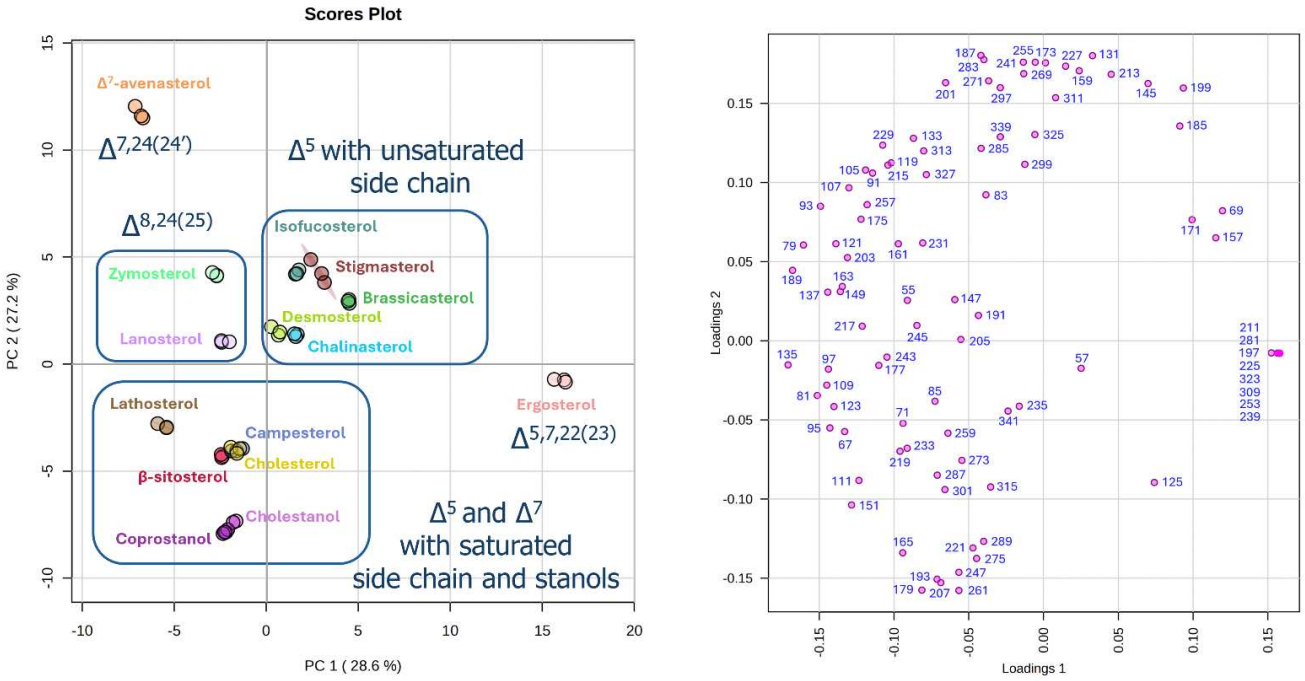


Figure A12. Scores and loading plots obtained from the Principal Component Analysis of relative intensities data referred to product ions detected in APCI(+)-HCD-FTMS/MS spectra of animal/fungal sterols/stanol analyzed in the present study and cholesterol and phytosterols considered in Ref. 49. Each compound was analyzed in triplicate; thus, three symbols are referred to each compound in the scores plot. Major structural characteristics related to groups or single compounds, namely the saturation or unsaturation of the side chain and the occurrence of C=C bonds (D) on the steroidal backbone and on the side chain are evidenced. In the loadings plot each point represents the tip of the vector corresponding to a variable, *i.e.*, to a specific product ion, labelled by its nominal *m/z* ratio.

Table A1. Summary of chromatographic resolution and selectivity values evaluated for couples of close sterol/stanol peaks after the RPLC-APCI(+)-FTMS analysis of their standard mixture performed under isocratic or linear gradient conditions (see chromatograms reported in Figure 2).

Compounds	Isocratic		Linear gradient	
	Resolution	**Selectivity**	**Resolution**	**Selectivity**
Desmosterol - Zymosterol	0.88	1.03	0.00	1.00
Ergosterol - Chalinasterol	0.45	1.02	0.23	1.01
Lathosterol - Cholesterol	0.00	1.00	1.33	1.03
Cholesterol - Lanosterol	1.53	1.06	2.52	1.06
Lanosterol - Coprostanol	3.49	1.13	3.49	1.08
Coprostanol – Cholestanol	5.29	1.19	2.98	1.06

Table A2. Summary of mass spectrometric information concerning product ions detected in the APCI(+)-HCD-FTMS/MS spectra of the $[M+H-H_2O]^+$ ions of sterols/stanols analysed in this chapter. Product ions are grouped by the number of carbon atoms in their structures, within clusters labelled in alphabetical order, according to **Figures 3** and **4**. Experimental *m/z* values, expressed with four decimal places, and the corresponding molecular formulas, assigned as those consistent with the best mass accuracy, are reported along with values of the latter. Relative intensities are reported for each ion and each compound, expressed as mean ± standard deviation, as calculated after three independent acquisitions. The predominant relative intensity within each cluster is indicated in **bold**.

Ion cluster	Molecular formula	Experim. *m/z*	Accuracy [ppm]	Relative Intensity [%]							
				Latho-sterol	Desmo-sterol	Zymo-sterol	Lano-sterol	Chole-stanol	Copro-stanol	Ergo-sterol	Chalina-sterol
A	C_4H_7	55.0551	16	7.8 ± 0.4	1.5 ± 0.4	2.0 ± 0.3	1.9 ± 0.2	1.8 ± 0.2	1.8 ± 0.3	/	3.8 ± 0.2
	C_4H_9	57.0708	16	**14.7 ± 0.6**	**3.8 ± 0.2**	**3.8 ± 0.4**	**5.0 ± 0.2**	**9.4 ± 0.5**	**9.5 ± 0.8**	**14.6 ± 0.6**	**6.8 ± 0.4**
B	C_5H_7	67.0552	15	11.0 ± 0.7	6.8 ± 0.4	10.8 ± 0.4	7.0 ± 0.3	14.5 ± 0.7	14.3 ± 0.6	3.7 ± 0.3	5.8 ± 0.2
	C_5H_9	69.0708	13	**23.7 ± 1.4**	**17.6 ± 1.3**	**31 ± 2**	**25.7 ± 0.6**	**19.6 ± 0.5**	**20 ± 0.4**	**100 ± 0**	**11.5 ± 0.4**
	C_5H_{11}	71.0862	10	17 ± 2	3.7 ± 0.5	3.7 ± 0.3	3.1 ± 0.2	9.4 ± 0.5	9.6 ± 0.4	1.7 ± 0.3	4.8 ± 0.3
C	C_6H_7	79.0550	10	5.8 ± 0.4	2.9 ± 0.1	4.7 ± 0.4	3.2 ± 0.2	3.6 ± 0.6	3.5 ± 0.4	/	2.0 ± 0.1
	C_6H_9	81.0708	11	56.7 ± 1.5	**37 ± 2**	**59.7 ± 1.4**	**42.0 ± 0.6**	**67.4 ± 1.1**	**68.7 ± 1.1**	9.9 ± 0.2	**29.0 ± 1.4**
	C_6H_{11}	83.0861	7	**59 ± 2**	12.0 ± 1.0	24.6 ± 1.1	18.5 ± 0.9	29.0 ± 1.0	30.8 ± 0.9	**29.1 ± 1.2**	17.5 ± 0.3
	C_6H_{13}	85.1020	9	7.5 ± 1.0	/	/	1.5 ± 0.4	4.4 ± 0.4	4.5 ± 0.5	/	2.2 ± 0.3
D	C_7H_7	91.0548	7	4.4 ± 0.9	2.9 ± 0.1	4.9 ± 0.3	1.9 ± 0.1	/	/	/	2.0 ± 0.1
	C_7H_9	93.0706	8	16.5 ± 0.8	10.8 ± 0.2	16.1 ± 0.2	15.8 ± 0.2	9.8 ± 0.4	9.6 ± 0.3	3.1 ± 0.1	7.5 ± 0.7
	C_7H_{11}	95.0863	8	**86.5 ± 1.0**	**44.4 ± 1.3**	**78.5 ± 1.8**	**78.0 ± 1.8**	**100 ± 0**	**100 ± 0**	**9.5 ± 0.4**	**39.0 ± 1.4**
	C_7H_{13}	97.1015	3	34.3 ± 1.2	8.2 ± 0.4	11.7 ± 0.6	14.4 ± 0.7	24.3 ± 0.9	24.9 ± 0.9	2.7 ± 0.3	13.7 ± 0.5
E	C_8H_9	105.0701	2	16.6 ± 1.1	9.1 ± 0.3	13.5 ± 0.7	7.4 ± 0.6	/	/	/	6.6 ± 0.3
	C_8H_{11}	107.0858	3	27.5 ± 1.5	17.4 ± 0.4	32.2 ± 0.9	35.8 ± 0.2	16.4 ± 0.7	16.4 ± 0.9	**6.7 ± 0.3**	13.4 ± 0.4
	C_8H_{13}	109.1017	3	**48.3 ± 0.3**	**44.0 ± 1.5**	**71 ± 2**	**95.2 ± 0.9**	**70 ± 2**	**75 ± 2**	6.1 ± 0.1	**36.0 ± 1.4**
	C_8H_{15}	111.1170	2	23.5 ± 0.7	8.9 ± 0.4	8.7 ± 0.4	9.2 ± 0.7	18.0 ± 1.2	17 ± 2	6.3 ± 1.0	6.9 ± 0.1
F	C_9H_{11}	119.086	4	16.8 ± 0.6	8.7 ± 0.7	15.8 ± 1.1	11.5 ± 0.7	/	/	3.6 ± 0.4	7.3 ± 0.4
	C_9H_{13}	121.1016	3	29.3 ± 1.4	22.2 ± 0.7	**41.7 ± 1.7**	**51.5 ± 0.9**	29.5 ± 1.6	35.0 ± 0.8	5.8 ± 0.3	19.5 ± 0.7

	C_9H_{15}	123.1172	3	**31 ± 2**	**23.6 ± 0.7**	26.8 ± 0.4	47.4 ± 0.7	**43 ± 2**	**43 ± 2**	6.0 ± 0.1	**21.5 ± 0.7**
	C_9H_{17}	125.1328	2	5.2 ± 0.7	1.7 ± 0.3	/	1.9 ± 0.2	5.1 ± 0.9	5.5 ± 1.0	**9.5 ± 0.5**	3.1 ± 0.2
G	$C_{10}H_{11}$	131.0858	2	/	4.2 ± 0.3	4.9 ± 0.4	1.8 ± 0.2	/	/	4.8 ± 0.2	3.2 ± 0.2
	$C_{10}H_{13}$	133.1016	3	20.9 ± 0.2	16.4 ± 0.7	22.4 ± 1.4	14.4 ± 1.3	/	/	**6.8 ± 0.2**	12.5 ± 0.2
	$C_{10}H_{15}$	135.1171	2	**50 ± 3**	**46.3 ± 1.2**	**43 ± 2**	**61.4 ± 1.9**	**55.4 ± 1.0**	**54.7 ± 0.6**	4.1 ± 0.2	**33.5 ± 0.7**
	$C_{10}H_{17}$	137.1327	1	14.8 ± 0.2	21.1 ± 1.0	17.1 ± 0.5	23.3 ± 1.8	21 ± 2	21.3 ± 1.1	/	12.6 ± 0.5
H	$C_{11}H_{11}$	143.0853	-1	/	/	/	/	/	/	3.3 ± 0.3	/
	$C_{11}H_{13}$	145.1009	-2	5.3 ± 0.6	8.3 ± 0.5	9.7 ± 0.5	3.5 ± 0.5	/	/	**17.6 ± 0.4**	7.7 ± 0.4
	$C_{11}H_{15}$	147.117	1	39.2 ± 0.2	**59.6 ± 1.1**	30.8 ± 1.5	26.1 ± 1.3	6.4 ± 0.7	6.4 ± 0.7	7.8 ± 0.3	**51 ± 2**
	$C_{11}H_{17}$	149.1328	2	**69 ± 2**	29.3 ± 1.8	**52 ± 2**	**100 ± 0**	**57 ± 2**	**57 ± 2**	5.0 ± 0.1	23.2 ± 0.3
	$C_{11}H_{19}$	151.1484	2	10.9 ± 0.4	5.3 ± 0.4	6.1 ± 0.1	4.6 ± 0.5	14.2 ± 1.6	14.2 ± 1.3	/	6.4 ± 0.3
I	$C_{12}H_{13}$	157.1014	1	/	/	/	/	/	/	4.2 ± 0.2	/
	$C_{12}H_{15}$	159.1171	2	6.5 ± 0.5	25.0 ± 1.3	12.9 ± 0.5	5.7 ± 0.3	/	/	**20.0 ± 1.2**	23.5 ± 1.2
	$C_{12}H_{17}$	161.1325	2	**75 ± 2**	**57.5 ± 0.9**	37 ± 2	22.4 ± 1.2	6.0 ± 0.1	6.0 ± 0.2	4.7 ± 0.3	**50.0 ± 1.4**
	$C_{12}H_{19}$	163.1484	2	25.7 ± 0.5	16.1 ± 1.4	**45.4 ± 1.7**	**24.9 ± 0.6**	**32.9 ± 1.8**	**35 ± 2**	3.1 ± 0.1	15.7 ± 0.4
	$C_{12}H_{21}$	165.164	1	4.7 ± 0.6	1.8 ± 0.1	1.8 ± 0.4	1.7 ± 0.3	9.7 ± 0.6	10.1 ± 1.0	/	3.0 ± 0.1
J	$C_{13}H_{15}$	171.1169	1	/	/	/	/	/	/	3.2 ± 0.2	/
	$C_{13}H_{17}$	173.1328	2	4.9 ± 0.2	16.2 ± 0.4	11.7 ± 0.4	5.8 ± 0.4	/	/	**5.0 ± 0.1**	15.3 ± 0.5
	$C_{13}H_{19}$	175.1483	1	**43.5 ± 1.3**	**27.1 ± 1.2**	**36.8 ± 1.1**	**13.5 ± 0.8**	6.6 ± 0.7	6.5 ± 0.9	1.9 ± 0.1	**22.6 ± 0.6**
	$C_{13}H_{21}$	177.164	1	8.1 ± 0.4	8.2 ± 0.3	17.6 ± 0.7	10.3 ± 0.3	**21.5 ± 0.7**	**22.0 ± 0.6**	1.8 ± 0.2	10.1 ± 0.2
	$C_{13}H_{23}$	179.1795	1	5.2 ± 0.4	2.1 ± 0.1	1.8 ± 0.3	2.7 ± 0.4	7.2 ± 0.5	7.8 ± 0.7	/	/
K	$C_{14}H_{17}$	185.1321	-2	/	1.9 ± 0.3	/	1.8 ± 0.3	/	/	**4.2 ± 0.3**	/
	$C_{14}H_{19}$	187.1483	1	7.7 ± 0.6	10.2 ± 0.2	13.8 ± 0.3	5.9 ± 0.5	/	/	3.2 ± 0.2	10.7 ± 0.4
	$C_{14}H_{21}$	189.1639	1	**29.6 ± 0.5**	**13.9 ± 0.8**	**26.7 ± 0.5**	16.3 ± 0.7	**16.9 ± 1.8**	**17.1 ± 1.8**	/	**12.9 ± 1.3**
	$C_{14}H_{23}$	191.1796	1	6.1 ± 0.2	5.9 ± 0.3	23 ± 0.4	78.1 ± 1.7	8.3 ± 0.4	8.5 ± 0.4	/	5.8 ± 0.3
	$C_{14}H_{25}$	193.1955	2	7.3 ± 0.3	1.9 ± 0.1	/	/	7.1 ± 0.5	7.6 ± 0.5	/	/
L	$C_{15}H_{17}$	197.1321	-2	/	/	/	/	/	/	2.0 ± 0.1	/
	$C_{15}H_{19}$	199.1483	1	/	4.8 ± 0.4	3.8 ± 0.5	1.8 ± 0.2	/	/	**6.7 ± 0.2**	5.8 ± 0.3
	$C_{15}H_{21}$	201.1639	0	16.7 ± 0.7	11.5 ± 1.1	29.2 ± 0.4	7 ± 0.1	/	/	4.2 ± 0.3	12.5 ± 0.7

	$C_{15}H_{23}$	203.1797	1	**33.7 ± 0.6**	**19.7 ± 0.9**	**41.5 ± 1.5**	**47.8 ± 1.0**	**14.7 ± 0.6**	**16.4 ± 1.7**	/	**20.0 ± 0.5**
	$C_{15}H_{25}$	205.1954	1	12.8 ± 0.5	6.4 ± 0.4	9.1 ± 0.5	45 ± 2	6.9 ± 0.7	6.4 ± 1.2	/	/
	$C_{15}H_{27}$	207.2109	1	7.8 ± 0.4	/	/	/	9.0 ± 0.9	9.9 ± 0.1	/	/
M	$C_{16}H_{19}$	211.1477	-2	/	/	/	/	/	/	2.1 ± 0.1	/
	$C_{16}H_{21}$	213.164	1	/	6.7 ± 0.6	5.8 ± 0.4	1.7 ± 0.3	/	/	**5.0 ± 0.1**	7.4 ± 0.5
	$C_{16}H_{23}$	215.1796	1	**45.9 ± 1.6**	**18.8 ± 1.1**	**41 ± 2**	6.6 ± 0.4	/	/	2.0 ± 0.1	**16.0 ± 0.1**
	$C_{16}H_{25}$	217.1952	0	16.5 ± 1.3	9.4 ± 0.6	17.8 ± 0.7	**32.6 ± 0.6**	**9.9 ± 0.8**	**9.9 ± 0.8**	/	7.3 ± 0.5
	$C_{16}H_{27}$	219.211	1	12.0 ± 0.6	4.1 ± 0.2	/	5.6 ± 0.6	5.6 ± 0.6	5.7 ± 0.6	/	3.9 ± 0.1
	$C_{16}H_{29}$	221.2257	-3	/	/	/	/	1.8 ± 0.2	1.8 ± 0.3	/	/
N	$C_{17}H_{21}$	225.1631	-3	/	/	/	/	/	/	2.2 ± 0.2	/
	$C_{17}H_{23}$	227.1789	-2	/	4.0 ± 0.2	3.9 ± 0.4	/	/	/	**2.7 ± 0.3**	3.3 ± 0.5
	$C_{17}H_{25}$	229.1946	0	**14.8 ± 0.8**	**13.1 ± 1.1**	**16.1 ± 0.3**	6.7 ± 0.3	/	/	/	**11.7 ± 1.0**
	$C_{17}H_{27}$	231.211	1	3.7 ± 0.7	8.1 ± 0.4	9.1 ± 0.5	**8.4 ± 0.8**	**6.3 ± 0.3**	**5.5 ± 0.3**	/	5.9 ± 0.2
	$C_{17}H_{29}$	233.2266	1	6.3 ± 0.8	4.5 ± 0.6	/	/	5.2 ± 0.2	5.4 ± 0.4	/	2.5 ± 0.8
	$C_{17}H_{31}$	235.2421	0	/	/	/	/	/	/	/	/
O	$C_{18}H_{23}$	239.179	-2	/	/	/	/	/	/	**3.8 ± 0.2**	/
	$C_{18}H_{25}$	241.1953	1	/	5.2 ± 0.4	3.8 ± 0.3	3.9 ± 0.2	/	/	1.6 ± 0.3	5.8 ± 0.3
	$C_{18}H_{27}$	243.2102	-2	**21.4 ± 0.6**	**12.3 ± 0.3**	**10.5 ± 1.1**	**12.2 ± 0.2**	/	/	/	**6.7 ± 0.5**
	$C_{18}H_{29}$	245.2258	-2	6.0 ± 0.2	6.0 ± 0.1	**1.9 ± 0.1**	4.3 ± 0.6	4.5 ± 0.5	4.5 ± 0.3	/	6.2 ± 0.2
	$C_{18}H_{31}$	247.2414	-2	5.7 ± 0.6	/	/	/	**7.0 ± 0.1**	**6.5 ± 0.4**	/	3.3 ± 0.5
P	$C_{19}H_{25}$	253.1952	0	/	/	/	/	/	/	**9.8 ± 0.3**	/
	$C_{19}H_{27}$	255.2108	0	2.7 ± 0.5	8.0 ± 0.3	10.1 ± 0.3	3.9 ± 0.2	/	/	1.8 ± 0.2	**9.6 ± 0.5**
	$C_{19}H_{29}$	257.2265	0	**26.0 ± 0.4**	**15.6 ± 1**	**28 ± 1.0**	**11.5 ± 0.7**	/	/	/	9.3 ± 0.4
	$C_{19}H_{31}$	259.2422	1	17.7 ± 1.2	4.1 ± 0.2	/	3.2 ± 0.3	3.6 ± 0.5	3.4 ± 0.4	/	3.0 ± 0.2
	$C_{19}H_{33}$	261.2581	2	1.8 ± 0.4	/	/	/	**10.1 ± 0.6**	**10.2 ± 0.2**	/	/
Q	$C_{20}H_{27}$	267.2102	-2	/	/	/	/	/	/	**1.7 ± 0.3**	/
	$C_{20}H_{29}$	269.2257	-3	/	1.8 ± 0.4	6.9 ± 0.4	2.0 ± 0.2	/	/	/	2.3 ± 0.4
	$C_{20}H_{31}$	271.242	0	/	**7.1 ± 0.2**	**7.8 ± 0.5**	**6.4 ± 0.5**	/	/	/	**8.7 ± 0.4**
	$C_{20}H_{33}$	273.2577	0	**10.7 ± 0.6**	1.5 ± 0.3	**1.7 ± 0.4**	1.9 ± 0.1	2.2 ± 0.2	2.2 ± 0.2	/	3.8 ± 0.4

	$C_{20}H_{35}$	275.2735	1	/	/	/	/	**5.8 ± 1.2**	**5.8 ± 1.2**	/	/
R	$C_{21}H_{29}$	281.226	-1	/	/	/	/	/	/	**1.7 ± 0.1**	/
	$C_{21}H_{31}$	283.2424	1	/	4.5 ± 0.5	9.2 ± 0.5	1.6 ± 0.4	/	/	/	**4.9 ± 0.2**
	$C_{21}H_{33}$	285.2579	1	1.9 ± 0.4	**9.5 ± 0.8**	**26 ± 2**	**4.1 ± 0.2**	/	/	/	4.3 ± 0.4
	$C_{21}H_{35}$	287.2736	1	**24.9 ± 1.9**	/	/	/	2.1 ± 0.1	2.2 ± 0.2	/	/
	$C_{21}H_{37}$	289.2892	1	/	/	/	/	**3.1 ± 0.1**	**3.0 ± 0.2**	/	/
S	$C_{22}H_{31}$	295.2418	-1	/	/	/	/	/	/	**4.2 ± 0.2**	/
	$C_{22}H_{33}$	297.258	1	/	**3.0 ± 0.1**	**5.8 ± 0.4**	3.1 ± 0.2	/	/	/	**8.1 ± 0.1**
	$C_{22}H_{35}$	299.2734	0	/	/	3.2 ± 0.2	**5.5 ± 1.0**	/	/	/	5.9 ± 0.2
	$C_{22}H_{37}$	301.2891	0	**9.7 ± 0.4**	/	/	/	**2.1 ± 0.1**	**2.1 ± 0.1**	/	/
T	$C_{23}H_{33}$	309.2579	1	/	/	/	/	/	/	**4.9 ± 0.1**	/
	$C_{23}H_{35}$	311.2734	0	/	**3.4 ± 0.4**	**12.1 ± 0.5**	**5.7 ± 0.6**	/	/	/	**7.9 ± 0.3**
	$C_{23}H_{37}$	313.289	0	**3.2 ± 0.5**	/	/	1.8 ± 0.1	/	/	/	/
	$C_{23}H_{39}$	315.3047	0	/	/	/	/	**3.1 ± 0.2**	**2.9 ± 0.1**	/	/
U	$C_{24}H_{35}$	323.2727	-2	/	/	/	/	/	/	**1.5 ± 0.3**	/
	$C_{24}H_{37}$	325.2892	1	/	/	/	**3.7 ± 0.2**	/	/	/	**1.9 ± 0.1**
	$C_{24}H_{39}$	327.3047	0	/	/	/	2.1 ± 0.3	/	/	/	/
V	$C_{25}H_{39}$	339.3049	1	/	/	/	2.6 ± 0.5	/	/	/	/
	$C_{25}H_{41}$	341.3205	1	/	/	/	/	/	/	/	/
Precursor ion	$C_{27}H_{43}$	367.3362	1	/	/	**100 ± 0**	/	/	/	/	/
	$C_{27}H_{45}$	369.3519	1	**100 ± 0**	**100 ± 0**	/	/	/	/	/	/
	$C_{27}H_{47}$	371.3672	1	/	/	/	/	**42.7 ± 2.1**	**42.7 ± 2.1**	/	/
	$C_{28}H_{43}$	379.3363	1	/	/	/	/	/	/	**16.2 ± 1.3**	/
	$C2_8H_{45}$	381.3519	1	/	/	/	/	/	/	/	**100 ± 0**
	$C_{30}H_{49}$	409.3832	1	/	/	/	**33.4 ± 1.1**	/	/	/	/

Chapter 3

Comparative quantitative study of free sterols in kale and broccoli raab across growth stages and processing conditions using RPLC-APCI-FTMS

3.1 Introduction

As mentioned in the foreword, innovative edible plant products harvested at early developmental stages, compared with their commonly consumed mature counterparts, have gained increasing attention in the agri-food market. This growing interest arises both from their eco-sustainable cultivation practices and from their frequently higher content of bioactive compounds compared to mature vegetables[1]. Among these products, microgreens, *i.e.*, tender seedlings harvested 7 to 21 days after sowing, once the cotyledonary leaves are expanded and the first true leaves have emerged, have been the major focus of research[2-9]. Microgreens are typically cultivated through soilless systems, such as hydroponics, which minimise water consumption and eliminate the need for agrochemicals, offering a sustainable alternative to conventional agriculture[1-10-12]. Extensive studies have explored various aspects of their production, including nutrient solution management, LED-based light irradiation, and biofortification strategies designed to meet specific nutritional needs[2,13-24]. Similarly, baby leaves, defined by European Regulation 752/2014 as "*young leaves and petioles of any product, harvested up to the stage of the eighth true leaf*"[1], have been investigated as additional sources of nutraceutical compounds, often in comparison with microgreens and mature plants[25-29].

Building on this background, the study described in the present chapter extends the comparative evaluation of the nutraceutical profiles of these innovative vegetal products to include the so-called *micro leaves*, harvested during the developmental stage characterized by the emergence of the first five true leaves. The research focused on kale (*Brassica oleracea* L. var. *acephala*) and broccoli raab (*Brassica rapa* L. subsp. *sylvestris* L. Janch. var. *esculenta* Hort.), both belonging to the *Brassicaceae* family, plants well known for their richness in bioactive compounds such as polyphenols and glucosinolates[30-38].

To further assess their nutraceutical potential, attention was directed toward free sterols (FSs), owing to their recognized biological activity, leading to anti-inflammatory, anticancer, antidiabetic, and anti-

obesity properties, and to the capacity of reducing serum LDL cholesterol levels, thus contributing to the prevention of diseases such as atherosclerosis[39-41].

As discussed in the first chapter, PSs are key structural components of vegetal cells membranes, where they regulate permeability, fluidity, and lipid bilayer integrity, while also participating in essential processes like signal transduction, membrane trafficking, and cell-to-cell communication through plasmodesmata [41-46]. They play crucial roles in plant growth and development by influencing cell division, elongation, and differentiation[43,46,47]. More than 250 PSs have been identified to date[41,48].

As emphasized in **Figure 1**, beside free sterols described previously, phytosterols include further compounds arising from reactions occurring on the hydroxyl group at C3. Indeed, this group can be esterified by a fatty acid to form steryl esters (SEs) or bound through a 1-*O*-β-glycosidic linkage to a hexose, generating steryl glycosides (SGs) or acylated steryl glycosides (ASGs), the latter containing a fatty acyl chain esterifying the hydroxyl group at the C6′ position of the sugar[41,43,49,50]. Given this structural diversity, analytical investigations often target total FSs obtained after basic hydrolysis, which converts SEs and ASGs into the corresponding free forms. In contrast, acid hydrolysis, though capable of breaking glycosidic bonds, thus promoting the conversion of SGs to FSs, is generally avoided because it may induce artifacts such as the generation of isomerization products[51,52].

As mentioned in the first chapter, sterol structural diversity further arises from methylation at the C4 position, leading to three major types: desmethyl-, 4α-methyl-, and 4,4-dimethylsterols[41,50,53], yet, as 4,4-dimethylsterols serve mainly as precursors of demethylated sterols, they are less abundant in plant tissues[54]. FSs are additionally classified as Δ^5-, Δ^7-, $\Delta^{5,7}$-, or Δ^8-sterols, based on the position of double bond(s) within the steroidal B-ring, or as stanols when fully saturated[41,44,50]. As illustrated in **Figure 1** for Δ^5-sterols (so called according to the IUPAC numbering of atoms in steroids[55]), the side chain structure provides additional variability. In particular, β-sitosterol and campesterol, the most abundant FSs in plants, possess a fully saturated side chain branched at C24[39,43,50]. Alkylation at this position, catalysed by sterol methyltransferase (SMT), generates both α- and β-methylated epimers, with a preference for α-ethylated forms[43,46,56,57]. Other common sterols, such as brassicasterol and

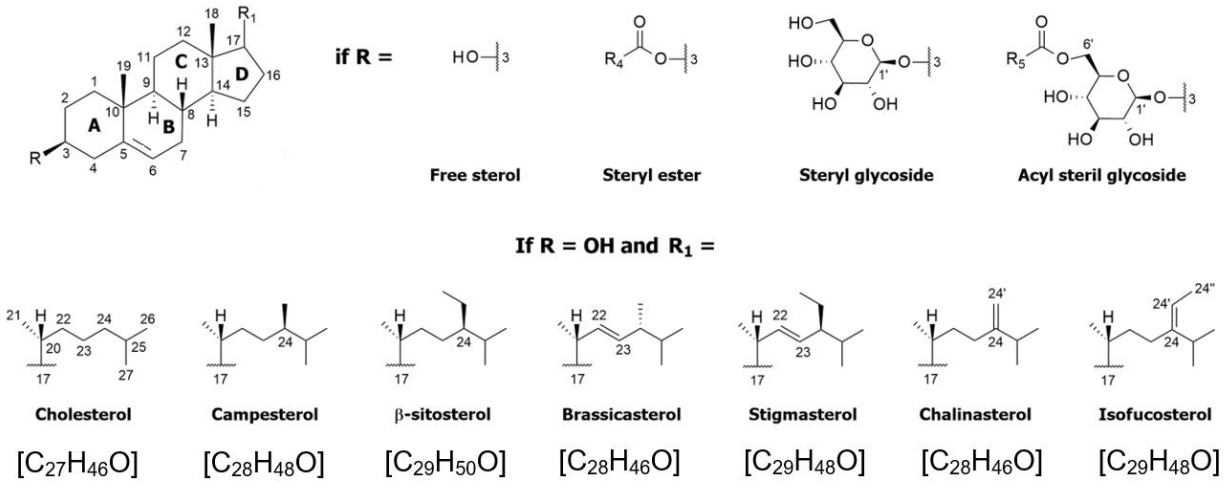


Figure 1. Top left) *trans*-planar tetracyclic structure of Δ^5-sterols, numbered according to IUPAC nomenclature[55]. Top right) general structures of the R group linked to C3, determining sterols classification as free sterols (FSs), steryl esters (SEs), steryl glycosides (SGs) and acyl steryl glycosides (ASGs). Bottom) side chains, indicated as R_1, of the most relevant plant FSs and of cholesterol.

stigmasterol, include a C=C double bond between C22 and C23[41,43], whereas chalinasterol and isofucosterol are their respective positional isomers (**Figure 1**). The Δ^7 isomer of isofucosterol, known as Δ^7-avenasterol, is also found in plants, although it is not represented in **Figure 1**. Several studies have investigated FSs in mature Brassica vegetables[58-65]; however, to date, only one report has specifically addressed their characterization in microgreens, using gas chromatography–tandem mass spectrometry (GC–MS/MS)[66]. Consequently, the RPLC-APCI-FTMS method described in the first chapter and in Ref. 67 was validated and systematically applied to the quantification of typical plant free sterols, along with cholesterol and its Δ^7 analogue, lathosterol, in microgreens, micro leaves, baby leaves, and mature forms of kale and broccoli raab. Additional sterols, potentially corresponding to previously unreported isomers, were also observed in some samples at very low concentrations and tentatively identified through the evaluation of their chromatographic behaviour and MS/MS spectral pattern. Finally, the influence on sterol content of cultivation season for microgreens and micro leaves, and of cooking procedures (steaming and boiling) for mature forms was evaluated.

3.2 Materials and methods

3.2.1 Chemicals. LC-MS grade acetonitrile (ACN), water (H_2O) and formic acid (FA), employed for mobile phase preparation, HPLC grade chloroform ($CHCl_3$) and ethanol (EtOH), used as solvents for stock solutions, HPLC grade methanol (MeOH), hexane, sodium hydroxide (NaOH), orthophosphoric acid (H_3PO_4) (85% w/w) and sodium chloride (NaCl) used for sterol extraction from *Brassica* vegetables, were purchased from Merck (Milan, Italy). Standards of cholesterol-d6 (cholest-5-en-26,26,26,27,27,27-d_6-3β-ol), cholesterol (cholest-5-en-3β-ol), campesterol (campest-5-en-3β-ol), β-sitosterol (stigmast-5-en-3β-ol), brassicasterol (ergosta-5,22E-dien-3β-ol), stigmasterol (stigmasta-5,22E-dien-3β-ol), isofucosterol (24Z-ethylidene-cholest-5-en-3β-ol) and Δ^7-avenasterol (24Z-ethylidene-cholest-7-en-3β-ol) were acquired from Cayman Chemical (Ann Arbor, MI, USA). Standards of lathosterol (cholest-7-en-3β-ol) and chalinasterol (24-methylene-cholest-5-en-3β-ol) were purchased from Merck (Milan, Italy). Specific solutions for the calibration of mass spectrometer under positive or negative polarity conditions were bought from Thermo Scientific (Waltham, MA, USA).

3.2.2 Plant samples production. Two cultivation cycles were conducted to produce microgreens, micro leaves and baby leaves using a hydroponic system in a greenhouse located at the University of Bari Aldo Moro (41°06' N, 16°52' E; Southern Italy). The first cultivation cycle was conducted from January 9 to March 9, 2023 (winter cycle), the second one from March 21 to May 9, 2023 (spring cycle). Two different genotypes of Brassicaceae were grown for both experiments: *Brassica rapa* L. subsp. *sylvestris* L. Janch. var. *esculenta* Hort, local variety 'Cima di rapa novantina' (broccoli raab); *Brassica oleracea* L. var. *acephala*, local variety 'Cavolo riccio' (kale). High quality seeds, with 95% germination at a constant temperature of 20 °C, were adopted. Details on microgreens, micro leaves and baby leaves cultivation are reported in **Section A1** of Appendix 3.

The same genotypes of kale and broccoli raab were also grown in an open field in Valenzano

(geographical co-ordinates: 41°03′N 16°53′E), in the period from January to March 2023 (winter cycle) to obtain their mature counterparts. In this case, plants were also subjected to cooking by either steaming or boiling. Details on cultivation and cooking procedures are reported in **Section A2** of Appendix 3.

3.2.3 Sample preparation. Upon collection at the appropriate growth stages, all plant samples were immediately frozen at -20 °C. After four days, the samples were freeze-dried in a ScanVac CoolSafe 55-9 Pro freeze dryer (LaboGene ApS, Lynge, Denmark) for five days, and the resulting material was stored at -18 °C, until FSs extraction and analysis. It should be noted that, before being stored in the freezer, the dehydrated material corresponding to about six hundred microgreens, ten micro leaves, five baby leaves and three mature plants of both kale and broccoli raab was hand-ground and then pooled based on sample type. Prior to freezer storage, the dehydrated material from approximately 600 microgreens, 10 micro leaves, 5 baby leaves, and 3 mature plants of both kale and broccoli raab was manually ground and pooled according to sample type. The pooled material, comprising stems, leaves, and inflorescences (in the case of mature vegetables), was transferred to individual Falcon tubes for each sample type.

3.2.4 Sample extraction. Total FSs were extracted from freeze-dried microgreens, micro leaves, baby leaves, and mature forms of kale and broccoli raab following the protocol reported by Castellaneta *et al.*[66], after some modifications. Specifically, the freeze-dried plant samples were further crushed with a mortar, then 50 mg of powder were weighed and 1 mL of MeOH was added; the resulting suspension was sonicated in a water bath for 15 min at 30 °C. To release FSs from sterol SEs and ASGs, basic hydrolysis was performed by adding 2.5 mL of a solution of NaOH in MeOH (1 M) and incubating for 30 min at 60 °C. After cooling to room temperature, the excess base was neutralized by adding 3.5 mL of NaCl in H_2O (1 M) and 200 µL of aqueous H_3PO_4 solution (50% v/v). The extraction of total FSs, comprising both the ones originally present in the sample and those released through

saponification, was then carried out by adding 3.75 mL of hexane and centrifuging the mixture at 5000 rpm for 10 min. After complete phase separation, the supernatant was collected, and the extraction was repeated twice to ensure maximum recovery of FSs. The combined supernatants were then dried under a gentle stream of nitrogen at room temperature. The dry residue was reconstituted in 500 µL of a MeOH/$CHCl_3$ solution (2:1 v/v). Prior to RPLC-APCI(+)-FTMS analysis, the extract was diluted 1:5 (v/v) with ACN and cholesterol-d_6 was added as internal standard at a 10 µg/mL concentration.

3.2.5 Standard solutions for calibrations. Stock solutions of each standard (1 mg/mL) were prepared in an EtOH:$CHCl_3$ solution (2:1 v/v). Calibration curves were constructed for β-sitosterol, campesterol, brassicasterol, chalinasterol, isofucosterol, Δ^7-avenasterol, stigmasterol, cholesterol and lathosterol to quantify FSs in plant samples. Six calibration levels were prepared for each sterol by appropriate dilution in ACN, with values depending on the concentrations expected in real samples: 0.1, 1, 5, 25, 50 and 100 mg/mL for β-sitosterol; 0.1, 1, 5, 15, 25, and 50 mg/mL for campesterol; 0.01, 0.1, 0.5, 1, 5 and 10 mg/mL for brassicasterol, chalinasterol, isofucosterol and Δ^7-avenasterol; 0.001, 0.01, 0.05, 0.1, 1, 5 mg/mL for stigmasterol, cholesterol and lathosterol.

3.2.6 LC-MS instrumentation and operating conditions. Calibration solutions and plant samples extracts were analysed using an Ultimate 3000 HPLC system coupled with a Q Exactive high-resolution quadrupole-Orbitrap mass spectrometer through an APCI interface (Thermo Fisher, West Palm Beach, CA, USA). FSs separation was achieved using a C18 Ascentis Express HPLC column (150 × 2.1mm i.d., 2.7µm particle size) (Supelco, Bellefonte, PA) and the following multistep binary elution gradient, based on H_2O as phase A and ACN as phase B, both containing 0.1% (v/v) FA: 0-40 min, linear increase of B from 90% to 100%; 40-50 min, isocratic at 100% B; 50-52 min, linear decrease of B from 100% to 90%; 52−60 min, reconditioning at 90% B. Flow rate was set at 0.250 mL/min and column temperature was kept at 30°C; 5 µL sample volumes were injected. The

parameters of the APCI interface and of the ion optics of the Q Exactive spectrometer were set as follows: sheath gas flow rate) 40 a.u.; auxiliary gas flow rate) 10 a.u.; sweep gas flow rate) 5 a.u.; discharge current) 5μA; capillary temperature) 250 °C; S-lens RF Level) 55 a.u.; vaporizer temperature) 300°C. Full MS acquisitions in positive ion mode were performed in a 250-500 *m/z* interval at the maximum resolving power of the mass spectrometer (140000 at *m/z* 200); the Automatic Gain Control (AGC) level for the orbital trap filling was set at 1×10^6 and the maximum injection time was 100 ms. HCD-FTMS/MS acquisitions were performed at a 35000 resolving power in a 50−500 *m/z* interval, using a normalized collisional energy (NCE) of 30 units, and selecting a 1.0 *m/z* isolation window for precursor ions; the AGC level was set at 2×10^5 and the maximum injection time was 100 ms. The spectrometer was calibrated every two days by infusing, at a 30 μL/min flow rate, calibration solutions for positive or negative polarity acquisitions, thus obtaining a mass accuracy always better than 5 ppm.

3.3 Results and discussion

3.3.1 Identification of sterols by RPLC-APCI(+)-FTMS and FTMS/MS analysis. The developed RPLC-APCI(+)-FTMS method provided a comprehensive profile of FSs for all the vegetal products of interest. As an example, single or multiple Extracted Ion Current (EIC) chromatograms corresponding to monoisotopic *m/z* values of FS $[M+H–H_2O]^+$ ions detected in the kale microgreens extract are reported in **Figure 2**, with labels indicating either sterols recognized through comparison with standards or the respective steryl glycosides (SG).

In this case, lathosterol was successfully separated from cholesterol (**Figure 2A**), in accordance with the previously demonstrated ability of the developed RPLC gradient to resolve Δ^7 from Δ^5 sterols[67,68]. Although more characteristic of animal cells, the presence of lathosterol and cholesterol is not unexpected, as these sterols have been previously detected in mature *Brassica* vegetables as well as

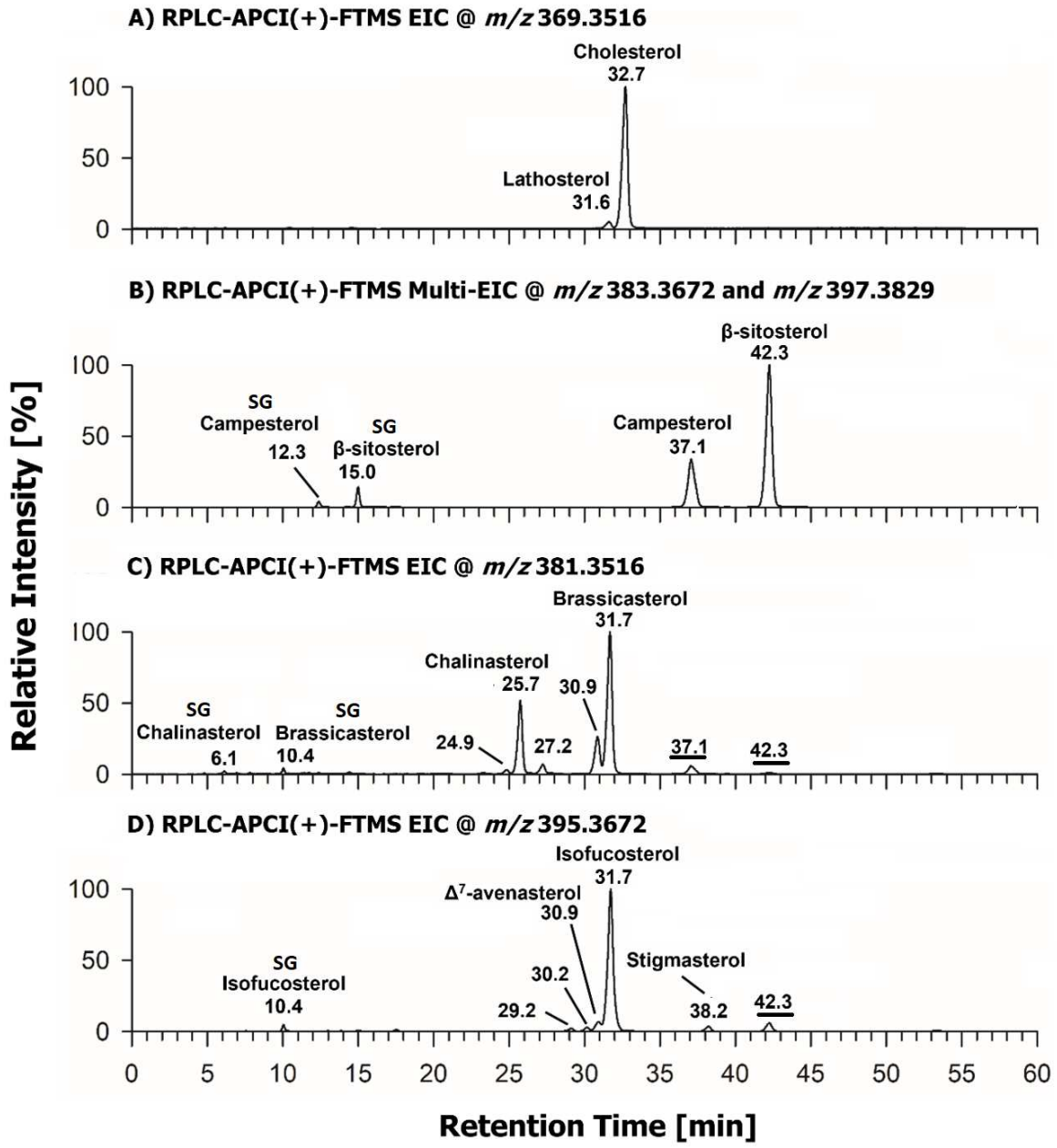


Figure 2. Extracted ion current (EIC) chromatograms referring to monoisotopic *m/z* values for $[M+H-H_2O]^+$ ions of sterols identified in a kale microgreen extract: A) 369.3516 - lathosterol and cholesterol B) 383.3672 and 397.3829 – campesterol and β-sitosterol, respectively C) 381.3516 - chalinasterol and brassicasterol D) 395.3672 - Δ^7-avenasterol, isofucosterol (Δ^5-avenasterol) and stigmasterol. Labelled peaks correspond to FSs identified using authentic standards; peaks at earlier retention times correspond to the related SGs. Underlined retention times (campesterol, 37.1 min; β-sitosterol, 42.3 min) indicate peaks arising from in-source fragmentation of the respective major sterol molecular ions. Non-underlined retention times correspond to sterols tentatively identified based on combined chromatographic and mass spectrometric data (see text for details).

in kale and broccoli raab microgreens[64,66]; moreover, cholesterol typically represents about 1% of the total PSs content[44,69]. Besides those of campesterol and β-sitosterol, two further peaks were observed,

at 12.3 and 15.0 min, in the multi-EIC trace corresponding to $[M+H–H_2O]^+$ ions with exact *m/z* values 383.3672 and 397.3829 (**Figure 2B**). They could be related to the corresponding SGs, that were co-extracted with their free counterparts but eluting earlier due to the presence of the polar sugar moiety, that reduces the interaction with the C18 stationary phase. The SG protonated forms underwent the neutral loss of the sugar moiety during the APCI process, thus yielding the same ions observed for free sterols, as confirmed also by their HCD-MS/MS spectra (data not shown). Chalinasterol and brassicasterol were readily recognized in the EIC chromatogram obtained for *m/z* 381.3516, while peaks eluting at 6.1 and 10.4 min corresponded to the respective SGs (**Figure 2C**). Additional weak chromatographic peaks detected after 37.1 and 42.3 min were found to correspond to product ions resulting from the $[M+H–H_2O]^+$ ions of campesterol and b-sitosterol upon APCI-induced neutral losses of H_2 and CH_4, respectively. Finally, peaks corresponding to isomeric Δ^7-avenasterol and isofucosterol (also known as Δ^5-avenasterol) as well as the very weak peak related to stigmasterol were readily recognized in the EIC trace obtained for *m/z* 395.3672 (**Figure 2D**). The peak detected at 10.4 min in this chromatogram corresponded to the SG of isofucosterol, as demonstrated by the HCD-MS/MS spectrum of the corresponding standard. Notably, a perfect alignment was observed for peaks related to brassicasterol and isofucosterol SGs, by analogy with their free forms. The last peak in plot D, eluted after 42.3 min, was actually related to the product ion resulting from the $[M+H–H_2O]^+$ ion of β-sitosterol upon H_2 loss in the APCI source.

The detection of additional peaks in the EIC chromatograms corresponding to *m/z* values 381.3516 (24.9, 27.2 and 30.9 min) and 395.3672 (29.2 and 30.2 min) suggested the presence of additional sterols. The identification of these compounds was attempted by integrating chromatographic and mass spectrometric data with information available on sterols in the dedicated section of the LipidMaps database (www.lipidmaps.org).

The investigations on phytosterols and animal/fungal sterols described in the first two chapters of this thesis and in Refs 67 and 68 demonstrated the existence of several diagnostic correlations between relative intensities of product ions detected in HCD-MS/MS spectra and important structural features,

including the number and position of double bonds on the B ring and the characteristics (unsaturation, branching) of the side chain. APCI-HCD-MS/MS spectra were therefore carefully averaged under peaks detected in the EIC chromatograms of **Figure 2** that could not be identified through comparison with major sterol standards; the resulting spectra are presented in **Figure 3**. By analogy with the approach adopted in the first two chpaters, signals of ions sharing the same number of carbon atoms and differing only in hydrogen content were grouped within a single cluster, designated by a capital letter.

The species corresponding to an exact *m/z* 381.3516 and eluting after 24.9 min exhibited a 0.8 min shift towards lower retention times compared to chalinasterol. By analogy with the chromatographic behaviour of sterol pairs lathosterol/cholesterol and D^7-avenasterol/isofucosterol, this feature suggested that it might correspond to the Δ^7 analogue of chalinasterol. This hypothesis was supported by the corresponding HCD-MS/MS spectrum (**Figure 3A**). Indeed, the high intensity observed in the respective clusters for product ions detected at *m/z* 69.0708 (cluster B), 149.1323 (cluster H), 161.1321 (cluster I) and 297.2568 (cluster S) was consistent with the typical fragmentative behaviour of D^7-sterols[67,68,70]. Moreover, the intensity profiles of clusters J-R and T-U, which are diagnostic for the position of the C=C double bond on the side chain[67,68], matched those found in the HCD-MS/MS spectrum of chalinasterol[68], thereby confirming its location between C24 and C24'. Notably, a D^7 analogue of chalinasterol, known as episterol (24-methylene-cholest-7-en-3β-ol), emerged from the search in the LipidMaps database.

The HCD-MS/MS spectrum obtained for the sterol generating an *m/z* 381.3516 ion in the APCI source and eluting after 27.2 min (**Figure 2C**) is shown in **Figure 3B**. Considering the effect of the side chain C=C bond on the retention on the C18 stationary phase, evidenced before in this thesis for sterols, the elution of this sterol between chalinasterol and brassicasterol, which include a C=C bond between C24 and C24' and between C22 and C23, respectively, suggested the presence of a C=C bond between C23 and C24. The structure of 24-methylcholesta-5,23E-dien-3β-ol, reported in the LipidMaps database, is consistent with this hypothesis. The relevant intensity of product ions at

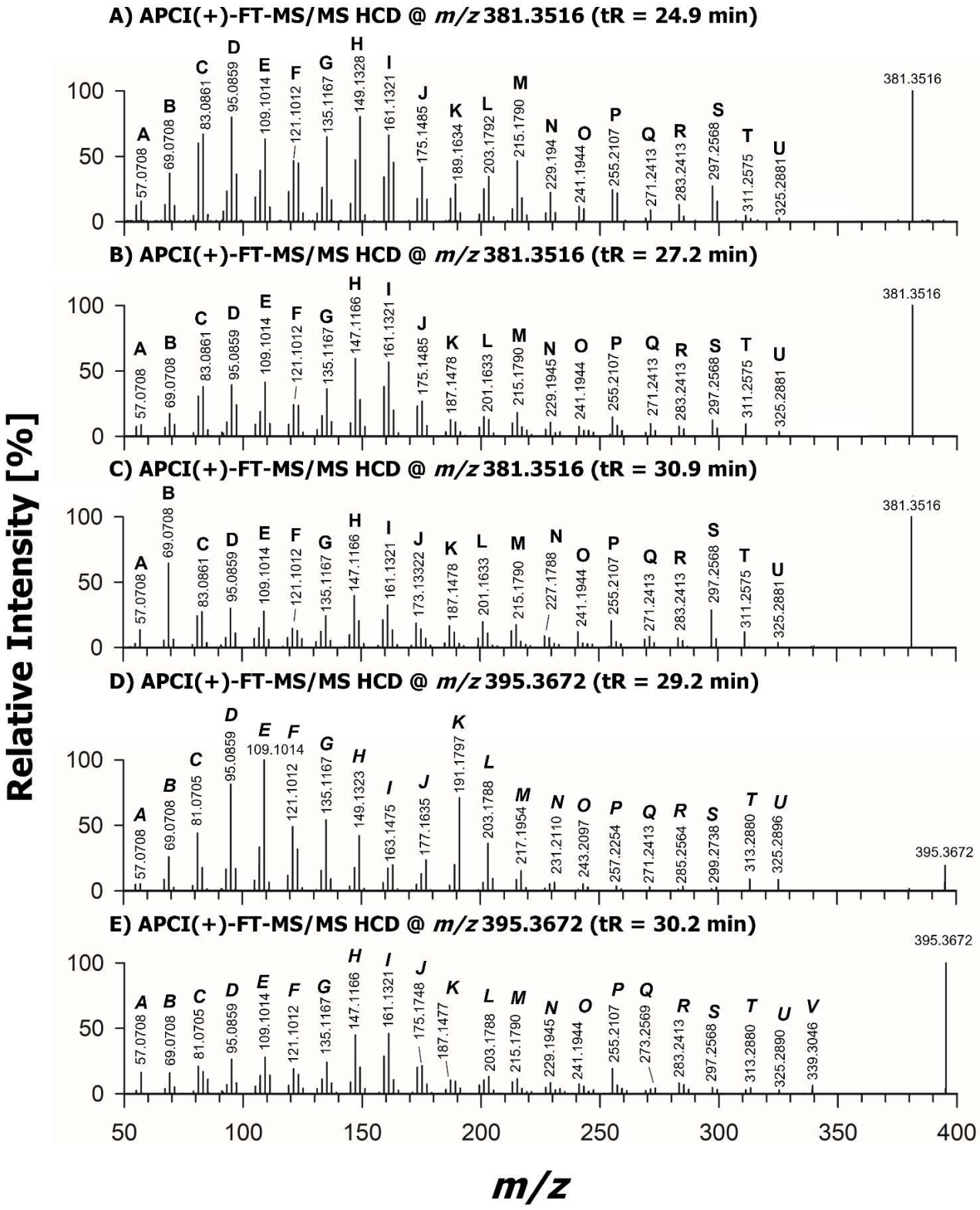


Figure 3. APCI(+)-HCD-FTMS/MS spectra acquired for the $[M+H-H_2O]^+$ ions of sterols whose peaks were detected at specific retention times in the EIC traces referred to exact *m/z* values 381.3516 (plots A, B and C) and 395.3672 (plots D and E) upon RPLC-APCI-FTMS analysis of a kale microgreens extract (see **Figure 2**). Peak signals of product ions sharing the same number of carbon atoms but differing in hydrogen atom count were grouped into clusters, each identified by a capital letter. The experimental m/z value of the most intense signal within each cluster is reported.

m/z 147.1166 and 161.1321 in the respective clusters (H and I) of the HCD-MS/MS spectrum (**Figure 3B**) supported the presence of a C=C bond between C5 and C6 on ring B[67,68]. Additionally, the slight predominance of the *m/z* 83.0861 ion over the one at *m/z* 81.0705 in cluster C was consistent with the occurrence of a fragmentation pathway ultimately leading to an allylic carbocation (exact *m/z* 83.0855) and favoured by the presence of a C=C bond between C23 and C24, as depicted in **Figure A1** of Appendix 3.

The last chromatographic peak observed in the EIC trace for *m/z* 381.3516 and not identifiable through comparison with standards was eluted after 30.9 min, *i.e.*, close to that of brassicasterol (**Figure 2C**). This behaviour suggested a strong structural similarity with the latter at the level of side chain; thus, the sterol was tentatively identified as the α epimer of brassicasterol, which is listed in the LipidMaps database as campesta-5,22E-dien-3β-ol, also known as 24-epibrassicasterol or crinosterol. The hypothesis was confirmed by the remarkable similarity observed between the HCD-MS/MS spectrum of the unknown sterol (**Figure 3C**) and that obtained for brassicasterol (see **Figure 4** in Chapter 1). Notably, nearly identical HCD-MS/MS spectra were obtained also for the epimeric stanols cholestanol and coprostanol. Furthermore, previous studies indicated that α epimers of sterols are eluted before the corresponding β epimers on a C18 stationary phase[71–73].

Turning to the EIC chromatogram obtained for *m/z* 395.3672 (**Figure 2D**), two peaks not corresponding to any of the available sterol standards were considered for a tentative identification. The peak eluting at 29.2 min exhibited the HCD-MS/MS spectrum shown in **Figure 3D**. Diagnostic ions identified for 4,4-dimethyl-Δ^8-sterols considering lanosterol as a model (see Chapter 2), such as those prevailing in clusters H, I, K, M and N, at *m/z* 149.1323, 163.1475, 191.1797, 217.1954 and 231.2110, respectively, were clearly detected. In contrast to lanosterol, no peak signal at *m/z* 339.3052 (*i.e.*, in cluster V), which would correspond to the carbocation of a Δ_8 steroidal backbone methylated twice on C4 and once on C14, was observed for the unknown sterol. Regarding the side chain of the unknown sterol, product ions prevailing in clusters J-S indicated the presence of a C=C bond between

C24 and C25, based on previously described fragmentation trends. By combining the information retrieved from the HCD-MS/MS spectrum with a search on the LipidMaps database, based on the *m/z* value found of its $[M+H-H_2O]^+$ ion, the sterol eluting at 29.2 min was tentatively identified as 14-demethyl-lanosterol, also known as 4,4-dimethylzymosterol or 4,4-dimethyl-5α-cholesta-8,24-dien-3β-ol. This assignment was also supported chromatographically: comparison with retention times previously observed under identical conditions for zymosterol and lanosterol indicated that 14-demethyl-lanosterol is eluted between these sterols. This finding reflects the retention order Δ^8-sterol < 4,4-dimethyl-Δ^8-sterol < 4,4,14-trimethyl-Δ^8-sterol, which is consistent with the increased hydrophobicity resulting from additional methylations on the steroidal backbone.

The final unidentified peak in the EIC chromatogram for *m/z* 395.3672 was eluted at 30.2 min (**Figure 2D**). The corresponding HCD-MS/MS spectrum (**Figure 3E**) exhibited prevailing product ions in clusters H and I at *m/z* 147.1166 and 161.1321, respectively, a feature previously recognized for Δ^5-sterols (see Chapters 1 and 2 and Refs 67-70). A key for identifying the side chain was provided by the prevailing ion in cluster T, at *m/z* 313.2880. This feature was not consistent with the side chain structure of stigmasterol and isofucosterol, including an ethyl moiety linked to C24 and a C=C bond (in the former case located within that moiety), although the *m/z* value of the precursor ion and the detection of prevailing product ions at *m/z* 325.2890 and 339.3046 in clusters U and V, respectively, were consistent with them. $\Delta^{5,24}$-stigmastadienol, which includes an ethyl moiety at C24 and a C=C bond between C24 and C25 was therefore considered as a possible assignment for the unknown sterol. This hypothesis was confirmed by the clear predominance of the *m/z* 255.2107 ion in cluster P (**Figure 3E**), a feature differing from those previously found for other sterols in this cluster. As illustrated in **Figure A2**, the concurrent presence of an ethyl moiety at C24 and a C=C bond between C24 and C25 can facilitate a specific fragmentation pathway leading to a product ion with exact *m/z* 255.2107, involving a 1,5 H-transfer from C16 to C23.

As a general comment on the sterols identified in kale microgreens, it is worth noting that chalinasterol has been previously detected in vegetal matrices only in *Cucurbitaceae* plants[74–76] and,

to the best of our knowledge, episterol and 24-epibrassicasterol, sterols found in fungi and algae respectively[77,78], have never been identified in vegetables. Similarly, while 14-demethyl-lanosterol is a free sterol typically found in fungi[79], $\Delta^{5,24}$-stigmastadienol has been identified so far only in plants belonging to *Graminaceae*[80], *Fabaceae*[81] and *Solanaceae*[82] families, but never in *Brassicaceae*. Therefore, the RPLC-APCI-FTMS/MS approach adopted during this thesis work enabled to extend the knowledge on the sterol profile of these plants. As discussed in the following sections, similar profiles were observed among the different products of kale and broccoli raab on a qualitative level. However, interesting differences were observed from a quantitative point of view.

3.3.2 Quantification of sterols: method development and validation. As a first step towards the quantification of sterols in vegetal products, six-levels external calibration was performed on the set of sterol standards considered in the present study. The analytical response was obtained from the EIC peak areas, normalized by the peak area of the internal standard (cholesterol-d_6). As evidenced in **Table 1**, response linearity in the explored concentration ranges was consistently excellent and the limits of detection (LOD) and quantification (LOQ), calculated as 3 and 10 times the s/b ratio, respectively, where s is the standard deviation of intercept and b is the slope of calibration line[83], ranged between 0.03 and 2 μg/mL (LOD) and between 0.11 and 7 μg/mL (LOQ).

The matrix effect was subsequently evaluated by the standard addition method, since no blank matrix was available. Each standard sterol was added to extracts of microgreens, micro leaves, baby leaves and mature forms of both kale and broccoli raab to reach the third and the sixth calibration level. Three spiking replicates were considered in each case, and the matrix effect was calculated according to this equation:

$$\frac{normalized\ peak\ area_{level\ 6\ (or\ 3)\ matrix} - normalized\ peak\ area_{level\ 0\ matrix}}{normalized\ peak\ area_{level\ 6\ (or\ 3)\ solvent}}$$

Table 1. Summary data concerning external calibration of standard sterols: concentration range, calibration line equation and coefficient of determination (R^2). The LOD and LOQ values (µg/mL) were determined as 3 and 10 times the ratio of the calibration intercept standard deviation to the slope, respectively.

Compound	Explored range (µg/mL)	Calibration line	R^2	LOD (µg/mL)	LOQ (µg/mL)
β-sitosterol	0.1-100	y = 0.0466x + 0.0321	0.9991	2	7
Campesterol	0.1-50	y = 0.1378x - 0.0757	0.9992	1.2	4
Brassicasterol	0.01-10	y = 0.0564x + 0.0021	0.9997	0.11	0.4
Chalinasterol	0.01-10	y = 0.0855x - 0.0031	0.9999	0.08	0.3
Isofucosterol	0.01-10	y = 0.1272x + 0.0082	0.9995	0.15	0.5
Δ^7-avenasterol	0.01-10	y = 0.0577x + 0.0015	0.9999	0.08	0.3
Stigmasterol	0.001-5	y = 0.4153x + 0.0067	0.9994	0.04	0.14
Cholesterol	0.001-5	y = 0.0972x + 0.0041	0.9994	0.08	0.3
Lathosterol	0.001-5	y = 0.0901x - 0.0002	0.9999	0.03	0.11

Here, the normalized peak area referred to level 0 in the matrix correspond to the response obtained for the non-spiked extract, reflecting the sterol originally present in the sample. Values between 90 and 110% were obtained for all sterols, indicating negligible matrix effects were in all the matrices of interest. Consequently, external calibrations curves could be reliably employed for sterol quantifications in real samples.

For the five sterols described in the previous section for which standards were unavailable, quantification was based on calibration lines of structurally similar sterols eluting at comparable retention times, thus under similar mobile phase conditions, assuming comparable ionization efficiencies and sensitivities. Specifically, episterol and 24-methylcholesta-5,23-dien-3β-ol were quantified using the chalinasterol calibration line; brassicasterol's calibration was used for 24-epi-brassicasterol, and 14-demethyl-lanosterol and $\Delta^{5,24}$-stigmastadienol were quantified using that of isofucosterol.

The recovery of sterols from the vegetal matrices was estimated in triplicate using kale microgreens as a model matrix. Three successive extraction steps were performed in each case, with the resulting supernatants collected and evaporated under nitrogen flow, and the resulting residues dissolved into 500 µL of a MeOH/$CHCl_3$ solution (2:1 v/v). Before RPLC-APCI(+)-FTMS analysis, the solutions were diluted 1:5 (v/v) with ACN and cholesterol-d_6 was added as the internal standard (IS) at a 10

μg/mL final concentration. The IS-normalized EIC peak area of each sterol for each extraction step could thus be correlated to the extracted amount and expressed as percentage of the total peak area obtained after three extraction steps. Average percentual recovery values obtained after each extraction step, reported in **Figure A3**, showed that at least 95% of the sterol amount obtained after three consecutive extractions could be extracted already after the first two steps. Moreover, the variabilities of recoveries did not exceed 7% for the first extraction and 5% for the second one, confirming the reproducibility and reliability of the adopted extraction protocol. Accordingly, the pooled first and second extracts were used for real-sample analysis, as described in the *Materials and Methods* section.

Finally, two aspects of method precision were assessed using kale microgreens as a reference: (i) instrumental precision and (ii) combined sampling and extraction precision. For the former, a single extract from one aliquot of freeze-dried kale microgreens was analysed by RPLC-APCI-FTMS on alternate days over a five-day period, with storage at –20 °C between analyses. The evaluation focused on sterols whose concentrations were higher than LOD values, thus excluding low concentrations sterols detected only by considering chromatographic and MS/MS data (excepting 24-epibrassicasterol) and lathosterol and stigmasterol, that could not be quantified in kale microgreens due to low concentration (*vide infra*). As shown in **Table 2** (third column), the relative standard deviations (RSDs) of normalized EIC peak areas obtained for selected sterols were excellent (< 6%), confirming the efficacy of response normalization based on isotopically labelled internal standard and the stability of sterols in extracts over a typical analytical timescale.

To assess variability due to sample heterogeneity, five separate aliquots sampled from the same batch of freeze-dried kale microgreens were independently extracted and analysed on the same day to minimize instrumental drift. The resulting RSDs of normalized EIC peak areas reflected sampling-related variability within a homogenized lot obtained from approximately 600 seedlings (including leaves and stems). Although this variability inherently includes a minor contribution from the extraction procedure, previous recovery experiments indicated that this contribution was marginal

Table 2. Percent relative standard deviation (RSD) values related to the sampling-extraction variability and the analytical response variability evaluated for standard sterols and for 24-epibrassicasterol in kale microgreens. Sampling-extraction variability was estimated from the extraction and LC-MS analysis of five separate aliquots processed on the same day. The analytical response variability was assessed by repeating the LC-MS analysis of a single extract for three times on alternate days within a week, with the extract being stored at -20°C between the analyses.

Compound	Sampling-extraction variability RSD %	Analytical response variability RSD %
β-sitosterol	15	4
Campesterol	12	0.8
Isofucosterol	15	4
Brassicasterol	20	3
Cholesterol	14	1.2
Chalinasterol	13	5
24-epibrassicasterol	21	4
Δ^7-avenasterol	15	6

relative to sampling variability. Consequently, data shown in the second column of **Table 2** can be considered mainly as an estimate of the sampling-related variability, in turn associated with the level of homogeneity of the freeze-dried material obtained for each type of vegetal product under study. As apparent, the resulting RSD was generally lower than 15%, being close to 20-21% only for two sterols among those considered.

3.3.3 RPLC-APCI-FTMS-based quantification of free sterols in microgreens, micro leaves, baby leaves and adult plants of kale and broccoli raab cultivated in the winter growing cycle.

In a first step, free sterols were quantified in microgreens, micro leaves, baby leaves, and mature forms of both kale and broccoli raab grown in the winter season (January–March), as this represents the typical cultivation period for mature forms. Five aliquots of freeze-dried material were separately sampled for each product type and subjected to sterol extraction followed by RPLC-APCI-FTMS analysis. Quantification was performed for each extract using external calibration as described in the previous section, and average concentrations were expressed as mg per 100 g of fresh weight (FW), accounting for water loss during freeze-drying of a specific quantity of fresh product. The resulting

data, expressed as 95% confidence intervals centered on means, are reported in **Table 3** and visualized as bar graphs in **Figure A4** in the appendix to this chapter. Stacked bar graphs were generated from these data to compare total sterol content in the four product types for each *Brassica* plant (**Figure 4**). Error bars in the figure represent the half-width of 95% confidence intervals centred on average total contents, calculated through error propagation from those referring to average contents of individual sterols.

Table 3. Concentrations of free sterols (mg/100 g fresh weight, FW) obtained by RPLC-APCI-FTMS analysis of extracts of microgreens, micro leaves, baby leaves and mature plants of kale and broccoli raab. Data represent 95% confidence intervals for mean concentrations (n = 5).

Compound	Kale				Broccoli raab			
	Micro-greens	Micro leaves	Baby leaves	Mature plants	Micro-greens	Micro leaves	Baby leaves	Mature plants
β-sitosterol	18 ± 2	18 ± 2	13 ± 2	23 ± 6	10.3 ± 1.1	18 ± 4	13 ± 5	21 ± 9
Campesterol	3.4 ± 0.3	2.6 ± 0.3	1.7 ± 0.3	2.6 ± 0.5	1.61 ± 0.16	2.0 ± 0.2	1.7 ± 0.5	2.1 ± 0.6
Isofucosterol	0.51 ± 0.15	0.33 ± 0.05	0.30 ± 0.05	0.16 ± 0.05	0.42 ± 0.05	0.8 ± 0.2	0.51 ± 0.18	0.4 ± 0.2
Brassicasterol	0.42 ± 0.18	< LOD	< LOD	< LOD	0.36 ± 0.07	< LOD	< LOD	< LOD
Cholesterol	0.27 ± 0.04	0.044 ± 0.016	0.052 ± 0.011	< LOD	0.21 ± 0.02	0.30 ± 0.09	0.21 ± 0.09	0.6 ± 0.3
Chalinasterol	0.20 ± 0.05	0.122 ± 0.007	0.11 ± 0.03	< LOD	0.115 ± 0.016	0.23 ± 0.06	0.23 ± 0.07	0.17 ± 0.07
24-epibrass.	0.19 ± 0.11	< LOD	< LOD	< LOD	0.09 ± 0.02	< LOD	< LOD	< LOD
Δ^7-avenasterol	0.14 ± 0.03	0.11 ± 0.03	0.13 ± 0.03	0.15 ± 0.05	0.062 ± 0.009	0.10 ± 0.03	0.11 ± 0.04	0.12 ± 0.08

In accordance with literature data on plant sterols[39,43,50], including those for *Brassicaceae* plants[39,59,61,63,64,66], β-sitosterol, followed by campesterol, exhibited the highest content in all products examined in this thesis work. As mentioned before, only 24-epibrassicasterol could be quantified, at least in microgreens, among sterols identified through chromatographic and MS/MS information. Despite being generally considered the third most abundant free sterol in plants[39,43,50], stigmasterol always exhibited concentrations lower than LOD, therefore it is not included in **Table 3**. Notably, the same result was recently obtained for adult forms of both kale and broccoli raab by Castellaneta *et al.*[66], and low stigmasterol amounts were also reported in the literature for several cruciferous vegetables[59,61,63–65]. Isofucosterol ranked as the third most concentrated sterol, whereas its positional isomer, Δ^7-avenasterol, was present at much lower concentrations. Unsurprisingly, cholesterol and chalinasterol, typically considered animal sterols, exhibited low concentrations, even falling below

LOD values in the case of mature kale. Lathosterol was also detected but not quantifiable in any product examined.

Specific considerations apply to brassicasterol and its epimer 24-epibrassicasterol, which could be quantified only in microgreens of both plants, thus indicating a sharp decrease in their abundance during plant growth. Remarkably, small amounts of brassicasterol have generally been reported for mature cruciferous plants[63,64,66].

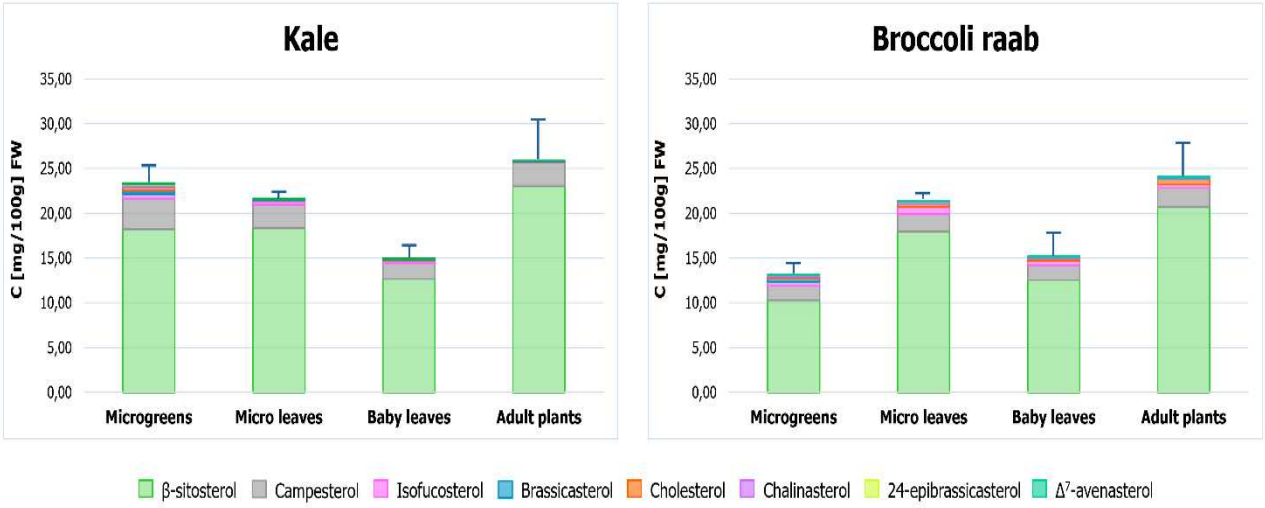


Figure 4. Stacked-bar graphs illustrating the concentrations of free sterols (FSs) found in different growth stages of kale and broccoli raab. Concentrations are expressed in mg/100g of fresh weight (FW). Error bars, calculated by uncertainty propagation, represent the 95% confidence intervals for the total sterol concentrations reported for each product.

Data reported in **Table 3** also reveal a generally higher variability in the sterol content of mature kale and broccoli raab, clearly emphasized by error bars in **Figure A4**. This result may reflect a greater variability in cultivation conditions (*e.g.,* soil type, climatic conditions, insect activity) when cultivation is conducted in the field, considering that changes in sterol contents allow plants to adapt to environmental stress conditions[84]. It may also depend on the intrinsic variation of the sterol content across different parts of mature forms, since all the edible parts of both plants (including small inflorescences in the case of broccoli raab) were subjected to freeze-drying and sterol extraction. Notably, Lu *et al.*[85] evidenced significant differences in the sterol content of bamboo shoots

depending on the plant parts and the harvest season. Roche *et al.*[86] found a remarkable increase in total sterol concentration in sunflower when seed formation occurred under higher temperatures.

Based on the results described so far and on the knowledge available on sterol biosynthetic pathways[43,68,87], it could be hypothesized that the C22-desaturase enzyme, which converts β-sitosterol into stigmasterol and campesterol in brassicasterol and 24-epibrassicasterol, is progressively inhibited in kale and broccoli raab during growth. Moreover, the Δ^{24}-reductase enzyme, which catalyses the conversion of isofucosterol to β-sitosterol and of chalinasterol to campesterol, appears to exhibit higher activity in mature kale products.

From a nutraceutical perspective, data reported in **Figure 4** suggest that microgreens and mature forms contain similar total free sterol contents, although microgreens exhibit greater diversification in their profile. In contrast, total sterol content is progressively decreased in microleaves and baby leaves. As for broccoli raab, micro leaves can be considered comparable to mature forms in terms of total content and diversification, whereas microgreens and baby leaves include lower total sterol amounts. Importantly, data reported in **Table 3** and **Figure 4** refer to raw products; however, mature kale and broccoli raab are typically cooked before consumption and this may have an impact on the actual sterol content available to consumers (*vide infra*).

To emphasize differences in terms of sterol profile observed among different products of the same plant, quantitative data were used, after autoscaling, as input variables for principal component Analysis (PCA). The resulting scores and loading plots are shown in **Figure 5**, in which 95% confidence regions for the four product types are also depicted. In the case of kale products (**Figures 5A** and **5B**) PC1, accounting for 82.4% of variance, clearly separated the most distant phenological stages, *i.e.*, mature forms, strongly associated with Δ^{7}-avenasterol and β-sitosterol, and microgreens, characterized by a higher incidence of all the other Δ^{5}-sterols. Micro and baby leaves occupied intermediate positions and co-clustered due to their greater similarity, although micro leaves sub-clustered more tightly. As evidenced in **Figure 5C**, representing the score plot for PC1 and PC2 referred to broccoli raab, mature forms were clearly distinguished from microgreens, although

separation occurred along PC2. The loadings plot (**Figure 5D**) emphasizes the similarity with kale in terms of higher incidence of brassicasterol and 24-epibrassicasterol in microgreen. A notable difference, however, is the substantially higher cholesterol concentration in mature broccoli raab compared to all other products, including microgreens. As for kale, micro leaves and baby leaves samples clustered together in the PCA score plot, with a similarly tight sub-clustering of microleaves samples.

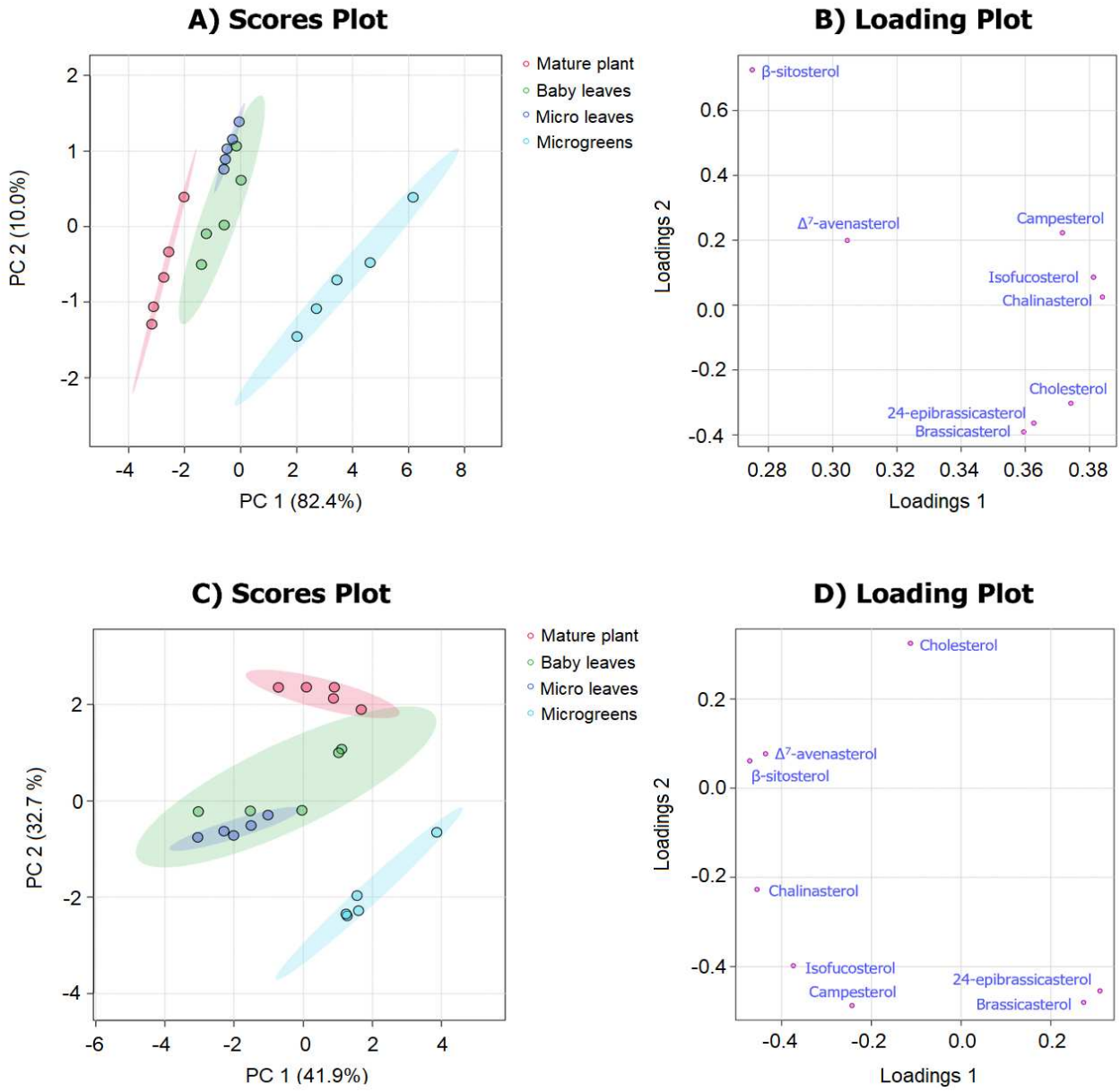


Figure 5. Scores and loading plots obtained for the first two principal components (PC1 and PC2) following PCA of sterol quantitative data for kale (plots A and B) and broccoli raab (plots C and D) microgreens, micro leaves, baby leaves and adult plants.

The higher incidence of brassicasterol and 24-epibrassicasterol in microgreens of both kale and broccoli raab may suggest an increased fluidity of their cell membranes. Indeed, the two sterols include a *trans* C=C bond at C22, like stigmasterol, and this structural feature has been reported to weaken van der Waals interactions with membrane lipids hydrocarbon chains, resulting in more fluid membranes[41]. Conversely, β-sitosterol, which is essential for maintaining cell rigidity and permeability[41,43,47], is more abundant in mature forms, consistently with the need for greater tissue strength. The higher cholesterol incidence in mature broccoli raab deserves further investigation, as cholesterol not only plays a critical role in abiotic stress response[84] but also act as a precursor of other bioactive substances like steroidal alkaloids and saponins[50].

3.3.4 Effect of cultivation season on the FS content in microgreens and micro leaves. The potential influence of the cultivation season on sterol content was evaluated in this study for microgreens and micro leaves of kale and broccoli raab, by also including products grown and harvested during spring. The 95% confidence intervals of sterol concentrations (n = 3), expressed in mg per 100 g of FW, obtained from RPLC-APCI-FTMS analyses are reported in **Table 4**. Values significantly different ($p < 0.05$, t-test) from those measured in products grown and harvested in winter are highlighted in bold in the table. A direct visual comparison with the corresponding winter data is provided in **Figure A6**.

As shown in **Table 4**, no significant seasonal variation was observed for kale and broccoli raab microgreens, except for a slight decrease in cholesterol and a modest increase in chalinasterol. In contrast, the micro leaves of both species exhibited a significant reduction in the two predominant sterols, β-sitosterol and campesterol. In the case of broccoli raab, these decreases extended to nearly all detected sterols, showing a generalized statistically significant reduction in total sterol content. As also observed for winter-grown micro leaves, brassicasterol and 24-epi-brassicasterol remained below their respective LOD values. Since all the analysed products were cultivated without artificial heating, the higher abundance of free sterols in micro leaves grown during winter might reflect a physiological

response to low-temperature exposure, a process known as cold acclimation, previously reported to increase the levels of unsaturated fatty acids and sterols, particularly 24-ethyl-sterols[46,84]. Indeed, as shown in **Figure A6**, reporting average, maximum and minimum daily values recorded inside the greenhouse during the two cultivation cycles, the average daily temperature generally ranged between 5 and 10°C during the winter cycle and between 10 and 20°C during the spring one.

Table 4. Free sterol contents (mg/100 g FW) found in microgreens (MG) and micro leaves (ML) of kale and broccoli raab cultivated during the spring cycle. 95% confidence intervals centred on mean concentrations (n = 3) are reported. Bold values indicate concentrations significantly different from those of the same product types grown in the winter season.

	β-sito-sterol	**Campe-sterol**	**Isofuco-sterol**	**Brassica-sterol**	**Chole-sterol**	**Chalina-sterol**	**24-epibrassica-sterol**	**Δ^7-avena-sterol**
Kale MG	15 ± 2	3.2 ± 0.7	0.41 ± 0.08	0.4 ± 0.2	**0.15 ± 0.03**	0.21 ± 0.08	0.116 ± 0.020	0.11 ± 0.03
Kale ML	**12 ± 4**	**1.9 ± 0.4**	0.28 ± 0.17	< LOD	0.04 ± 0.02	0.15 ± 0.14	< LOD	**0.15 ± 0.05**
Broccoli raab MG	14 ± 5	1.8 ± 0.3	0.6 ± 0.2	0.39 ± 0.09	0.21 ± 0.03	**0.20 ± 0.03**	0.098 ± 0.011	0.12 ± 0.07
Broccoli raab ML	**9 ± 2**	**1.3 ± 0.4**	**0.38 ± 0.17**	< LOD	**0.17 ± 0.09**	**0.11 ± 0.09**	< LOD	**0.063 ± 0.008**

The adaptive effect to temperature appears to be considerably less pronounced in microgreens, thus suggesting that the winter cultivation of kale and broccoli raab microgreens and micro leaves, besides aligning with the natural growth season of their mature counterparts, may be advantageous in terms of free sterol content.

3.3.5 Quantification of FSs in adult plants of kale and broccoli raab subjected to steaming or boiling in water. As mentioned earlier, mature forms of kale and broccoli raab are typically consumed after cooking, raising concerns that part of the sterol content present in raw tissues might be lost through thermal degradation. To evaluate the extent of this effect, mature plants of both species were subjected to two common cooking procedures, steaming and boiling in water, with three replicates considered for each condition (see **Section A2** in the appendix). After cooking, samples were freeze-dried prior to sterol extraction and RPLC-APCI-FTMS analysis, following the same

analytical workflow adopted for raw plants. Stacked-bar plots of the resulting average concentrations for single sterols, expressed as mg per 100 g FW (in this case referring to the weight of cooked samples before freeze-drying), along with 95% confidence intervals for total sterol concentrations, are reported in **Figure 6**, where they are also compared with data referring to raw mature forms (total sterol concentrations of cooked samples are also reported in tabular form in **Table A1**). Data on brassicasterol and its epimer were excluded, as their concentrations consistently fell below the LOD in cooked samples, in agreement with observations made on raw forms.

As inferred from **Table A1**, the two cooking methods generally produced comparable results in terms of final concentrations of single/total sterols in the two plants. In both cases, similar total FS concentrations were observed for raw and steamed samples, whereas a modest, statistically non-significant decrease or increase was observed for boiled kale and broccoli raab, respectively (**Figure 6**). Although unexpected, the increase observed in boiled broccoli raab aligns with findings reported for boiled forms of other cruciferous vegetables with similarly leathery tissues, such as broccoli and cabbage[59,62] and might be explained with a facilitated release of small additional amounts of sterols in the extraction solvent from less accessible membrane domains when boiled vegetables are considered.

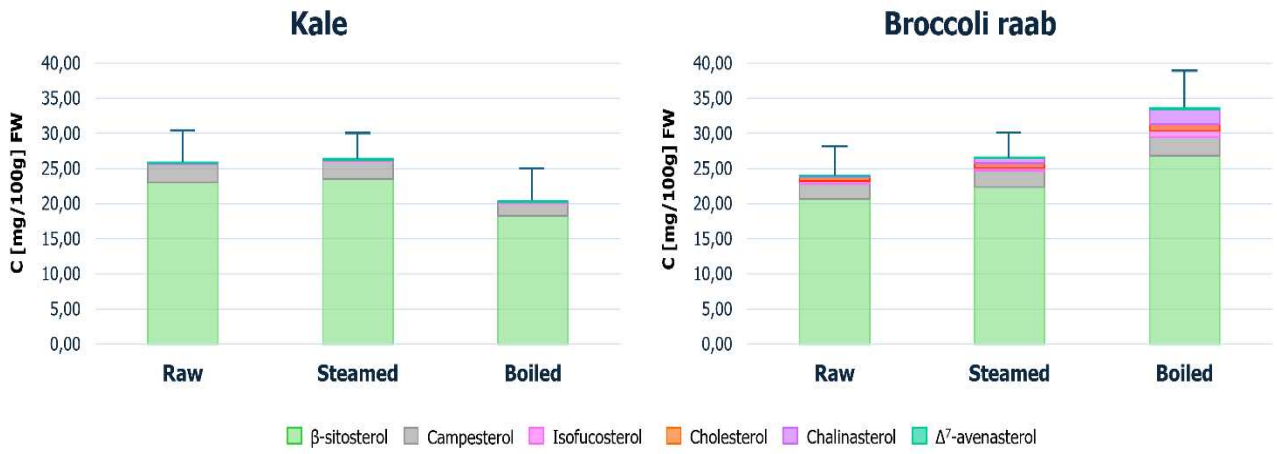


Figure 6. Stacked bar graphs showing free sterol contents in raw, steamed, and boiled mature forms of kale and broccoli raab. Concentrations are expressed as mg per 100 g of fresh weight (FW) and represent mean values obtained from three replicates. Error bars, derived by uncertainty propagation, indicate 95% confidence intervals for the total sterol concentrations reported for each product.

Notably, boiling is the more common cooking method adopted for the preparation of broccoli raab - based traditional dishes (*e.g., Orecchiette e cime di rapa*) in Southern Italy, where boiled vegetables represent a relevant component of the Mediterranean Diet[88].

Integrating the results obtained for microgreens, micro leaves and baby leaves (in particular, those cultivated in the winter cycle) with data collected for raw and cooked mature kale and broccoli raab, some general considerations can be drawn regarding the potential of those innovative *Brassicaceae* products as dietary sources of free sterols. In the case of kale, microgreens and micro leaves contained sterol amounts comparable to those of cooked mature forms, with the added benefit of a more diversified FS profile (see **Figure 4**). In broccoli raab, micro leaves exhibited the highest total FS concentration among the innovative products, only slightly lower than that of cooked mature plants. Therefore, despite their different culinary use, since they are ready-to-eat vegetables, those innovative products can be regarded as valuable sources of bioactive sterols. The consumption of 100 g of kale microgreens or broccoli raab micro leaves, *e.g.*, as a salad or fresh side dish, would supply approximately 20–25 mg of total FSs, corresponding to about 10% of the average daily intake estimated for a non-vegetarian diet[89]. The quantitative results obtained for free sterols could thus also contribute to the development of a Nutritional Quality Score for *Brassicaceae* innovative products, accounting for the relative dietary contribution of both macronutrients and micronutrients, including phytosterols, by analogy with an approach recently applied to certain *Asteraceae* products[90].

Considering both the nutritional aspects and the environmental advantages associated with their more sustainable cultivation, kale and broccoli raab innovative products, particularly microgreens and micro leaves, represent a promising alternative to their mature counterparts.

3.4 Conclusions

In this chapter, the free sterol composition of kale (*Brassica oleracea* var. *acephala*) and broccoli raab (*Brassica rapa* subsp. *sylvestris* var. *esculenta*) was systematically investigated across different

phenological stages, including microgreens, micro leaves, baby leaves and mature plants, using RPLC-APCI-FTMS. In addition, the effects of the growing season on early-harvested products and of common domestic cooking procedures on mature vegetables were evaluated to provide a comprehensive assessment of sterol profiles under relevant production and consumption conditions. The use of high-resolution combined with targeted HCD-MS/MS experiments enabled accurate mass determination and structural characterization of sterols based on diagnostic fragmentation pathways. This approach allowed the confident identification of the main plant sterols, namely β-sitosterol, campesterol, isofucosterol, brassicasterol, Δ^7-avenasterol, chalinasterol, cholesterol and lathosterol, and supported the tentative assignment of additional minor sterols, including episterol, 24-epibrassicasterol, 14-demethyl-lanosterol and $\Delta^{5,24}$-stigmastadienol.

The RPLC-APCI-FTMS method was subsequently validated for quantitative purposes and proved suitable for the reliable determination of free sterols in all the investigated matrices. Quantitative results confirmed β-sitosterol as the dominant sterol in all products, followed by campesterol and isofucosterol. Total free sterol contents in microgreens, micro leaves and baby leaves ranged between approximately 13 and 23 mg per 100 g of fresh weight, values comparable to those measured in raw and cooked mature vegetables. Seasonal effects were more pronounced in micro leaves, indicating a stronger influence of environmental conditions at this intermediate developmental stage. Cooking treatments applied to mature vegetables did not result in significant reductions in total free sterol content, demonstrating the substantial thermal stability of these compounds under typical culinary conditions. Moreover, multivariate analysis by principal component analysis (PCA) was applied to quantitative sterol data to highlight differences in sterol distribution among growth stages. PCA clearly discriminated products harvested at early growth stages from mature plants, revealing a more diversified sterol profile and a higher relative contribution of minor sterols in microgreens and micro leaves, whose abundance progressively decreased during plant development.

Overall, the results described in this chapter demonstrate that kale and broccoli raab harvested at early growth stages can represent quantitatively relevant dietary sources of free sterols and, at the same time, they exhibit a broader sterol spectrum than their mature counterparts. From a methodological point of view, the study highlights RPLC-APCI-FTMS/MS as a powerful analytical tool for a comprehensive sterol profiling in complex plant matrices, supporting its application in nutritional studies and food quality assessment of innovative vegetable products.

References

(1) Di Gioia, F.; Renna, M.; Santamaria, P. Sprouts, Microgreens and "Baby Leaf" Vegetables. *Minim. Process. Refrig. Fruits Veg.* **2017**, No. 11, 403–432. https://doi.org/DOI 10.1007/978-1-4939-7018-6_11.

(2) Renna, M.; Paradiso, V. M. Ongoing Research on Microgreens: Nutritional Properties, Shelf-Life, Sustainable Production, Innovative Growing and Processing Approaches. *Foods* **2020**, *9* (6), 1–5. https://doi.org/10.3390/foods9060826.

(3) Ebert, A. W. Sprouts and Microgreens—Novel Food Sources for Healthy Diets. *Plants* **2022**, *11* (4), 1–35. https://doi.org/10.3390/plants11040571.

(4) Sharma, S.; Shree, B.; Sharma, D.; Kumar, S.; Kumar, V.; Sharma, R.; Saini, R. Vegetable Microgreens: The Gleam of next Generation Super Foods, Their Genetic Enhancement, Health Benefits and Processing Approaches. *Food Res. Int.* **2022**, *155* (111038), 1–18. https://doi.org/10.1016/j.foodres.2022.111038.

(5) Partap, M.; Sharma, D.; HN, D.; Thakur, M.; Verma, V.; Ujala; Bhargava, B. Microgreen: A Tiny Plant with Superfood Potential. *J. Funct. Foods* **2023**, *107* (105697), 1–15. https://doi.org/10.1016/j.jff.2023.105697.

(6) Choe, U.; Yu, L. L.; Wang, T. T. Y. The Science behind Microgreens as an Exciting New Food for the 21st Century. *J. Agric. Food Chem.* **2018**, *66* (44), 1–39. https://doi.org/10.1021/acs.jafc.8b03096.

(7) Teng, J.; Liao, P.; Wang, M. The Role of Emerging Micro-Scale Vegetables in Human Diet and Health Benefits - An Updated Review Based on Microgreens. *Food Funct.* **2021**, *12* (5), 1914–1932. https://doi.org/10.1039/d0fo03299a.

(8) Treadwell, D. D.; Hochmuth, R.; Landrum, L.; Laughlin, W. Microgreens: A New Specialty Crop: HS1164, Rev. 9/2020. *Edis 2020* **2020**, No. 5, 1–3. https://doi.org/https://doi.org/10.32473/edis-hs1164-2020.

(9) Xiao, Z.; Lester, G. E.; Luo, Y.; Wang, Q. Assessment of Vitamin and Carotenoid Concentrations of Emerging Food Products: Edible Microgreens. *J. Agric. Food Chem.* **2012**, *60* (31), 7644–7651. https://doi.org/https://doi.org/10.1021/jf300459b.

(10) Aires, A. Hydroponic Production Systems: Impact on Nutritional Status and Bioactive

Compounds of Fresh Vegetables. *IntechOpen* **2018**, 55–66. https://doi.org/http://dx.doi.org/10.5772/intechopen.73011.

(11) Sambo, P.; Nicoletto, C.; Giro, A.; Pii, Y.; Valentinuzzi, F.; Mimmo, T.; Lugli, P.; Orzes, G.; Mazzetto, F.; Astolfi, S.; Terzano, R.; Cesco, S. Hydroponic Solutions for Soilless Production Systems: Issues and Opportunities in a Smart Agriculture Perspective. *Front. Plant Sci.* **2019**, *10* (July). https://doi.org/10.3389/fpls.2019.00923.

(12) Lenzi, A.; Orlandini, A.; Bulgari, R.; Ferrante, A.; Bruschi, P. Antioxidant and Mineral Composition of Three Wild Leafy Species: A Comparison between Microgreens and Baby Greens. *Foods* **2019**, *8* (10). https://doi.org/10.3390/foods8100487.

(13) Kyriacou, M. C.; Rouphael, Y.; Di Gioia, F.; Kyratzis, A.; Serio, F.; Renna, M.; De Pascale, S.; Santamaria, P. Micro-Scale Vegetable Production and the Rise of Microgreens. *Trends Food Sci. Technol.* **2016**, *57*, 103–115. https://doi.org/10.1016/j.tifs.2016.09.005.

(14) Renna, M.; Castellino, M.; Leoni, B.; Paradiso, V. M.; Santamaria, P. Microgreens Production with Low Potassium Content for Patients with Impaired Kidney Function. *Nutrients* **2018**, *10* (6). https://doi.org/10.3390/nu10060675.

(15) Di Gioia, F.; Petropoulos, S. A.; Ozores-Hampton, M.; Morgan, K.; Rosskopf, E. N. Zinc and Iron Agronomic Biofortification of Brassicaceae Microgreens. *Agronomy* **2019**, *9* (11), 1–20. https://doi.org/10.3390/agronomy9110677.

(16) Pannico, A.; El-Nakhel, C.; Graziani, G.; Kyriacou, M. C.; Giordano, M.; Soteriou, G. A.; Zarrelli, A.; Ritieni, A.; De Pascale, S.; Rouphael, Y. Selenium Biofortification Impacts the Nutritive Value, Polyphenolic Content, and Bioactive Constitution of Variable Microgreens Genotypes. *Antioxidants* **2020**, *9* (4). https://doi.org/10.3390/antiox9040272.

(17) Puccinelli, M.; Pezzarossa, B.; Pintimalli, L.; Malorgio, F. Selenium Biofortification of Three Wild Species, Rumex Acetosa l., Plantago Coronopus l., and Portulaca Oleracea l., Grown as Microgreens. *Agronomy* **2021**, *11* (6). https://doi.org/10.3390/agronomy11061155.

(18) Zhang, X.; Bian, Z.; Yuan, X.; Chen, X.; Lu, C. A Review on the Effects of Light-Emitting Diode (LED) Light on the Nutrients of Sprouts and Microgreens. *Trends Food Sci. Technol.* **2020**, *99* (February), 203–216. https://doi.org/10.1016/j.tifs.2020.02.031.

(19) Alrifai, O.; Hao, X.; Marcone, M. F.; Tsao, R. Current Review of the Modulatory Effects of LED Lights on Photosynthesis of Secondary Metabolites and Future Perspectives of Microgreen Vegetables. *J. Agric. Food Chem.* **2019**, *67* (22), 6075–6090.

https://doi.org/10.1021/acs.jafc.9b00819.

(20) Samuoliene, G.; Brazaityte, A.; Sirtautas, R.; Sakalauskiene, S.; Jankauskiene, J.; Duchovskis, P.; Novičkovas, A. The Impact of Supplementary Short-Term Red LED Lighting on the Antioxidant Properties of Microgreens. *Acta Hortic.* **2012**, *956*, 649–655. https://doi.org/10.17660/actahortic.2012.956.78.

(21) Samuoliene, G.; Brazaityte, A.; Jankauskiene, J.; Viršile, A.; Sirtautas, R.; Novičkovas, A.; Sakalauskiene, S.; Sakalauskaite, J.; Duchovskis, P. LED Irradiance Level Affects Growth and Nutritional Quality of Brassica Microgreens. *Cent. Eur. J. Biol.* **2013**, *8* (12), 1241–1249. https://doi.org/10.2478/s11535-013-0246-1.

(22) Brazaitytė, A.; Miliauskienė, J.; Vaštakaitė-Kairienė, V.; Sutulienė, R.; Laužikė, K.; Duchovskis, P.; Małek, S. Effect of Different Ratios of Blue and Red Led Light on Brassicaceae Microgreens under a Controlled Environment. *Plants* **2021**, *10* (4). https://doi.org/10.3390/plants10040801.

(23) Demir, K.; Sarıkamış, G.; Çakırer Seyrek, G. Effect of LED Lights on the Growth, Nutritional Quality and Glucosinolate Content of Broccoli, Cabbage and Radish Microgreens. *Food Chem.* **2023**, *401* (February 2022). https://doi.org/10.1016/j.foodchem.2022.134088.

(24) Samuolienė, G.; Viršilė, A.; Brazaitytė, A.; Jankauskienė, J.; Sakalauskienė, S.; Vaštakaitė, V.; Novičkovas, A.; Viškelienė, A.; Sasnauskas, A.; Duchovskis, P. Blue Light Dosage Affects Carotenoids and Tocopherols in Microgreens. *Food Chem.* **2017**, *228*, 50–56. https://doi.org/10.1016/j.foodchem.2017.01.144.

(25) Martínez-Ispizua, E.; Calatayud, Á.; Marsal, J. I.; Cannata, C.; Basile, F.; Abdelkhalik, A.; Soler, S.; Valcárcel, J. V.; Martínez-Cuenca, M. R. The Nutritional Quality Potential of Microgreens, Baby Leaves, and Adult Lettuce: An Underexploited Nutraceutical Source. *Foods* **2022**, *11* (3), 1–23. https://doi.org/10.3390/foods11030423.

(26) Martínez-Sánchez, A.; Gil-Izquierdo, A.; Gil, M. I.; Ferreres, F. A Comparative Study of Flavonoid Compounds, Vitamin C, and Antioxidant Properties of Baby Leaf Brassicaceae Species. *J. Agric. Food Chem.* **2008**, *56* (7), 2330–2340. https://doi.org/10.1021/jf072975+.

(27) Waterland, N. L.; Moon, Y.; Tou, J. C.; Kim, M. J.; Pena-Yewtukhiw, E. M.; Park, S. Mineral Content Differs among Microgreen, Baby Leaf, and Adult Stages in Three Cultivars of Kale. *HortScience* **2017**, *52* (4), 566–571. https://doi.org/10.21273/HORTSCI11499-16.

(28) Aires, A.; Carvalho, R.; Rosa, E. A. S.; Saavedra, M. J. Phytochemical Characterization and

Antioxidant Properties of Baby-Leaf Watercress Produced under Organic Production System. *CYTA - J. Food* **2013**, *11* (4), 343–351. https://doi.org/10.1080/19476337.2013.769025.

(29) Saini, R. K.; Ko, E. Y.; Keum, Y. S. Minimally Processed Ready-to-Eat Baby-Leaf Vegetables: Production, Processing, Storage, Microbial Safety, and Nutritional Potential. *Food Rev. Int.* **2017**, *33* (6), 644–663. https://doi.org/10.1080/87559129.2016.1204614.

(30) Ramirez, D.; Abellán-Victorio, A.; Beretta, V.; Camargo, A.; Moreno, D. A. Functional Ingredients from Brassicaceae Species: Overview and Perspectives. *Int. J. Mol. Sci.* **2020**, *21* (6), 1–21. https://doi.org/10.3390/ijms21061998.

(31) Le, T. N.; Chiu, C.-H.; Hsieh, P.-C. Bioactive Compounds and Bioactivities of Brassica Oleracea L. Var. Italica Sproutsand Microgreens : An Updated Overview from a Nutraceutical Perspective. *Plants* **2020**, *9* (946). https://doi.org/doi:10.3390/plants9080946.

(32) Vučetić, A.; Šovljanski, O.; Pezo, L.; Gligorijević, N.; Kostić, S.; Vulić, J.; Čanadanović-Brunet, J. A Comprehensive Antioxidant and Nutritional Profiling of Brassicaceae Microgreens. *Antioxidants* **2025**, *14* (2), 1–23. https://doi.org/10.3390/antiox14020191.

(33) Bafumo, R. F.; Alloggia, F. P.; Ramirez, D. A.; Maza, M. A.; Camargo, A. B.; Ramirez, D. A.; Camargo, A. B.; Maza, M. A.; Fontana, A.; Moreno, D. A. Optimal Brassicacea Family Microgreens from a Phytochemical and Sensory Perspective. *Food Res. Int.* **2024**, *193* (114812), 1–14. https://doi.org/10.1016/j.foodres.2024.114812.

(34) Xiao, Z.; Rausch, S. R.; Luo, Y.; Sun, J.; Yu, L.; Wang, Q.; Chen, P.; Yu, L.; Stommel, J. R. Microgreens of Brassicaceae: Genetic Diversity of Phytochemical Concentrations and Antioxidant Capacity. *LWT - Food Sci. Technol.* **2019**, *101* (October 2018), 731–737. https://doi.org/10.1016/j.lwt.2018.10.076.

(35) Liu, Z.; Shi, J.; Wan, J.; Pham, Q.; Zhang, Z.; Sun, J.; Yu, L.; Luo, Y.; Wang, T. T. Y.; Chen, P. Profiling of Polyphenols and Glucosinolates in Kale and Broccoli Microgreens Grown under Chamber and Windowsill Conditions by Ultrahigh-Performance Liquid Chromatography High-Resolution Mass Spectrometry. *ACS Food Sci. Technol.* **2022**, *2* (1), 101–113. https://doi.org/10.1021/acsfoodscitech.1c00355.

(36) Sun, J.; Xiao, Z.; Lin, L. Z.; Lester, G. E.; Wang, Q.; Harnly, J. M.; Chen, P. Profiling Polyphenols in Five Brassica Species Microgreens by UHPLC-PDA-ESI/HRMSn. *J. Agric. Food Chem.* **2013**, *61* (46), 10960–10970. https://doi.org/10.1021/jf401802n.

(37) Castellaneta, A.; Losito, I.; Cisternino, G.; Leoni, B.; Santamaria, P.; Calvano, C. D.; Bianco,

G.; Cataldi, T. R. I. All Ion Fragmentation Analysis Enhances the Untargeted Profiling of Glucosinolates in Brassica Microgreens by Liquid Chromatography and High-Resolution Mass Spectrometry. *J. Am. Soc. Mass Spectrom.* **2022**, *33* (11), 2108–2119. https://doi.org/10.1021/jasms.2c00208.

(38) Di Bella, M. C.; Toscano, S.; Arena, D.; Moreno, D. A.; Romano, D.; Branca, F. Effects of Growing Cycle and Genotype on the Morphometric Properties and Glucosinolates Amount and Profile of Sprouts, Microgreens and Baby Leaves of Broccoli (Brassica Oleracea l. Var. Italica Plenck) and Kale (b. Oleracea l. Var. Acephala Dc.). *Agronomy* **2021**, *11* (9). https://doi.org/10.3390/agronomy11091685.

(39) Poudel, P.; Petropoulos, S. A.; Di Gioia, F. *Plant Tocopherols and Phytosterols and Their Bioactive Properties*; 2023. https://doi.org/https://doi.org/10.1007/978-3-031-18587-8_8.

(40) De Jong, A.; Plat, J.; Mensink, R. P. Metabolic Effects of Plant Sterols and Stanols (Review). *J. Nutr. Biochem.* **2003**, *14* (7), 362–369. https://doi.org/10.1016/S0955-2863(03)00002-0.

(41) Piironen, V.; Lindsay, D. G.; Miettinen, T. A.; Toivo, J.; Lampi, A. M. Plant Sterols: Biosynthesis, Biological Function and Their Importance to Human Nutrition. *J. Sci. Food Agric.* **2000**, *80* (7), 939–966. https://doi.org/10.1002/(SICI)1097-0010(20000515)80:7<939::AID-JSFA644>3.0.CO;2-C.

(42) Mongrand, S.; Stanislas, T.; Bayer, E. M. F.; Lherminier, J.; Simon-Plas, F. Membrane Rafts in Plant Cells. *Trends Plant Sci.* **2010**, *15* (12), 656–663. https://doi.org/10.1016/j.tplants.2010.09.003.

(43) Valitova, J. N.; Sulkarnayeva, A. G.; Minibayeva, F. V. Plant Sterols: Diversity, Biosynthesis, and Physiological Functions. *Biochem.* **2016**, *81* (8), 819–834. https://doi.org/10.1134/S0006297916080046.

(44) Moreau, R. A.; Nyström, L.; Whitaker, B. D.; Winkler-Moser, J. K.; Baer, D. J.; Gebauer, S. K.; Hicks, K. B. Phytosterols and Their Derivatives: Structural Diversity, Distribution, Metabolism, Analysis, and Health-Promoting Uses. *Prog. Lipid Res.* **2018**, *70*, 35–61. https://doi.org/10.1016/j.plipres.2018.04.001.

(45) Simon-Plas, F.; Perraki, A.; Bayer, E.; Gerbeau-Pissot, P.; Mongrand, S. An Update on Plant Membrane Rafts. *Curr. Opin. Plant Biol.* **2011**, *14* (6), 642–649. https://doi.org/10.1016/j.pbi.2011.08.003.

(46) Du, Y.; Fu, X.; Chu, Y.; Wu, P.; Liu, Y.; Ma, L.; Tian, H.; Zhu, B. Biosynthesis and the Roles

of Plant Sterols in Development and Stress Responses. *Int. J. Mol. Sci.* **2022**, *23* (4). https://doi.org/10.3390/ijms23042332.

(47) Schaller, H. The Role of Sterols in Plant Growth and Development. *Prog. Lipid Res.* **2003**, *42*, 163–175. https://doi.org/DOI: 10.1016/s0163-7827(02)00047-4.

(48) Mo, S.; Dong, L.; Hurst, W. J.; Van Breemen, R. B. Quantitative Analysis of Phytosterols in Edible Oils Using APCI Liquid Chromatography-Tandem Mass Spectrometry. *Lipids* **2013**, *48* (9), 949–956. https://doi.org/10.1007/s11745-013-3813-3.

(49) Ferrer, A.; Altabella, T.; Arró, M.; Boronat, A. Emerging Roles for Conjugated Sterols in Plants. *Prog. Lipid Res.* **2017**, *67*, 27–37. https://doi.org/10.1016/j.plipres.2017.06.002.

(50) Moreau, R. A.; Whitaker, B. D.; Hicks, K. B. Phytosterols, Phytostanols, and Their Conjugates in Foods: Structural Diversity, Quantitative Analysis, and Health-Promoting Uses. *Prog. Lipid Res.* **2002**, *41* (6), 457–500. https://doi.org/10.1016/S0163-7827(02)00006-1.

(51) Münger, L. H.; Jutzi, S.; Lampi, A. M.; Nyström, L. Comparison of Enzymatic Hydrolysis and Acid Hydrolysis of Sterol Glycosides from Foods Rich in Δ7-Sterols. *Lipids* **2015**, *50* (8), 735–748. https://doi.org/10.1007/s11745-015-4002-3.

(52) Münger, L. H.; Nyström, L. Enzymatic Hydrolysis of Steryl Glycosides for Their Analysis in Foods. *Food Chem.* **2014**, *163*, 202–211. https://doi.org/10.1016/j.foodchem.2014.04.082.

(53) Evtyugin, D. D.; Evtuguin, D. V.; Casal, S.; Domingues, M. R. Advances and Challenges in Plant Sterol Research: Fundamentals, Analysis, Applications and Production. *Molecules* **2023**, *28* (18), 1–45. https://doi.org/10.3390/molecules28186526.

(54) Hartmann, M. A.; Benveniste, P. Plant Membrane Sterols: Isolation, Identification, and Biosynthesis. *Methods Enzymol.* **1987**, *148* (C), 632–650. https://doi.org/10.1016/0076-6879(87)48060-9.

(55) IUPAC-IUB Joint Commission on Biochemical Nomenclature (JCBN). The Nomenclature of Steroids. Recommendations 1989. *Eur. J. Biochem.* **1989**, *186* (3), 429–458. https://doi.org/10.1351/pac197645010011.

(56) Schlag, S.; Vetter, W. Quantitative Data of up to Thirty Sterols in Vegetable Oils and Fats. *Eur. Food Res. Technol.* **2024**, *250* (2), 469–482. https://doi.org/10.1007/s00217-023-04397-5.

(57) Nes, W. D. Biosynthesis of Cholesterol and Other Sterols. *Chem. Rev.* **2011**, *111* (10), 6423–6451. https://doi.org/10.1021/cr200021m.

(58) Gajewski, M.; Przybył, J. L.; Szymczak, P. Broccoli as the Source of Phytosterols in Nutrition. *Bull. Univ. Agric. Sci. Vet. Med. Cluj-Napoca* **2007**, *64*, 229–233. https://doi.org/DOI: https://doi.org/10.15835/buasvmcn-hort:1990.

(59) Gajewski, M.; PrzybyŁ, J. L.; Kosakowska, O.; Szymczak, P. Some Factors Influencing Free Sterols Content in Broccoli (Brassica Oleracea l. Var. Botrytis Italica Plenck.). *J. Food Biochem.* **2009**, *33* (6), 881–894. https://doi.org/10.1111/j.1745-4514.2009.00262.x.

(60) Baek, S. A.; Jung, Y. H.; Lim, S. H.; Park, S. U.; Kim, J. K. Metabolic Profiling in Chinese Cabbage (Brassica Rapa L. Subsp. Pekinensis) Cultivars Reveals That Glucosinolate Content Is Correlated with Carotenoid Content. *J. Agric. Food Chem.* **2016**, *64* (21), 4426–4434. https://doi.org/10.1021/acs.jafc.6b01323.

(61) Han, J. H.; Yang, Y. X.; Feng, M. Y. Contents of Phytosterols in Vegetables and Fruits Commonly Consumed in China. *Biomed. Environ. Sci.* **2008**, *21* (6), 449–453. https://doi.org/10.1016/S0895-3988(09)60001-5.

(62) Kaloustian, J.; Alhanout, K.; Amiot-Carlin, M. J.; Lairon, D.; Portugal, H.; Nicolay, A. Effect of Water Cooking on Free Phytosterol Levels in Beans and Vegetables. *Food Chem.* **2008**, *107* (4), 1379–1386. https://doi.org/10.1016/j.foodchem.2007.09.061.

(63) Bok, K.; Ye, L.; Kim, J.; Jin, H.; Choi, J.; Kwang, J. Phytochemical Profiles of Brassicaceae Vegetables and Their Multivariate Characterization Using Chemometrics. *Appl. Biol. Chem.* **2018**, *61* (2), 131–144. https://doi.org/10.1007/s13765-017-0340-6.

(64) Piironen, V.; Toivo, J.; Puupponen-Pimiä, R.; Lampi, A. M. Plant Sterols in Vegetables, Fruits and Berries. *J. Sci. Food Agric.* **2003**, *83* (4), 330–337. https://doi.org/10.1002/jsfa.1316.

(65) Normen, L. Plant Sterols in Vegetables and Fruits Commonly Consumed in Sweden. *Eur. J. Nutr.* **1999**, *38*, 84–89. https://doi.org/DOI: 10.1007/s003940050048.

(66) Castellaneta, A.; Losito, I.; Leoni, B.; Renna, M.; Mininni, C.; Santamaria, P.; Calvano, C. D.; Cataldi, T. R. I.; Liebisch, G.; Matysik, S. A Targeted GC-MS/MS Approach for the Determination of Eight Sterols in Microgreen and Mature Plant Material. *J. Steroid Biochem. Mol. Biol.* **2023**, *232* (106361), 1–10. https://doi.org/10.1016/j.jsbmb.2023.106361.

(67) Cinquepalmi, V.; Losito, I.; Castellaneta, A.; Calvano, C. D.; Cataldi, T. R. I. APCI-Multistage Mass Spectrometry Following Liquid Chromatography for Selected 4-Desmethyl-Sterols and Their Deuterium-Labelled Analogues Unveils Characteristic Fragmentation Routes for Cholesterol and Phytosterols Identification. *Rapid Commun. Mass Spectrom.* **2025**, *39* (13). https://doi.org/10.1002/rcm.10039.

(68) Cinquepalmi, V.; Losito, I.; Castellaneta, A.; Calvano, C. D.; Cataldi, T. R. I. Diagnostic Fragmentations of Animal and Fungal Sterols/Stanols Obtained by APCI–Tandem Mass Spectrometry: A Route Towards Unknown Free Sterol Identification. *Metabolites* **2025**, *15*, 674. https://doi.org/10.3390/metabo15100674.

(69) Sonawane, P. D.; Pollier, J.; Panda, S.; Szymanski, J.; Massalha, H.; Yona, M.; Unger, T.; Malitsky, S.; Arendt, P.; Pauwels, L.; Almekias-Siegl, E.; Rogachev, I.; Meir, S.; Cárdenas, P. D.; Masri, A.; Petrikov, M.; Schaller, H.; Schaffer, A. A.; Kamble, A.; Giri, A. P.; Goossens, A.; Aharoni, A. Plant Cholesterol Biosynthetic Pathway Overlaps with Phytosterol Metabolism. *Nat. Plants* **2016**, *3* (16205), 1–13. https://doi.org/10.1038/nplants.2016.205.

(70) Münger, L. H.; Boulos, S.; Nyström, L. UPLC-MS/MS Based Identification of Dietary Steryl Glucosides by Investigation of Corresponding Free Sterols. *Front. Chem.* **2018**, *6*, 1–19. https://doi.org/10.3389/fchem.2018.00342.

(71) Kikuchi, T.; Kadota, S.; Shima, T.; Ikekawa, N.; Fujimoto, Y. Effective Separation of Sterol C-24 Epimers by Reversed-Phase High Performance Liquid Chromatography. *Chem. Pharm. Bull.* **1984**, *32* (9), 3779–3782. https://doi.org/https://doi.org/10.1016/S0021-9673(00)96308-8.

(72) Ikekawa, N.; Fujimoto, Y.; Kadota, S.; Kikuchi, T. Effective Separation of Sterol C-24 Epimers. *J. Chromatogr. A* **1989**, *468* (C), 91–98. https://doi.org/10.1016/S0021-9673(00)96308-8.

(73) Chitwood, D. J.; Patterson, G. W. Separation of Epimeric Pairs of C-24 Alkylsterols by Reversed-Phase High Performance Liquid Chromatography of the Free Sterols at Subambient Temperature. *J. Liq. Chromatogr.* **1991**, *14* (1), 151–163. https://doi.org/10.1080/01483919108049603.

(74) Akihisa (ne Itoh), T.; Ghosh, P.; Thakur, S.; Rosentein, F. U.; Matsumoto, T. Sterol Compositions of Seeds and Mature Plants of Family Cucurbitaceae. *J. Am. Oil Chem. Soc.* **1986**, *63* (5), 653–658. https://doi.org/10.1007/BF02638231.

(75) Akihisa, T.; Thakur, S.; Rosenstein, F. U.; Matsumoto, T. Sterols of Cucurbitaceae: The Configurations at C-24 of 24-Alkyl-Δ5-,Δ7- and Δ8-Sterols. *Lipids* **1986**, *21* (1), 39–47.

https://doi.org/10.1007/BF02534301.

(76) Garg, V. K.; Nes, W. R. Occurrence of Δ5-Sterols in Plants Producing Predominantly Δ7-Sterols: Studies on the Sterol Compositions of Six Cucurbitaceae Seeds. *Phytochemistry* **1986**, *25* (11), 2591–2597. https://doi.org/10.1016/S0031-9422(00)84516-1.

(77) Bolker, H. I. Crinosterol: A Unique Sterol from a Comatulid Crinoid [13]. *Nature* **1967**, *213* (5079), 905–906. https://doi.org/10.1038/213905a0.

(78) Griffiths, K. M.; Bacic, A.; Howlett, B. J. Sterol Composition of Mycelia of the Plant Pathogenic Ascomycete Leptosphaeria Maculans. *Phytochemistry* **2003**, *62* (2), 147–153. https://doi.org/10.1016/S0031-9422(02)00505-8.

(79) Aoyama, Y.; Yoshida, Y.; Sato, R. Yeast Cytochrome P-450 Catalyzing Lanosterol 14α-Demethylation. II. Lanosterol Metabolism by Purified P-450(14DM) and by Intact Microsomes. *J. Biol. Chem.* **1984**, *259* (3), 1661–1666. https://doi.org/10.1016/s0021-9258(17)43459-4.

(80) Misso, N. L. A.; Goad, L. J. Investigations on the Δ23-, Δ24(28)- and Δ25-Sterols of Zea Mays. *Phytochemistry* **1984**, *23* (I), 73–82. https://doi.org/https://doi.org/10.1016/0031-9422(84)83081-2.

(81) Ki Kim, S.; Akihisa, T.; Tamura, T.; Matsumoto, T.; Yokota, T.; Takahashi, N. 24-Methylene-25-Methylcholesterol in Phaseolus Vulgaris Seed: Structural Relation to Brassinosteroids. *Phytochemistry* **1988**, *27* (2), 629–631. https://doi.org/10.1016/0031-9422(88)83160-1.

(82) Shepherd, T.; Dobson, G.; Verrall, S. R.; Conner, S.; Griffiths, D. W.; McNicol, J. W.; Davies, H. V.; Stewart, D. Potato Metabolomics by GC-MS: What Are the Limiting Factors? *Metabolomics* **2007**, *3* (4), 475–488. https://doi.org/10.1007/s11306-007-0058-2.

(83) Kruve, A.; Rebane, R.; Kipper, K.; Oldekop, M. L.; Evard, H.; Herodes, K.; Ravio, P.; Leito, I. Tutorial Review on Validation of Liquid Chromatography-Mass Spectrometry Methods: Part I. *Anal. Chim. Acta* **2015**, *870* (1), 29–44. https://doi.org/10.1016/j.aca.2015.02.017.

(84) Rogowska, A.; Szakiel, A. The Role of Sterols in Plant Response to Abiotic Stress. *Phytochem. Rev.* **2020**, *19* (6), 1525–1538. https://doi.org/10.1007/s11101-020-09708-2.

(85) Lu, B.; Ren, Y.; Zhang, Y.; Gong, J. Effects of genetic variability, parts and seasons on the sterol content and composition in bamboo shoots. *Food Chem.* **2008**, *112*, 1016-1021.

https://doi.org/ 10.1016/j.foodchem.2008.06.059

(86) Roche, J.; Alignan, M.; Bouniols, A.; Cerny, M.; Mouloungui, Z.; Vear, F.; Merah, O. Sterol content in sunflower seeds (*Helianthus annuus* L.) as affected by genotypes and environmental conditions. *Food Chem.* **2010**, *121,* 990-995. https://doi.org/ 10.1016/j.foodchem.2010.01.036.

(87) Morikawa, T.; Mizutani, M.; Aoki, N.; Watanabe, B.; Saga, H.; Saito, S.; Oikawa, A.; Suzuki, H.; Sakurai, N.; Shibata, D.; Wadano, A.; Sakata, K.; Ohta, D. Cytochrome P450 CYP710A Encodes the Sterol C-22 Desaturase in Arabidopsis and Tomato. *Plant Cell* **2006**, *18* (4), 1008–1022. https://doi.org/10.1105/tpc.105.036012.

(88) Renna, M.; Rinaldi, V.A.; Gonnella, M. The Mediterranean Diet between traditional foods and human health: The culinary example of Puglia (Southern Italy). *Int. J. Gastr. Food Sci.* **2015**, *2*, 63-71. https://doi.org/ 10.1016/j.ijgfs.2014.12.001.

(89) Piironen, V.; Lindsay, D.G.;, Miettinen, T.A.; Toivo, J.; Lampi, A.-M. Plant sterols: biosynthesis, biological function and their importance to human nutrition. *J. Sci. Food Agric.* **2000**, *80*, 939–966. https://doi.org/ 10.1002/(SICI)1097-0010(20000515)80:7<939::AID-JSFA644>3.0.CO;2-C.

(90) Renna, M.; Somma, A.; Leoni, B.; Castellaneta, A.; Cinquepalmi, V.; Losito, I.; Cataldi, T.R.I., Santamaria P. Globe artichoke's offshoots: from by-product to new horticultural product. *Acta Hort.* **2025**, *1424*, 111-118. https://doi.org/ 10.17660/ActaHortic.2025.1424.14.

Appendix 3

Section A1. Details on the cultivation of kale and broccoli raab microgreens, micro leaves and baby leaves . Plants were grown in plastic trays (microgreens) or pots (micro leaves and baby leaves) filled with a peat-based commercial growing media (Brill® 3 Special). The seeds were uniformly broadcasted on the surface of the growing media using a seeding density of 4 seeds/cm^2 for microgreens, 0.076 seeds/cm^2 for micro leaves and 0.038 seeds/cm^2 for baby leaves. During the first 4 days, trays and pots were covered with plastic film for seed germination. On day five, the seedlings were exposed to light inside the greenhouse. Trays and pots were irrigated every day using rainwater until the germination was complete. In both cycles, after germination, trays and pots were fertigated with a half-strength Hoagland nutrient solution with two interventions per day. For microgreens, plants were harvested at the first true-leaf stage. In the first cultivation cycle, broccoli raab and kale microgreens were harvested 18 and 25 days after sowing, respectively; in the second cycle they were harvested 16 and 18 days after sowing, respectively. For micro leaves, plants were harvested at the 4–5 true-leaf stage; in the first cycle broccoli raab and kale were harvested 36 and 44 days after sowing, respectively; in the second cycle harvests occurred at 29 and 30 days after sowing, respectively. Baby leaves were grown only during the winter cycle and harvested at the 7-8 true leaf stage, corresponding to 49 and 58 days after sowing for broccoli raab and kale, respectively.

Section A2. Details on the cultivation and cooking of mature forms of kale and broccoli raab. Kale and broccoli raab plants were cultivated until they reached the mature form using first an N-based fertilizer, to promote the development and strengthening, and then with a K-based fertilizer, to promote fruiting, while the irrigation was carried out every other day with about 10 L of water. After harvest, plants were washed with tap water, blotted dry with paper towels and cut to obtain edible portions. In particular, plants for each genotype were mixed, with 1350 g being taken and divided up

into three portions (450 g for each application). One portion was retained raw, while the others were cooked in two different ways. In the first case (boiling) vegetables were boiled in a steel pot with distilled water (99 ± 1 ◦C) at a sample weight/water volume ratio of 1:7 for 5 min. The boiled samples were drained off and rapidly cooled on ice. In the second case (steaming) vegetables were placed on a tray in a steam cooker (VC 101 630, Tefal, Milan, Italy), covered with a lid and cooked with water vapour (99 ± 1 ◦C) under atmospheric pressure for 10 min. Cooking conditions were determined with a preliminary experiment. Three treatment series for each application (about 150 g of vegetable) were prepared in order to provide independent replicates for each cooking method and for the uncooked samples.

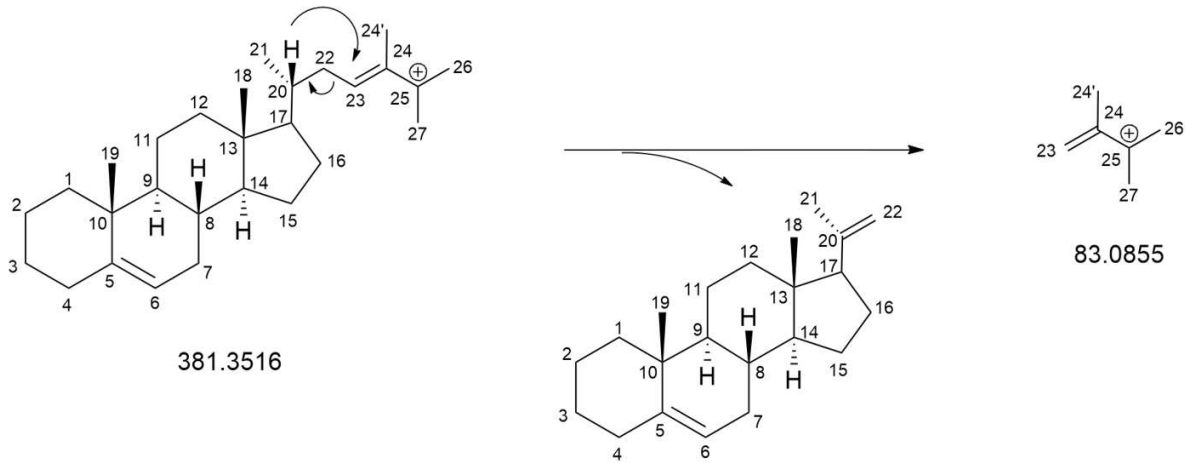


Figure A1. Proposed fragmentation mechanism for the generation of a product ion with exact *m/z* 83.0855, consistent with one of the peak signals detected in the APCI(+)-HCD-FTMS/MS spectrum of the sterol eluting at 27.2 min in the EIC chromatogram obtained for *m/z* 381.3516 upon RPLC-APCI(+)-FTMS analysis of a kale microgreen extract (**Figure 2C**). The sterol was tentatively identified as 24-methylcholesta-5,23E-dien-3β-ol, based on its MS/MS profile (see main text for details). Exact monoisotopic *m/z* ratios, rounded off to the fourth decimal place, are reported.

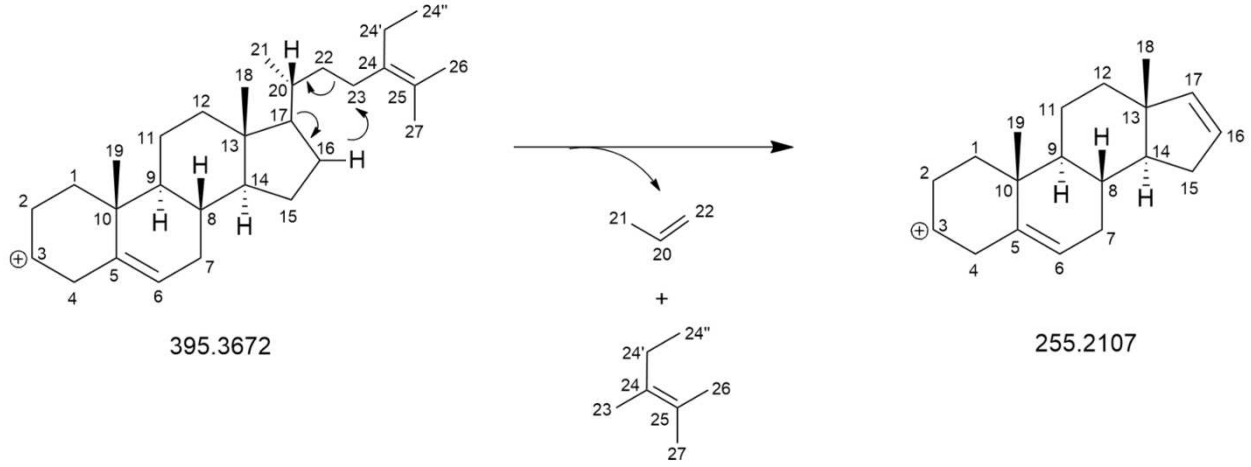


Figure A2. Proposed fragmentation mechanism for the generation of a product ion with exact *m/z* 255.2107, consistent with one of the peak signals detected in the APCI(+)-HCD-FTMS/MS spectrum of the sterol eluting at 30.2 min in the EIC chromatogram obtained for *m/z* 395.3672 upon RPLC-APCI(+)-FTMS analysis of a kale microgreen extract (Figure 2D). The sterol was tentatively identified as $\Delta^{5,24}$-stigmastadienol, based on its MS/MS spectrum. Exact monoisotopic *m/z* ratios, rounded off to the fourth decimal place, are reported.

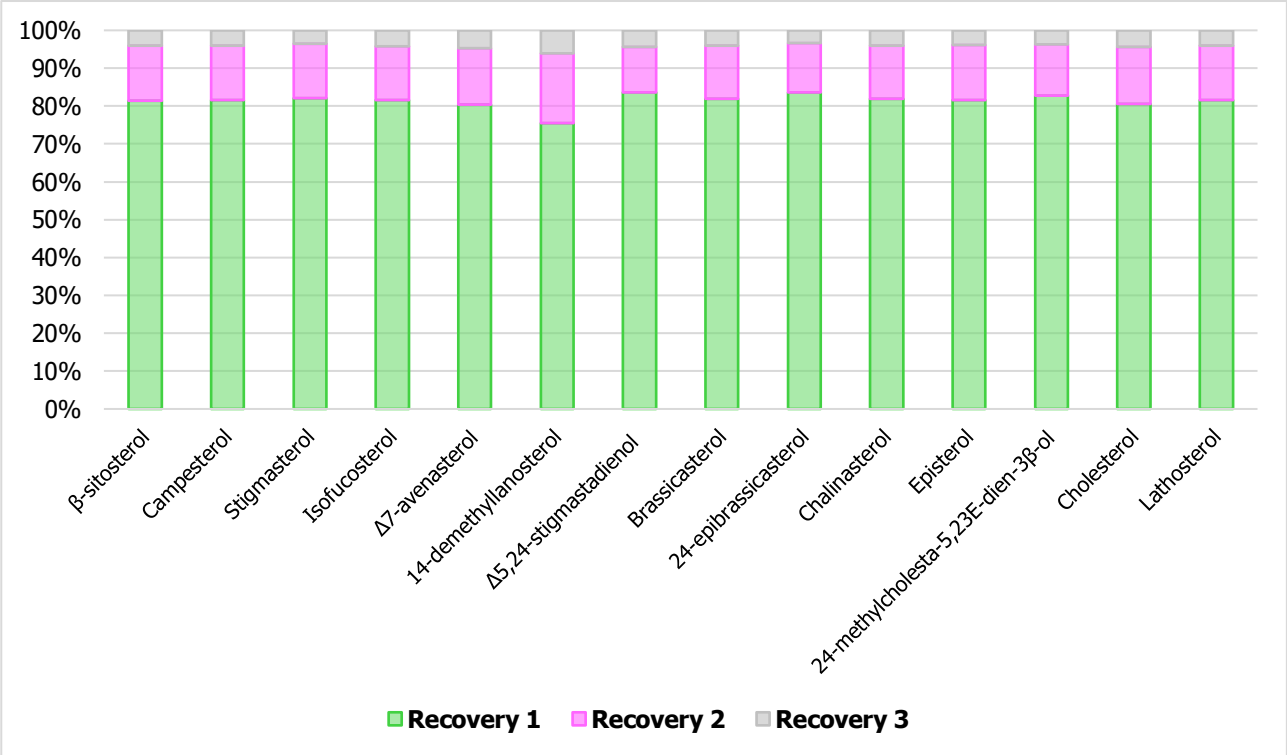


Figure A3: Stacked-bar graph reporting the average cumulative percentual recovery (n = 3) of main sterols detected in kale microgreens evaluated after each of three successive extraction steps.

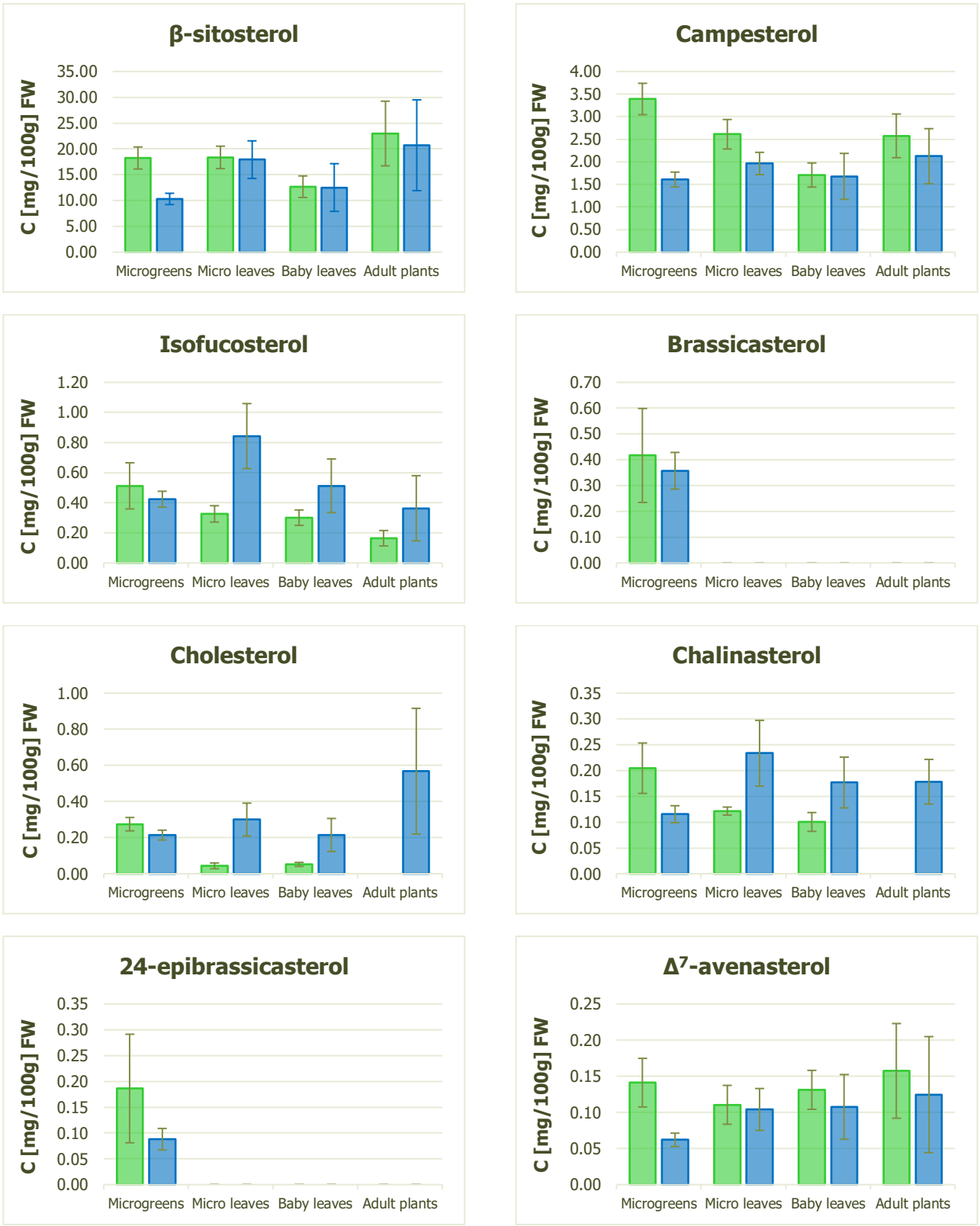


Figure A4: Bar graphs showing average concentrations of specific free sterols in winter-cultivated kale (green bars) and broccoli raab (blue bars) at different growth stages: microgreens, micro leaves, baby leaves and adult plants. Values are expressed as mg per 100 g fresh weight (FW), with error bars representing 95% confidence intervals (n = 5 biological replicates per product type).

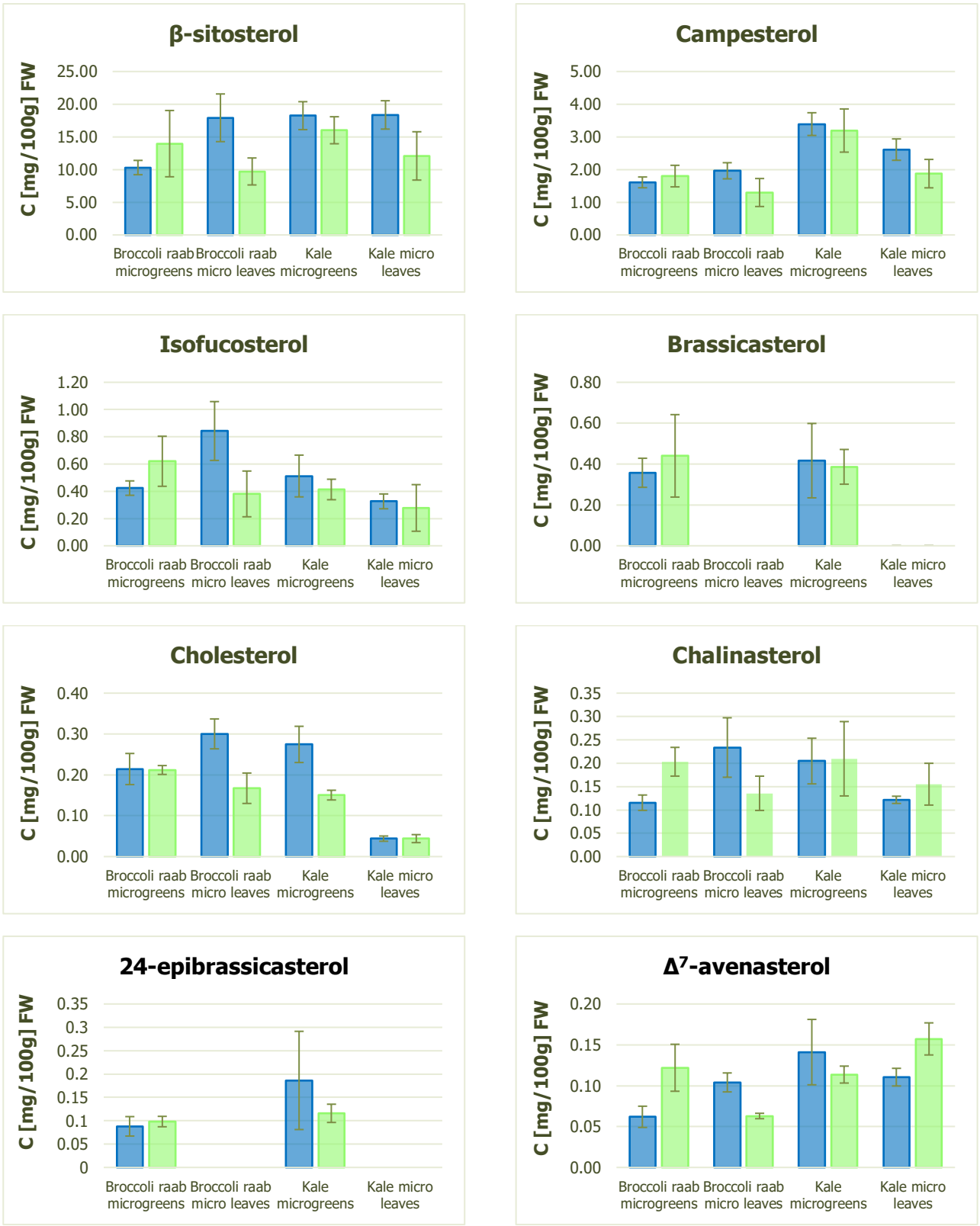


Figure A5: Bar graphs showing average free sterol concentrations (mg/100g FW) in microgreens and micro leaves of kale and broccoli raab grown in winter (blue bars) and spring (green bars). Error bars represent 95% confidence intervals (n = 5 biological replicates).

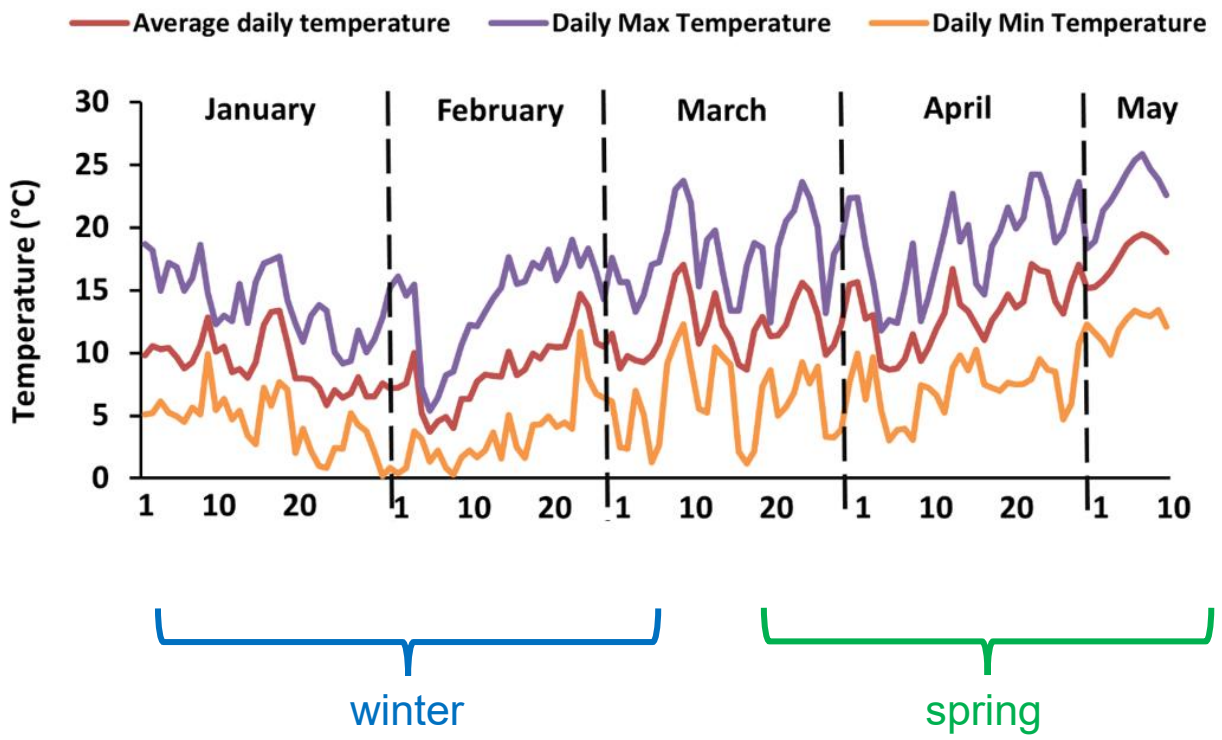


Figure A6. Average, minimum and maximum temperatures recorded inside the greenhouse during the two growing cycles (winter: January 9-March 9, 2023; spring: March 21-May 9, 2023) adopted for the cultivation of microgreens and micro leaves of kale and broccoli raab.

Table A1. Free sterol contents (mg/100 g FW) of mature kale and broccoli raab after steaming or boiling in water. Values represent 95% confidence intervals centred on means (n = 3).

Plant	Cooking method	β-sitosterol	Campesterol	Isofucosterol	Cholesterol	Chalinasterol	Δ^7-avenasterol
Kale	Steamed	23 ± 6	2.6 ± 0.6	0.18 ± 0.08	< LOD	< LOD	0.18 ± 0.10
	Boiled	18 ± 7	1.8 ± 0.6	0.16 ± 0.06	< LOD	< LOD	0.11 ± 0.06
Broccoli raab	Steamed	22 ± 5	2.3 ± 0.8	0.42 ± 0.14	0.67 ± 0.17	1.1 ± 0.2	0.12 ± 0.03
	Boiled	27 ± 9	2.7 ± 1.3	0.9 ± 0.6	1.0 ± 0.4	3 ± 2	0.25 ± 0.17

Chapter 4

Quantification of carotenoids and α-tocopherol in innovative and conventional Brassica vegetables by RPLC-APCI-FTMS

4.1. Introduction

Carotenoids and α-tocopherol stand out among secondary vegetal metabolites for their essential role in plant physiology and, when introduced through diet, also in human health[1–3]. Carotenoids are liposoluble compounds synthesized by photosynthetic organisms, mainly plants, where they accumulate in different cellular compartments according to their function. In the chromoplasts of non-photosynthetic tissues, carotenoids impart colour that attracts pollinating insects. Additionally, they assist photosynthesis in the chloroplasts of photosynthetic tissues by acting as light collectors while, under conditions of excess energy, they activate the xanthophyll cycle and act as photoprotectors, inhibiting the formation of singlet oxygen and thus preserving lipids and membrane proteins from oxidative damage[2,4–7]. Like carotenoids, α-tocopherol is biosynthesized by eukaryotic organisms, essentially plants, and it is found in the membrane and plastoglobuli of chloroplasts. Inside plants, α-tocopherol regulates membrane fluidity and permeability, similarly to cholesterol in animal cells, and also exerts a powerful antioxidant action by protecting lipids from peroxidation caused by reactive oxygen species (ROS), modulating their accumulation[3,8,9].

From a chemical point of view, carotenoids are tetraterpenoids arising from the condensation of eight isoprene units, which constitute their all-*trans* conjugated acyclic backbone[4,10,11]. This structure is modified by several enzymatic processes such as cyclization at one or both ends, hydrogenation, dehydrogenation, chain modifications, isomerization and oxidation[10,11]. In cyclic carotenoids, the polyene chain is provided with end groups (*e.g.*, β, ε, ψ, γ, φ, χ, κ) that modulate the conjugation length and, consequently, their antioxidant activity, as well as their spectroscopic and chemical properties[1,12]. In fact, through the extended conjugate system of π electrons, carotenoids are able to scavenge ROS, including singlet oxygen and peroxyl radicals[13–16]; the polyenic chain ensures the characteristic absorption in the visible region but, contextually, makes carotenoids prone to degradation reactions[2,4,10]. According to their elemental composition, carotenoids are divided into carotenes, *i.e.* hydrocarbon compounds, and xanthophylls, which contain oxygenated functional

groups, including hydroxyl, epoxy and carbonyl ones, that modulate their polarity as well as their role in plant cell membranes[2,13,17].

The structures of the most relevant plant carotenoids including cyclic moieties, in terms of abundance and bioactivity, are reported in **Figure 1**. β-carotene, whose carbon atoms are numbered in the figure according to International Union of Pure and Applied Chemistry (IUPAC) rules[11], includes a central polyenic chain and two β-end groups. β-carotene is the predominant carotenoid in coloured fruits and vegetables and, due its 11 conjugated C=C double bonds, exhibits a strong antioxidant activity[16,18] .

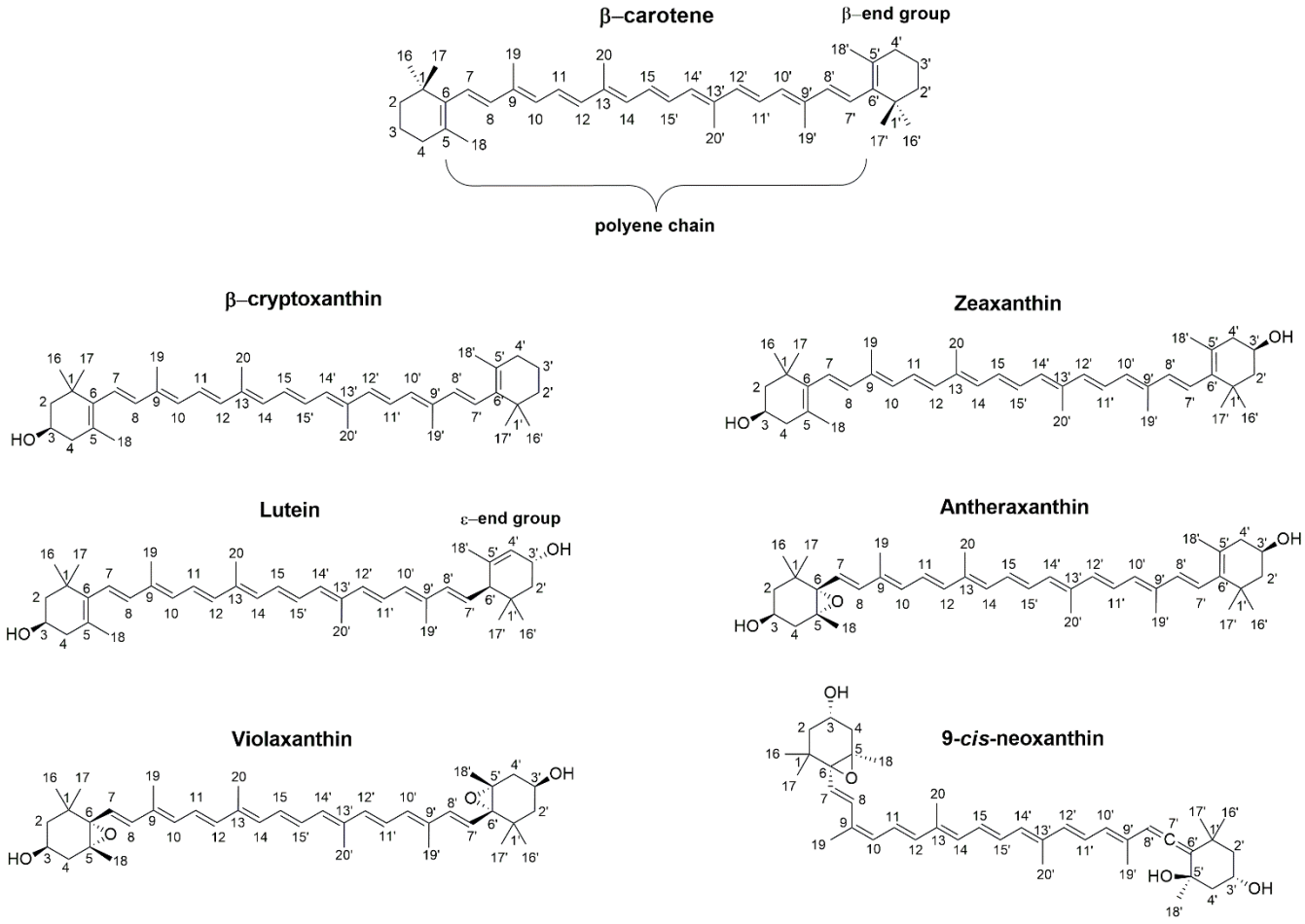


Figure 1. Chemical structures of the most representative carotenoids occurring in plants. β-Carotene, taken as a model compound for the carotene subclass, was numbered according to IUPAC recommendations, highlighting the characteristic conjugated polyenic chain and the two β end-groups. Representative xanthophylls are also illustrated, including isomeric β-cryptoxanthin, zeaxanthin and lutein (the latter characterized by the presence of an ε end-group), as well as the epoxy xanthophylls antheraxanthin, violaxanthin and 9-*cis*-neoxanthin.

The corresponding hydroxylated xanthophylls are β-cryptoxanthin and zeaxanthin, which share the same polyene chain and include an -OH group on one or both β-end groups, respectively. Lutein, one of the most important isomers of zeaxanthin, is characterized by the presence of a β- and an ε-end group, the latter partially interrupting conjugation. Lutein represents 50% of total carotenoids in chloroplasts and it is the most abundant carotenoid in leaves and green vegetables[6,10]. Epoxy xanthophylls include antheraxanthin and violaxanthin which, along with zeaxanthin, are involved in the xanthophyll cycle[4,19]. Finally, 9-*cis*-neoxanthin is an hydroxyl-epoxy xanthophyll, also known as photosynthetic xanthophyll, since it plays a fundamental role to transfer energy to chlorophyll in reaction center[6,20].

α-tocopherol is an amphipathic molecule belonging to the group of isoprenoid chromanols and consisting of the hydrophilic chromanol ring and a liposoluble phytyl side chain[3]. **Figure 2** illustrates the prevailing form of α-tocopherol in nature, also numbered according to IUPAC rules[21]. It is characterized by a 2*R*,4'*R*,8'*R* stereochemistry and is also called d-α-tocopherol or RRR-α-tocopherol[3,22].

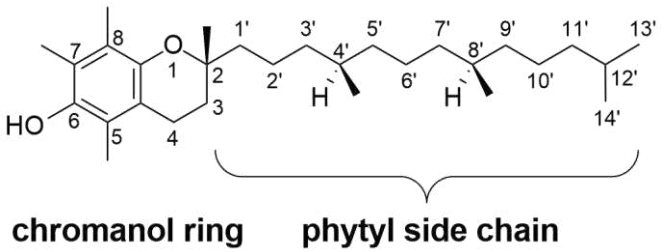


Figure 2. Chemical structure of α-tocopherol, numbered according to IUPAC rules, in the configuration 2*R*,4'*R*,8'*R* corresponding to the most abundant form in nature, *i.e.* RRR-α-tocopherol. The chromanol ring and phytyl side chain were highlighted.

α-tocopherol is the most widespread and bioactive form in nature[3,8] among several tocopherols and tocotrienols representing the vitamers of vitamin E. Its antioxidant properties are related to the methyl groups linked to the chromanol ring, which make the hydrogen atom in the hydroxyl group bound to C6 prone to transfer to the peroxyl radicals[8,9].

Beyond their physiological functions in plants, carotenoids and α-tocopherol are commonly recognized for their beneficial effects on human health[15], with protective roles against oxidative stress-related pathologies, including certain cancers, metabolic disorders, and cardiovascular and neurodegenerative diseases [3,22,23]. Moreover, β-carotene, α-carotene and β-cryptoxanthin show a strong provitamin A activity, acting as precursors of retinol, thus preventing diseases such as cataracts and age-related macular degeneration[15,24]. Eye health is also related to lutein and zeaxanthin, which accumulate physiologically in the macula of the human retina, contributing to visual performance and photoprotection[25,26]. α-tocopherol is the most bioactive form of vitamin E in mammals due to its selective retention in the body through the action of a specific hepatic *α-tocopherol transfer protein* (α-TTP)[9,22]. α-tocopherol is an essential compound for preserving the immunity system and its deficiency is associated with neurologic and muscle damage[8,22].

Since humans, as well as animals, are unable to synthesize carotenoids and α-tocopherol, the intake of these bioactive metabolites can occur only through diet, especially if it is rich in vegetables[3,5]. In recent years, the research in the field of vegetal food products has shown a growing interest in vegetables harvested in the early stages of growth, like the so-called microgreens and baby leaves, demonstrating that they can often be richer in bioactive substances than the corresponding mature forms[27–29]. In this context, the present study aims to quantify carotenoids and α-tocopherol in early growth stage vegetables and, for comparison, in adult forms of kale (*Brassica oleracea* L. var. *acephala*) and broccoli raab (*Brassica rapa* L. subsp. *sylvestris* L. Janch. var. *esculenta* Hort.), two plants of the *Brassicaceae* family, whose members has been already studied as sources of bioactive compounds[30,31]. In particular, microgreens, micro leaves and baby leaves, *i.e.*, products harvested at phenological stages marked by the formation of an increasing number of true leaves, were investigated[27,32]. These innovative vegetables are typically grown in hydroponic systems, that require a lower water and agrochemical consumption than conventional agriculture[27,33] and enable a precise control of the composition of nutritional solutions, also facilitating specific biofortifications[27,28,34,35]. In addition, the use of supplemental LED lighting during cultivation can be exploited to increase the

accumulation of bioactive compounds, including carotenoids and α-tocopherol[36–38]. These innovative products can be marketed together with their growing medium, allowing harvesting immediately before consumption, which minimizes the enzymatic degradation associated with cutting. Moreover, they can be eaten without prior cooking, thus preserving thermolabile bioactive compounds[27,35,39].

In the literature, several studies have being dedicated to the analysis of carotenoids and α-tocopherol in *Brassica* microgreens, baby leaves and adult forms, but focusing mainly on the main carotenoids (*e.g.* β-carotene, lutein, zeaxanthin, violaxanthin)[32,40–48], and thus neglecting the contribution of minor isomeric species, which can be relevant in terms of total carotenoid content and discrimination between growth stages. The present study aims to fill this gap through the development and validation of a quantitative method based on reversed phase liquid chromatography coupled to Fourier transform mass spectrometry with atmospheric pressure chemical ionization source (RPLC-APCI-FTMS). Specifically, a ternary gradient elution was developed employing a C18 stationary phase which, compared to the C30 phase often used for the separation of carotenoids, enabled shorter analysis times while ensuring a suitable separation of xanthophylls, the most abundant class of carotenoids in green leafy matrices. APCI was selected for its better ionization efficiency compared to electrospray ionization (ESI), based on the predominant generation of $[M+H]^+$ or $[M+H-H_2O]^+$ ions, minimizing signal dispersion on additional ionic species, such as the radical cation $[M]^{\cdot+}$ [17,49], and providing characteristic in-source fragmentation patterns, that were very useful to relate minor isomeric carotenoids to the respective major counterparts. Contextually to the quantitative approach, a comprehensive qualitative investigation was undertaken to elucidate the structure of the carotenoid isomers detected in plant samples. To this end, UV-Vis absorption spectroscopy was employed as one of the detection approaches, as, due to the intrinsic absorption properties of carotenoids, it can provide information-rich fingerprints for carotenoid recognition[10,50]. In addition, due to the inability of tandem mass spectrometry (MS/MS) to discriminate between carotenoid isomers[51,52], travelling wave ion mobility spectrometry-mass spectrometry (TWIM-MS) and ion mobility spectrometry-tandem mass spectrometry (IMS-MS/MS) analyses were integrated into the analytical workflow. By allowing gas-

phase separation of ions based on their size, shape and three-dimensional conformation, ion mobility spectrometry (IMS) provides a supplementary and independent dimension of separation beyond *m/z* ratio, defined by drift time and collision cross section (CCS). When coupled with MS/MS, this approach enables the selective fragmentation of mobility-resolved species, thereby facilitating a more accurate structural elucidation of isomeric carotenoids. Overall, the combined use of UV-Vis spectroscopy, TWIMS-MS and IMS-MS/MS provided useful structural information on several xanthophyll isomers, which is fundamental, given the close relationship existing between the molecular structure of carotenoids and their bioactivity[16,53]. Moreover, the inclusion of minor isomers strengthened the quantitative analysis, enabling a deeper comparison of the carotenoid profiles across different phenological stages and ultimately supporting a more robust assessment of their nutritional relevance in *Brassica* vegetables.

4.2. Materials and methods

4.2.1 Chemicals. LC-MS grade isopropanol (i-PrOH), acetonitrile (ACN), water (H_2O) and formic acid (FA), employed for mobile phase preparation, along with HPLC grade hexane, GC grade acetone and ethanol (EtOH), used for the preparation of stock solutions and/or for the extraction of carotenoids from vegetal matrices, and butylhydroxytoluene (BHT), adopted as antioxidant agent, were acquired from Merck (Milan, Italy). Standards of β-carotene, zeaxanthin and lutein were bought from Cayman Chemical (Ann Arbor, MI, USA). Standards of β-cryptoxanthin, 9-*cis*-antheraxanthin, violaxanthin, 9-*cis*-neoxanthin, (±)-α-tocopherol and vitamin K_2 were purchased from Merck (Milan, Italy). Poly-DL-alanine, employed to build a collision cross section calibration curve, was bought from Merck (Milan, Italy). Solutions for the calibration of the Q Exactive mass spectrometer under positive or negative polarity conditions were purchased from Thermo Scientific (Waltham, MA, USA). Leucine-Enkephalin, used as lock mass solution for the Synapt G2-S HDMS mass spectrometer, was acquired from Waters™ (Milford, MA, USA).

4.2.2 Plants cultivation. Microgreens, micro leaves and baby leaves subjected to the extraction and analysis of carotenoids and α-tocopherol were cultivated using a hydroponic system in a greenhouse located at the University of Bari Aldo Moro (41°06' N, 16°52' E; Southern Italy). The cultivation cycle was conducted in winter, specifically from January 9 to March 9, 2023, involving two different genotypes of *Brassicaceae*: *Brassica rapa L. subsp. sylvestris L. Janch. var. esculenta Hort*, local variety 'Cima di rapa novantina' (broccoli raab); *Brassica oleracea L. var. acephala*, local variety 'Cavolo riccio' (kale). High quality seeds, with 95% germination at a constant temperature of 20 °C, were adopted. Details on microgreens, micro leaves and baby leaves cultivation can be found in **Section A1** of the Appendix to Chapter 3.

The same genotypes of kale and broccoli raab were also grown in the same period of the year in an open field in Valenzano (geographical co-ordinates: 41°03′N 16°53′E; Southern Italy), to obtain their mature counterparts. In this case, plants were also subjected to cooking by either steaming or boiling. Details on cultivation and cooking procedures for adult forms are reported in **Section A2** of Appendix 3.

4.2.3 Sample preparation. Once the plant samples were harvested at the appropriate phenological stages, they were stored at −20 °C to preserve carotenoids and α-tocopherol from degradation inducted by heat. After four days of storage, the material was freeze-dried for five days using a ScanVac CoolSafe 55-9 Pro freeze dryer (LaboGene ApS, Lynge, Denmark). The freeze-dried material obtained from about 600 microgreens, 10 micro leaves, 5 baby leaves and 3 mature plants of both kale and broccoli raab was manually ground and put aside. For each sample type, the homogenized material, consisting of stems, leaves and, in the case of mature plants, inflorescences, was transferred to individual Falcon tubes and stored at -18 °C until carotenoids and α-tocopherols were extracted and analysed.

4.2.4 Sample extraction. The extraction of carotenoids and α-tocopherol from *Brassica* vegetables was carried out following the protocol of Guzman *et al.*[40] with slight modifications. In detail, 50 mg of freeze-dried plant material were weighed and pounded with a mortar to obtain a more homogenous powder, which was then suspended in 1.25 mL of EtOH containing 0.1% (w/v) BHT. The resulting suspension was placed in an ice bath and sonicated for 15 min in the dark. After centrifugation for 10 min the supernatant was collected, and the procedure was repeated four times on the pellet. The supernatants obtained after the sequential extraction steps were joined and dried under a nitrogen flow. Afterwards, the dry residue was redissolved in 500 µL of EtOH and the resulting solution was transferred to Eppendorf tubes and subjected to ultracentrifugation for 15 min at 14500 rpm, to separate eventual solid residues. The final supernatant was collected and diluted 1:1 in ACN, then 5 mL of a 1000 µg/mL solution were added to reach a 10 µg/mL concentration of vitamin K2, to be used as internal standard (IS), before proceeding to RPLC-DAD-APCI-FTMS and RPLC-ESI-IMS analyses. Notably, the described extraction protocol was performed at low temperature and in the dark, also adding an antioxidant agent to the extraction solvent, to prevent endogenous carotenoids and α-tocopherol from undergoing degradation reactions, such as isomerization and oxidation[3,17].

4.2.5 Standard solutions. Stock solutions of each standard (1000 mg/mL) were prepared in a hexane:acetone:ethanol (2:1:1 v/v) solution containing 0.1% (w/v) of BHT. A solution of each standard was prepared at a concentration of 10 mg/mL in ACN for qualitative purposes. Calibration curves were then obtained for β-carotene, β-cryptoxanthin, lutein, violaxanthin, 9-*cis*-neoxanthin and (±)-α-tocopherol, each involving six calibration levels, prepared by appropriate dilution of stock solutions in ACN, with values depending on the concentrations expected in plant samples: 1, 5, 10, 25, 50 and 100 mg/mL for β-carotene, violaxanthin and α-tocopherol; 0.1, 0.5, 1, 5, 25, and 50 mg/mL for lutein; 0.1, 0.5, 1, 2.5, 5 and 10 mg/mL for β-cryptoxanthin and 9-*cis*-neoxanthin.

4.2.6 RPLC-DAD-APCI-FTMS instrumentation and operating conditions. Calibration solutions and plant samples extracts were analysed using an Ultimate 3000 HPLC quaternary chromatographic system equipped with diode array detector (DAD) and coupled with a Q Exactive high-resolution quadrupole-Orbitrap mass spectrometer through an APCI interface (Thermo Fisher, West Palm Beach, CA, USA). Carotenoids and α-tocopherol separation was achieved using a C18 Ascentis Express HPLC column (150 × 2.1 mm i.d., 2.7 μm particle size) (Supelco, Bellefonte, PA) and the following multi-step ternary elution gradient, based on ACN as phase A, ACN:iPrOH (80:20 v/v) solution as phase B and H_2O as phase C, all containing 0.1% (v/v) FA: 0-15 min, isocratic at 85% A, 0% B and 15% C; 15-17 min, linear increase of B from 0% to 35%, linear decrease of A from 85% to 63% and of C from 15% to 2%; 17-47 min, linear increase of B from 35% to 98%, linear decrease of A from 63% to 0% and isocratic at 2% C; 47-50 min, isocratic at 0% A, 98% B and 2% C; 50-52 min, linear decrease of B from 98% to 0% and linear increase of A from 0% to 85% and C from 2% to 15%; 52-60 min, reconditioning at 85% A, 0% B and 15% C. Flow rate was set at 0.250 mL/min and column temperature was kept at 35°C; 5 μL sample volumes were injected. For the acquisition of UV-Vis spectra after RPLC separations, the Diode Array Detector (DAD) was employed setting the following parameters: minimum acquisition wavelength) 190 nm; maximum acquisition wavelength) 800 nm; bunch width) 1 nm; data collection rate) 5 Hz; response time) 2 s. The parameters of the APCI interface and of the ion optics of the Q Exactive spectrometer were set as follows: sheath gas flow rate) 40 a.u.; auxiliary gas flow rate) 10 a.u.; sweep gas flow rate) 5 a.u.; discharge current) 5 μA; capillary temperature) 300 °C; S-lens RF Level) 55 a.u.; vaporizer temperature) 250°C. Full MS acquisitions in positive ion mode were performed in a 300-1200 *m/z* interval at the maximum resolving power of the mass spectrometer (140000 at *m/z* 200); the Automatic Gain Control (AGC) level for the orbital trap filling was set at 1×10^6 and the maximum injection time was 100 ms. The spectrometer was calibrated every two days by infusing, at a 30 μL/min flow rate, calibration solutions for positive or negative polarity acquisitions; a mass accuracy always better than 5 ppm was achieved.

4.2.7 RPLC-ESI-TWIMS-MS and MS/MS instrumentation and operating conditions. Standard carotenoid solutions and plant samples extracts were analysed using an Acquity UPLC binary chromatographic system coupled with a Synapt G2-S HDMS Travelling Wave Ion Mobility hybrid quadrupole-Time of Flight mass spectrometer through a z-spray electrospray interface (Waters™, Milford, MA, USA). In order to obtain a carotenoid separation similar to the one achieved using the Ultimate 3000 HPLC quaternary chromatographic system, the same C18 column was employed but, due to the availability of a binary chromatograph, the ternary gradient had to be converted into the following multi-step binary gradient, using a ACN:H_2O (85:15 v/v) mixture as phase A and a ACN:iPrOH (80:20 v/v) mixture as phase B, both containing 0.1% (v/v) FA: 0-15 min, isocratic at 100% A; 15-17 min, linear increase of B from 0% to 35%; 17-47 min, linear increase of B from 35% to 98%; 47-50 min, isocratic at 98% B; 50-52 min, linear increase of A from 2% to 100%; 52-60 min, reconditioning at 100% A. The flow rate was set at 0.250 mL/min and the column temperature was kept at 35°C; 5 µL sample volumes were injected. The parameters of the ESI interface were set as follows: capillary voltage) 2.5 kV; cone voltage) 40 V; source offset voltage) 80 V; source temperature) 120 °C; desolvation temperature) 500 °C; cone gas flow) 50 L/h; desolvation gas flow) 800 L/h; nebuliser gas pressure) 6.0 bar. A leucine-enkephalin solution (2 ng/µL), used as lock mass (*m/z* 556.2771), was infused in the mass spectrometer at a 15 µL/min flow rate. The parameters for traveling wave ion mobility spectrometry (TWIMS) measurements were set as follows: *TRIWAVE DC* - Trap DC: Entrance) 3; Bias) 60; Trap DC) 0; Exit) 3; IMS DC: Entrance) 25; Helium cell DC) 35; Helium exit) −5; Bias) 3; Exit) 0; Transfer DC: Entrance) 3; Exit) 3; *TRIWAVE* - Trap: Wave velocity) 311 m/s; Wave height) 4 V; IMS: Wave velocity) 530 m/s; Wave height) 40 V; Transfer: Wave velocity) 191 m/s; Wave height) 4 V. In the ion mobility cell, the He gas flow was set at 180 mL/min and the N_2 gas flow was set at 90 mL/min. The EDC delay coefficient was specified as 1.58 V. Full IMS acquisitions in positive ion mode were performed in a 50-2000 *m/z* scan range in V mode. Full IMS-MS/MS acquisitions were acquired in transfer fragmentation mode, using a fixed collision energy of 15 V.

4.2.8 Collision cross section calibration curve. Once the ESI and TWIMS parameters were optimized, ion mobility measurements were performed by infusing a 1 mg/mL solution of poly-DL-alanine in ACN:H_2O (50:50 v/v) for 3 min at a flow rate of 10 μL/min. The acquired data were processed using Driftscope 2.1 (Waters™, Milford, MA, USA) software, to generate the CCS calibration curve based on the corresponding reference database. Once the CCS = *f*(drift time) calibration function was established, experimental CCS values were obtained by extrapolation from the measured drift times.

4.3. Results and discussion

4.3.1 Identification of carotenoids and α-tocopherol by RPLC-DAD-APCI(+)-FTMS analysis. Extracted Ion Current (EIC) chromatograms related to the monoisotopic *m/z* values of specific carotenoids and α-tocopherol $[M+H]^+$ (plot A, C, D and E) ions, and of lutein $[M+H-H_2O]^+$ ion (plot B), obtained after the RPLC-APCI(+)-FTMS analysis of the kale microgreen extract are shown in **Figure 3** as an example of the separation achieved using the elution program developed during this study. The combination of the C18 stationary phase with a ternary elution gradient, in which the elution strength of the mobile phase was finely modulated, enabled the separation of carotenoids based on subtle differences in polarity, degree of oxygenation and geometric configuration, leading to the distinct detection of 28 compounds of interest, including α-tocopherol, the main carotenoids and a wide array of other isomeric carotenoids. As inferred from plot A, referred to $[M+H]^+$ ions with monoisotopic *m/z* 601.4251, the initial (15 min) isocratic stage based on 85% ACN and 15% H_2O allowed the separation of 9-*cis*-neoxanthin and violaxanthin, which, as confirmed by the corresponding standards, eluted after 3.4 minutes and 4.4 minutes, and of 10 further species isomeric with them.

In detail, 9-*cis*-neoxanthin eluted earlier than its isomer violaxanthin due to its higher overall polarity, which arises from the presence of three hydroxy groups, one epoxy moiety, an allene functionality and also by the *cis* configuration of the C=C double bond at C9 (see **Figure 1**), which induces a kink

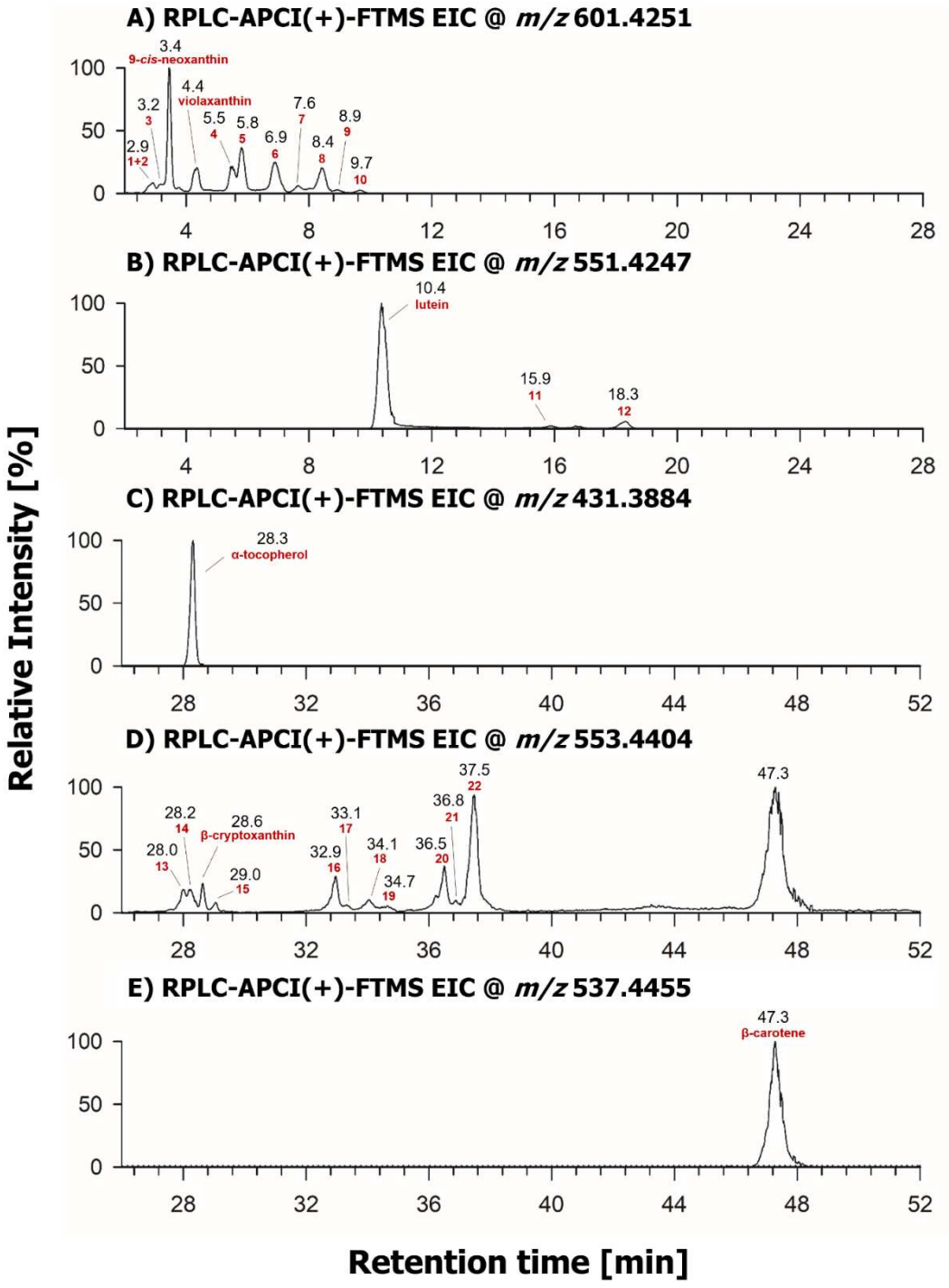


Figure 3. Extracted ion current (EIC) chromatograms obtained by RPLC-APCI(+)-FTMS analysis of a kale microgreens extract for selected carotenoids and α-tocopherol. Plot A shows the EIC at *m/z* 601.4251, corresponding to the $[M+H]^+$ ions of 9-*cis*-neoxanthin, violaxanthin and their isomers. Plot B reports the EIC at *m/z* 551.4247, assigned to the $[M+H–H_2O]^+$ ion of lutein. Plot C displays the EIC for $[M+H]^+$ ion at *m/z* 431.3884 of α-tocopherol. Plot D shows the EIC at *m/z* 553.4404, corresponding to the $[M+H]^+$ ion of β-cryptoxanthin and its isomers. Plot E reports the EIC for $[M+H]^+$ ion at *m/z* 537.4455 of β-carotene. Peaks labelled with compound names correspond to analytes identified using authentic standards, whereas numbered peaks indicate carotenoid isomers tentatively assigned based on the combined chromatographic retention and high-resolution mass spectrometric data (see text for details).

in the polyene chain, potentially reducing the hydrophobic interaction with the C18 chains of the stationary phase. On the other hand, violaxanthin bears one hydroxy group and one epoxy moiety on each end group and displays an all-*trans* polyene chain, features that are expected to reduce polarity and thus increase the retention on the C18 stationary phase. As illustrated in plot B, referred to its $[M+H-H_2O]^+$ ion (monoisotopic *m/z* 551.4247), lutein, which is characterized by just two OH groups, one on each end group, elutes even later (10.4 min), as confirmed by the corresponding standard, and its peak is followed by those of two minor isomeric species (peaks labelled as 11 and 12), eluting at 15.9 and 18.3 min, respectively. It is worth noting that zeaxanthin and 9-*cis*-antheraxanthin, whose analytical standards were analysed distinctly under the same chromatographic conditions, were not detected in any of the broccoli raab and kale samples investigated.

As expected, α-tocopherol, β-cryptoxanthin and a group of potential isomers (corresponding to peaks labelled as 13 to 22 in **Figure 3**), as well as β-carotene, *i.e.,* less oxygenated or fully aliphatic compounds, were eluted at longer retention times from the C18 stationary phase, owing to the increased elution strength of the mobile phase provided by isopropanol. Specifically, α-tocopherol, which likely interacts with the C18 stationary phase mainly through its phytyl side chain[54], eluted at 28.3 min, as confirmed by the corresponding standard (see plot C). Further vitamers belonging to vitamin E group, including β-tocopherol, γ-tocopherol, δ-tocopherol and the corresponding tocotrienols, were searched for but not found in the examined samples, as they are typical of seeds[3,8]. Peaks related to β-cryptoxanthin (28.6 min) and to ten further isomeric species can be distinguished in plot D of **Figure 3**, where the EIC chromatogram of the $[M+H]^+$ ion with monoisotopic *m/z* 553.4404 is reported. It should be noted that β-cryptoxanthin and α-tocopherol showed comparable retention on the C18 stationary phase, likely due to a comparable balance between their hydrophobic and polar moieties. In β-cryptoxanthin, retention is likely governed by the β-end group lacking the OH group, whereas in α-tocopherol it is expected to be predominantly driven by the aliphatic chain, as reported before. This hydrophobic contribution is, however, partially compensated by the chromanol ring, whose oxygenated functionalities and aromatic system increase polarity, resulting in

an overall interaction strength comparable to that of the polyene chain. Despite the lack of chromatographic separation, peaks related to the two compounds could be distinctly recognized, and then integrated, in the respective EIC traces, *i.e.*, by exploiting the separation in the *m/z* domain.

As shown in plot E of **Figure 3**, referred to the $[M+H]^+$ ion with monoisotopic *m/z* 537.4455, β-carotene was the last carotenoid eluted from the C18 column, at 47.3 min, due to its very low polarity. Notably, evidence for its partial oxidation in the APCI source was provided by the peak observed at the same retention time in plot D, whose *m/z* value is consistent with the β-carotene molecular structure modified by the presence of an O atom. Therefore, RPLC-APCI(+)-FTMS analysis indicated β-carotene as the only carotene detected, and this result was confirmed for all the analyzed vegetal products, thus highlighting that green leafy vegetables exhibit a more complex xanthophyll profile compared to that of carotenes.

In a subsequent step of the study, UV-Vis spectra and in-source fragmentation patterns inferred from APCI(+)-FTMS spectra of the unknown xanthophyll isomers clearly evidenced by EIC chromatograms shown in **Figure 3** were synergically combined with their retention times and this information was then compared with that arising from standard carotenoids to draw structural information about those isomers. Firstly, for many years UV-Vis spectroscopy has been considered the technique of choice for the identification of carotenoids because, through the absorption properties conferred by the conjugate system, it can provide key information on the chromophore structure and geometric isomerism. In detail, the absorption spectrum of carotenoids is usually characterized by three wavelengths of maximum absorption (λ_{abs}), which are characteristic of each chromophore. The shape of the spectrum, which coincides with the vibrational fine structure, is commonly described quantitatively as the D_{III}/D_{II} ratio, *i.e.* the ratio between the heights of the third and the second peak of maximum absorption, that reflects the extent of the π-electron conjugation and thus offers information on the number of conjugated C=C bonds. In addition, the presence of a double bond with a *cis* configuration induces both hypsochromic and hypochromic shift with respect to the corresponding all-*trans* carotenoid and gives rise to the so-called *cis* peak. The D_B/D_{II}, *i.e.* the ratio

between the heights of the *cis* peak and the second peak of maximum absorption, is used to infer the position of the *cis* double bond along the polyene chain. On the other hand, as already highlighted by several studies, the pattern of fragmentation occurring inside the MS ionization source indicates the occurrence of allyl -OH groups[51,55,56] and, as described below, provides information on the number of free OH groups potentially present in the carotenoid structure. Therefore, in order to obtain a first classification of xanthophyll isomers based on APCI in-source fragmentation patterns, Principal Component Analysis (PCA) was performed considering as variables the relative intensity values related to $[M+H]^+$ and $[M+H-nH_2O]^+$ ions (with n = 1-4) detected in the full-MS spectrum of each carotenoid separated during the RPLC-APCI(+)-FTMS analysis of a kale microgreens extract, chosen as a model matrix for all the products under study. Those intensity values, which are reported in **Table A1** of the Appendix to this chapter, were then integrated with values inferred from the APCI(+)-FTMS analysis of standards of 9-cis-neoxanthin, violaxanthin, lutein, b-cryptoxanthin and b-carotene.

Very interesting indications were inferred from the score plot and the loading plot related to the first two principal components obtained by PCA, reported in **Figure 4**. Firstly, points related to standards were very close, if not coinciding, with those related to the respective major carotenoids found in the kale microgreens extract. This finding indicates that the recognition of such compounds in the real sample was confirmed both by the alignment of retention times and by the strict similarity of in-source fragmentation patterns obtained for the corresponding standards. It also emphasizes indirectly the reproducibility of those patterns, which could be clearly assessed also when considering APCI(+)-FTMS spectra obtained for the same carotenoids in the other products of interest (data not shown). Additionally, the PCA score plot, in synergy with chromatographic information displayed in **Figure 3**, clearly indicated that unknown isomeric species clustered nicely with four specifics major xanthophylls, *i.e.*, violaxanthin, 9-cis-neoxanthin, lutein and b-cryptoxanthin, thus suggesting the occurrence of structural similarities with them. Based on this finding, objects related to unknown isomers were marked in the PCA scoreplot (and in the last column of **Table A1**) with a label vx, nx,

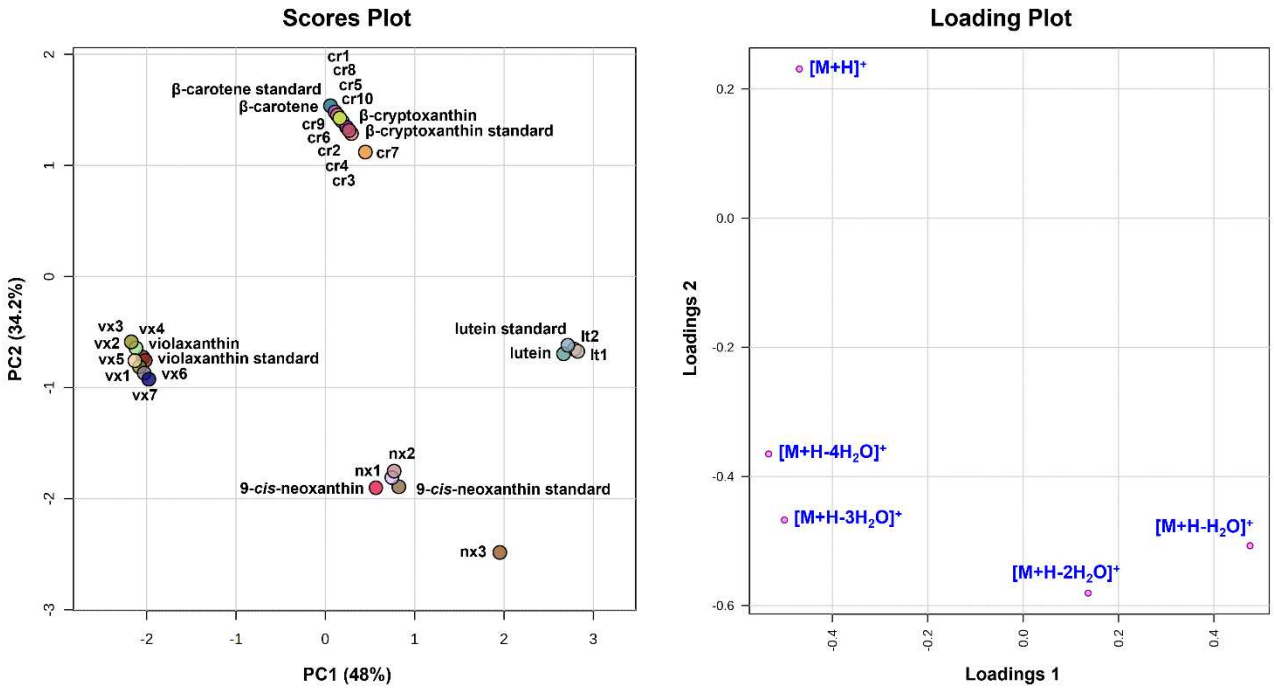


Figure 4. Scores and loading plots obtained for the first two principal components (PC1 and PC2) from the PCA performed on the relative intensity values of the $[M+H]^+$ and $[M+H-nH_2O]^+$ ions related to the in-source fragmentation pattern of carotenoids detected in the kale microgreens extract and, if available, of the corresponding standards.

lt or cr, respectively, followed by a progressive number reflecting their increased retention in the C18 column.

In detail, scores obtained for the PC1, accounting for 48% of total variance, clearly separated seven violaxanthin-related isomers (vx1-vx7, corresponding to peaks from 4 to 10 in **Figure 3**) from two lutein-related ones (lt1, lt2, corresponding to peaks 11 and 12 in **Figure 3**). On the other hand, isomers putatively related to b-cryptoxanthin (cr3-cr10, peaks 15-22) and 9-*cis*-neoxanthin (nx1-nx3, peaks 1-3) were very well separated along PC2 (accounting for 34.2% of total variance). As a result, four clusters of objects could be easily recognized in the PCA score plot. The loading plot shown in **Figure 4** explains how in-source fragmentation patterns led to this neat discrimination between groups of major xanthophylls and their putative isomeric species. Indeed, xanthophylls including two or more oxygen atoms, characterized by negative values of PC2, were generally characterized by a not surprising higher relevance of product ions resulting from water losses in the APCI(+)-FTMS spectrum. More specifically, 9-*cis*-neoxanthin and its putative isomers nx1-nx3 exhibited intense peak

signals for product ions $[M+H-H_2O]^+$ and $[M+H-2H_2O]^+$ (see **Table A1**), with the former ion representing even the base peak in the case of nx3. The relevance of this ion is likely attributable to the formation of an allylic carbocation at C5', *i.e.*, the carbon atom adjacent to the allene moiety (see **Figure 1)**, upon H_2O loss through a *charge-driven fragmentation* (CDF) following the protonation of the OH group linked to C5'. In this case, the subsequent loss as water of the OH group linked to C3', along with a H atom linked to C4', would turn C5' into a very stable bis-allylic carbocation, thus explaining why the second loss of water was also relevant in the case of 9-*cis*-neoxanthin. Since this behaviour was observed also for its putative isomers (nx1-nx3), it can be hypothesized that they likely share with 9-*cis*-neoxanthin an end group including two OH groups and an allene moiety. Given the lower retention times observed for nx1-nx2 compared to 9-*cis*-neoxanthin (see **Figure 3** and **Table A1**), those compounds might be isomers of this xanthophyll including either a *cis* double bond shifted toward the central region of the polyene chain or even two *cis* double bonds on the latter. As mentioned before, such structural features are expected to induce a more curved molecular conformation, thus reducing hydrophobic interactions with the C18 stationary phase and resulting in shorter retention times. To confirm this hypothesis, the UV-Vis data reported in **Table 1** were considered. Both nx1 and nx2 displayed hypsochromic shifts with respect to 9-*cis*-neoxanthin, whose assignment was unequivocally confirmed using the reference standard. Moreover, the corresponding D_B/D_{II} ratios were indicative of di-*Z* neoxanthin isomers, as their values closely matched those reported for di-*Z* violaxanthin isomers in the studies of Molnar *et al.*[57] and Meléndez-Martínez *et al.*[58]. In particular, considering that the most thermodynamically stable *cis* geometries are 9-*Z*, 13-*Z* and 15-*Z*, and their combinations for di-*Z*, and taking into account the observed retention time and D_B/D_{II} ratios, nx1 and nx2 were tentatively assigned to 9,15-di-*Z*-neoxanthin and 9,13-di-*Z*-neoxanthin, respectively, whose structures are reported in **Figure 5**.

As for nx3, its retention time is very similar to that of 9-*cis*-neoxanthin, yet it is characterized by a high intensity of the $[M+H-H_2O]^+$ ion, which in fact represents the base peak of the APCI(+)-FTMS spectrum (see **Table A1**). These results suggest that the right end group of 9-*cis*-neoxanthin, as

Table 1. Retention times and UV-Vis absorption spectra features of carotenoids detected in the kale microgreen extract. The wavelength of the *cis* peak (if present) and of the three typical carotenoids absorptions (λ_{abs}) and the spectral ratios D_B/D_{II} and D_{III}/D_{II} were reported. Tentative assignments for minor isomers, based on chromatographic retention times, absorption spectra-related information and APCI in-source fragmentation patterns, are reported in the last column, along with those of major carotenoids (evidenced by bold characters), resulting from the comparison with the respective standards. Note that β-cryptoxanthin and nine of the 10 isomers related to it are not included in the table because their UV-Vis absorption was overlapped by that of other matrix components co-eluting with them.

Compound	Retention time (min)	*cis* peak	λ_{abs}	D_B/D_{II}	D_{III}/D_{II}	Hypothesized carotenoid
nx1	2.8	328	(408),430,456	0.400	30	9,15-di-*Z*-neoxanthin
nx2	2.9	328	(408),430,456	0.370	10	9,13-di-*Z*-neoxanthin
nx3	3.2	/	400,422,449	/	90	(8R)-neochrome
9-*cis*-neoxanthin	3.4	328	413,436,465	0.095	80	**9-*cis*-neoxanthin**
violaxanthin	4.4	/	418,440,468	/	90	**violaxanthin**
vx1	5.5	/	400,422,448	/	80	(8S)-luteoxanthin
vx2	5.8	/	400,422,448	/	80	(8'R)-luteoxanthin
vx3	6.9	/	385,402,426	/	100	(8S,8'S)-auroxanthin
vx4	7.6	/	400,421,443	/	10	luteoxanthin like
vx5	8.4	/	385,402,426	/	100	(8R,8'S)-auroxanthin
vx6	8.9	/	405,425,449	/	10	luteoxanthin like
vx7	9.7	/	383,400,421	/	100	(8R,8'R)-auroxanthin
lutein	10.4	/	446,473	/	50	**lutein**
lt1	15.9	/	441,468	/	20	β-cryptoxanthin 5,6-epoxide
lt2	18.3	/	441,468	/	20	2-hydroxy-beta-carotene 5,6-epoxide
cr10	37.5	/	424,450	/	10	citroxanthin
β-carotene	47.3	/	452,476	/	10	**β-carotene**

displayed in **Figure 1**, is shared also with the nx3 isomer but do not clarify how the nx3 structure differs from that of its major counterpart. The spectral features observed after UV-Vis measurements, in particular the lack of the *cis* peak (see **Table 1**), suggested that no cis C=C bond is present on the nx3 molecular structure. Notably, the all-*trans* form of neoxanthin would be consistent with this observation, yet it should be eluted after 9-*cis*-neoxanthin from the C18 chain, but this was not the case. For this reason, nx3 might correspond to all-*trans*-neochrome and specifically, given the observed retention time, to (8R)-neochrome[50,51,59]. In this carotenoid, besides the geometry change from *cis* to *trans* of the C=C bond C9-C10 along the chain, the epoxydic moiety occurring in one of the end group of 9-*cis*-neoxanthin is turned into a furanoid moiety, with the former epoxydic O atom being linked to C8 and a C=C bond shifting from the C5-C6 to the C6-C7 position (see **Figure 5**).

This modification of the end group might lead to a lower retention on the C18 stationary phase, thus compensating for the higher interaction with the latter arising from the all-*trans* polyenic chain and ultimately leading to a slightly lower retention time compared to 9-*cis*-neoxanthin.

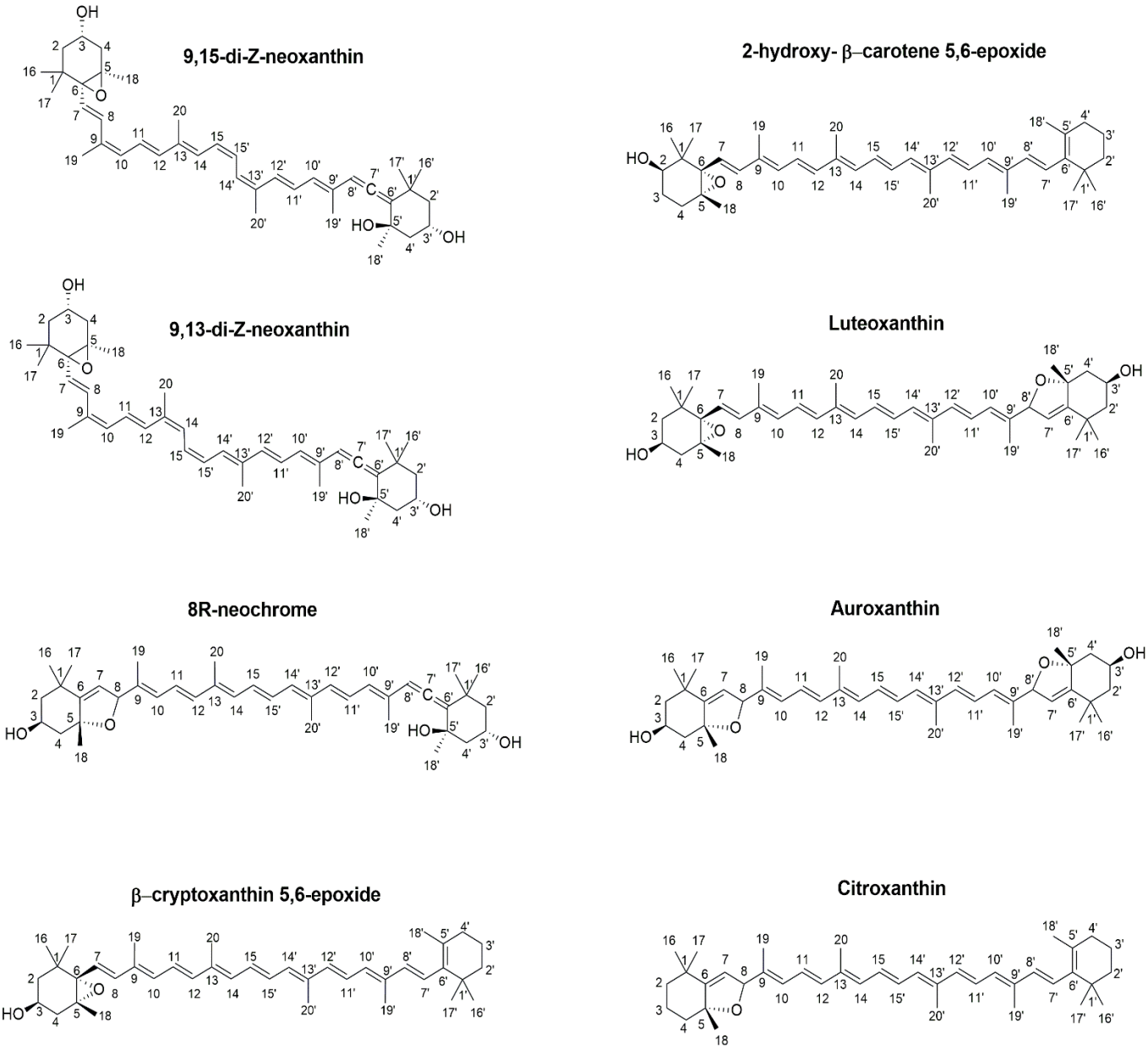


Figure 5. Chemical structures tentatively assigned to minor carotenoid isomers detected upon RPLC-APCI(+)-FTMS analysis of extracts of kale and broccoli raab innovative products and mature forms. General structures are shown for luteoxanthin and auroxanthin, for which the occurrence of different stereoisomers was hypothesized. See text and **Table 1** for details.

Notably, both nx1-nx3 and 9-*cis*-neoxanthin shared relatively high intensities also for peak signals in the APCI(+)-FTMS spectrum related to three or four total water losses (see **Table A1**). Based on the structures of 9-*cis*-neoxanthin and on those hypothesised for isomers nx1 and nx2, these losses must inevitably involve both the OH groups and the epoxide moiety located on the end groups (see **Figure 1**). In particular, the protonation of the epoxydic oxygen and the subsequent opening of the epoxide ring would lead to the transformation of either C6 or C5 into a carbocation, with the former being favoured, since it would be an allylic and tertiary carbocation. The subsequent b-elimination of water, with detachment of the OH group linked to C5 and a H atom from C4, would turn the latter into a stable bis-allylic carbocation. This mechanism, joined with the one previously described for the first water loss, suggests that different structures might be related to $[M+H-H_2O]^+$ ions for 9-*cis*-neoxanthin and isomers nx1-nx2. In the specific case, the three further water losses would clearly involve the remaining three OH groups or the two OH groups and the epoxide group, according to the case, whose loss would generate conjugated C=C bonds in both cases. As for the nx3 isomer, its putative assignment as 8R-neochrome is consistent with the observation of up to four in-source water losses. In this case, one of the structures potentially corresponding to the $[M+H]^+$ ion would arise from the initial protonation of the furanoid O atom, followed by the breakage of its bond with the C8 atom and thus the turning of the latter into a very stable bis-allylic carbocation, also susceptible to resonance of the positive charge on the polyenic chain. The subsequent loss of water, with detachment of the OH group located on C5 and a H atom linked to C4 would lead to a further extension of this resonance. This feature might explain the characteristic abundance observed for the $[M+H-H_2O]^+$ ion in the APCI spectrum of isomer nx3 (see **Table A1**). Although APCI-MS and UV-Vis measurements provided interesting structural information on isomers nx1-nx3, IMS data were also collected from them to confirm the hypothesized structures and will be described in detail in the next paragraph.

Lutein and compounds 11 and 12, named as lt1 and lt2, respectively, after PCA was performed (see **Figure 4** and **Table A1**), were associated with a very relevant intensity for the $[M+H-H_2O]^+$ ion, representing the base peak of the APCI(+)-FTMS spectrum, whereas the peak related to two water

losses was quite weak (see **Table A1**). In the case of lutein, the first water loss is expected to occur after protonation of the OH group located on the ε-end group, via a CDF process leading to the formation of a stable allylic carbocation, whereas the second water loss can reasonably occur, on the other end group, only as a *charge-remote fragmentation* (CRF), finally leading to a C=C bond between C3 and C4. Indeed, a CDF process on that end group would imply the protonation of the OH group linked to C3 (see **Figure 1**), but the subsequent water loss would lead to a relatively less stable secondary carbocation. Obviously, no other water loss could be observed for lutein (see **Table A1**), due to the lack of other oxygenated moieties. As evidenced in **Table A1**, the fragmentative behaviour of lt1 and lt2 isomers was almost identical to that of their major counterpart, thus suggesting the occurrence of two oxygenated moieties able to lead to water loss. On the other hand, they eluted 5.5 min and 7.9 min after lutein, respectively, indicating a relevant increase in hydrophobicity. This finding would suggest that lt1 and lt2 might bear both oxygenated groups on the same end group, thus making the other end group much more hydrophobic and able to interact more strongly with the C18 stationary phase. When UV-Vis data were collected (see **Table 1**) and then compared with literature data, it was noted that the λ_{abs} and peak shape of lt1 and lt2 absorption spectra, both lacking the *cis* peak, as lutein, closely matched those reported for all-*trans* carotenoids b-cryptoxanthin-5,6-epoxide and 2-hydroxy-β-carotene-5,6-epoxide, respectively (see **Figure 5**). These compounds are characterized by the presence of an epoxide group between C5 and C6, while differing in the position of the OH group located on the same end group, *e.g.* C3 and C2, respectively. In this context, the very high relative intensity of the $[M+H-H_2O]^+$ ion observed in APCI(+)-FTMS spectra for isomers lt1 and lt2 can be rationalized by assuming that the opening of the epoxy ring after the initial protonation of the corresponding O atom leads to the generation of an allylic/tertiary carbocation on C6, subsequently further stabilized by the loss of water, with generation of a C=C bond between C4 and C5, since this makes it a bis-allylic carbocation.

As for violaxanthin and its putative vx3-vx7 isomers, in-source water losses were much less relevant compared to 9-*cis*-neoxanthin and nx1-nx3, with a systematic decrease of intensity for all [M+H-

$nH_2O]^+$ ions (see **Table A1**). This finding emphasizes that the observed in-source fragmentation pattern is influenced not just by the number but also by the nature of oxygenated moieties. Indeed, violaxanthin, bearing only 2 free OH groups, may undergo, at most, a single dehydration via a CDF process, reasonably consisting in the protonation of one of the epoxydic O atoms with opening of the epoxide ring and generation of an allylic carbocation on C6 or, equivalently, on C6'. After this process, other water losses can occur only through CRF processes, with the one involving the other epoxide ring being quite complex (since a preliminary opening of the epoxide ring, not triggered by protonation, is required). At a closer look, isomeric species vx1, vx2 and vx4 exhibited an in-source fragmentation pattern more similar to the one of violaxanthin (see **Table A1**) than vx3 and vx5-vx7 isomers. Nonetheless, all these compounds were more retained on the C18 stationary phase than their major counterpart. This behaviour might be explained by the replacement of one or both epoxidic groups with the already described furanoid moiety, in which the former epoxydic oxygen is linked to C8 (or C8'), generating a 5-terms cycle, and a C=C bond is located between C6 and C7 (or C6' and C7'). As mentioned before, the furanoid moiety is characterized by a lower polarity than the epoxydic group, thus its presence would lead to a retention time increase. According to the UV-Vis data obtained for violaxanthin isomers (see **Table 1**) and based on a comparison with the literature[50,51], vx1 and vx2 might correspond to two stereoisomers of luteoxanthin (see **Figure 5**), *i.e.* the 5',8'-furanoid isomer of violaxanthin. Considering their retention times, vx1 and vx2 were tentatively assigned to (8′S)-luteoxanthin and (8′R)-luteoxanthin, respectively, reflecting differences in the spatial orientation of the furan moiety with respect to the free -OH group located on the same end group.

A UV-Vis absorption spectrum similar to that of vx1 and vx2 was observed for vx4 and vx6 which, however, displayed a D_{III}/D_{II} ratio typical of carotenoids bearing 11 conjugated C=C double bonds in their structure. In the absence of a match with the literature, these isomers could be just named as "luteoxanthin like". Isomers vx3, vx5 and vx7 exhibited an absorption spectrum that, considering the λ_{abs} and peak shape, was ascribable to different possible stereoisomers of auroxanthin[50,51], *i.e.* the 5,8-

5',8'-furanoid isomers of violaxanthin (see **Figure 5**). Based on chromatographic retention and considering the spatial arrangement of the furanoid moieties relative to the free -OH group, the isomers vx3, vx5, and vx7 were tentatively assigned to (8S,8′S)-auroxanthin, (8R,8′S)-auroxanthin, and (8R,8′R)-auroxanthin, respectively. Since tandem MS was unable to distinguish isomers with epoxy and furanoid moieties[51], further information was collected on violaxanthin-related isomers using IMS-MS/MS, as described in the next paragraph.

The final important finding inferred from the PCA loading plot, clearly shown in **Figure 4**, was that β-cryptoxanthin and its putative isomers were grouped together with β-carotene, being all characterized by the prevalence of the $[M+H]^+$ ion in their APCI(+)-FTMS spectra. On the other hand, β-cryptoxanthin and its putative isomers underwent also a water loss, which was obviously impossible in the case of β-carotene, that lacks oxygenated groups. The detection of β-carotene as protonated form suggests that a H^+ ion can be efficiently captured by one of its C=C bonds, leading to the generation of an allylic carbocation that is subsequently stabilized by resonance along part of the polyene chain. Notably, the interaction with the APCI plasma was reported to promote the π-electrons of the carotenoid polyene chain to excited electronic states, leading to an increase of the proton affinity of the molecule with respect to the ground state and thus allowing efficient proton transfer reactions also in the case of carotenes[60]. A similar process might occur also in the case of β-cryptoxanthin and its putative isomers, as an alternative to the protonation of the OH group, that would lead to the generation of a less stable secondary carbocation upon water loss. In this case, the protonation on the polyene chain would subsequently lead to a loss of water as a CRF process, with the generation of a C=C bond between C3 and C4 atoms being the most likely outcome, since it would imply an extension of the C=C bonds conjugation. Notably, the significantly lower intensity of the $[M+H-H_2O]^+$ ion in APCI(+)-FTMS spectra of isomers cr8-cr10 (see **Table A1**), compared to cr1-cr7 isomers and b-cryptoxanthin, might be related to a particular location of the double bond on the oxygenated end group, not enabling an extension of conjugation after water loss or to the occurrence of an oxygenated moiety less prone to water loss. Unfortunately, with the exception of cr10, UV-Vis

data were not available for b-cryptoxanthin-related isomers, due to the low abundance of these species and to the co-elution with pheophytins and chlorophylls in the same chromatographic region, whose absorbance in the UV-Vis region prevailed, as also observed in the case of b-cryptoxanthin itself. On the other hand, the absorption spectrum of the cr10 isomer (see **Table 1**) agreed with that of citroxanthin[50], an isomer of β-cryptoxanthin including a furanoid moiety inside one end group but missing the OH group (see **Figure 5**). Notably, this feature is consistent with the very low abundance of the $[M+H-H_2O]^+$ ion in the APCI(+)-FTMS spectrum of isomer cr10 (see **Table A1**).

It is worth emphasizing that the possibility of protonation on the polyene chain, as an alternative to the one occurring on the end-groups, cannot be ruled out, at least in principle, also in the case of xanthophylls including more than a single oxygenated moiety. This aspect will be discussed in detail in the next paragraph of this chapter. In any case, apart from some differences in their quantitative profile, minor carotenoids discussed in this paragraph were detected in all other products, both of kale and of broccoli raab, considered during this study.

4.3.2 RPLC-ESI-TWIMS-MS and IMS-MS/MS analysis of carotenoid isomers. To the best of our knowledge, only a few studies have been involved so far in the characterization of carotenoids by IMS, eventually coupled to MS and/or MS/MS. The reported results suggest that a single *m/z* value ion detected in the MS spectrum corresponding to the chromatographic peak of a carotenoid is often associated with multiple mobility peaks. The latter has been usually assigned either to the *cis* isomers of all-*trans* carotenoids, generated by isomerization reactions occurring in atmospheric pressure ionization (API) sources[52,61,62] or to isomeric compounds not separated by chromatography[63]. In this case, if the IMS-MS/MS combination is available, the acquisition of specific MS/MS spectra is possible for isobaric ions displaying different mobilities, potentially providing useful structural information. In light of these considerations, *Brassica* plant extracts were analyzed during this thesis work using also RPLC-ESI followed by TWIMS-MS or IMS-MS/MS combined detections, aiming at obtaining further structural information on minor isomeric carotenoids. **Figure 6** shows the RPLC-

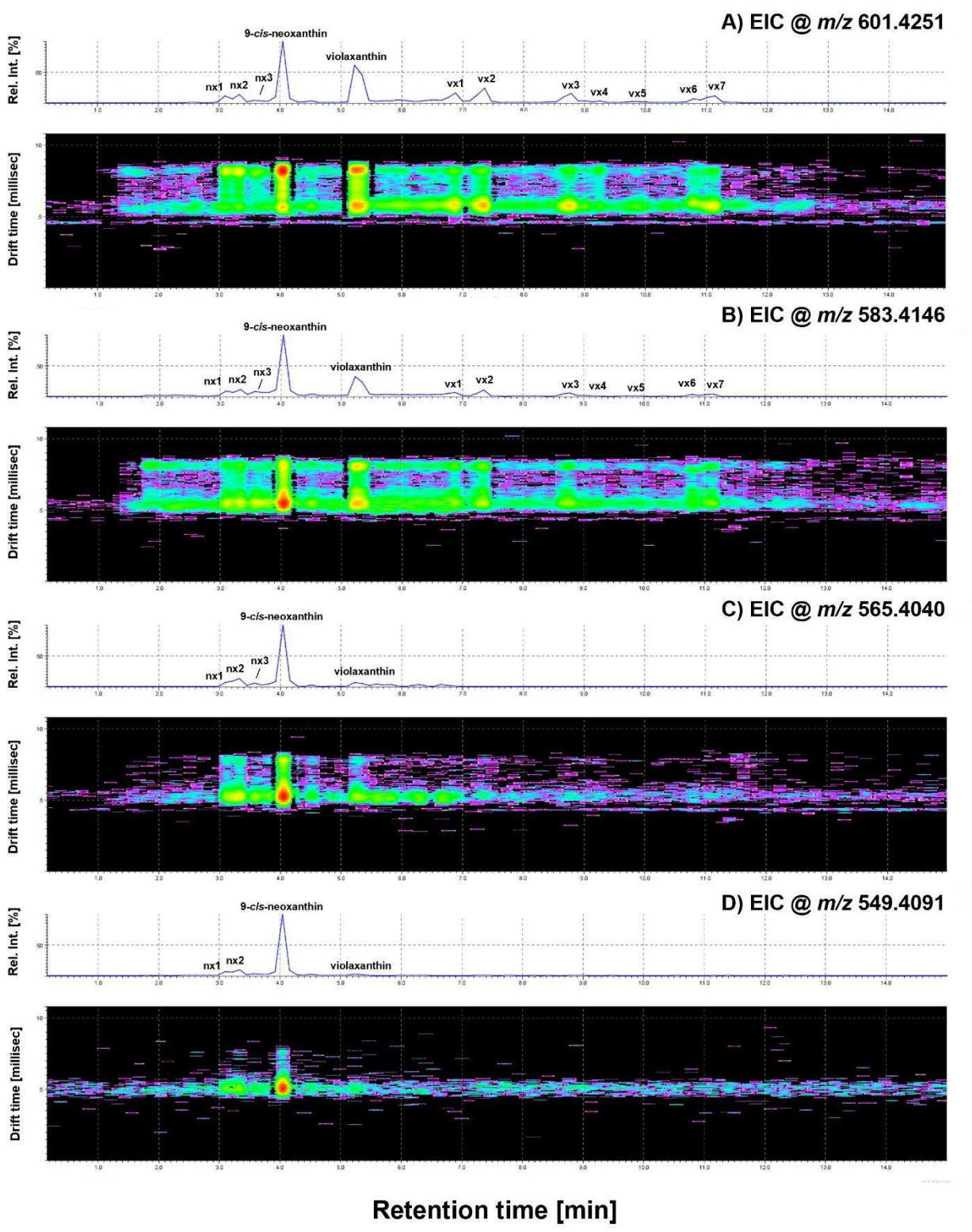


Figure 6. Panel A) EIC chromatogram and two-dimensional "drift time versus retention time" plot obtained for the $[M+H]^+$ ion at *m/z* 601.4251 relating to 9-*cis*-neoxanthin, violaxanthin and their isomers after the RPLC-ESI(+)-TWIMS analysis of a kale microgreens extract. The following panels show EIC chromatograms and "two-dimensional drift time versus retention time plots" referred to the ions $[M+H-H_2O]^+$ (B), $[M+H-2H_2O]^+$ (C) and $[M+H-3H_2O]^+$ (D) generated in the source for each isomer considered. See text for details.

ESI(+) EIC chromatograms, obtained after the analysis of a kale microgreens extract, related to the $[M+H]^+$ (plot A), $[M+H-H_2O]^+$ (plot B), $[M+H-2H_2O]^+$ (plot C) and $[M+H-3H_2O]^+$ (plot D) ions of 9-*cis*-neoxanthin, violaxanthin and their isomers, generated by protonation followed by subsequent dehydration reactions in the ESI source, the same processes occurring in the APCI source.

The ion mobility profile of each of these species was reported, under the corresponding EIC chromatogram, as a two-dimensional plot correlating the drift time measured using TWIMS with the RPLC retention time. As inferred from **Figure 6**, each ionic species usually corresponded to at least two different mobilities, suggesting the presence of multiple gas-phase conformers. For each compound, the drift times and the collision cross section ($^{TW}CCS_{N_2}$) values of the most abundant conformers, calculated by extrapolation using a poly-DL-alanine calibration curve, were summarized in **Table A2**, along with CCS values reported in the literature ($CCS_{theor.}$), if available, and the difference, $\Delta\Omega$, observed between the experimental and the reported CCS values, measured as a percentage of the latter. Note that, in the case of minor isomers, the reported CCS values were obtained considering the putative identifications based on UV-Vis spectroscopy.

For the $[M+H]^+$ ions of 9-*cis*-neoxanthin, its isomers (nx1–nx3), and violaxanthin, the most intense conformers were characterized by longer drift times, comprised between 8.11 and 8.31 ms, and, consequently, larger CCS values. In contrast, the most abundant conformers of the $[M+H]^+$ ions of violaxanthin isomers (vx1–vx7) displayed shorter drift times (5.64 - 5.89 ms) and lower CCS values. As inferred from **Table A2** and from the 2D plots relating to the $[M+H-nH_2O]^+$ ions, a systematic trend emerged, with increasing dehydration degrees being associated with progressively shorter drift times and correspondingly smaller CCS values for the main conformers. This behaviour is consistent with a gradual contraction of the ion structure in the gas phase, plausibly driven by the sequential loss of hydroxyl and/or epoxy or furanoid functionalities. Notably, the mobility peak related to the lower drift time became progressively prevailing when extensively dehydrated ions, *i.e.*, $[M+H-3H_2O]^+$ and $[M+H-4H_2O]^+$ ions were considered (see the lower panels in **Figure 6**). Considering that

oxygenated moieties, from which water losses occur, represent the most plausible protonation sites for xanthophylls, this finding suggests that the multiple mobility features detected for the protonated and partially dehydrated ions are not primarily attributable to geometric isomerism, as previously proposed in the literature, but rather to the presence of protomers, *i.e.* species differing in the site of protonation. Upon complete loss of oxygenated moieties, the number of available protonation sites is drastically reduced, effectively "freezing" the charge at a single location, likely corresponding to a stabilized carbocation, as discussed before. In turn, this process results in the observation of almost a unique mobility species. Notably, if an isomerization reaction occurring in the source was responsible for the multiple mobility, it would involve the polyene chain and additional mobility peaks would be expected also for highly dehydrated ions, such as $[M+H-2H_2O]^+$ of violaxanthin and $[M+H-3H_2O]^+$ of 9-*cis*-neoxanthin and its isomers. The role of protomers in determining the multiple mobility is particularly plausible for the $[M+H]^+$ and $[M+H-H_2O]^+$ ions, which still retain several hydroxyl and or epoxy/furanoid groups, in addition to the polyene chain, all potentially involved in proton transfer reactions. Nonetheless, the role played by protonation occurring on the polyene chain cannot be considered marginal in determining multiple mobilities, for the reasons discussed before.

The hypothesis of protomerism is further supported by the presence in the literature of very similar CCS values for *cis*/*trans* carotenoid isomers and by the fact that, at least for lipids, ion mobility spectrometers with resolving power greater than 250 are required to discriminate geometric chain isomers[64]. Finally, the presence of protomers has already been documented for other classes of metabolites[65–68], and their presence in carotenoids, in particular in xanthophylls, where charge delocalization could involve both the polyene chain and the oxygenated groups, appears plausible.

The association of multiple mobility peaks to protomers of the same ion is unequivocally demonstrated by the IMS-MS/MS spectra of the individual conformers of the $[M+H]^+$ ion of violaxanthin (*m/z* 601.4251), reported in **Figure A1**. The precursor ion was retained, together with the sequential dehydration products corresponding to $[M+H-H_2O]^+$ and $[M+H-2H_2O]^+$ ions, having *m/z* values 583.4139 and 565.4179, respectively, in the MS/MS spectrum of the protomer

characterized by a drift time of 5.6 ms (plot A). The peak signal detected at *m/z* 491.3540, corresponding to a $[M+H-H_2O-92]^+$ ion, was also observed in the spectrum and it is diagnostic of a toluene loss occurring from the polyene chain. The base peak, at *m/z* 221.1551, corresponds to the product ion arising from the cleavage of the C10-C11 bond and is diagnostic of an end group bearing both hydroxyl and epoxy functional groups, while the ion at *m/z* 165.0939 results from the cleavage of the bond between C8 and C9 and is diagnostic of a dehydrated end group bearing an epoxide moiety[69,70]. This fragmentation pattern indicates that, for this protomer, the positive charge is localized and stabilized on one the oxygenated functions of the molecule, probably on the O of one the epoxide groups, corroborating the hypotheses discussed in the previous paragraph of this chapter. Conversely, the IMS-MS/MS spectrum of the protomer characterized by a drift time of 8.1 ms (see plot B in **Figure A1**) exhibited a complete depletion of the precursor ion and an extensive fragmentation of the polyene chain. The ions produced at *m/z* 119.0875, 133.1026, 145.1019, 159.1189 and 171.1163 correspond to aliphatic fragments resulting from the sequential breaking of the polyene chain[69,71]. This fragmentation pattern unambiguously demonstrates that, in this protomer, the positive charge is delocalized along the polyene chain. According to the study by Konovalov and Kispert[72], the most stable protonation sites in β-carotene and canthaxanthin are located at C7, C5 and C11. Notably, the authors demonstrated that, even in the presence of electronegative O atoms, protonation along the polyene chain remains competitive, as it enables extensive charge delocalization. This result suggests that for the protomers of the $[M+H]^+$ ions of 9-*cis*-neoxanthin, its isomers (nx1–nx3) and violaxanthin displaying a drift time of 8 ms protonation on at least one of those C atoms of the polyene chain is favoured over that of oxygenated functions, leading to the formation of the most stable conformer. In contrast, for luteoxanthin and auroxanthin isomers, both the C5 and C7 positions are involved in the furanoid moiety and, consequently, protonation at the oxygen atom represents the most plausible charge localization site, thus protomers with a short drift time prevail (see **Table A2**).

The findings discussed so far indicate that when the positive charge is localized along the polyene backbone the resulting ion adopts a more extended, quasi-linear conformation, reflected in larger CCS values. Conversely, when protonation occurs at the oxygenated end groups, charge localization induces structural folding of the gas phase ion, accounting for the smaller CCS values observed. On the basis of these considerations, a structural interpretation of the CCS values reported in **Table A2** was hypothesised. For the $[M+H]^+$ ion of 9-*cis*-neoxanthin, its isomers nx1–nx3 and violaxanthin, which are expected to preferentially localize the positive charge along the polyene chain, a clear relationship between geometry and ion mobility is observed. Specifically, CCS values decrease as the number of *cis* double bonds increases and as these are progressively positioned next to the centre of the polyene backbone. A peculiar trend is evident for the nx3 isomer, putatively identified as (8R)-neochrome. Although this compound formally exhibits an all-*trans* configuration, both C5 and C7 are involved in epoxide and furanoid rings, leaving C11 as the most plausible protonation site along the polyene chain. Charge localization in a more central region of the polyene chain likely induces a partial bending of the ion structure, resulting in a reduced CCS (see **Table A2**). In contrast, the CCS values of the $[M+H]^+$ ions of luteoxanthin and auroxanthin epimers, expected to preferentially accommodate the positive charge on an O atom, do not provide clear discrimination among several species. Slightly higher CCS values were observed for the isomers previously classified as "luteoxanthin-like"; however, these differences are insufficient for a reliable compound assignment based exclusively on ion mobility. More diagnostic information was provided by the dehydrated species. For the $[M+H-H_2O]^+$ ion of 9-*cis*-neoxanthin, its isomers and violaxanthin, dehydration is expected to shift charge localization toward the end groups. In this case, higher CCS values are associated with the all-*trans* structures, namely neochrome and violaxanthin, reflecting a more extended and linear gas-phase ion geometry. This interpretation remains consistent for higher-order dehydrated species $[M+H-nH_2O]^+$, when detected. The $[M+H-H_2O]^+$ ions of luteoxanthin epimers and of the "luteoxanthin-like" isomers display CCS values lower than those of violaxanthin and comparable to those of the di-*Z* isomers of 9-*cis*-neoxanthin. This behaviour suggests that the

presence of furanoid functionalities promotes a more compact ion structure, yielding a degree of conformational contraction comparable to that induced by multiple *cis* double bonds along the polyene chain. Finally, **Table A2** shows that CCS data are not available in current online databases for several carotenoid species detected during the present study. Consequently, many CCS values reported here represent reference data that expand the ion mobility characterization of carotenoids.

Once the nature of multiple mobility peaks was clarified, IMS-MS/MS on protomers related to different carotenoid isomers was further evaluated in terms of its ability to provide an unambiguous identification, a challenge that cannot be achieved with conventional MS/MS alone. To this aim, **Figure A2** reports the IMS-MS/MS spectra of the protomers characterized by drift times close to 5 ms for the $[M+H]^+$ ions (*m/z* 601.4251) of violaxanthin (plot A), luteoxanthin (plot B), and auroxanthin (plot C). In all cases, the precursor ion was partially preserved and the already discussed product ion having nominal *m/z* 221 was observed as the base peak in the spectrum. In the case of luteoxanthin, a distinctive product ion was clearly detected at *m/z* 352.2406; as reported in literature, this fragment retains the end group and originates from the cleavage of the polyene chain between C12 and C13[69,70]. The same fragment ion was also observed in the IMS-MS/MS spectra of the violaxanthin and auroxanthin protomers, although with lower intensity, particularly for violaxanthin. Although the IMS-MS/MS spectra of violaxanthin and auroxanthin appear approximately similar, a relevant discriminating feature is provided by the ion at *m/z* 287.1989, which results from cleavage between C14 and C15 and retains the hydroxylated end group together with the epoxide ring[70]. This fragment is clearly detected in the violaxanthin IMS-MS/MS spectrum and, although with reduced intensity, in that of luteoxanthin, whereas it is absent in the auroxanthin spectrum. This behaviour can be reasonably related to the steric hindrance imposed by the furanoid ring in auroxanthin, which likely hinders the formation or stabilization of this fragment ion.

Taken together, the TWIMS and IMS-MS/MS results discussed in this section confirm that the combination of ion mobility-based separation with selective fragmentation of individual protomers provides a level of structural information that is significantly higher than that afforded by MS/MS

alone. This integrated approach enables both the discrimination of species protonated at different sites and the differentiation of closely related structural isomers, thereby proving particularly effective for the selective identification of carotenoids in complex matrices while reducing interpretative ambiguity.

Once a structural assignment was given to most of minor carotenoids detected in the vegetal products of interest in this study, combining the multi-dimensional information provided by RPLC along with FTMS, UV-Vis, and IMS-MS and MS/MS detections, the development of a quantitative method for major and minor carotenoids and for α-tocopherol in those products was undertaken. As described in detail in the next paragraph, due to the unavailability of standards for minor carotenoids, the latter were quantified in real samples considering the calibrations obtained for major counterparts related to them after the processing of in-source fragmentation patterns processing by PCA. Indeed, this approach was considered as the one leading to the most reliable quantitative results.

4.3.3 Development and validation of a quantitative method for carotenoids. As a first step of the quantitative method development, calibrations were performed on α-tocopherol and main carotenoids considering standard solutions prepared in pure solvent, with six concentration levels involved in each case, covering the ranges indicated in the second column of **Table 2**. The peak area resulting from the EIC chromatogram for each compound, normalised by the peak area of the IS (vitamin K_2), was adopted as a measure of analytical response and a linear model was adopted for calibration. The resulting coefficients of determination (R^2), limit of detection (LOD) and limit of quantification (LOQ) are also reported in **Table 2**.

Table 2. Concentration range, coefficient of determination (R^2), LOD and LOQ values related to the linear calibration of MS responses for major carotenoids and α-tocopherol dissolved in pure solvent.

Compound	Concentration range (μg/mL)	R^2	LOD (μg/mL)	LOQ (μg/mL)
β-carotene	1-100	0.999	1.1	4
β-cryptoxanthin	0.1-10	0.999	0.11	0.4
lutein	0.01-50	0.999	0.4	1.3
violaxanthin	1-100	0.999	1.2	4
9-*cis*-neoxanthin	0.1-10	0.999	0.2	0.8
α-tocopherol	1-100	0.999	0.3	1.2

In this case LOD and LOQ values were calculated as 3×s/b and 10×s/b, respectively, where s is the standard deviation of intercept and b is the slope of calibration line. As evidenced by the table, an excellent linearity was always achieved in the explored concentration intervals and LOQ values ranging between 0.4 and 4 mg/mL were calculated.

On the other hand, considering the intrinsic complexity expected for the extracts obtained from the vegetal matrices of interest, posing the risk of co-elution between the target analytes and matrix components, with a consequent potential competition for ionization, the matrix effect was evaluated. In this case the standard addition method represents the only possible approach to estimate matrix effect, since no kale or broccoli raab product free of the compounds of interest was available. The extracts obtained for microgreens, baby leaves and mature forms of both kale and broccoli raab were thus considered as model matrices, whereas micro leaves were excluded, due to their similarity with microgreens (*vide infra*). Extracts were divided into three aliquots, one of which left as such (level 0) and the other two being spiked with a carotenoid or α-tocopherol either at level 3 or at level 6 of the calibration line, so that a medium and a high concentration in the extract could be explored. The entire procedure, including subsequent RPLC-APCI(+)-FTMS analysis, was performed in triplicate in each case.

After the analysis, the matrix effect was calculated, for both explored levels, according to this equation:

$$\frac{A\,l_{level\ 6\ (or\ 3)\ matrix} - A_{\ level\ 0\ matrix}}{A_{\ level\ 6\ (or\ 3)\ solvent}}$$

in which A values represent EIC peak areas normalized to that of the IS, obtained in the spiked or the as such matrix or in pure solvent, according to the case. The results obtained for each growth stage of kale and broccoli raab were comparable between the two plant species and, consequently, the mean values, reported in **Table 3**, were considered for an evaluation.

Table 3. Matrix effects estimated for of α-tocopherol and major carotenoids in the extracts of three different vegetal matrices of interest for this study: microgreen, baby leaf and mature plant, based on the standard addition method. Values reported represent averages obtained for a specific growth stage for kale and broccoli raab, since the obtained values were similar for the two plants.

Plant product	**Compound**					
	α-tocopherol	β-carotene	β-cryptoxanthin	lutein	violaxanthin	9-*cis*-neoxanthin
Microgreen	111	112	102	36	49	71
Baby leaf	112	113	108	38	47	56
Mature plant	106	108	110	32	38	47

In the case of α-tocopherol, β-carotene and β-cryptoxanthin, values comprised between 100 and 120% were found, suggesting that for these analytes the matrix effect can be considered negligible. Therefore, the calibration lines constructed in pure solvent were used to quantify these substances in plant samples. On the other hand, the most oxygenated xanthophylls, such as lutein, violaxanthin and 9-*cis*-neoxanthin, suffered from a severe matrix effect. An inspection of APCI(+)-FTMS spectra averaged under the respective chromatographic peaks showed that the effect was likely caused by the co-elution of diacylglycerols (DAGs), which were co-extracted and then competed for ionization. Based on this result, the quantification of lutein, violaxanthin and 9-*cis*-neoxanthin in vegetal extracts was performed using the calibration lines obtained in pure solvent but applying an appropriate correction for the observed matrix effect. As clearly observed in **Table 3**, matrix effects were generally similar, for a specific carotenoid, in the case of microgreens and baby leaves. This outcome indirectly confirmed that they were similar also between microgreens and the intermediate growth stage between them and baby leaves, *i.e.*, micro leaves.

As mentioned before, the quantification of minor isomeric species detected in APCI(+)-FTMS chromatograms was based on the calibration of major species with which they were grouped after the PCA processing of *in-source* fragmentation data. In the case of putative β-cryptoxanthin isomers, the calibration for this xanthophyll was considered, despite the similarity observed also with b-carotene in terms of $[M+H]^+$ ion prevalence in APCI(+)-FTMS spectra, since they certainly include an oxygenated moiety, like β-cryptoxanthin, and this can influence the ionization yield.

As a further step of the method validation procedure, the estimation of the recovery of main carotenoids and α-tocopherol from plant matrices was carried out in triplicate adopting kale microgreens as a model matrix. For each replicate, six successive extraction steps were carried out on the same aliquot of lyophilized vegetal matrix and the single supernatants obtained from each step were subjected to the procedure described in the *Materials and Methods* section before RPLC-APCI(+)-FTMS analysis. The EIC peak areas of main carotenoids and α-tocopherol, normalized to the IS area, were used to relate signal intensity to the extracted amounts and were expressed as a percentage of the cumulative peak area obtained after six consecutive extraction steps. The mean percentage recoveries achieved in each extraction step are reported in **Figure A3** in the Appendix. As shown in the figure, for all compounds but violaxanthin the amount extracted in the sixth step was very low or even negligible, thus suggesting that almost the entire content of each compound in the extracted vegetal sample was recovered. Starting from this assumption, four consecutive extraction steps were able to extract at least 90% of the total amount of those compounds, thus justifying the choice of pooling the supernatants obtained after four extraction steps on the same aliquot of vegetal sample. The only exception to the described scenario was represented by violaxanthin, for which even the sixth extraction step seemed not to be definitive, and, additionally, the first four steps accounted for about 75% of the amount obtained after six steps. In the literature violaxanthin has been reported to be associated with *light-harvesting complexes* (LHCs) proteins through a peripheral and weak binding site, ensuring ready availability for xanthophyll cycle activation[19,20]. The peripheral location

of this binding site, which is partially shielded, compared to those of lutein and 9-*cis*-neoxanthin, might hinder the access to solvents and thus limit the efficiency of violaxanthin extraction. In order to account for this specific behaviour, the measured amounts of violaxanthin in the different real samples were adjusted by applying a correction factor. It is worth noting that the variations observed in recovery percentages for a specific extraction step between the three replicated experiments were always very limited (usually below 5%), thus indicating that the extraction reproducibility was good. Another partially unexpected finding, clearly inferred from data shown in **Figure A3** and common to all the involved compounds, was the estimation of a higher extracted amount after the second step, compared to the first one. A possible explanation for this result was obtained after observing that the volume of supernatant retrieved after the second extraction step was greater than that obtained after the first step. This discrepancy could be explained only considering the trapping of a relevant amount of the solvent added during the first extraction step by the lyophilized samples, likely due to the imbibition of the dry vegetal tissues. The trapped solvent likely dissolved a part of the sample a-tocopherol/carotenoid content, yet it could not be recovered after centrifugation. That portion of the total content of each analyte could be recovered only after adding the second extraction solvent aliquot, once the vegetal tissue had been swelled by the solvent, thus leading to a higher amount extracted after the second step. The result of the sequential extraction experiment described so far emphasizes the importance of considering very carefully the extractability of target compounds from complex matrices like lyophilized vegetables.

As the final step of validation, some aspects related to method precision were taken into account, still considering kale microgreens as a model matrix. Firstly, the precision related to extraction was evaluated. At this aim, five aliquots of kale microgreens were sampled from the same batch, previously obtained by pooling the lyophilized material resulting from 600 individual young plants, including leaves and stems, since both are supposed to be consumed when microgreens are used as a food product. Each aliquot was extracted according to the procedure reported in the *Materials and methods* section, thus using four consecutive extraction steps in each case. The RPLC-APCI(+)-

FTMS analysis of each extract was then performed during the same working day, to minimize any effect due to instrumental response fluctuation, although the normalization of EIC peak areas by the IS one was performed as usual. As evidenced in the second column of **Table 4**, the relative standard deviations referred to the mean values of IS-normalized peak areas obtained for a-tocopherol and for

Table 4. Relative standard deviation (RSD) values related to the sampling-extraction variability and to the between-day response variability for the same extract evaluated for α-tocopherol and main carotenoids found in kale microgreen extracts. See text for details.

Compound	Sampling-extraction variability	Between-day response variability (same extract)
	RSD %	RSD %
α-tocopherol	10	11
β-carotene	14	12
β-cryptoxanthin	15	24
lutein	8	10
violaxanthin	48	64
9-*cis*-neoxanthin	7	17

major carotenoids but violaxanthin were lower than 15%. Considering that those RSDs are inevitably influenced both by the extraction yield reproducibility and by the variability in the target analytes content naturally occurring inside the batch of lyophilized microgreens, and thus by the batch sampling variability, their limited values confirmed the reproducibility of extraction yield and, at the same time, indicated that a good uniformity in analyte content occurred in the batch. Once again, violaxanthin represented a remarkable exception, since a 48% value was found for its sampling/extraction RSD. This result was carefully taken into account when considering the variability observed after the analyses of replicates when comparisons between sample types had to be made (*vide infra*).

As a part of the evaluation of the reproducibility of analytical response, an experiment was performed by analysing the same kale microgreens extract every other day over a period of seven days, with storage of the extract at -20 °C between measurements. The RSD values obtained for the IS-normalized EIC peak areas for the target analytes are reported in the third column of **Table 4**. It is worth noting that those values cannot be affected by sampling/extraction reproducibility but only, in

principle, by between-day instrumental response fluctuations and by the eventual degradation of the analytes during storage. As shown in the table, they kept below 12% for α-tocopherol, β-carotene and lutein, whereas they were higher for 9-*cis*-neoxanthin, β-cryptoxanthin and violaxanthin, reaching a surprising 64% for the latter compound. Considering that the between-day instrumental response fluctuations are expected to be compensated in this case by IS-based normalization, the medium to high RSD values observed for some xanthophylls likely reflect the occurrence of degradation processes occurring on them during extract storage. Indeed, some oxygenated xanthophylls have been reported to be prone to degradation reactions, especially violaxanthin, which can be turned into the corresponding 5,8-furanoid isomers as a result of thermal instability[20]. The results obtained by this experiment were carefully taken into account before the analyses of large sets of vegetal samples, which were planned so that the time elapsing between analytes extraction and RPLC-APCI(+)-FTMS run was minimized.

4.3.4 RPLC-APCI(+)-FTMS quantification of carotenoids and α-tocopherol in microgreens, micro leaves, baby leaves and adult plants of broccoli raab and kale. The amounts of the main carotenoids and their isomers, as well as α-tocopherol, were determined in microgreens, micro leaves, baby leaves and mature plants of both kale and broccoli raab. For each available lot of freeze-dried vegetable five independent aliquots were sampled and processed separately, according to the extraction protocol, then each extract was analyzed by RPLC-APCI(+)-FTMS. As discussed before, quantification was carried out using solvent calibration curves for α-tocopherol, β-carotene, and for β-cryptoxanthin and related isomers, whereas matrix calibration curves were adopted for lutein, violaxanthin and 9-*cis*-neoxanthin and for the respective related isomers. Mean concentration values were calculated and expressed in mg for 100 g of fresh weight (FW), after a correction for the water loss occurring during freeze-drying. These values and the corresponding 95% confidence intervals were reported in **Table 5** and displayed as column charts with error bars in **Figure A4**. The concentrations reported for the isomers related to violaxanthin, 9-*cis*-neoxanthin and β-cryptoxanthin

represent the sums of the mean concentrations obtained for the single isomers in each group. This approach was adopted to provide a representative estimate of their overall contribution to the total carotenoid content, reflecting their abundance and nutritional relevance in the examined matrices.

Table 5. Concentrations of carotenoids and α-tocopherol expressed as mg/100g of fresh weight (FW) obtained by RPLC-APCI-FTMS analysis of extracts of microgreens, micro leaves, baby leaves and mature plants of broccoli raab and kale. Data represent 95% confidence intervals for mean concentrations (n = 5). Half-widths of confidence intervals are expressed with one significant figure, unless the first significant figure is equal to 1 (in this case the subsequent significant figure is also reported).

Compounds	Broccoli raab				Kale			
	Microgreens	Micro leaves	Baby leaves	Adult plants	Microgreens	Micro leaves	Baby leaves	Adult plants
β-carotene	12.4 ± 1.8	10 ± 3	13 ± 4	9 ± 5	10 ± 3	7.4 ± 1.1	7 ± 2	27 ± 5
lutein	4.3 ± 0.4	4.4 ± 1.7	4.3 ± 1.2	2.9 ± 1.3	5.0 ± 1.3	3.8 ± 1.2	3.4 ± 1.7	8 ± 3
violaxanthin	0.7 ± 0.2	2.1 ± 0.6	1.6 ± 0.7	3.0 ± 1.3	< LOD	< LOD	0.41 ± 0.19	8 ± 3
Violaxanthin-related isomers	2.51 ± 0.12	4.4 ± 0.8	4.9 ± 0.7	< LOD	3.2 ± 0.5	2.00 ± 0.19	2.4 ± 0.6	4.1 ± 1.2
9-*cis*-neoxanthin	0.79 ± 0.09	0.9 ± 0.2	1.1 ± 0.3	0.8 ± 0.5	0.8 ± 0.3	0.70 ± 0.17	0.68 ± 0.18	2.7 ± 0.5
9-*cis*-neoxanthin-related isomers	0.22 ± 0.04	0.22 ± 0.05	0.21 ± 0.05	0.21 ± 0.05	0.26 ± 0.12	0.19 ± 0.04	0.22 ± 0.05	0.60 ± 0.15
β-cryptoxanthin	0.105 ± 0.013	0.16 ± 0.04	0.18 ± 0.08	0.10 ± 0.06	0.10 ± 0.03	0.16 ± 0.05	0.15 ± 0.05	0.21 ± 0.05
β-cryptoxanthin-related isomers	1.6 ± 0.4	2.3 ± 0.6	1.7 ± 0.4	1.2 ± 0.6	2.3 ± 0.5	1.7 ± 0.5	1.1 ± 0.3	2.1 ± 0.5
α-tocopherol	1.2 ± 0.3	0.36 ± 0.09	0.60 ± 0.16	0.32 ± 0.12	0.41 ± 0.14	0.24 ± 0.19	0.19 ± 0.07	2.6 ± 0.4

Figure 7 reports stacked-column graphs comparing the overall contents of carotenoids and α-tocopherol across the four different growth stages of Broccoli raab and Kale. Error bars in the figure represent the half-widths of 95% confidence intervals centred on average total contents, calculated through error propagation from those referring to average contents of individual analytes.

β-carotene and lutein represented the most abundant carotenoids in both broccoli raab and kale, in agreement with data reported for *Brassica* young and mature vegetables[31,32,42]. In broccoli raab, statistically comparable levels of the two carotenoids were observed in all growth stages, whereas kale showed an accumulation of both β-carotene and lutein in adult plants (see also **Figure A4**), contributing to make them the richest matrices in terms of total carotenoid content among the investigated samples (see **Figure 7**). Interestingly, the content of violaxanthin was moderate in the mature forms of both plants, whereas it was very low in the early growth stages, being even lower than LOD values in the case of kale microgreens and micro leaves (see **Figure A4**). On the other hand, violaxanthin-relate isomers seemed to be preferentially accumulated in early-growth stages for

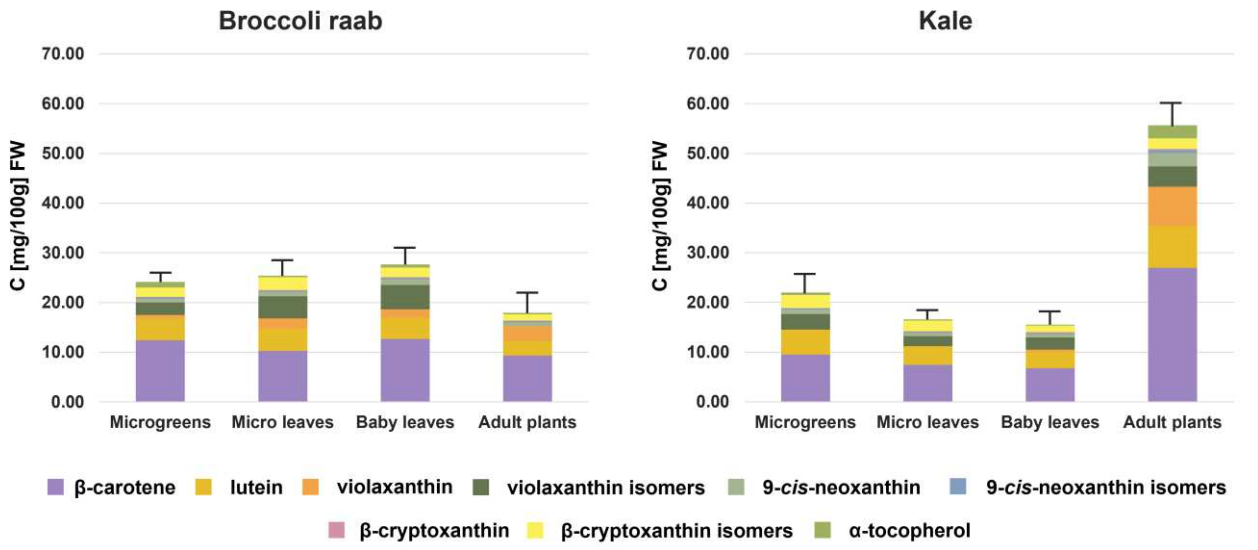


Figure 7. Stacked-column graphs illustrating the concentrations of free sterols (FSs) found in different growth stages of kale and broccoli raab. Concentrations are expressed in mg/100g of fresh weight (FW). Error bars, calculated by uncertainty propagation, represent the half-width of 95% confidence intervals for the total sterol concentrations reported for each product.

broccoli raab, being undetectable in the mature form. Comparable amounts for them were found across all growth stages in the case of kale (see **Figure A4**).

These result suggests that violaxanthin is converted into its epoxy/furanoid derivatives in early growth stages, whereas it is largely preserved in the mature forms of the two plants. Notably, the xanthophyll cycle does not appear to be activated in mature vegetables, which are grown under open-field conditions and direct solar irradiation. This inference is supported not only by the stability of violaxanthin but also by the absence of antheraxanthin and zeaxanthin, the key intermediates of this photoprotective cycle. As regards 9-*cis*-neoxanthin, relatively constant levels were observed across the developmental stages of broccoli raab, whereas a clear accumulation was, again, detected in mature kale (see **Figure A4**). The related isomeric carotenoids followed the same overall trend, although occurring at lower absolute concentrations, as expected given the lower natural abundance of *cis* carotenoids. β-cryptoxanthin was detected at low but consistent levels in all the analyzed samples and, surprisingly, isomers related to it were found to have, cumulatively, higher amounts in both plants (see **Figure A4**). Finally, α-tocopherol showed accumulation in broccoli raab microgreens and baby leaves, compared to the other growth stages, while in kale the content found in the adult

plant was absolutely prevailing (see **Figure A4**). Since some characteristic plant-/growth-related trends were observed for carotenoids and a-tocopherol, quantitative data were processed using principal component analysis with autoscaling, to emphasize the differences between the two plants and/or their growth stages. The resulting score and loading plots for PC1 and PC2 are reported in **Figure 8**.

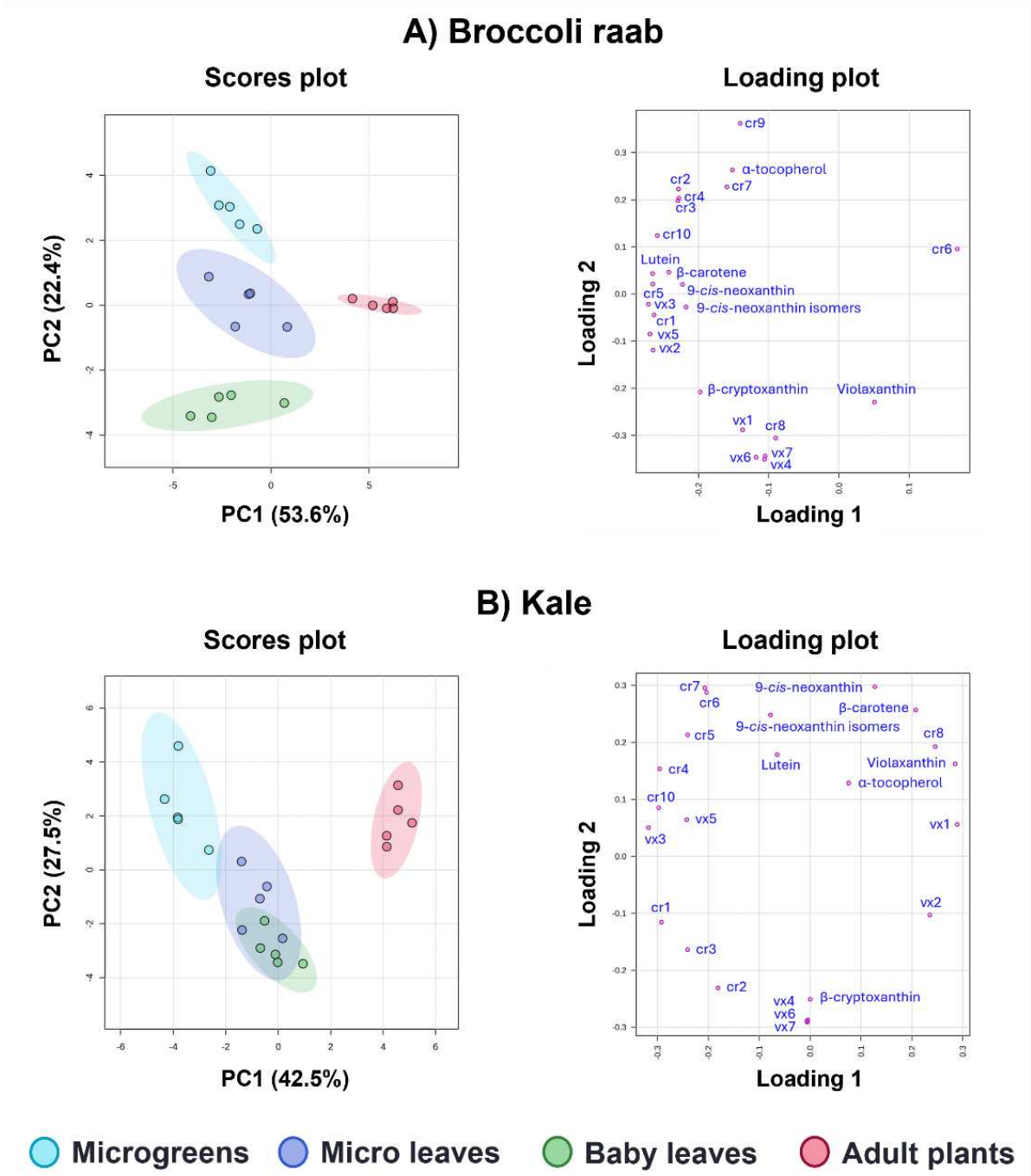


Figure 8. Scores and loading plots obtained for the first two principal components (PC1 and PC2) following PCA performed on carotenoids and α-tocopherols quantitative data related to broccoli raab (plot A) and kale (plots B) microgreens, micro leaves, baby leaves and adult plants.

Notably, quantitative data for single minor carotenoid isomers were considered distinctly for PCA provided that their chromatographic peaks could be integrated reliably. The first two principal components accounted for 76.0% of the total variance (PC1: 53.6%; PC2: 22.4%) in the case of broccoli raab and 70.0% (PC1: 42.5%; PC2: 27.5%) for kale.

For both plant species, PC1 discriminated plants obtained in early developmental stages from adult ones, confirming the changes in the carotenoids and α-tocopherol profiles occurring across growth stages. As evidenced by 95% confidence ellipses referred to sample groups, shown in the score plots, microgreens, micro leaves and baby leaves were separated better for broccoli raab than for kale, where a clear demarcation between micro and baby leaves could not be obtained. The PCA loading plot indicated that broccoli raab adult plants were clustered on the positive side of PC1 mainly due to the content of violaxanthin and of the β-cryptoxanthin-related isomer cr6. Conversely, microgreens were characterized by higher contributions of α-tocopherol and of several β-cryptoxanthin-related isomers, including cr7, cr9 and cr10. Micro leaves were preferentially associated with lutein, β-carotene and with 9-*cis*-neoxanthin and related isomers, together with some specific violaxanthin-related isomers, namely vx2, vx3 and vx5. Baby leaves formed a distinct cluster characterized by a higher incidence of β-cryptoxanthin and several violaxanthin-derived isomers, *e.g.* vx1, vx4, vx6 and vx7. In kale, adult plants were preferentially associated with α-tocopherol, β-carotene, 9-*cis*-neoxanthin and related isomers, violaxanthin and its isomers vx1 and vx2, and the β-cryptoxanthin-related isomer cr8. Kale microgreens clustered separately and were mainly characterized by a higher incidence of violaxanthin-related isomers vx3 and vx5, together with several β-cryptoxanthin-related isomers, including cr7 and cr10. As mentioned before, kale micro leaves and baby leaves showed partially overlapping clusters in the score plot and were distinguished by β-cryptoxanthin and its isomers cr1, cr2 and cr3, as well as by violaxanthin isomers vx4, vx6 and vx7, similarly to broccoli raab baby leaves, suggesting that the latter isomers are characteristic of intermediate growth stages.

To further corroborate the patterns highlighted by PCA, a hierarchical cluster analysis (HCA) was performed on the same quantitative dataset, and the results are displayed as a heatmap with double

dendrogram in **Figure 9**. The analysis reveals a clear organization of samples according to both species and developmental stage, confirming a growth-dependent modulation of carotenoids and α-tocopherol contents. The horizontal dendrogram, referring to samples shows a primary separation between adult plants and early developmental stages for both broccoli raab and kale, in agreement with the discrimination observed along PC1 in the PCA score plot. Within the early growth stage cluster, kale microgreens were clearly distinguished from micro leaves and baby leaves, which were clustered together, reflecting intermediate compositional profiles. In the case of broccoli raab microgreens and micro leaves were grouped at a higher level of similarity compared to baby leaves.

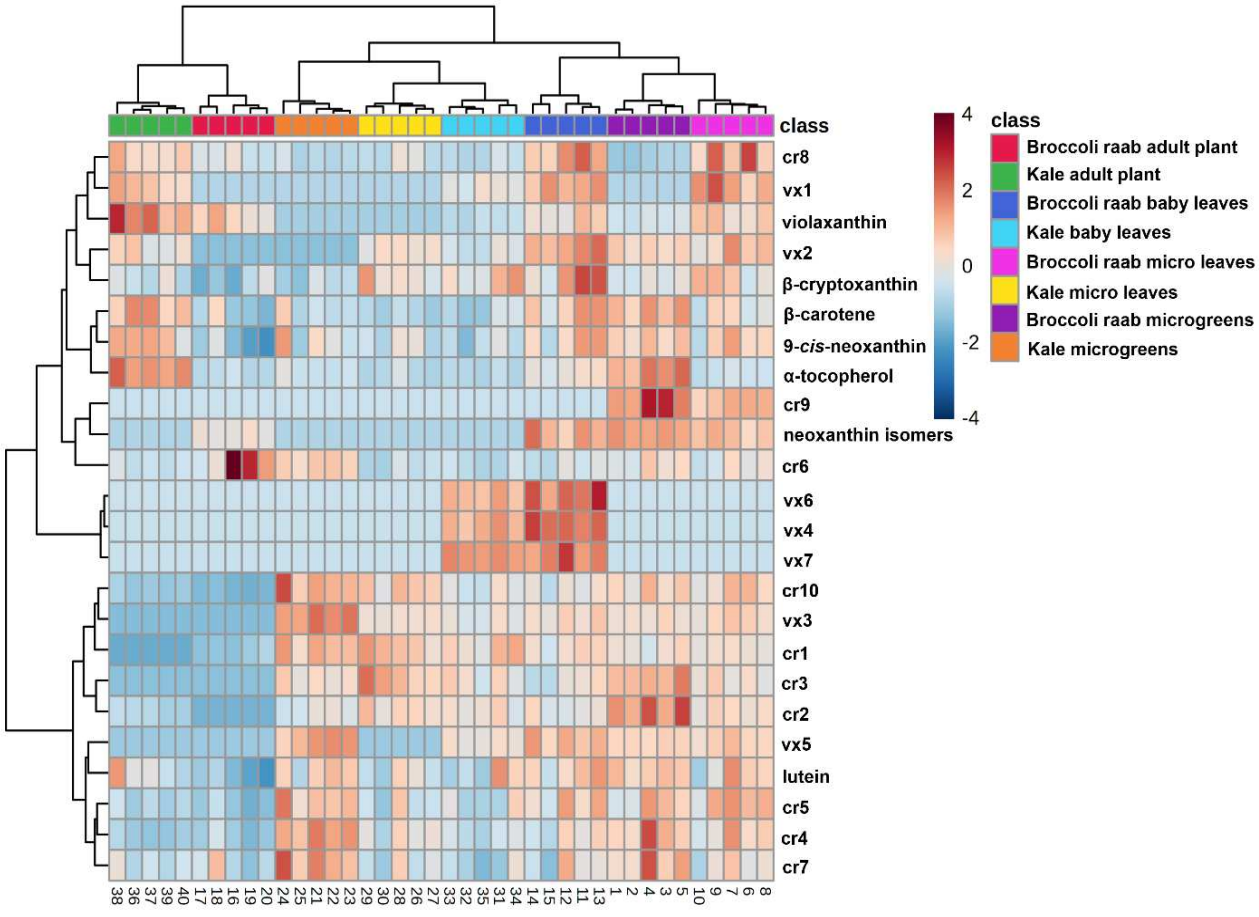


Figure 9. Double dendrogram (horizontal for objects and vertical for variables) with heatmap obtained from the Hierarchical Cluster Analysis of carotenoids and α-tocopherols quantitative data found in microgreens, micro leaves, baby leaves and adult plants of both broccoli raab and kale (five samples for each product type).

The vertical dendrogram obtained by HCA, referring to variables, is characterized by two main cluster, the first including β-carotene, violaxanthin, 9-*cis*-neoxanthin, β-cryptoxanthin and α-tocopherol, along with some minor isomers, with most of these compounds being particularly expressed in mature plants, and the second including only lutein as a major carotenoid, accompanied by several minor isomers related to violaxanthin and β-cryptoxanthin, mainly associated with younger plants. Overall, HCA reinforced the PCA findings by highlighting coherent groupings of samples and metabolites and emphasized that minor carotenoid isomers, despite their limited abundance, can contribute substantially to the discrimination of growth stages. The results of chemometrics further demonstrated that early developmental stages in broccoli raab and kale are characterized by a higher structural diversity of xanthophylls, while plant maturation is associated with the accumulation of major carotenoids, *e.g.* β-carotene and violaxanthin, and α-tocopherol.

4.3.5 Quantification of carotenoids and α-tocopherol in steamed and boiled broccoli raab and kale adult plants. The last step of this thesis work dealt with the quantification of carotenoids and α-tocopherol, compounds known to be prone to thermal degradation, in cooked mature forms of broccoli raab and kale. While early growth stage vegetables are typically consumed raw, mature leafy vegetables are generally subjected to cooking prior to consumption and this processing might lead to a decrease in the content of carotenoids. To evaluate potential cooking-induced changes in both the qualitative and quantitative profile of carotenoids and α-tocopherol, five samples of both mature broccoli raab and kale were processed using two common domestic cooking methods, namely steaming and boiling. After being appropriately drained and cooled, cooked samples were freeze-dried and stored at -18° before proceeding to extraction and the RPLC-APCI-FTMS analysis, in accordance with the procedures described in the *Material and Methods* section. As for non-cooked samples, drained and cooled cooked ones were weighed before and after freeze-drying, so that the amount of water still included in the vegetal tissues after cooking could be measured. Once RPLC-APCI-FTMS analysis was performed and quantification in cooked samples extracts was completed,

the estimate of water amount enabled the calculation of carotenoids and α-tocopherol contents expressed as mg per 100 g of FW, where FW is referred to the drained cooked product, *i.e.*, the product ready to be eaten.

Mean values and 95% confidence intervals inferred for carotenoids and α-tocopherol in boiled and steamed broccoli raab and kale mature plants were reported in **Table A3** of the Appendix and displayed as stacked-column plots in **Figure 10**. In both cases, data previously obtained for raw mature plants were also reported, to facilitate the comparison. For data consistency, the concentrations inferred for the detected isomers related to violaxanthin, 9-*cis*-neoxanthin and β-cryptoxanthin were expressed as cumulative values, calculated as the sum of the single isomers contributions. Error bars reported in **Figure 10** correspond to 95% confidence intervals for total concentrations, calculated through uncertainty propagation from those inferred for single analytes or analyte groups (in the case of minor carotenoids).

As inferred from **Figure 10**, a severe reduction in the total carotenoid and α-tocopherol content was observed upon cooking for mature kale plants, mainly related to a decrease in β-carotene, violaxanthin and related isomers and 9-*cis*-neoxanthin (see **Table A3**), whereas lutein was unaffected by the cooking process. The thermal degradation was less severe in the case of broccoli raab, with only violaxanthin being remarkably affected, as evidenced in **Table A3** (note that violaxanthin-related isomers displayed concentrations below LOD both for raw and for cooked samples in this case).

These findings suggest that highly oxygenated xanthophylls are more susceptible to thermal degradation, whereas no significant variations were detected for β-cryptoxanthin, a mono-oxygenated carotenoid. The results are consistent with those found in other studied dealing with the cooking of adult broccoli and kale samples[52–54].

As for α-tocopherol, its content decreased in cooked mature kale samples, while an increase was surprisingly observed in cooked broccoli raab (see **Table A3**). This behaviour resembles the one previously discussed in this thesis for phytosterols analysed in the same plant matrices, suggesting

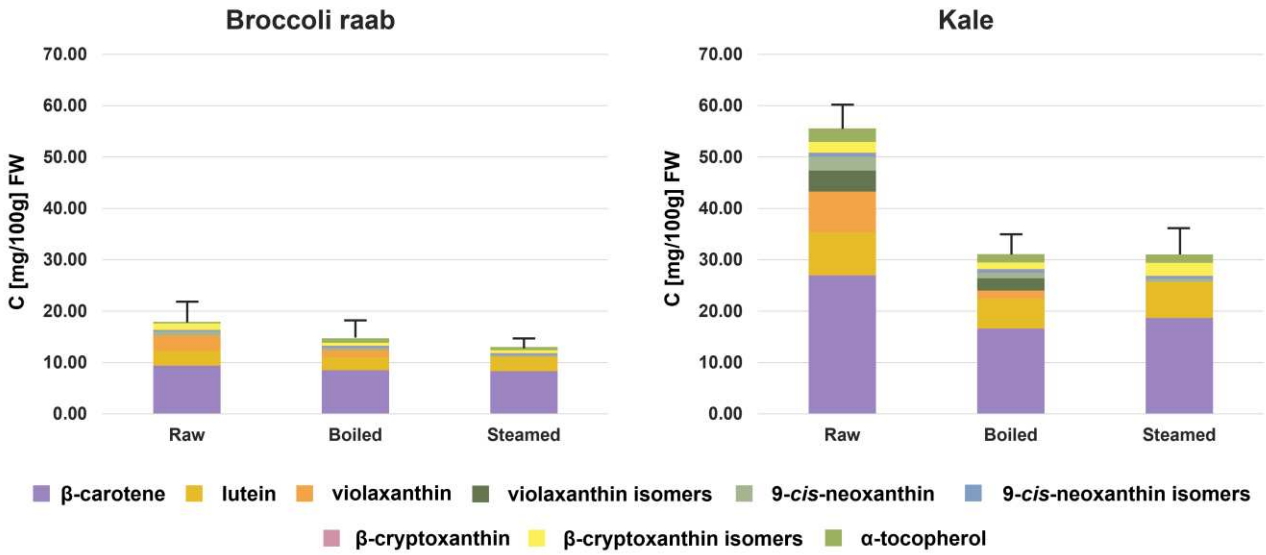


Figure 10. Stacked column graphs displayng carotenoids and α-tocopherol contents in raw, boiled and steamed mature plants of broccoli raab and kale. Concentrations, expressed as mg per 100 g of fresh weight (FW), represent mean values (n=5) and the corresponding error bars, derived by uncertainty propagation, indicate 95% confidence intervals.

that the cooking process may differentially affect tissue integrity, eventually facilitating the extraction of some metabolites.

Starting from quantitative data previously obtained for early growth stage products and those obtained for cooked adult plants, some considerations can be made about the possible role of these products as sources of carotenoids and α-tocopherol in the daily diet. In the case of broccoli raab early growth stage products, a total content always greater than 20 mg per 100 g FW was estimated, clearly exceeding the one inferred for the cooked mature counterparts (see **Figures 7** and **10**). Conversely, even if cooking determined a remarkable decrease, down to ca. 30 mg/100 g FW, kale adult plants kept a slight advantage over early growth stage products, whose overall content did not exceed 20 mg/100 g FW. Apart from these general quantitative comparisons, microgreens, micro leaves and baby leaves of both plants were characterized by a more pronounced diversification in the carotenoids profile.

Based on these findings, early growth stage products obtained for the two *Brassica* plants confirmed their role as convenient, ready-to-eat alternatives to the conventional mature counterparts also from the point of view of carotenoids and α-tocopherol.

4.4 Conclusions

In this chapter, a comprehensive qualitative and quantitative evaluation of carotenoids and α-tocopherol in broccoli raab and kale at different developmental stages could be achieved by combining RPLC chromatographic separation with multidimensional detection and multivariate data analysis.

The developed RPLC-APCI(+)-FTMS approach enabled an efficient separation of main carotenoids and of several minor isomers by using a conventional C18 stationary phase and a ternary gradient, ensuring adequate resolution of xanthophylls while maintaining robustness and repeatability and limiting the occurrence of matrix effects to a few target analytes, despite the complexity of vegetal extracts. The APCI source, favouring the formation of $[M+H]^+$ and $[M+H–nH_2O]^+$ ions, provided informative in-source fragmentation patterns, with differences in dehydration processes reflecting the number and type of oxygenated groups and enabling a correlation between major and minor isomeric carotenoids. On the other hand, more detailed structural information on the latter could be obtained only by a combination of data resulting from detection by UV-Vis spectroscopy and TWIMS-MS and MS/MS, which led to hypothesize putative identifications for several 9-*cis*-neoxanthin, violaxanthin, lutein and β-cryptoxanthin-related isomers, whose contribution is rarely addressed in quantitative studies on carotenoids.

From a quantitative perspective, the use of matrix calibration (standard addition) strategies proved crucial to account for the pronounced matrix effects observed on some carotenoids, ensuring a reliable determination for all target analytes across the investigated compounds. In this context, the cumulative expression of the contents of 9-*cis*-neoxanthin, violaxanthin and β-cryptoxanthin-related minor isomers was essential to obtain a comprehensive representation of their abundance. The results

of quantitative analysis clearly indicated that microgreens, micro leaves and baby leaves of broccoli raab and kale can represent a relevant source of carotenoids and α-tocopherol, with overall contents close, if not higher, to those found in the mature counterparts after cooking processes, that were found to determine a significant degradation of highly oxygenated xanthophylls.

Finally, multivariate analyses (PCA and HCA) confirmed that the carotenoid composition is strongly modulated by plant species and developmental stage, revealing that minor xanthophyll isomers play a non-negligible role in differentiating samples.

Overall, the study described in this chapter underlines the importance of comprehensive carotenoid profiling, including minor isomeric forms, for an accurate assessment of the nutritional quality of *Brassica* vegetables and supports the relevance of both early growth stage products and mature leafy greens in the daily diet.

References

(1) Maoka, T. Carotenoids as Natural Functional Pigments. *J. Nat. Med.* **2020**, *74* (1), 1–16. https://doi.org/10.1007/s11418-019-01364-x.

(2) Britton, G. Structure and Properties of Carotenoids in Relation to Function. *FASEB J.* **1995**, *9*, 1551–1558. https://doi.org/https://doi.org/10.1096/fasebj.9.15.8529834.

(3) Szyma, R.; Nowicka, B.; Trela, A.; Kruk, J. Vitamin E: Structure and Forms. *Mol. Nutr.* **2020**, 67–90. https://doi.org/10.1016/B978-0-12-811907-5.00021-X.

(4) Bartley, G. E.; Scolnik, P. A. Plant Carotenoids: Pigments for Photoprotection, Visual Attraction, and Human Health. *Plant Cell* **1995**, *7* (7), 1027–1038. https://doi.org/10.2307/3870055.

(5) Cazzonelli, C. I. Carotenoids in Nature: Insights from Plants and Beyond. *Funct. Plant Biol.* **2011**, *38* (11), 833–847. https://doi.org/10.1071/FP11192.

(6) Meléndez-Martínez, A. J.; Mandić, A. I.; Bantis, F.; Böhm, V.; Borge, G. I. A.; Brnčić, M.; Bysted, A.; Cano, M. P.; Dias, M. G.; Elgersma, A.; Fikselová, M.; García-Alonso, J.; Giuffrida, D.; Gonçalves, V. S. S.; Hornero-Méndez, D.; Kljak, K.; Lavelli, V.; Manganaris, G. A.; Mapelli-Brahm, P.; Marounek, M.; Olmedilla-Alonso, B.; Periago-Castón, M. J.; Pintea, A.; Sheehan, J. J.; Tumbas Šaponjac, V.; Valšíková-Frey, M.; Meulebroek, L. Van; O'Brien, N. A Comprehensive Review on Carotenoids in Foods and Feeds: Status Quo, Applications, Patents, and Research Needs. *Crit. Rev. Food Sci. Nutr.* **2022**, *62* (8), 1999–2049. https://doi.org/10.1080/10408398.2020.1867959.

(7) Demmig-Adams, B.; Gilmore, A. M.; Iii, W. W. A. In Vivo Functions of Carotenoids in Higher Plants. *FASEB J.* **1996**, *10* (4), 403–412. https://doi.org/10.1096/fasebj.10.4.8647339.

(8) Schneider, C. Chemistry and Biology of Vitamin E. *Mol. Nutr. Food Res.* **2005**, *49*, 7–30. https://doi.org/10.1002/mnfr.200400049.

(9) Munoz, P.; Munné-Bosch, S. Vitamin E in Plants : Biosynthesis , Transport , and Function. *Trends Plant Sci.* **2019**, 1–12. https://doi.org/10.1016/j.tplants.2019.08.006.

(10) Rodriguez-Amaya, D. B. *A Guide To Carotenoid Analysis in Foods*; 2001.

(11) NOMENCLATURE OF CAROTENOIDS (RULES APPROVED 1974). *IUPAC Commission on the Nomenclature of Organic Chemistry; Nomeclature, IUPAC—IUB Commission on Biochemical*; 1974.

(12) Fernandes, S.; Fernandes, A. S.; Rosso, V. V. De; Rosso, V. V. De; Jacob-lopes, E.; Zepka, L. Q. Carotenoids : A Brief Overview on Its Structure , Biosynthesis , Synthesis , and Applications Andrêssa And. *Prog. Carotenoid Res.* **2018**, 1–16. https://doi.org/10.5772/intechopen.79542.

(13) Polyakov, N. E.; Focsan, A. L.; Gao, Y. The Endless World of Carotenoids — Structural , Chemical and Biological Aspects of Some Rare Carotenoids. *Internatiol J. Mol. Sci.* **2023**, *24*, 1–19. https://doi.org/https://doi.org/10.3390/ ijms24129885.

(14) Rodriguez-Concepcion, M.; Avalos, J.; Bonet, M. L.; Boronat, A.; Gomez-Gomez, L.; Hornero-Mendez, D.; Limon, M. C.; Meléndez-Martínez, A. J.; Olmedilla-Alonso, B.; Palou, A.; Ribot, J.; Rodrigo, M. J.; Zacarias, L.; Zhu, C. A Global Perspective on Carotenoids: Metabolism, Biotechnology, and Benefits for Nutrition and Health. *Prog. Lipid Res.* **2018**, *70*, 62–93. https://doi.org/10.1016/j.plipres.2018.04.004.

(15) Stahl, W.; Sies, H. Bioactivity and Protective Effects of Natural Carotenoids. *Biochim. Biophys. Acta* **2005**, *1740*, 101–107. https://doi.org/10.1016/j.bbadis.2004.12.006.

(16) Paiva, S. A. R.; Russell, R. M.; Paiva, S. A. R.; Russell, R. M. β-Carotene and Other Carotenoids as Antioxidants. *J. Am. Coll. Nutr.* **2013**, *18:5*, 426–433. https://doi.org/10.1080/07315724.1999.10718880.

(17) Amorim-Carrilho, K. T.; Cepeda, A.; Fente, C.; Regal, P. Review of Methods for Analysis of Carotenoids. *TrAC - Trends Anal. Chem.* **2014**, *56*, 49–73. https://doi.org/10.1016/j.trac.2013.12.011.

(18) Tsuchihashi, H.; Kigoshi, M.; Iwatsuki, M.; Niki, E. Action of β-Carotene as an Antioxidant against Lipid Peroxidation. *Arch. Biochem. Biophys.* **1995**, *323* (1), 137–147. https://doi.org/https://doi.org/10.1006/abbi.1995.0019.

(19) Havaux, M. Carotenoids as Membrane Stabilizers in Chloroplasts. *Trends Plant Sci.* **1998**, *3* (4), 147–151. https://doi.org/10.1016/S1360-1385(98)01200-X.

(20) Giossi, C.; Cartaxana, P.; Cruz, S. Photoprotective Role of Neoxanthin in Plants and Algae. *Molecules* **2020**, *25* (20), 1–16. https://doi.org/10.3390/molecules25204617.

(21) Nomenclature of Tocopherols and Related Compounds. *IUPAC-IUB Commission on Biochemical Nomenclature (CBN)*; 1974; Vol. 165, pp 6–8.

(22) Brigelius-Flohé, R. Bioactivity of Vitamin E. *Nutr. Res. Rev.* **2006**, *19*, 174–186. https://doi.org/10.1017/NRR2006125.

(23) Meléndez-Martínez, A. J. An Overview of Carotenoids, Apocarotenoids, and Vitamin A in Agro-Food, Nutrition, Health, and Disease. *Mol. Nutr. Food Res.* **2019**, *63* (15), 1–11. https://doi.org/10.1002/mnfr.201801045.

(24) Amengual, J. Bioactive Properties of Carotenoids in Human Health. *Nutrients* **2019**, *11*, 1–6. https://doi.org/doi:10.3390/nu11102388.

(25) Ribaya-Mercado, J. D.; Blumberg, J. B. Lutein and Zeaxanthin and Their Potential Roles in Disease Prevention. *J. Am. Coll. Nutr.* **2013**, 37–41. https://doi.org/10.1080/07315724.2004.10719427.

(26) Mrowicka, M.; Mrowicki, J.; Kucharska, E.; Majsterek, I. Lutein and Zeaxanthin and Their Roles in Age-Related Macular. *Nutrients* **2022**, *14* (827), 1–14. https://doi.org/https://doi.org/10.3390/nu14040827.

(27) Di Gioia, F.; Renna, M.; Santamaria, P. Sprouts, Microgreens and "Baby Leaf" Vegetables. *Minim. Process. Refrig. Fruits Veg.* **2017**, No. 11, 403–432. https://doi.org/DOI 10.1007/978-1-4939-7018-6_11.

(28) Kyriacou, M. C.; Rouphael, Y.; Di Gioia, F.; Kyratzis, A.; Serio, F.; Renna, M.; De Pascale, S.; Santamaria, P. Micro-Scale Vegetable Production and the Rise of Microgreens. *Trends Food Sci. Technol.* **2016**, *57*, 103–115. https://doi.org/10.1016/j.tifs.2016.09.005.

(29) Teng, J.; Liao, P.; Wang, M. The Role of Emerging Micro-Scale Vegetables in Human Diet and Health Benefits - An Updated Review Based on Microgreens. *Food Funct.* **2021**, *12* (5), 1914–1932. https://doi.org/10.1039/d0fo03299a.

(30) Ramirez, D.; Abellán-Victorio, A.; Beretta, V.; Camargo, A.; Moreno, D. A. Functional Ingredients from Brassicaceae Species: Overview and Perspectives. *Int. J. Mol. Sci.* **2020**, *21* (6), 1–21. https://doi.org/10.3390/ijms21061998.

(31) Podsędek, A. Natural Antioxidants and Antioxidant Capacity of Brassica Vegetables : A Review. *LWT - Food Sci. Technol.* **2007**, *40*, 1–11. https://doi.org/10.1016/j.lwt.2005.07.023.

(32) Xiao, Z.; Lester, G. E.; Luo, Y.; Wang, Q. Assessment of Vitamin and Carotenoid Concentrations of Emerging Food Products: Edible Microgreens. *J. Agric. Food Chem.* **2012**, *60* (31), 7644–7651. https://doi.org/https://doi.org/10.1021/jf300459b.

(33) Weber, C. F. Broccoli Microgreens: A Mineral-Rich Crop That Can Diversify Food Systems. *Front. Nutr.* **2017**, *4* (March), 1–9. https://doi.org/10.3389/fnut.2017.00007.

(34) Renna, M.; Paradiso, V. M. Ongoing Research on Microgreens: Nutritional Properties, Shelf-Life, Sustainable Production, Innovative Growing and Processing Approaches. *Foods* **2020**, *9* (6), 1–5. https://doi.org/10.3390/foods9060826.

(35) Sharma, S.; Shree, B.; Sharma, D.; Kumar, S.; Kumar, V.; Sharma, R.; Saini, R. Vegetable Microgreens: The Gleam of next Generation Super Foods, Their Genetic Enhancement, Health

Benefits and Processing Approaches. *Food Res. Int.* **2022**, *155* (111038), 1–18. https://doi.org/10.1016/j.foodres.2022.111038.

(36) Samuolienė, G.; Viršilė, A.; Brazaitytė, A.; Jankauskienė, J.; Sakalauskienė, S.; Vaštakaitė, V.; Novičkovas, A.; Viškelienė, A.; Sasnauskas, A.; Duchovskis, P. Blue Light Dosage Affects Carotenoids and Tocopherols in Microgreens. *Food Chem.* **2017**, *228*, 50–56. https://doi.org/10.1016/j.foodchem.2017.01.144.

(37) Brazaityte, A.; Sakalauskiene, S.; Samuoliene, G.; Jankauskiene, J.; Viršile, A.; Novičkovas, A.; Sirtautas, R.; Miliauskiene, J.; Vaštakaite, V.; Dabašinskas, L.; Duchovskis, P. The Effects of LED Illumination Spectra and Intensity on Carotenoid Content in Brassicaceae Microgreens. *Food Chem.* **2015**, *173*, 600–606. https://doi.org/10.1016/j.foodchem.2014.10.077.

(38) Podsędek, A.; Frąszczak, B.; Sosnowska, D.; Kajszczak, D.; Szymczak, K.; Bonikowski, R. LED Light Quality Affected Bioactive Compounds, Antioxidant Potential, and Nutritional Value of Red and White Cabbage Microgreens. *Appl. Sci.* **2023**, *13* (9). https://doi.org/10.3390/app13095435.

(39) Turner, E. R.; Luo, Y.; Buchanan, R. L. Microgreen Nutrition, Food Safety, and Shelf Life: A Review. *J. Food Sci.* **2020**, *85* (4), 870–882. https://doi.org/10.1111/1750-3841.15049.

(40) Guzman, I.; Yousef, G. G.; Brown, A. F. Simultaneous Extraction and Quantitation of Carotenoids, Chlorophylls, and Tocopherols in Brassica Vegetables. *J. Agric. Food Chem.* **2012**, *60* (29), 7238–7244. https://doi.org/10.1021/jf302475d.

(41) Xiao, Z.; Rausch, S. R.; Luo, Y.; Sun, J.; Yu, L.; Wang, Q.; Chen, P.; Yu, L.; Stommel, J. R. Microgreens of Brassicaceae: Genetic Diversity of Phytochemical Concentrations and Antioxidant Capacity. *LWT - Food Sci. Technol.* **2019**, *101*, 731–737. https://doi.org/10.1016/j.lwt.2018.10.076.

(42) Caroline, L.; Ruffo, V.; Oliveira, D.; Hickmann, S.; Elisabeth, M.; Hagen, K.; Rios, A. D. O. Carotenoids, Flavonoids, Chlorophylls, Phenolic Compunds and Antioxidant Activity in Fresh and Cooked Broccoli (Brassica Oleracea Var. Avenger) and Cauliflower (Brassica Oleracea Var. Alphina F1). *LWT - Food Sci. Technol.* **2015**, *63*, 177–183. https://doi.org/10.1016/j.lwt.2015.03.089.

(43) Lefsrud, M.; Kopsell, D.; Wenzel, A.; Sheehan, J. Changes in Kale (Brassica Oleracea L . Var . Acephala) Carotenoid and Chlorophyll Pigment Concentrations during Leaf Ontogeny. *Sci. Hortic. (Amsterdam).* **2007**, *112*, 136–141. https://doi.org/10.1016/j.scienta.2006.12.026.

(44) Kurilich, A. C.; Tsau, G. J.; Brown, A.; Howard, L.; Klein, B. P.; Jeffery, E. H.; Kushad, M.; Wallig, M. A.; Juvik, J. A. Carotene , Tocopherol , and Ascorbate Contents in Subspecies of Brassica Oleracea. *J. Agric. Food Chem.* **1999**, *47*, 1576–1581. https://doi.org/10.1021/jf9810158.

(45) Farnham, M. W.; Vegetable, U. S. Importance of Genotype on Carotenoid and Chlorophyll Levels in Broccoli Heads. *HortScience* **2009**, *44* (5), 1248–1253. https://doi.org/DOI: 10.21273/HORTSCI.44.5.1248.

(46) Kim, M. J.; Chiu, Y.; Ku, K. Glucosinolates , Carotenoids , and Vitamins E and K Variation from Selected Kale and Collard Cultivars. *J. Food Qual.* **2017**, *2017*. https://doi.org/10.1155/2017/5123572.

(47) Mageney, V.; Baldermann, S.; Albach, D. C. Intraspecific Variation in Carotenoids of Brassica Oleracea Var. Sabellica. *J. Agric. Food Chem.* **2016**, *64*, 3251–3257. https://doi.org/10.1021/acs.jafc.6b00268.

(48) Ferioli, F.; Giambanelli, E.; D'Antuono, F. L.; Costa, H. S.; Albuquerque, T. G.; Silva, A. S.; Hayran, O.; Koçaoglu, B. Comparison of Leafy Kale Populations from Italy , Portugal , and Turkey for Their Bioactive Compound Content : Phenolics , Glucosinolates , Carotenoids , and Chlorophylls. *J. Sci. Food Agric.* **2013**, *93*, 3478–3489. https://doi.org/10.1002/jsfa.6253.

(49) Rezanka, T.; Olsovska, J.; Sobotka, M.; Sigler, K. The Use of APCI-MS with HPLC and Other Separation Techniques for Identification of Carotenoids and Related Compounds. *Curr. Anal. Chem.* **2009**, *5* (1), 1–25. https://doi.org/10.2174/157341109787047862.

(50) Britton, G.; Liaaen-Jensen, S.; Pfander, H. *Carotenoids: Handbook*; 2004. https://doi.org/DOI 10.1007/978-3-0348-7836-4.

(51) Crupi, P.; Milella, R. A.; Antonacci, D. Simultaneous HPLC-DAD-MS (ESI+) Determination of Structural and Geometrical Isomers of Carotenoids in Mature Grapes. *J. Mass Spectrom.* **2010**, *45* (9), 971–980. https://doi.org/10.1002/jms.1794.

(52) Dong, L.; Shion, H.; Davis, R. G.; Terry-penak, B.; Castro-perez, J.; Breemen, R. B. Van. Collision Cross-Section Determination and Tandem Mass Spectrometric Analysis of Isomeric Carotenoids Using Electrospray Ion Mobility Time-of-Flight Mass Spectrometry. *Anal. Chem.* **2010**, *82* (21), 9014–9021. https://doi.org/10.1021/ac101974g.

(53) Schieber, A.; Carle, R. Occurrence of Carotenoid Cis-Isomers in Food: Technological, Analytical, and Nutritional Implications. *Trends Food Sci. Technol.* **2005**, *16* (9), 416–422. https://doi.org/10.1016/j.tifs.2005.03.018.

(54) Ruperez, F. J.; Martın, D.; Herrera, E.; Barbas, C. Chromatographic Analysis of α-Tocopherol and Related Compounds in Various Matrices. *J. Chromatogr. A* **2001**, *935*, 45–69. https://doi.org/https://doi.org/10.1016/S0021-9673(01)01101-3.

(55) Neto, F. C.; Guaratini, T.; Costa-lotufo, L.; Colepicolo, P. Re-Investigation of the Fragmentation of Protonated Carotenoids by Electrospray Ionization and Nanospray Tandem

Mass Spectrometry. *Rapid Commun. Mass Spectrom.* **2016**, *30* (February), 1540–1548. https://doi.org/10.1002/rcm.7589.

(56) Arrizabalaga-Larrañaga, A.; Rodríguez, P.; Medina, M.; Santos, F. J.; Moyano, E. Simultaneous Analysis of Natural Pigments and E-141i in Olive Oils by Liquid Chromatography–Tandem Mass Spectrometry. *Anal. Bioanal. Chem.* **2019**, *411* (21), 5577–5591. https://doi.org/10.1007/s00216-019-01939-3.

(57) Molnar, P.; Szabolcs, J.; Radics, L. Naturally Occurring Di-Cis-Violaxanthin from Viola Tricolor: Isolation and Identification by 1H NMR Spectroscopy of Four Di-Cis-Isomers. *Phytochemistry* **1986**, *25*, 195–199. https://doi.org/https://doi.org/10.1016/S0031-9422(00)94528-X.

(58) Meléndez-Martínez, A. J.; Vicario, I. M.; Heredia, F. J. Geometrical Isomers of Violaxanthin in Orange Juice. *Food Chem.* **2006**, *104* (1), 169–175. https://doi.org/10.1016/j.foodchem.2006.11.017.

(59) Kao, T. H.; Loh, C. H.; Inbaraj, B. S.; Chen, B. H. Determination of Carotenoids in Taraxacum Formosanum by HPLC-DAD-APCI-MS and Preparation by Column Chromatography. *J. Pharm. Biomed. Anal.* **2012**, *66*, 144–153. https://doi.org/10.1016/j.jpba.2012.03.035.

(60) van Breemen, R. B.; Huang, C.; Tan, Y.; Sander, L. C.; Schilling, A. B. Liquid Chromatography / Mass Spectrometry of Carotenoids Using Atmospheric Pressure Chemical Ionization. *J. Mass Spectrom.* **1996**, *31* (March 1995), 975–981. https://doi.org/https://doi.org/10.1002/(SICI)1096-9888(199609)31:9<975::AID-JMS380>3.0.CO;2-S.

(61) Donato, P.; Giuffrida, D.; Oteri, M.; Inferrera, V.; Dugo, P.; Mondello, L. Supercritical Fluid Chromatography × Ultra-High Pressure Liquid Chromatography for Red Chilli Pepper Fingerprinting by Photodiode Array , Quadrupole-Time-of-Flight and Ion Mobility Mass Spectrometry. *Food Anal. Methods* **2018**, 3331–3341. https://doi.org/https://doi.org/10.1007/s12161-018-1307-x Supercritical.

(62) Schenk, E. R.; Mendez, V.; Landrum, J. T.; Ridgeway, M. E.; Park, M. A.; Fernandez-lima, F. Direct Observation of Differences of Carotenoid Polyene Chain Cis/Trans Isomers Resulting from Structural Topology. *Anal. Chem.* **2014**, *86*. https://doi.org/dx.doi.org/10.1021/ac403153m.

(63) Pacini, T.; Fu, W.; Gudmundsson, S.; Chiaravalle, A. E.; Brynjolfson, S.; Palsson, B. O.; Astarita, G.; Paglia, G. Multidimensional Analytical Approach Based on UHPLC-UV-Ion Mobility-MS for the Screening of Natural Pigments. *Anal. Chem.* **2015**, *87* (5), 2593–2599. https://doi.org/10.1021/ac504707n.

(64) Groessl, M.; Graf, S.; Knochenmuss, R. High Resolution Ion Mobility-Mass Spectrometry for Separation and Identification of Isomeric Lipids. *Analyst* **2015**.

https://doi.org/10.1039/c5an00838g.

(65) Lalli, P. M.; Iglesias, B. A.; Toma, H. E.; Sa, G. F. De; Daroda, R. J.; Filho, C. S.; Szulejko, J. E.; Eberlin, M. N. Protomers:Formation, Separation and Characterization via Travelling Wave Ion Mobility Mass Spectrometry. *J. Mass Spectrom.* **2012**, No. March, 712–719. https://doi.org/10.1002/jms.2999.

(66) Xia, H.; Attygalle, A. B. Transformation of the Gas - Phase Favored O-protomer of P-aminobenzoic Acid to Its Unfavored N-protomer by Ion Activation in the Presence of Water Vapor: An Ion - Mobility Mass Spectrometry Study. *J. Mass Spectrom.* **2018**, No. December 2017, 353–360. https://doi.org/10.1002/jms.4066.

(67) Aderorho, R.; Chouinard, C. D. Determining Protonation Site in Fentanyl Protomers Using Ion Mobility-Aligned MS/MS Fragmentation. *Int. J. Mass Spectrom.* **2024**, *496* (December 2023), 117185. https://doi.org/10.1016/j.ijms.2023.117185.

(68) McCullagh, M.; Giles, K.; Richardson, K.; Stead, S.; Palmer, M. Investigations into the Performance of Travelling Wave Enabled Conventional and Cyclic Ion Mobility Systems to Characterise Protomers of Fluoroquinolone Antibiotic Residues. *Rapid Commun. Mass Spectrom.* **2019**, *33* (December 2018), 11–21. https://doi.org/10.1002/rcm.8371.

(69) Rivera, S. M.; Christou, P.; Canela-garayoa, R.; Introduction, I. IDENTIFICATION OF CAROTENOIDS USING MASS SPECTROMETRY. *Mass Spectrom. Rev.* **2014**, *33*, 353–372. https://doi.org/10.1002/mas.21390.

(70) Maoka, T.; Fujiwara, Y.; Hashimoto, K.; Akimoto, N. Characterization of Epoxy Carotenoids by Fast Atom Bombardment Collision-Induced Dissociation MS/MS. *Lipids* **2004**, *39* (2), 179–183. https://doi.org/10.1007/s11745-004-1217-3.

(71) van Breemen, R.; Schmitz, H. H.; Schwartz, S. J. Fast Atom Bombardment Tandem Mass Spectrometry of Carotenoids. *J. Agric. Food Chem.* **1995**, *43*, 384–389. https://doi.org/https://doi.org/10.1021/jf00050a024.

(72) Konovalov, V.V.; Kispert, L.D. AM1, INDO/S and optical studies of carbocations of carotenoid molecules. Acid induced isomerization. J. Chem. Soc., Perkin Trans. 2 **1999**, *4*, 901-910. https://doi.org/10.1039/A800551F.

Appendix 4

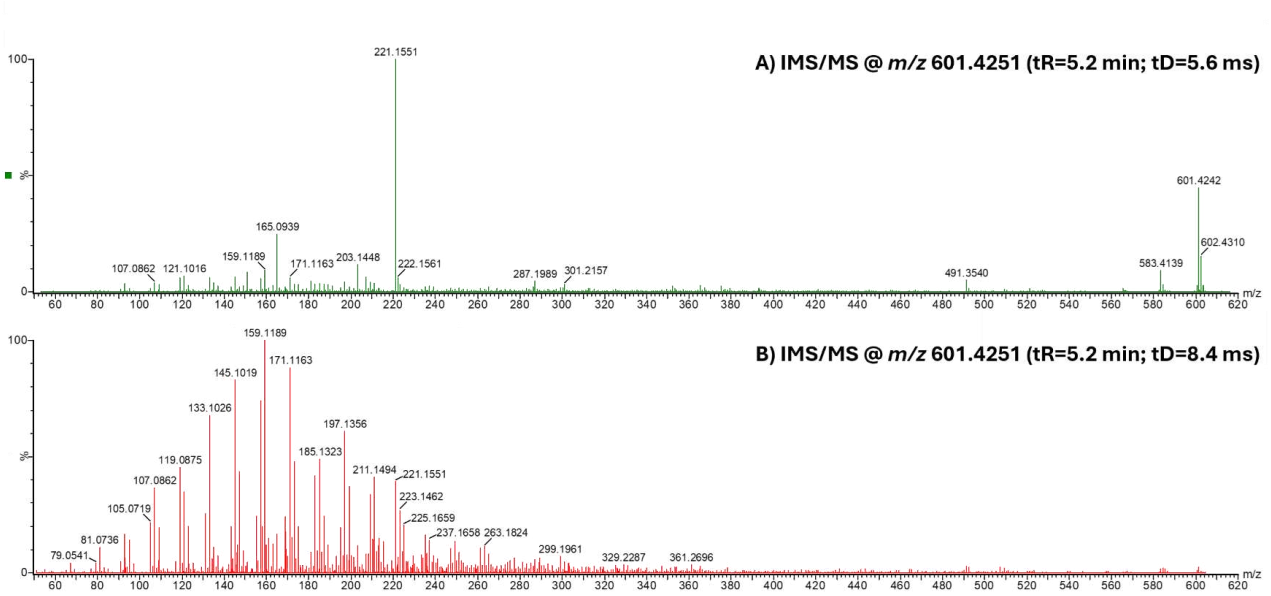


Figure A1. IMS-MS/MS spectra of the protomers of the $[M+H]^+$ ion of violaxanthin (*m/z* 601.4251) exhibiting drift times of 5.6 ms (plot A) and 8.1 ms (plot B).

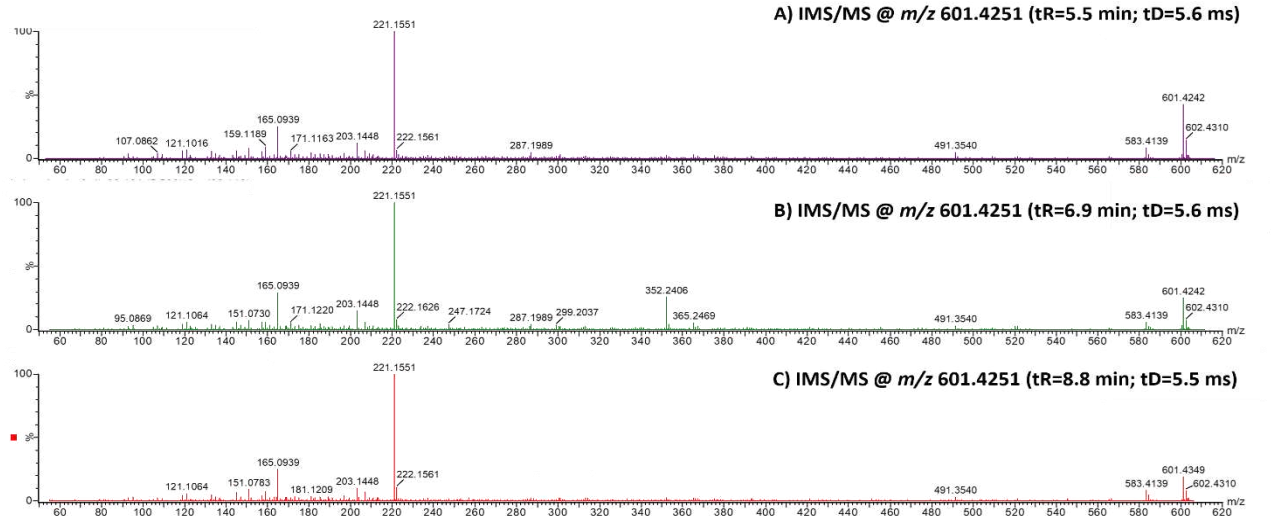


Figure A2. IMS-MS/MS spectra of the protomers with a drift time of 5.5-5.6 ms associated with the $[M+H]^+$ ions at *m/z* 601.4251 of violaxanthin (plot A), luteoxanthin (plot B) and auroxanthin (plot C).

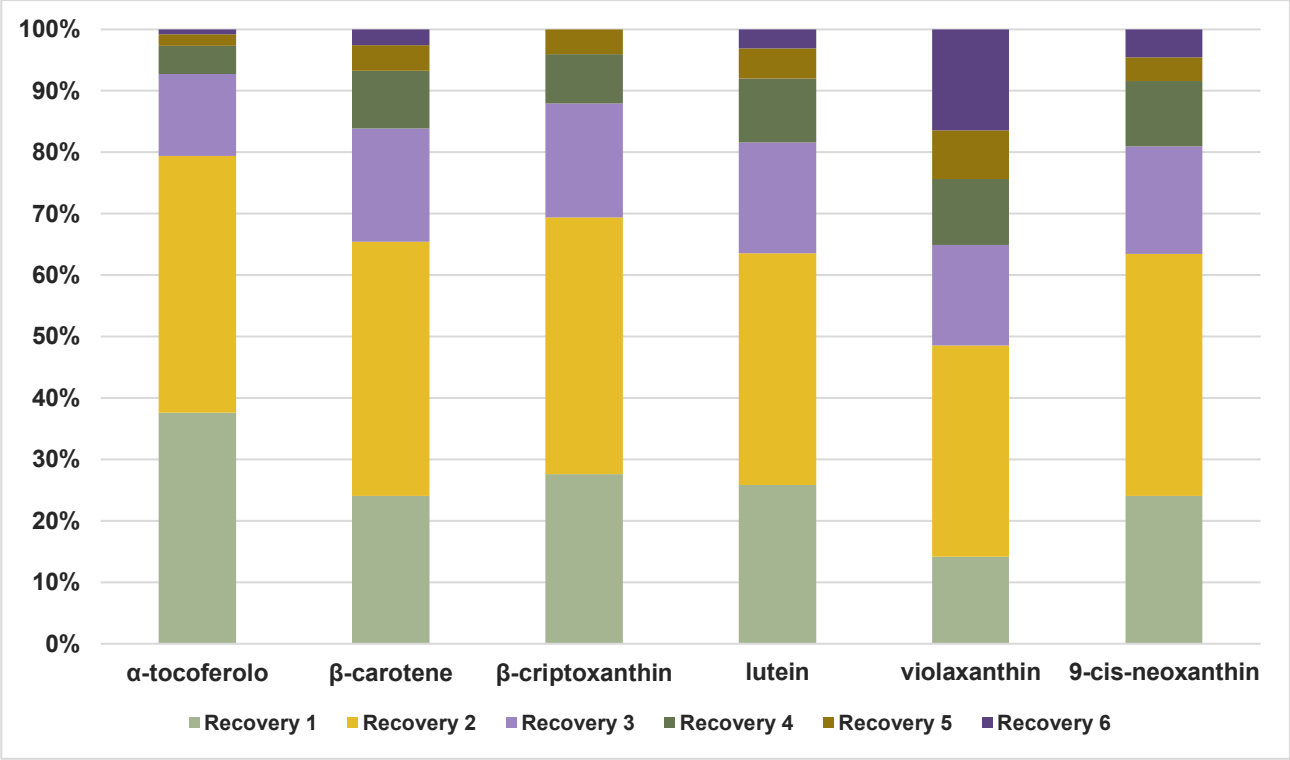


Figure A3. Stacked-bar graph reporting the average cumulative percentual recovery (n = 3) of α-tocopherol and main carotenoids detected in kale microgreens, evaluated after each of six successive extraction steps.

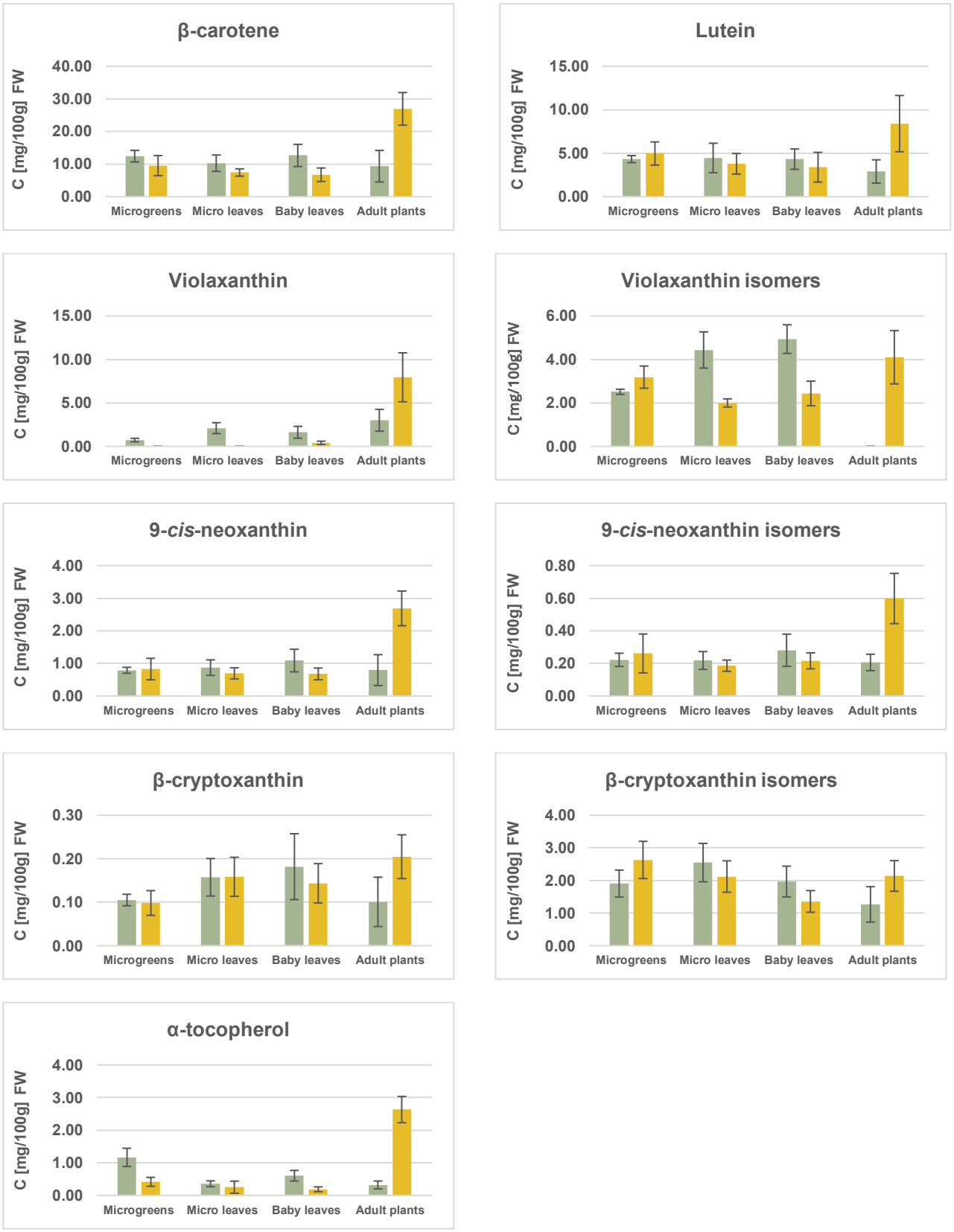


Figure A4. Column charts representing the amounts of carotenoids and α-tocopherol, expressed as mg/100g of fresh weight (FW), estimated as means for five samples of microgreens, micro leaves, baby leaves and adult plants of both broccoli raab (green) and kale (yellow). Error bars represent 95% confidence intervals.

Table A1. Retention times and relative intensity values of ions produced by in-source fragmentation and observed in the full-MS spectrum of each carotenoid detected in the kale microgreen extract. Peak labelling adopted for EIC chromatograms is reported in the second column, whereas the last column shows the nomenclature of the xanthophylls isomers assigned following Principal Component Analysis (PCA).

Retention time (min)	**Compound**	**$[M+H]^+$**	**$[M+H-H_2O]^+$**	**$[M+H-2H_2O]^+$**	**$[M+H-3H_2O]^+$**	**$[M+H-4H_2O]^+$**	**Compound post PCA**
2.8	1	100	77	26	2	1	nx1
2.9	2	100	76	26	2	1	nx2
3.2	3	62	100	28	2	1	nx3
3.4	9-*cis*-neoxanthin	100	82	30	3	1	9-*cis*-neoxanthin
4.4	violaxanthin	100	18	2	0.5	0.5	violaxanthin
5.5	4	100	15	2	0.5	0.5	vx1
5.8	5	100	13	2	0.5	0.5	vx2
6.9	6	100	12	0.5	0.5	0.5	vx3
7.6	7	100	10	2	0.5	0.5	vx4
8.4	8	100	13	0.5	0.5	0.5	vx5
8.9	9	100	16	0.5	0.5	0.5	vx6
9.7	10	100	18	0.5	0.5	0.5	vx7
10.4	lutein	32	100	4	/	/	lutein
15.9	11	24	100	2	/	/	lt1
18.3	12	22	100	2	/	/	lt2
28.0	13	100	16	/	/	/	cr1
28.2	14	100	16	/	/	/	cr2
28.6	β-crypto-xanthin	100	15	/	/	/	β-crypto-xanthin
29.0	15	100	14	/	/	/	cr3
32.9	16	100	10	/	/	/	cr4
33.1	17	100	14	/	/	/	cr5
34.1	18	100	16	/	/	/	cr6
34.7	19	100	15	/	/	/	cr7
36.5	20	100	6	/	/	/	cr8
36.8	21	100	8	/	/	/	cr9
37.5	22	100	4	/	/	/	cr10
47.3	β-carotene	100	/	/	/	/	β-carotene

Table A2. Summary of the information inferred for carotenoids after the RPLC-ESI(+)-TWIMS analysis of kale microgreens extracts, chosen as a representative matrix of those investigated in this thesis work. In the table $^{TW}CCS_{N2}$ and CCS_{theor} represent collision cross sections measured during this work or reported in the literature, respectively, whereas DW represents the difference observed between the experimental and the reported CCS value for a specific isomer, measured as a percentage of the latter.

Compound	Hypothesized compound	Retention time (min)	$[M+H]^+$				$[M+H-H_2O]^+$				$[M+H-2H_2O]^+$				$[M+H-3H_2O]^+$			
			Drift time (milli sec)	$^{TW}CCS_{N_2}$ (Å²)	ΔΩ (%)	$CCS_{theor.}$ (Å²)	Drift time (milli sec)	$^{TW}CCS_{N_2}$ (Å²)	ΔΩ (%)	$CCS_{theor.}$ (Å²)	Drift time (milli sec)	$^{TW}CCS_{N_2}$ (Å²)	ΔΩ (%)	$CCS_{theor.}$ (Å²)	Drift time (milli sec)	$^{TW}CCS_{N_2}$ (Å²)	ΔΩ (%)	$CCS_{theor.}$ (Å²)
nx1	9,15-di-*Z*-neoxanthin	3.1	8.17	316.914	/	Not available	5.39	252.384	/	Not available	5.31	250.327	/	Not available	5.10	244.858	/	Not available
nx2	9,13-di-*Z*-neoxanthin	3.3	8.22	317.974	/	Not available	5.41	252.897	/	Not available	5.32	250.585	/	Not available	5.10	244.858	/	Not available
nx3	(8'R)-neochrome	3.6	8.11	315.638	28.6	245.5	5.52	255.699	/	Not available	5.38	252.128	/	Not available	/	/	/	/
9-*cis*-neoxanthin	9-*cis*-neoxanthin	4.0	8.25	318.609	28.3	247.0	5.42	253.182	1.6	249.1	5.31	250.327	/	Not available	5.13	245.648	/	Not available
violaxanthin	violaxanthin	5.2	8.31	319.875	29.5	247.7	5.53	255.986	2.4	250.1	5.40	252.641	/	Not available	5.15	246.169	/	Not available
vx1	(8S)-luteoxanthin	6.9	5.75	261.477	5.7	247.3	5.39	252.384	1.5	248.6	/	/	/	/	/	/	/	/
vx2	(8'R)-luteoxanthin	7.4	5.73	260.979	5.5	247.3	5.41	252.897	1.7	248.6	/	/	/	/	/	/	/	/
vx3	(8S,8'S)-auroxanthin	8.8	5.68	259.729	/	Not available	5.48	254.683	/	Not available	/	/	/	/	/	/	/	/
vx4	luteoxanthin like	9.3	5.89	264.943	/	Not available	5.39	252.384	/	Not available	/	/	/	/	/	/	/	/
vx5	(8R,8'S)-auroxanthin	9.8	5.64	258.727	/	Not available	5.49	254.937	/	Not available	/	/	/	/	/	/	/	/
vx6	luteoxanthin like	10.8	5.82	263.214	/	Not available	5.41	252.897	/	Not available	/	/	/	/	/	/	/	/
vx7	(8R,8'R)-auroxanthin	11.1	5.68	259.729	/	Not available	5.49	254.937	/	Not available	/	/	/	/	/	/	/	/

Table A3. Mean values and 95% confidence intervals (n = 5) obtained for the concentrations of carotenoids and α-tocopherol in raw, boiled and steamed mature plants of broccoli raab and kale and expressed as mg per 100 g of fresh weight (FW). In the case of cooked samples, FW is meant as the weight found after cooking and draining, before proceeding to freeze-drying. Concentration values referred to isomers related to violaxanthin, 9-cis-neoxanthin and β-cryptoxanthin, were expressed cumulatively.

Compounds	Broccoli raab			Kale		
	Raw	Boiled	Steamed	Raw	Boiled	Steamed
β-carotene	9 ± 5	8 ± 3	8 ± 2	27 ± 5	16 ± 4	19 ± 7
lutein	2.9 ± 1.3	2.5 ± 1.0	2.8 ± 0.7	8 ± 3	6 ± 2	7 ± 3
violaxanthin	3.0 ± 1.3	1.3 ± 0.3	< LOD	8 ± 3	1.5 ± 0.4	< LOD
violaxanthin isomers	< LOD	< LOD	< LOD	4.1 ± 1.2	2.4 ± 0.4	< LOD
9-*cis*-neoxanthin	0.8 ± 0.5	0.5 ± 0.2	0.36 ± 0.18	2.7 ± 0.5	1.1 ± 0.3	0.6 ± 0.2
9-*cis*-neoxanthin isomers	0.21 ± 0.05	0.22 ± 0.11	0.19 ± 0.05	0.60 ± 0.15	0.58 ± 0.14	0.40 ± 0.19
β-cryptoxanthin	0.10 ± 0.06	0.13 ± 0.04	0.16 ± 0.08	0.21 ± 0.05	0.151 ± 0.018	0.19 ± 0.04
β-cryptoxanthin isomers	1.2 ± 0.6	0.6 ± 0.06	0.6 ± 0.06	2.1 ± 0.5	1.34 ± 0.12	2.6 ± 0.3
α-tocopherol	0.32 ± 0.12	0.9 ± 0.2	0.67 ± 0.17	2.6 ± 0.4	1.6 ± 0.3	1.6 ± 0.4

Concluding remarks

This thesis work started with the main goal of achieving a deeper insight into the profile of important vegetal nutraceuticals, like phytosterols, carotenoids and α-tocopherol, in innovative products of two plants of the *Brassicaceae* family, kale and broccoli raab, whose adult forms have both gastronomical and economical relevance in Southern Italy. The achievement of this goal led to important results both from a methodological point of view and in terms of new knowledge on the nutraceutical potential of vegetal products like microgreens, micro leaves and baby leaves, as well as on the relationship between them and their adult counterparts.

As for the methodological advancements, this work showed that, although targeted metabolomics based on state-of-the-art mass spectrometry techniques has progressively achieved very important results also when applied to vegetal matrices, there is still room for significant improvements in terms of fundamental knowledge on plant metabolites. Indeed, the careful development of elution programs to be used with conventional reversed phase liquid chromatography columns led to emphasize, both for phytosterols and for carotenoids, the presence of several compounds in addition to major ones, that could be easily recognized through the comparison with commercial standards.

The tentative identification of minor metabolites belonging to the two classes represented a very hard challenge but, at the same time, provided the opportunity to push liquid chromatography-mass spectrometry towards new limits. In the case of phytosterols, the systematic interpretation of the complex MS/MS fragmentation patterns obtained for protonated/dehydrated ions resulting from APCI ionization of selected standards, including both vegetal sterols and animal/fungal sterols, led to unveil very interesting trends in fragmentation processes, enabling the establishment of several diagnostic correlations with specific structural features. The interpretation of fragmentation patterns, only partially considered so far in the literature, was greatly enhanced by the application of MS/MS also to standards of major sterols isotopically labelled not on the steroidal ring, as occurred in previous

studies, but on specific positions of the respective side chains. Indeed, characteristic product ions certainly related to this part of the molecular structure were evidenced and, notably, their generation clearly implied the occurrence of a very characteristic and rare process during the fragmentation of sterol positive ions, *i.e.*, the intra-molecular transfer of hydride ions, opening the way to the relocation of the original positive charge on other positions of the molecular structure, favoured by the greater stability of the resulting carbocations.

In the case of carotenoids, the complexity of the profile emerging from the coupling of RPLC with APCI-HRMS required an even stronger effort in terms of structural interpretation, since the occurrence of a remarkable number of minor compounds, isomeric with major xanthophylls, was evidenced upon the analysis of innovative and conventional forms of the two plants under study. To add further difficulty to this scenario, MS/MS was unable, by itself, to provide definitive information on the minor carotenoids structures, as the respective fragmentation patterns were generally very similar. In this case only a multi-dimensional detection approach, including not only HRMS but also UV-Vis spectroscopy and ion mobility spectrometry, as such or coupled with MS/MS, led to useful information on at least part of the minor compounds. In fact, characteristic in-source fragmentation patterns, related to sequential water molecules losses, were observed in their HRMS spectra and enabled a nice association between them and major carotenoids using chemometrics. In a subsequent step, spectral features evidenced in UV-Vis spectra enabled the inference of the number and position of C=C bonds in the molecular structures, leading to the first tentative identifications. Finally, MS/MS spectra obtained for isomeric ions resulting from the same carotenoid and preliminarily separated in a travelling wave ion mobility cell, due to differences in collision cross sections, helped in confirming the structural hypotheses by considering that specific product ions could be generated only if the positive charge of the precursor ions was located on certain positions. In turn, this observation led to hypothesise that the multiple mobilities observed for $[M\text{-}nH_2O]^+$ ions of carotenoids during IMS analyses could be related to protomers, rather than conformers or, even more unlikely, to geometric

isomers. This is, *per se*, a very important achievement in terms of fundamental knowledge for the IMS-MS analysis of carotenoids.

Once detailed qualitative profiles were obtained both for phytosterols and carotenoids, the respective quantification could be performed in all the vegetal products of interest. In this case, great care was preliminarily posed in maximising the yield related to the adopted extraction protocols and in evaluating the occurrence of matrix effects, that are often overlooked in targeted vegetal metabolomics, despite the complexity of matrices. Moreover, the variability related to the sampling of lots of freeze-dried vegetal products, that had to be produced by pooling the material resulting from single young plants, in the case of innovative products, was carefully evaluated.

Both for phytosterols and for carotenoids quantitative data indicated microgreens, micro leaves and/or baby leaves of kale and broccoli raab as potential alternatives to the respective adult counterparts, since one or more of them contained total amounts of the two types of metabolites comparable to those occurring in adult forms. In this case the comparison was performed not only versus raw adult forms, as often made in the literature when nutraceuticals are evaluated in innovative vegetal products, but also considering adult plants preliminarily subjected to cooking, through boiling or steaming, since these processes have to be adopted to make those plants edible. As a result, while cooking did not determine a decrease in the total phytosterol content, the carotenoid content was slightly altered for broccoli raab and significantly affected by both cooking approaches in the case of kale, with a reduction to almost 50% with respect to the raw adult form of this plant.

Besides the advantage of consumption without preliminary cooking, microgreens, micro leaves and baby leaves of both kale and broccoli raab exhibited a more diversified profile both for phytosterols and carotenoids. This characteristic, that led to an interesting discrimination between them and adult forms when chemometrics (PCA and HCA) was performed on quantitative data, opens important perspectives for the future evaluation of the nutraceutical potential of these products. This is particularly relevant in the case of carotenoids, since, when considered cumulatively, minor isomers

exhibited a remarkable contribution to the total content, whereas they were sometimes totally absent in mature forms.

The outcomes of this thesis work thus strengthen the hypothesis that innovative products like microgreens, micro leaves and baby leaves, originally considered almost as a culinary oddness, but subsequently, and currently, evaluated as fresh vegetables suitable for cultivation and consumption in space stations/colonies, can become a healthy and sustainable complement, as ready-to-eat products, of conventional vegetables in the human diet for the future.